THE PROCEEDINGS OF
THE PHYSICAL SOCIETY

Section A

VOL. 63, PART 8 1 August 1950 No. 368 A

The Sliding Surface *

By G. I. FINCH

34th Guthrie Lecture, delivered 3rd March 1950

§ 1. INTRODUCTION

LIFE is possible because some assemblages of matter can store sunlight as chemical energy. Other organisms, unable to do this directly, absorb these stores to supply their own energy needs; and some, like man, prey on both to live. Man alone supplements the body's production of physical energy by using inanimate devices to unlock the stores of energy latent in the remnants of past life. The key is the machine, which works because smooth surfaces can slide over each other. The sliding surface is, therefore, fundamental to our modern way of life.

The sliding surface was known long before the machine; away back in antiquity man had used it to ease the burden on his back. He had also learnt the value of a generous supply of some slippery substance. So when the machine did arrive the engineer saw to it that its sliding surfaces were lubricated; so well, indeed, that they were kept apart by an oil layer many hundreds or even thousands of molecules thick. Nowadays, however, sliding surfaces are usually so heavily pressed together that the lubricant film cannot be more than a few molecules thick, and is often penetrated or disrupted so that the sliding surfaces touch in places.

Thick-layer, or, as it is generally known, hydrodynamic lubrication (Reynolds 1886) favours easy sliding without wear other than that due to corrosion and erosion, but with boundary (or molecular film) conditions † of lubrication, where the sliding surfaces often come into contact, suppression of wear becomes the main problem. Thus, in hydrodynamic lubrication chief interest is directed to the lubricant, but in boundary lubrication it is the sliding surface which claims first attention. What causes rubbing surfaces to wear and how do they wear? What peculiarity in the surface helps to reduce wear and how does it work? How do the surfaces slide when they touch each other? What is it about the surfaces that helps them to slide and how does it help? We must first seek the answers to questions like these before turning to the study of the lubricant boundary film.

As far back as the eighteenth century Coulomb (1781) thought that resistance to sliding was due to the interlocking of surface asperities, and that the fracture of these during sliding was responsible for wear. Ewing (1912) and Hardy and

---

* This lecture also appeared in the July issue of Section B, p. 465.

† The term 'boundary conditions' was first used by Reynolds.

Hardy (1919), on the other hand, believed that the interplay of surface cohesive forces was the dominant factor. While Coulomb's view may once have served a useful purpose, it is completely at variance with modern engineering experience. Furthermore, the results of critical surface studies by Beilby (1921), Hardy (1936), Finch (1937), Bowden and Tabor (1939) and Parker and Hatch (1950) do not support Coulomb's hypothesis but are readily interpreted in terms of surface cohesive forces.

The forces which produce cohesion within a block of metal must also act at the surface of contact between two blocks; they should, therefore, resist stress as if the blocks were one. There are, indeed, facts which support this conclusion. Slip gauges left 'wrung' together eventually seize and are damaged when separated. Hardy and Hardy (1919) found that some solids seized together on contact. Fifteen years ago I showed—and it must have been known long before then—that mica cleavage surfaces could adhere firmly when brought together (Demonstration). But experience also shows that surfaces can, and often do, slide easily over each other, even in the absence of lubricating oil.

Although a solid exerts a cohesive force on an atom beyond its surface, the intensity of the force decreases rapidly with distance, to become negligible a few atomic radii away. Contact between two surfaces, therefore, implies approach to within this distance. It is possible, by cleaving certain mineral crystals, to produce atomically smooth plane surfaces of considerable area, but otherwise such a degree of smoothness cannot in general be achieved or even approached. Hence, when two nominally plane surfaces formed, let us suppose, on two blocks of the same metal are placed together, contact can occur only at three points. If the surfaces are now loaded, stress at the points of contact must exceed the elastic limit. Plastic flow will then enlarge the points of contact to areas, and fresh points of contact expanding to still more areas will be established, until the load is borne without further deformation of the material.[*] A considerable effort should now be required to pull or shear the blocks apart because, at the areas of contact, they should have become united. Experiment, however, gives a different result. Thus, mica cleavage surfaces which have been exposed to the atmosphere for some time, or momentarily immersed in water, will no longer adhere, no matter how hard they are forced together (Demonstration). If, instead of being 'wrung', two slip gauges are merely pressed together, they do not stick but fall apart when the pressure is released (Demonstration). Mechanically or anodically polished surfaces of copper, iron, silver, tin and other metals behave similarly, provided the pressure does not cause general plastic flow at the surfaces (Demonstration). An atomic degree of smoothness, superimposed, it is true, on a large-scale waviness of small amplitude, may be imparted to a face of a copper single-crystal by anodic polishing; nevertheless, a degree of pressure short of that causing permanent distortion will not even partially weld two such surfaces together (Demonstration). In this case the undimmed clarity of the electron diffraction pattern shows that any adsorbed layer cannot be more than two or three atoms thick (Figure 1).[†]

---

[*] I frame these conclusions on the basis of Amontons' (1699) experimental law according to which the coefficient of friction is independent of the area of the sliding surfaces. The validity of this law has often been confirmed. The reasons for apparent exceptions are well understood; they do not affect the issue.

[†] Figures 1 and 3–20 are photographs and are printed together opposite p. 472.

It may therefore be inferred that true contact is not as a rule established when even atomically smooth solid surfaces are pressed together, but that they are kept apart by adsorbed surface layers which, while satisfying the cohesive forces at the surfaces, exert little or no attraction towards each other. The remarkable resistance of these layers to penetration appears to be independent of their nature (if it is assumed that this varies with the metal) and determined mainly by the physical properties of the metal, general plastic flow of which might be expected to rupture such a layer by extending its surface, and thus allowing welding to occur through direct metal-to-metal contact. It will be evident that this adsorbed layer is of vital importance. Without it, a pair of surfaces at rest under load would seize together over an area proportional to the imposed load. It cannot be supposed that welds are formed only to be broken when, on release of pressure, the surfaces are forced apart by a recovery of the metal about those areas where the elastic limit has not been exceeded; for the metal in such welds, being itself compressed to the elastic limit, would have the greater range of recovery on release of the pressure.

When the surfaces are not only pressed together but forced to slide past each other, the effectiveness of the adsorbed layers in preventing metal-to-metal contact varies greatly according to the nature of the metal. Anodically polished single-crystal copper or aluminium surfaces at first slide then suddenly lock firmly together, even with light loading (Demonstration). Similarly prepared polycrystalline surfaces of these metals also seize quickly, though not quite so readily as single crystals (Demonstration); the corresponding mechanically polished surfaces slide more easily and are much more resistant to seizure (Demonstration). Anodically polished polycrystalline silver or iron single-crystal pairs slide freely and must be heavily loaded before signs of seizure appear (Demonstration), and similar experiments with combinations of anodically polished single-crystal and polycrystalline surfaces of various metals reveal further wide differences in the ease or otherwise with which sliding and particularly seizure take place. But whether this is to be attributed to the physical properties of the metal, as in the case of the loaded surface pair at rest, or whether the nature of the adsorbed layer is also significant, remains to be seen.

The existence of these layers has long been known. Faraday (1838) and De la Rive (1839) recognized their importance in heterogeneous catalysis, and they have since been much studied by the chemist. The physicist's interest seems to have been first fully aroused by their effect on thermionic and photoelectric emission (Langmuir 1916). The engineer, so long accustomed to hydrodynamic lubrication, has been slower to appreciate their value.

The layer is difficult to remove from a metal surface. It can be done by scraping or evaporating *in vacuo* and so exposing a fresh surface, or by heating to a high temperature *in vacuo* or in the presence of atomic hydrogen; but the layer re-forms spontaneously and rapidly, even at room temperature, on exposure to air. These facts suggest that the adsorption is chemical rather than physical, and that the layer is an oxide of the metal. This has been amply confirmed by electron diffraction.

Although oxidation is the immediate result of the exposure of a fresh metal surface to the atmosphere, the microbalance reveals that a moisture film of considerable thickness (as much as 80 molecular layers and possibly more) may be adsorbed on the oxide surface. When fresh, this layer is as a rule not strongly held and is removed by the electron beam in the evacuated diffraction camera.

§ 2. THE SLIDING ELEMENT

It is clear that the sliding element of the modern machine must be a highly complex system. Actually its simplest form comprises at least nine distinct components (Figure 2). These are (i) and (ii) the metallic backings supporting (iii) and (iv) the pair of metal surface layers or so-called bearing surfaces which, in turn, carry (v) and (vi) their appropriate oxide layers each with its (vii) and (viii) adsorbed boundary layer of lubricant, and (ix) an oil film of varying thickness held between the boundary layers and more or less charged with debris, moisture and gas bubbles. The components in each pair may differ widely in nature and properties, even in the case of the two lubricant boundary layers. Furthermore, a change in any one component may also affect the behaviour of the others. It is this astonishing complexity in what at first sight appears to be a simple system that explains why, in the past, research has been for the most part directed towards the special circumstance of practice, rather than to a fundamental study from which broad generalizations might be drawn. Clearly, the physicist's approach to the problem must be to break down the sliding element into its simplest components and to examine each in turn, first by itself and then in relation to the others.

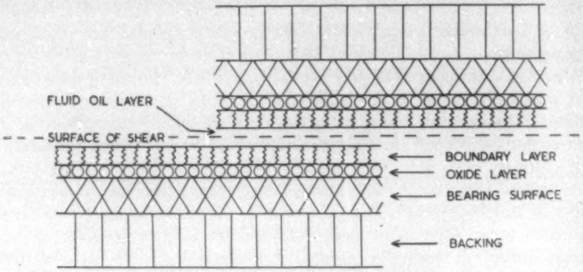

Figure 2. Diagram of the sliding element.

§ 3. THE BACKING

The backing is rigidly secured, directly or indirectly, to an appropriate member of the machine. Its function is to support the bearing surface so that its motion is constrained to the desired degree or degrees of freedom with respect to the other sliding member. In the case of a journal bearing, the force tending to rotate the backing in its housing may be considerable and is given by the product of the coefficient of friction between the sliding members and the load. Since the polar distribution of the load may vary periodically between wide extremes, particularly in the case of the internal combustion engine, the backing tends to oscillate in the housing. This may lead to serious frettage corrosion and loss of fit.

Backing and bearing surface may be composed of the same metal, as in the shaft of a journal bearing; or the metals may differ, as in the liner of the housing within which the shaft rotates. As the properties of the backing may affect the behaviour of the bearing surface, it will be convenient to defer its further discussion.

§4. THE BEARING SURFACE

The bearing surface is developed in practice as a plane or surface of revolution by abrasion processes such as cutting, grinding, honing and lapping. These operations reduce the crystal size of the metal at the surface, and often to a considerable depth below it (Figure 3). This 'work-hardening' can seriously impair the efficiency of the bearing surface, and for this reason the more severe operations of cutting and grinding should be followed by annealing to restore the uniformity of crystal size and relieve stress (Finch 1945). The texture of the finished surface is, in terms of atomic dimensions, exceedingly rough and made up of rows of steep hills and valleys, each with smaller irregularities and lying roughly parallel to the direction of cutting. The ridge crests are seen by electron diffraction to be crystalline (Figure 4).

General experience has shown that the fresh bearing surface must not be subjected to full loads and sliding speeds until it has been 'run-in' under light loads with copious supplies of lubricant. If the protuberances are not gradually reduced, as they are by 'running-in', the crystal structure will be broken up to such a depth below the surface as permanently to impair the sliding and resistance to wear of the surface. The effect of 'running-in' may be explained briefly as follows. Consider, first, bearing surfaces of similar metal. When, through breakdown of the oil and oxide layers, metal-to-metal contact is established between opposing high spots of the bearing surfaces, a weld is formed. As sliding motion proceeds the weld is stressed and eventually ruptured. If the crystal structure in the surfaces has not previously been broken up and therefore hardened, the weld will shear at or near one of the surfaces. On the other hand, if, owing to previous unduly severe conditions of machining or sliding, work-hardening has occurred to some depth below the surface, the weld, instead of rupturing virtually in the plane of sliding, will continue to adhere to one surface and pull out work-hardened metal to a considerable depth from the other (Figure 5). The protruding metal will then score and break up the crystal structure in this surface until it has been worn away; or it may break off and roll between the surfaces and damage them by crushing (Figure 6).

It is now known that sliding causes a profound and important change, not only in the texture but also in the structure of the metal surface. At first, rubbing of the sharper asperities on the opposing fresh bearing surfaces results largely in wear and the production of debris. As the surface becomes smoother, however, wear decreases and much of the metal removed from the hills 'flows', as Beilby (1921) puts it, into the valleys. Thus 'running-in' levels off the mountain ridges and fills the valleys to leave a texture like undulating hills. This smoothing is accompanied by a remarkable change in structure (Finch, Quarrell and Wilman 1935). Not only are the crystals broken up to a depth below the surface depending on the severity of 'running-in', but the surface layer structure becomes amorphous (Figure 7), as if 'flowing' consisted of the transfer of molten metal from one part of the surface to another where, having escaped the polishing action, it freezes too rapidly to crystallize. The thickness of this so-called Beilby layer depends, like that of the work-hardened crystalline zone beneath, on the severity of the 'running-in' conditions. Layers of only about fifteen atoms thick have been produced (Hopkins 1935) and others about 100 atoms thick have been successfully detached from their substrates (Cochrane 1938); but a vigorous polishing results in a much thicker layer (Finch, Quarrell and Roebuck 1934).

The following experiments will show how great is the protection afforded to the oxide layer by the support of even a very thin Beilby layer. Severe welding and extensive damage occurs when two anodically polished copper single-crystal surfaces are slid past each other (Figure 8) (Demonstration). The behaviour of a similar pair of surfaces, on one of which, however, a very thin Beilby layer has been formed by light polishing with rouge, is very different. Much heavier pressure is needed to cause welding, and on forcible separation of the surfaces metal is pulled out from the polished surface only to a shallow depth (Figure 9) (Demonstration). Thus the Beilby layer performs important functions in sliding. Its comparative smoothness favours a wide distribution of load where 'high spots' meet as the bearing surfaces slide past each other; it is more rigid than the underlying crystalline metal and thus better able to support the oxide layer and preserve it from injury; and a cold weld, with its tendency to pull out near the zone where the amorphous merges into the undisturbed crystalline structure, will do least damage if the Beilby layer is thin.

The relative amounts of metal worn away (and thus lost to the surface) and metal which is merely displaced to form the Beilby layer, are affected by the direction of the ridge and valley lines produced in machining in relation to that of sliding (Finch and Zahoorbux 1937). It has been found that the heaviest wear occurs when these lines in both bearing surfaces lie in the direction of sliding, and that wear is least when they are at right angles to the sliding direction. If the lines on one surface are parallel to the direction of sliding, while those on the other are at right angles to it, then wear of the former surface is high. The explanation is simple. When the lines in both surfaces are parallel to the sliding direction, the metal, severely stressed in localized contacts has farther to flow before it can escape and congeal beyond the pressure zone, and is thus more likely to form unattached detritus than when the ridges and valleys lie at right angles to the sliding. The importance of the 'run' of tooling tracks in relation to the sliding direction is now appreciated in engineering practice.

We have seen that when two nominally plane surfaces are pressed together the total cross-sectional area of the resulting intermetallic contact is proportional to the load. The force required to start sliding is therefore also proportional to the load; its value per unit load is known as the coefficient of static friction. To maintain sliding, work must be done. The necessary force is again proportional to the load, provided shear occurs at the interface and the strength of the metal in the contacts is unchanged. Under such conditions the dynamic and static coefficients of friction should be equal. Micrographic examination shows, however, that the cold welds formed on contact between, for example, single-crystal copper surfaces are strain-hardened as sliding proceeds, and also that the surrounding metal is similarly affected to a considerable depth (Figures 5 and 8). Hence, instead of the welds shearing at the interface, metal is pulled out bodily from below one surface to be dragged along and ruck and score the other (Figure 5). Under such conditions the dynamic coefficient exceeds the static. In normal practical conditions of sliding, of course, the reverse is the case, as the oxide and lubricant films together greatly limit intermetallic contact during sliding and may even in some cases inhibit it. Nevertheless, as a rule, spasmodic intermetallic contact does occur, and its contribution to the total resistance to sliding may be called intermetallic friction. Its most undesirable feature is that it causes wear.

A sliding element in which the intermetallic component of the total friction is considerable is therefore unsatisfactory.

So far we have considered bearing surface pairs of the same metal. In practice, however, where sliding speeds are high, this combination is avoided except in the case of cast iron. Otherwise the engineer's empirical rule is that the mating bearing surfaces should consist of metals of widely differing melting points. It can, indeed, be inferred from Bowden and Ridler's (1936) measurements of the temperatures attained at metal contacts in sliding that localized fusion followed by hot welding should occur more readily with like than with unlike metals. The matter, however, goes deeper than this. Solid mercury and gold would make an unsatisfactory pair of bearing surfaces.

Now, we have seen that in addition to hot welding due to melting of rubbing high spots on both bearing surfaces, cold welding also occurs on contact of the solid metals. Indeed, under the conditions of the experiments I showed you, the friction and surface damage was entirely due to cold welding and its after effects. Even with like metals, it is only under severe sliding conditions and more particularly at high speeds that hot welding becomes important. It will be evident, therefore, that in selecting metals for a bearing surface pair, one criterion is the intensity of the cohesive force across the interface of intermetallic contact, rather than disparity in their melting points. If this interfacial cohesion is less than that within the weaker of the two metals, intermetallic contacts will shear in the interface. The other criterion, which concerns the nature of the oxide layer, will be discussed later.

The problem of estimating this cohesive force from a knowledge of the structures of the outer electron shells of the atoms of which the contacting surfaces are composed has not been solved. However, a study of the coordination relationships between epitaxial metallic deposits and metallic single-crystal substrates is now being carried out in my laboratory (Finch and Sun 1936, Finch and Williams 1937, Finch, Wilman and Yang 1947); this seems to offer a promising line of experimental approach to the problem. In the meantime, as a rough and ready rule, we may take it that the more rigid the metals of a pair and the higher their melting points, the less will be the tendency to form *cold* welds.*

It would, I think, be fair to say that, as in the development of most aspects of the sliding surface, the choice of metals for bearing surface pairs has been empirical. The modern journal bearing practice is to use pairs in which one metal is hard and has a high melting point and the other is relatively soft and fusible. In the sliding of such combinations new phenomena appear.

Bowden and Hughes (1937) showed that when certain solids were rubbed together it was not the harder surface which caused the softer to flow and thus be polished, but that the more fusible surface was polished by the more refractory one, irrespective of their relative hardnesses at room temperature. In practice, however, sliding surfaces may well behave differently. For example, a type of journal bearing in common use consists of a superficially hardened alloy steel shaft rotating against a bearing surface of a rather soft tin-base alloy melting at about 250° c. Since the steel melts at roughly 1,400° c. the alloy surface becomes polished as one expects; what is surprising, however, is that the hardened surface of the shaft also flows and is polished as running-in of the bearing proceeds. Similar observations have been made in reciprocating sliding. Indeed, in all practical cases so far examined this mutual polishing of sliding metal surfaces has proved to be the rule, irrespective of the difference in hardness or fusibility of the bearing surface metals. The explanation is to be sought in the nature and properties, including the geometry, of the oxide layers and metals of the bearing surfaces, and will be discussed later.

---

* It would be virtually impossible to put together even two perfectly plane complementary single-crystal surfaces on a pair of blocks of the same metal in such a way as to restore the original atom coordination across the interface. The higher the mobility of the atoms, however, the greater is the chance of the atoms in the opposing faces moving into and being retained in sites of lowest potential energy. This is akin to a process of recrystallization whereby the two blocks eventually become welded together into a single crystal.

Quite apart from the reduction in welding, and hence in friction and wear, further advantages can accrue from the use of a relatively fusible soft alloy sliding on a hard refractory bearing surface. Owing to the comparative ease with which the softer metal is plastically deformed, it was long thought necessary to restrict the load intensity. The further disadvantage of the low ductility and proneness to fracture of the customary rather thick strip of soft metal was overcome, at least in part, by welding to a massive backing of a metal of more suitable mechanical properties, which was then secured in an appropriate housing. The resulting bearing, however, was large and massive in relation to the applied load. Hopkins and Palm (1932) realized that, by taking advantage of the cohesion between the bearing surface and the backing metals, the softer metal could be made to withstand a load intensity far greater than hitherto thought practicable. The underlying principle is simple. The ability of a soft body to resist deformation when compressed between two hard plane surfaces increases as its thickness is reduced by plastic flow until, long before the soft material can be totally extruded, the hard metals themselves begin to flow and deform. For example, it is impossible to force out completely even an oil film from between two plane surfaces, no matter how heavy the load or how rigid the metal may be. This is due to the reinforcing of the cohesion between the oil molecules by their adhesion to the surfaces. In fact, the thinner the film, the more do its mechanical properties approximate to those of the solid substrate. Similarly, whilst a bearing metal layer of the once customary thickness can support only a relatively low load intensity, a much thinner layer can carry a far heavier load without being permanently deformed. The thickness of this layer need be no greater than that corresponding to the maximum wear loss which can be tolerated before the fit becomes so slack as to render the bearing useless. For example, the 'big-end' crankshaft bearing of an internal combustion engine, which previously consisted of a 5/100 in. thick tin-base alloy fused on to a massive bronze backing, has now been replaced by a 5/1,000 in. thick layer on a thin steel strip, the weights of the liners being 218 and 60 gm. respectively (Exhibits).

The tin-base type of bearing metal alloy, though relatively soft, is too hard to be scratched with the finger nail. This form of alloy, though extremely wear-resisting, causes considerable wear of the hardened steel surface against which it slides. As we shall see later, this is due partly to the softness of the alloy and partly to the nature of its oxide layer. There is little evidence to support the view that embedded detritus particles are the cause. A further notable advance therefore was made by the recent introduction of bearing metals whose surfaces cause very little wear of the steel bearing surface. Lead and indium, the chief metals of this kind, are so soft that they and their alloys can be scratched with the finger nail.

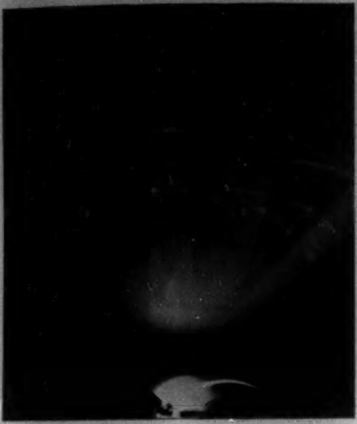

Figure 1. Electron-diffraction pattern from a copper single-crystal electropolished cube face; beam along cube edge. The sharp Kikuchi lines and the narrow circular Laue zone show that the surface is atomically smooth and of quite remarkable lattice perfection. The clarity in detail near the shadow edge is such as to show that the oxide layer cannot be more than two or three molecules thick.

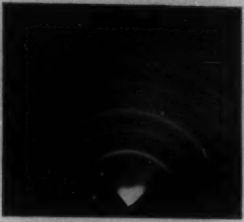

Figure 4. α-iron pattern from the freshly honed surface of an austenitic steel cylinder liner.

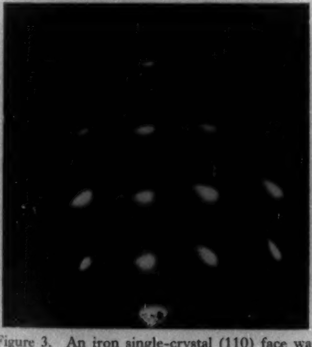

Figure 3. An iron single-crystal (110) face was lightly honed along a [110] direction and then etched to expose the sub-surface damage. The pattern (beam along [001]) reveals that the original single-crystal structure has been distorted by a process of rotational slip (Wilman 1950) on (001) about a [001] axis. This slipping represents the initial stage in crystal break-up. Note that the fragments are still coherent across the planes of rotational slip.

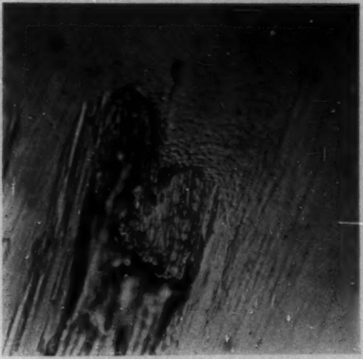

Figure 5. Scoring damage due to welding between a pair of copper single-crystal sliding surfaces. 450×.

To face page 792

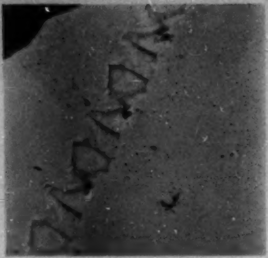

Figure 6. Track of a broken-off weld particle rolling on a copper single-crystal surface. 'Formvar' replica; gold shadowed. 10,000×.

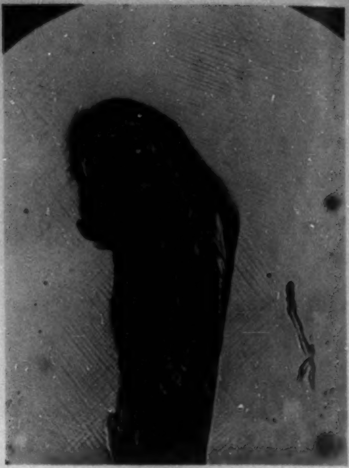

Figure 8. Surface damage resulting from weld formation between a pair of copper single-crystal surfaces. Note widespread regions of deformation bands formed ahead of and at the sides of the main damage area. 450×.

Figure 7. Mechanically polished copper surface. The pattern consists of two ill-defined broad haloes. Patterns of this kind are obtained from glass,' fused ' quartz, cellulose, and from mechanically polished metal surfaces in general.

Figure 10. Pattern from an austenitic steel internal combustion engine liner after 120 hours' running. The halo pattern reveals the presence of amorphous iron and an amorphous iron oxide. The faint streak above the undeflected beam spot is due to a graphite film the crystals of which are orientated with their cleavage planes parallel to the liner surface.

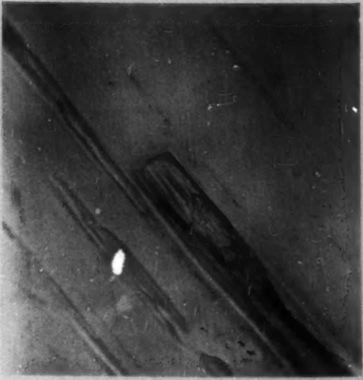

Figure 9. The weld damage is greatly restricted when one of the copper single-crystal surfaces is first lightly mechanically polished. The vertical lines are due to the polishing medium. 450×.

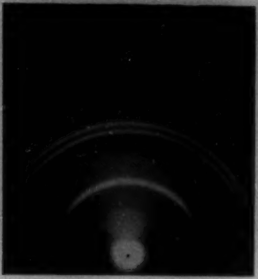

Figure 11. A scratched cast-iron piston-ring surface yields a pattern due to disorientated graphite crystals.

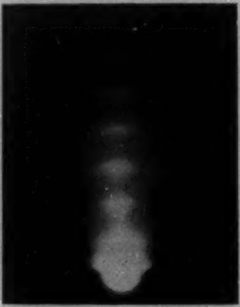

Figure 12. Light rubbing with the thumb suffices to orientate the graphite crystals with their cleavage planes parallel to the piston-ring surface. This pattern identifies the streak in Figure 10 as being due to graphite.

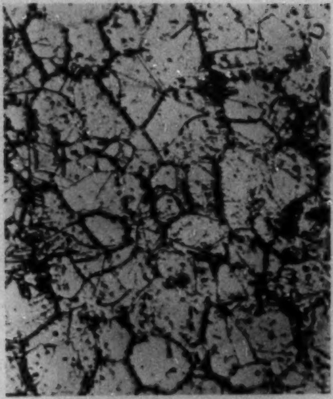

Figure 13. Polycrystalline copper surface after removing an oxide film. The crystal boundaries have been more attacked than the crystal surfaces.

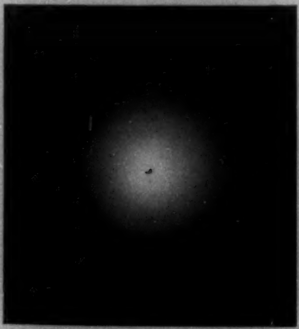

Figure 14. Amorphous iron oxide film removed from a mild steel surface.

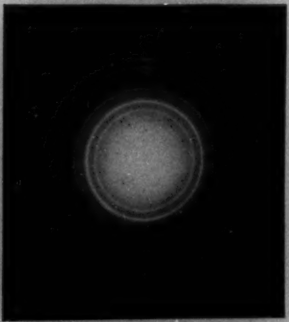

Figure 15. γ–Fe_2O_3 formed by heating the amorphous oxide film of Figure 14.

Figure 16. A copper single-crystal surface immediately after anodic polishing.

Figure 17. The same surface after 30 hours' exposure to air at room temperature becomes covered with an amorphous oxide layer which is thick enough (>40 A.) to obscure the single-crystal pattern.

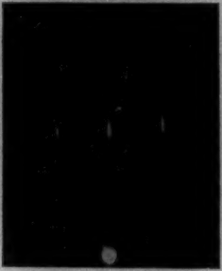

Figure 18. Cuprous oxide growing epitaxially on a heated macro-crystalline copper surface.

Figure 19. γ-Fe_2O_3 formed on a heated steel surface. The tendency is for needle-like crystals to form with [110] axes normal to the surface.

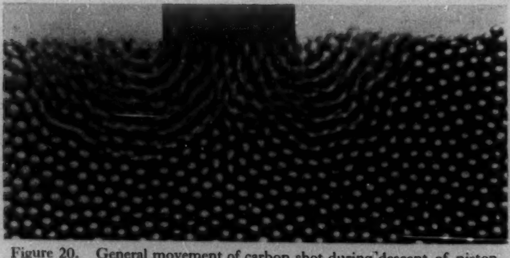

Figure 20. General movement of carbon shot during descent of piston. (*From* Andrade and Fox (1949).)

Nevertheless, when bonded in a sufficiently thin layer to a steel backing, they can support unusually heavy loading. One such backing-bearing surface combination consists of a hard steel strip to which is bonded a thin copper–bronze alloy strip on which a layer of lead is electrodeposited. A thin 'flash' of indium is electrodeposited and later thermally diffused into the lead. The copper–bronze strip is necessary as, owing to the differences in crystal structure and lattice constants, it is difficult to deposit lead electrolytically on steel in such a way as to ensure a satisfactorily close co-ordination, and therefore good cohesion, between the atoms across the interface. The total thickness of the lead–indium layer is 1/1,000 in. The rate of wear of both bearing surfaces is so small in relation to that of the other sliding surfaces of the engine that this thickness is ample (Exhibits).

An important question relating to bearing surfaces which has so far received less attention than it undoubtedly merits is that of the effect of sliding on the surface composition of alloys. In the few cases in which this has been examined experimentally it has been found that polishing increases the proportion of one or more of the constituents in the surface of the alloy, and hence also affects the composition of the oxide layer. Thus polishing a chromium steel alloy produces a surface which is either greatly enriched in chromium content or is even pure chromium covered by a layer of chromium oxide (Vernon, Wormwell and Nurse 1944). A similar effect has been observed in this laboratory with magnesium–aluminium alloys (De Brouckère 1945), α-brass and bronze (Bryant 1936) which become richer in magnesium, copper and tin respectively. Such changes may well be significant, not only because of their possible effect on the surface hardness and fusibility, but also because they must determine the nature of the oxide layer.

The demands made on the reciprocating bearing surfaces in the cylinder of the internal combustion engine are in many respects much more severe than in the journal type of bearing. Surface temperatures are high, particularly near the combustion zone, and the pressure distribution on the piston crown is seldom uniform, especially at the start of the expansion stroke. Further, the change from dynamic to static conditions at the end of each stroke not only imposes unusual demands on the lubricant layers but also results in an uneven load distribution between the sliding surfaces. Finally, the reaction products cause corrosion wear (Williams 1937).

Nominally, the bearing surfaces are those of the cylinder wall and piston rings, but the piston itself at times also rubs against the cylinder wall. For reasons of mechanical strength, lightness and thermal conductivity, the piston may consist of an aluminium alloy with copper and some magnesium, though in diesel engines a cast-iron skirt with an alloy steel crown is more usual. The cylinder bearing surface is a cast-iron, austenitic steel or other ferrous alloy, sometimes with a coating of electrodeposited chromium. The piston rings, however, are always made of cast iron. Alloys with better mechanical properties have been tried as piston-ring metal in low-compression engines but their adequate lubrication presents difficulties. The graphite in the cast-iron ring helps greatly in the suppression of wear of both cylinder and ring (Finch, Quarrell and Wilman 1935, Finch and Whitmore 1938). Electron diffraction has shown not only that the 'run-in' surfaces of the cylinder and cast-iron piston ring are covered with an amorphous oxide layer (Figure 10) but has also revealed the presence of an exceedingly thin adsorbed graphite layer (Figures 11 and 12), the flakes of which are orientated with their cleavage planes parallel to the surface. It is probable that this layer acts as a temporary lubricant and protection to the oxide layer when the oil boundary layer breaks down.*

The effect of direct sliding contact between the exceedingly hard corundum coating on the aluminium alloy piston and the oxide layer on the cylinder wall seems to be mitigated by the formation of magnesium spinel (Finch 1937). There is some evidence also that the rubbing of the corundum or spinel layers against the ferric oxide layer on the cylinder wall may lead to the formation of iron spinels (Thirsk and Whitmore 1940).

§ 5. THE OXIDE LAYER

In modern engineering practice, where frequent penetration of the lubricant boundary layer occurs, the part played by the oxide layers in facilitating sliding and preventing metal-to-metal contact is obviously of great importance. It is now known that most metals, if not indeed all, oxidize in dry air, however low the temperature. The primary oxide layer is formed very quickly, even at the temperature of liquid air, and then acts as a barrier against continued easy access of oxygen to the surface. Thus the subsequent rate of growth of the oxide layer decreases rapidly, and may become negligible at a thickness of the order of a few tens of atomic radii. Should further oxidation occur, it is very slow, even at room temperature, provided secondary effects, such as attack of the oxide films by adsorbed moisture, are avoided. Cabrera and Mott (1949) explain the mechanism of oxidation subsequent to the formation of the first oxygen layer in terms of the high contact potential gradient between the metal and the layer, which enables the metal ions to move through it without much help from thermal motion. There is, however, evidence which suggests that oxidation can also be due to oxygen gaining access to the metal through crystal boundaries. Thus, we have observed than an anodically polished single-crystal metal surface oxidizes more slowly than a similarly treated microcrystalline surface. Further, on removing with citric acid a relatively thick oxide film grown at 180° c. on anodically polished polycrystalline copper, it was seen that the crystal boundaries, barely visible before oxidation, had become strongly outlined and deepened (Figure 13).

The surface oxidation of metals is, in general, a highly energetic process. At low temperatures, therefore, the rapid arrival of oxygen molecules and the low mobility of its atoms over the surface may be expected to favour the growth of amorphous rather than crystalline layers. There are many examples of films having been grown on single-crystal substrates cooled to liquid air temperatures and, as far as I am aware, all have been found to be amorphous or so submicroscopically crystalline as to be indistinguishable from amorphous; yet the same substances deposited on the heated substrates have grown epitaxially. Even when a metal surface is oxidized at room temperature the oxide layer usually seems to be amorphous. This is certainly so in the cases of aluminium, chromium and iron (Figures 14 and 15); and recently Dr. Leu, working in my laboratory, has found that the oxide film formed on an anodically polished copper single-crystal face exposed to air at room temperature is also amorphous (Figures 16 and 17).

---

* It is commonly supposed that the crystals of layer-lattice structures such as mica, graphite and molybdenum sulphide, which are sometimes used as dry lubricants, act like orientated packs of playing cards. This cannot be so because, as I demonstrated earlier in this lecture, the layers can only be separated by cleaving in such a manner that the bonds between the layers are broken one by one. I also showed that, though freshly cleaved mica surfaces would adhere firmly on being first put together and could not be pulled apart by stress applied in a direction lying in the cleavage plane (i.e. attempting to rupture the bonds simultaneously), they lost this property on prolonged exposure to air or moisture. Thus the ability of layer-lattice cleavage surfaces to slide easily over each other is due to adsorbed layers. Layer-lattice crystals with their *c* axes parallel to, and crushed between, loaded sliding surfaces will be cleaved, but will also abrade the sliding surfaces. It follows that layer-lattice crystals in which the ratio of exposed cleavage plane area to thickness in the *c* direction is a maximum make the best form of solid lubricant. It is known from electron diffraction (Finch and Wilman 1936) and electron-microscopic studies (Rao, recent work in this laboratory) that the smaller the volume of a graphite crystal the higher is the value of the above ratio. A layer-lattice lubricant should, therefore, consist of crystals in the finest possible state of subdivision compatible with a maximum surface to thickness ratio. Sliding of the lubricated mechanism should not be relied on to break up the crystals, as this must result in wear.

On heating to above room temperature, amorphous oxide films differ widely in behaviour. Those on aluminium and chromium remain amorphous at temperatures up to about 600° c. and can grow in thickness only very slowly, if at all (Preston and Bircumshaw 1936, De Brouckère 1945). On copper, cuprous oxide grows epitaxially (Figure 18) and, at higher temperatures, becomes in turn superficially oxidized to cupric oxide (tenorite). These films, although coherent, are fairly easily permeable by both oxygen and copper ions, and thus do not give a high degree of protection against oxidation. Still less protection is given by the crystalline iron oxide films ($FeO \rightarrow Fe_3O_4 \rightarrow Fe_2O_3$) (Figure 19) formed under such conditions that the crystals have a marked tendency to grow outwards from the surface along an atom row of high atom population density. With other metals the crystalline oxide layer formed on heating is orientated in such a way that the crystals have in common a plane of high atom-population density parallel to the metal surface. They also cohere to each other and form a continuous film which hinders access of oxygen to the surface even when the metals are molten. Well-known examples are tin, zinc, antimony, bismuth, cadmium and lead. Oxide layers grown on heated metals when the rate of supply of oxygen is sufficiently reduced, are often epitaxial, i.e. the crystal orientation in the oxide layer is related to and determined by that of the metal surface. Such an oxide layer grown on a single crystal is itself virtually a single crystal. Epitaxial oxide growth can also occur during the oxidation of polycrystalline surfaces, even though the metal crystals have no common direction or directions of orientation. Then, however, the crystalline continuity of the deposited layer is further disturbed by the epitaxial reproduction of the irregularities which constitute the crystal boundaries.

Crystalline oxide layers on the sliding surface are probably of rare occurrence. Although a metal surface exposed momentarily through rubbing may be extremely hot, it is, as we know from the formation of the Beilby layer, disturbed and very rapidly cooled, so that there will be a tendency for any re-formed oxide layer to be amorphous. Many 'run-in' bearing surfaces have been examined by electron diffraction; their oxide layers have been found to be amorphous. The thickness of the amorphous films so far studied appears to be relatively uniform, so that the surface texture is a fair representation of that of the underlying metal. Indeed, the amorphous aluminium oxide layer has been used as a replica in the electron-microscopic study of the texture of aluminium surfaces.

The adhesion of the oxide film to its substrate can be expected to be good by reason of its nature, though pseudomorphic strain in the initial layers may not be without influence (Finch and Quarrell 1933, Cabrera and Mott 1949). As the film is amorphous, and therefore isotropic, it should be equally strong in all directions in the surface. Its cohesive strength in the case of iron and aluminium is shown by the way in which detached films, less than 100 A. thick, of amorphous ferric or aluminium oxide can be lifted off a water surface on a wide-meshed (80/inch) gauze without tearing, a process which also demonstrates their flexibility.

We may now examine how the oxide layer is so effective in preventing metal-to-metal contact when two surfaces are pressed together. When the surfaces first come together they make a three-point contact. This does not mean that three pairs of points meet. The probability is rather that three asperities of small radii of curvature will lodge on surfaces of large radii. Such a contact pair may be represented by Figure 20 (Andrade and Fox 1949). If pressure is now applied, the load will be distributed far more widely over the lower, flatter surface than over the point. Hence the point will flow and spread and, though in so doing its oxide layer may be disrupted and thus expose the metal surface, the distribution of pressure ensured by the other, largely intact, oxide layer reduces the loading intensity on the opposing metal surface. The oxide layers are even more effective when the initial point contacts occur between areas of low curvature. On loading, conditions then approximate to the case of the pressing together of two plane surfaces separated by adhesive layers. Not until extensive plastic flow takes place at both metal surfaces will their oxide films be broken and metallic contact be established. Since such contact cannot take place before the disruption of both oxide layers, it would be impossible to press two plane surfaces into metallic contact where one surface is soft and the other hard, unless the softer metal in flowing plastically were to shear the oxide layer off the hard surface. This occurs when, for example, a lead column is compressed between a pair of anodically polished plane surfaces of polycrystalline copper; after extensive flow, the lead begins to form welds with the copper (Demonstration).

We will now consider the behaviour of the oxide layers under normal sliding conditions, that is, after 'running-in' has prepared the surface for full loading. Where the lubricant boundary layers break down, the oxide layers must come into contact and slide over each other. Both films may then rupture, allowing metallic contact and cold or hot welding; or one film may be ruptured and the other survive; or both films may survive, with or without the help of a re-forming of the lubricant boundary layers. Wherever they are in sliding contact, heat will be liberated in the oxide layers.

The facts concerning the oxide layers which bear on the rôle they play in sliding may be briefly summarized as follows. They consist of extremely thin amorphous films strongly held to the metal (ionic binding). The melting points and hardnesses of some of the oxides and other products of possible interest in sliding surface practice are given in the following Table.

It will be evident from the table that the poor protection afforded by the oxide layers to single-crystal surfaces of copper or aluminium sliding under light loads at a low rate cannot be ascribed to either the refractoriness or hardness of the oxide layer. On the contrary, the oxide layer on the harder iron single-crystal surface gives a considerable measure of protection, although the fusibility and hardness of ferric oxide lie between those of cuprous oxide and aluminium oxide. We have also seen that a thin Beilby layer on one of a pair of copper single-crystal surfaces rubbing together somehow increases the resistance of its oxide layer to rupture.

Experiments with pairs of dissimilar metals lead to similar results. Thus a copper single crystal sliding on aluminium under a light load almost immediately seizes (Demonstration), and the welds break in the body of the aluminium; obviously both oxide layers are injured. On the other hand, when a copper single crystal slides over an iron single crystal under a much heavier load, no seizure occurs (Demonstration). Yet the cuprous oxide film is broken in many places

Table 1

Compound	M.P. (° c.)	Hardness (Moh)	M.P. of metal (° c.)
Fe_2O_3 (haematite)	1565	6½	1535
Fe_3O_4 (magnetite)	1538 (decomposes)	6½	
FeS_2 (pyrite)	1171	6¼	
FeS (troilite)	1193	4¼	
$FeCl_2$ (laurenite)	670	Soft	
FeOCl	—	—	
Fe_2P	1290	—	
Fe_3P	1100	—	
$(Fe, Ni)_9S_8$ (pentlandite)	878	3¼–4	
$FeCr_2O_4$ (chromite)	—	5½	
NiO (bunsenite)	2090	5½	1455
NiS (millerite)	797	3½	
$(Ni, Fe)S_2$ (bravoite)	$\sim$ 900	5½–6	
CoO	1935	—	1495
CoS (jaipurite)	$>$1165	—	
$(Co, Ni, Fe)S_2$ (hengleinite)	$\sim$1000	5	
Cr_2O_3	1990	—	1615
CrN	1500 (decomposes)	—	
CrF_3	1000	—	
Ag_2S (argentite)	825	2½	960
AgCl (cerargyrite)	455	1½	
MnO (manganosite)	1650	5½	1260
Mn_3O_4 (hausmannite)	1705	5½–6	
MnS_2 (hauerite)	—	4	
Al_2O_3 (corundum)	2050	9	660
MoO_3	700	Soft	2620
MoS_2 (molybdenite)	1185	Soft	
SnO_2 (cassiterite)	1127 (decomposes)	6–7	232
SnO	$<$ 950 (decomposes)	—	
SnS	882	—	
TiO_2 (rutile)	2130	6–6½	1800
MgO (periclase)	2500–2800	5½–6	651
ZnO (zincite)	1670	4½	419
ZnS (sphalerite)	1049	4	
Cu_2O	1235	—	1083
CuO (tenorite)	1026 (decomposes to Cu_2O)	3–4	
CuCl (nantokite)	422	—	
Cu_2S (chalcocite)	1100	3	
CuS (covellite)	220 (decomposes)	—	
PbO_2 (plattnerite)	290 (decomposes)	5½	
PbO (litharge)	888	2	327
$PbCl_2 . 2PbO$ (mendipite)	693	3	
$PbO . PbSO_4$ (lanarkite)	977	2½	
$PbSO_4$ (anglesite)	1000 (decomposes)	3	
$PbFe_4O_7$ (plumboferrite)	1530	5	
CdO	1426	3	321
CdS (greenockite)	900 (sublimes)	3½	
ZrO_2 (zirconia)	$>$2950	6½	1900
Sb_2O_3	656	2½	630
Sb_2S_3 (stibnite)	550	2	
Bi_2O_3	820	4½	271
V_2O_3	1970	—	1720
InO_2	700 (sublimes)	—	155
Spinels (Mg, Fe, Ni, Cr, Mn, or $ZnAl_2O_4$)	1800	6–8	
Magnetites (Mg, Fe, Zn, or $NiFe_2O_4$)	1500	5½–6½	
Chromites (Mg or $FeCr_2O_4$)		5½	

Among other surface compounds of possible interest are the selenides, tellurides, arsenides, phosphates and borates.

and the structure of the underlying metal is disturbed; the iron oxide, however, survives and thus prevents metal-to-metal contact. The oxide layers on surfaces of metals of high rigidity, such as hardened alloy steels, resist rupture at low sliding speeds, even when heavily loaded. Examples are afforded by ball-bearing and gear-tooth surfaces in both of which, although the load intensity is high, the sliding speeds are low or very low. Such bearings, even without a lubricant, are for a time capable of carrying surprisingly heavy loads at low speeds without forming welds. It is evident, therefore, that the resistance of the oxide layer to injury during sliding must, irrespective of its nature, depend in the first place on the rigidity of the supporting metal.

As the severity of the sliding conditions increases, however, it becomes apparent that the behaviour of the oxide layer is determined not only by the supporting metal but also by its own properties. For example, when the bearing surfaces consist of the same hard metal, the frequency of intermetallic contact and welding increases when the sliding speed or load is raised. As we shall see later, however, a change in the chemical composition of the oxide layer alone may reduce or even eliminate intermetallic contact and welding.

It seems to me that these facts are best explained as follows. The ratio of the load to the area of contact is constant and a measure of the rigidity of the softer of the two metals of the opposing surfaces. Hence, with a given load, the loading intensity increases with the rigidity of the softer metal or with that of the metal common to both surfaces. Therefore, since heat is developed in the oxide layers wherever their surfaces are sliding in contact, the local temperature attained must, under comparable conditions, be higher with rigid metals than when one or both are soft. Further, these local temperatures must increase with the speed of sliding. High local temperatures have, indeed, been observed during the sliding of glass or quartz surface pairs (Bowden, Stone and Tudor 1947), and this suggests that the factor limiting the possible temperature rise is the fusion of the oxide layer. If the softening temperature of the oxide layer is higher than that of the metal, the latter will melt and thus no longer support the oxide layer, and the ensuing hot metal-to-metal contact will lead to the formation of a hot weld.

To test this view we may consider the hypoid gear which was introduced about 1930. Though the sliding speeds in this type of gear are low, the load on the bearing surfaces is unusually high, and excessive wear due to welding was common. Some years previously it had been found that wear in cutting tools could be reduced by adding finely divided sulphur to the cutting lubricant. The sulphur seemed to act by forming a protective film on the tool tip. When, therefore, the best of the then known gear lubricants, such as castor oil and metallic soaps, had failed to give proper protection to the hypoid gear surfaces of hard ferrous alloy, it was a short but important step to the introduction by Evans (1937) of oil-soluble organic sulphur compounds which form surface films capable of preventing metal-to-metal contact under severe conditions of both loading and sliding speeds. Since then a bewildering variety of so-called 'extreme-pressure' additives has been increased by compounds containing chlorine or phosphorus. In 1942, Evans showed that the additive molecules did not perform their function by merely becoming adsorbed as such on the bearing surface, but found that a useful working hypothesis was to suppose that sulphide, chloride or phosphide layers were formed. Since then the formation of an unidentified iron sulphide compound, possibly FeS_2

(Simard, Russell and Nelson 1941), of an iron phosphide (Fe_3P) (Beeck, Givens and Williams 1941, Brummage 1942), ferrous chloride ($FeCl_2$) (Brummage 1942) and ferric oxychloride ($FeOCl$) (Brummage 1949, private communication) on ferrous bearing surfaces lubricated by oils containing the appropriate additives has been observed. Other layers produced in a similar manner have been identified on α-brass (cuprous chloride, $CuCl$) (Bryant 1936) and on silver (silver sulphide, Ag_2S). The formation of a sulphur compound layer has also been confirmed by the use of an additive containing radioactive sulphur (Clark, Gallo and Lincoln 1943). Thus Evans' view that the extreme-pressure additive forms a layer by a chemical attack can be accepted. Up to the present, however, no reasonable hypothesis has been put forward to account for the remarkable resistance of this layer to rupture. Indeed, wear of the properly lubricated hypoid gear is so slight that metal-to-metal contact and welding must be of rare occurrence.

Now, it is well known that an injury to the oxide layer on, for example, a ferrous bearing surface is almost immediately healed on renewal of the boundary layer owing to the action on the exposed metal of air and other oxidizing products dissolved in the ordinary lubricant. It is clear, therefore, that the superior protection afforded by the sulphide (or chloride or phosphide) layer formed by the extreme-pressure additive is due to some property inherent in the nature of this surface compound. It cannot be a question of hardness because, excepting pyrite, the sulphides, chlorides and phosphides of iron are softer than the oxides. A significant fact, however, is that, with few exceptions (the noble and platinum-group metals, tantalum, molybdenum and tungsten), the oxides likely to be formed on bearing surfaces are more refractory than the corresponding metals. On the other hand, the sulphides, chlorides and phosphides of the chief constituents of the alloy steels used in hypoid gears are more, or even much more, fusible than the metals. Finally, a zone of sliding contact between the oxide layers is a region of high temperature and, possibly, high pressure.

With these facts in mind, it seems to me that the extreme-pressure additive acts in the following way. Before the frictional temperature at areas of rubbing contact becomes high enough to soften the underlying metal and thus rob the oxide layer of its support, the additive reacts with the oxide to form a layer of a compound, such as a sulphide or oxysulphide, which is more fusible than the metal. If the local temperature should rise sufficiently to melt the compound, some of the molten layer will smear and thus act for a time as a lubricant. The one or two molecular layers next to the metal, being more strongly held, will, however, remain intact and continue to resist rupture, because the melting point of the compound is too low to impair the rigidity of the metal and thus deprive these last molecular layers of their support. This view is further supported by Greenhill's (1948) experiments which showed that the friction between sliding pairs of steel or copper surfaces was much reduced on replacing the oxide layers by sulphides.

It has already been remarked that it is a common experience that in time both bearing surfaces of a sliding element become polished, no matter how widely their melting points or hardnesses may differ. At first sight this seems to conflict with the results obtained by Bowden and Hughes (1937) who found that a soft material could polish a hard one of lower melting point without itself being polished.

The explanation lies in the difference between the conditions under which their experiments were carried out and those of normal sliding-surface practice. There are, indeed, conditions in which hardness and fusibility are of secondary importance. For example, platinum (H.4 : M.P. 1,775°) is polished by a high-speed buff dressed with rouge (H.6½ : M.P. 1,565°). A diamond tool tip (H.10 : M.P. >3,500°) is worn and smoothed by corundum (H.9 : M.P. 2,050°) during the turning of aluminium. A rotating pad dressed with corundum polishes periclase (H. 5½–6 : M.P. 2,500–2,800°). Synthetic fibres wear and polish the hard steel surfaces over which they slide in textile machinery. The end of a rod of camphor (M.P. 178° c.) is caused to flow and be polished by a swiftly moving ribbon of Wood's metal (M.P. 73° c.) (Spurr, recent experiments carried out in this laboratory). These examples suffice to show the importance of the effect of a continual changing or otherwise of the rubbing surface. When two surfaces are in rubbing contact, the heat developed is shared by both. If one surface is always in rubbing contact, e.g. the tool tip, its temperature will exceed that of the other surface which is continually changing, despite conduction losses. For example, a small steel specimen describing a continually changing path on a brass surface can be run without seizure under much more severe conditions than vice versa (Brummage, private communication). In both cases, the small specimen reaches a high temperature, which the steel, because of its higher melting point, is better able to withstand. This is precisely what happens on running in a sliding element pair consisting of a hard and a soft metal. The soft metal is first polished and smoothed. The asperities on the hard surface then form small surfaces which continue to rub in relatively long contact paths over rounded hill tops on the softer surface and are thus in their turn smoothed and polished. In general, where high spots are in sliding contact, the one of smaller radius of curvature will attain the highest temperature, and this may well exceed the melting point of the layer on the surface of larger radius of curvature.

§ 6. THE BOUNDARY LAYER

The function of the oxide layers is to prevent intermetallic friction with its more or less destructive consequences. The oxide-layer (or sulphide etc.) component of friction, however, is still too high to be tolerated in general sliding practice, even supposing the layers could remain intact. It is the function of the boundary layers of the lubricant to replace the oxide-layer component of friction by one of still lower value.

The lubricants consist, in general, of mixtures of straight-chain hydrocarbon molecules (paraffins) or their end-substituted products (alcohols, esters, ketones, acids). At temperatures below the melting point of the hydrocarbons, the chains, 4·5 A. apart, are grouped in bundles, like sticks in fascines. Such bundles are in fact crystals. When grown from the melt or solution on a solid surface the crystals are orientated with the chains either vertical or inclined to the surface at an angle characteristic of the compound. The thickness of such an orientated crystalline layer may be as much as 50 molecules or more (for references see Brummage 1947).

When such layers are heated, as they are under practical conditions of sliding, the fascines break up at a temperature close to the melting point, leaving a true boundary layer of molecules. The molecules attached directly to the surface are normal or steeply inclined to it; above them is a layer of less pronounced orientation, and by the time the fourth layer is reached the orientation is practically non-existent (Finch and Zahoorbux 1937); that is to say, the film has now become fluid. The maximum thickness of the boundary layer is therefore of the order of less than 200 A.

The chains of the first layer in the boundary film are all adsorbed with one end attached to the oxide film, the radicle end in the case of end-substituted molecules. Owing to the polar nature of these, they are more firmly held than the normal paraffins. Further, acids or esters may react with the oxide, sulphide or other layer to form soaps; in this case the relatively thick crystalline layer persists up to the softening temperature of the soap (Brummage 1947, Tingle 1950).

The transition from a crystalline to a boundary film is reversible in that, on cooling, the crystals are re-formed (Brummage 1947). In consequence, new orientations of the crystals or fascines are observed after rubbing. For example, solidified fatty acid films are frequently found to contain crystals in which the molecules are aligned in the direction of sliding at an angle of about 5° to the surface (Finch 1938, Germer and Storks 1939).

Boundary-layer friction is lower with end-substituted than with normal paraffins of similar chain lengths (Hardy 1936). This has generally been attributed to their stronger adhesion to the oxide layer. It is difficult, however, to see how this can materially reduce friction. It may be said, indeed, that present views on the mechanism of the facilitating of sliding by the lubricant boundary layer are inadequate. It is true that I have at times likened the boundary layer to a velvet pile or the bristles of a brush, and have also drawn attention to the thermal motion of the molecules of the layer and to possible effects of their polarity. But all these ideas are at best working hypotheses meant only to serve as guides to further experimental enquiry.

§7. THE INTER-BOUNDARY LUBRICANT FILM

The inter-boundary lubricant film exists only in regions of relatively light loading. Osborne Reynolds (1886) recognized its fluid character, and his theory of hydrodynamic flow not only represents the first broad generalization in the science of lubrication but has also dominated the geometrical design of the sliding element to this day. This is as it should be, for the shear strength of the fluid film is less than that between any of the other surface pairs involved in the sliding element. Boundary conditions of sliding should therefore be restricted as far as possible to those areas of heavier loading where the fluid film can no longer survive as such.

In addition to keeping the boundary layers apart and reducing friction in the more lightly stressed regions, the fluid film has other important functions to fulfil. It must replenish supplies to the boundary layers, bring up oxidizing agents (oxygen, sulphur, halogens etc.) to repair damage sustained by the oxide layers or suitably to modify these, and carry off debris, clothing each particle with a protective boundary layer. Finally, the fluid layer also helps to carry off frictional heat.

The main sources of wear in hydrodynamic lubrication are chemical corrosion and erosion. Erosive wear is chiefly due to debris rolling (Figure 6) between or striking sliding surfaces, and to cavitation (Munroe; see Rayleigh 1917) effects resulting from the collapse of bubbles suspended in the oil and in contact with the sliding surface.

§ 8. CONCLUSION

The problem of the sliding element is a complex one. A distinguished physicist once spoke of it to me as 'a very messy business'. This complexity together with the success of the empirical approach has undoubtedly deterred scientific research into the subject. Since Osborne Reynolds' triumphant framing of the theory of hydrodynamic lubrication, only four schools have attempted to carry the matter further. Beilby's (1921) work on surface flow and Hardy's (1936) views on surface forces were destined, as we have seen, to prove of fundamental importance. The other two schools, both active to-day, are those of Bowden in Cambridge and my own in South Kensington. Hitherto all these workers have been concerned mainly with the metallic bearing surface and the oil *qua* lubricant. If, in this lecture, I have laid particular emphasis on the oxide layer and on the oil as purveyor of oxidant to the high temperature zone of solid-to-solid sliding contact, it is because I believe that it is in this direction that the next great advance will be made. Without the oxide layer and oil-borne oxidants, whose interaction is confined to regions of high temperature, sliding under boundary conditions would be a practical impossibility.

ACKNOWLEDGMENTS

I have to thank Professor E. N. da C. Andrade and Dr. J. W. Fox for Figure 20, M. M. Bluhm for Figure 6, Dr. K. Leu for Figures 16 and 17, D. P. D. Webb for Figure 2, Dr. H. Wilman and D. Layton for Figure 3 and R. T. Spurr for Figures 5, 8 and 9 and for his help, particularly with the single crystal experiments.

My thanks are also due to Dr. K. G. Brummage (Anglo-Iranian Oil Company's Research Laboratories) and to Mr. E. A. Evans (C. C. Wakefield Company's Research Laboratories) for helpful discussions, to Mr. D. Green (Vandervell Limited) for the loan of bearing liners exhibited at my lecture and to Mr. G. Whipple (Hilger and Watts Ltd.) for the loan of a set of slip gauges.

I also wish to record my thanks for financial assistance given to the work carried out in this field in my laboratories by E. G. Acheson Ltd., Anglo-Iranian Oil Company Ltd., Ferranti Ltd., C. C. Wakefield Ltd., the Department of Scientific and Industrial Research, and the University of London Central Research Fund (for the provision of a 200 kv. generator).

REFERENCES

Amontons, G., 1699, see *Encyclopaedia Britannica*, 13th Ed., 1926.

Andrade, E. N. da C., and Fox, J. W., 1949, *Proc. Phys. Soc.* B, **62**, 483.

Beeck, O., Givens, J. W., and Williams, E. C., 1941, *Proc. Roy. Soc.* A, **177**, 103.

Beilby, G., 1903, *Proc. Roy. Soc.* A, **72**, 218; 1921, *Aggregation and Flow of Solids* (London: Macmillan).

Bowden, F. P., and Hughes, T. P., 1937, *Proc. Roy. Soc.* A, **160**, 575.

Bowden, F. P., and Ridler, K. E. W., 1936, *Proc. Roy. Soc.* A, **154**, 640.

Bowden, F. P., Stone, M. A., and Tudor, G. R., 1947, *Proc. Roy. Soc.* A, **188**, 329.

Bowden, F. P., and Tabor, D., 1939, *Proc. Roy. Soc.* A, **169**, 391; 1945, *Annual Reports Chem. Soc.*, **42**, 20.

Brummage, K. G., 1942, *Ph.D. Thesis, London University*; 1947, *Proc. Roy. Soc.* A, **188**, 414, **191**, 243.

Bryant, F. J., 1936, *Ph.D. Thesis, London University*.

Cabrera, N., and Mott, N. F., 1949, *Rep. Prog. Phys.*, **12**, 163.

Clark, G. L., Gallo, S. G., Lincoln, B. H., 1943, *J. Appl. Phys.*, **14**, 428.

Cochrane, W., 1938, *Proc. Roy. Soc.* A, **166**, 228.

Coulomb, C. A., 1781, see *Encyclopaedia Brittanica*, 13th Ed., 1926, article on ' Friction ' by A. B. W. Kennedy and W. E. Dalby.

De Brouckère, L., 1945, *J. Inst. Metals*, **71**, 131.

De la Rive, A. A., 1839, *Ann. Chim. (Phys).*, **39**, 328.

Evans, E. A., 1937, *Proc. Instn. Mech. Engrs.*, General Discussion on Lubrication; 1942, *Proc. Instn. Auto. Engrs.*, **37**, 1.

Ewing, A., 1912, *J. Inst. Metals*, **8**, 30.

Faraday, M., 1838, see *Experimental Researches in Chemistry and Physics* (London : Taylor and Francis, 1859).

Finch, G. I., 1937, *Science Progress*, **31**, 609; 1938, *J. Chem. Soc.*, 1144; 1945, *Proc. Instn. Mech. Engrs.*, **153**, 331.

Finch, G I., and Quarrell, A. G., 1933, *Proc. Roy. Soc.* A, **141**, 398.

Finch, G. I., Quarrell, A. G., and Roebuck, J. S., 1934, *Proc. Roy. Soc.* A, **145**, 676.

Finch, G. I., Quarrell, A. G., and Wilman, H., 1935, *Trans. Faraday Soc.*, **31**, 28.

Finch, G. I., and Sun, C. H., 1936, *Trans. Faraday Soc.*, **32**, 852.

Finch, G. I., and Whitmore, E. J., 1938, *Engineering*, **146**, 91.

Finch, G. I., and Williams, A. L., 1937, *Trans. Faraday Soc.*, **32**, 852.

Finch, G. I., and Wilman, H., 1936, *Proc. Roy. Soc.* A, **155**, 345.

Finch, G. I., Wilman, H., and Yang, L., 1947, *Discussions, Faraday Soc.*, **43A**, 144.

Finch, G. I., and Zahoorbux, F. D., 1937, *Proc. Instn. Mech. Engrs.*, General Discussion on Lubrication.

Germer, L. H., and Storks, K. H., 1939, *Phys. Rev.*, **55**, 648.

Greenhill, E. B., 1948, *J. Inst. Petrol.*, **34**, 659.

Hardy, W. B., 1936, *Collected Scientific Papers* (Cambridge : University Press).

Hardy, W. B., and Hardy, J. K., 1919, *Phil. Mag.*, **38**, 32.

Hopkins, B. F., and Palm, J. V. O., 1932, British Patent No. 409,289 (accepted 1934).

Hopkins, H. G., 1935, *Trans. Faraday Soc.*, **31**, 1095.

Langmuir, I., 1916, *J. Amer. Chem. Soc.*, **38**, 2269; see also, 1920, *Gen. Elect. Rev.*, **23**, 503.

Parker, R. C., and Hatch, D., 1950, *Proc. Phys. Soc.* B, **63**, 185.

Preston, G. D., and Bircumshaw, L. L., 1936, *Phil. Mag.*, **22**, 654.

Rayleigh, Lord, 1917, *Phil. Mag.*, **34**, 94.

Reynolds, O., 1886, *Philos. Trans.*, **177**, 156.

Simard, G. L., Russell, H. W., and Nelson, H. R., 1941, *Industr. Engng. Chem.*, **33**, 1352.

Thirsk, H. R., and Whitmore, E. J., 1940, *Trans. Faraday Soc.*, **36**, 565, 862.

Tingle, E. D., 1940, *Trans. Faraday Soc.*, **46**, 93.

Vernon, W. H. J., Wormwell, F., and Nurse, T. J., 1944, *J. Iron and Steel Inst.*, **150**, 81.

Williams, C. G., 1937, *Proc. Instn. Mech. Engrs.*, Discussion on Lubrication.

Wilman, H., 1950, *Nature, Lond.*, **165**, 321, *Proc. Phys. Soc.* A, **63**, 298.

The Planar Vibrations of Tetra-chloro-ethylene: an Example of a Complete Normal Coordinate Analysis

By P. TORKINGTON*

Department of Theoretical Physics, King's College, London

Communicated by C. A. Coulson; MS. received 24th November 1949

ABSTRACT. A normal coordinate analysis of the planar vibrations of tetra-chloro-ethylene is carried out. For the B_{1g}, B_{2u} and B_{3u} modes the analysis is complete, including the calculation of the coefficients in the transformation to normal coordinates, the components in the displacements, the directions of the displacement vectors and the distribution of the potential energy, as well as the force constants, for a range of solutions; in each case, two alternative assignments are employed. For the A_g vibrations, several ranges of possible solutions are obtained. Curves are given in every case, and corrections for variable structural parameters calculated for selected solutions. The results for the various symmetry classes are discussed and correlated, and the most likely set of force constants in the valence-force potential function deduced. Details of the method of analysis are given.

§ 1. INTRODUCTION

RECENTLY, the mechanism for carrying out normal coordinate analyses has been thoroughly overhauled, making possible more consistent treatments and giving more idea of the allowed ranges of solutions for the force constants in any given case (Torkington 1949 a, b). Previously, force constants were solved for by substituting trial-and-error values into the secular equation and adjusting to fit the observed vibration frequencies; it is now more usual to solve for the constants explicitly, at least in equations of low degree. In the present paper, the planar vibrations of tetra-chloro-ethylene are subjected to a complete normal coordinate analysis, in order to illustrate such a complete analysis, and to determine finally the force-field of this molecule, which has been investigated in some detail at intervals during the last twelve years (Duchesne 1937, 1938, 1942, 1943, 1948, Thompson and Linnett 1937, Torkington 1949 c). Many data on the nature of the normal modes associated with various allowed solutions have been accumulated during the course of the investigation, and these are of interest in connection with vibrational assignments and with molecular vibrations in general. Tetra-chloro-ethylene is of considerable interest as the key compound for the group of chlorine-substituted ethylenes; in the other members of the group, the force-fields are complicated by the presence of C–H bonds. Recently, a normal coordinate analysis of the planar vibrations of substituted ethylenes was begun by examining various solutions for the C–H bending modes (Torkington 1949 d); before extending the analysis to the skeletal vibrations it is convenient to deal with a completely substituted ethylene in some detail, to gain some idea of the nature of the forces where there are no C–H bonds present. Tetra-chloro-ethylene is the only completely substituted ethylene for which the infra-red and Raman spectra are reasonably complete; the data for the mono- and di-substituted compounds are also satisfactory.

§ 2. THE VIBRATIONAL ASSIGNMENTS

The vibrational assignments have been recently discussed by the author (Torkington 1949 c), who has also carried out calculations of the thermodynamic functions (1950), in order to decide between doubtful frequencies when experimental data on the specific heat are available. Since it seems unlikely that further

---

* Now at British Rayon Research Association, Urmston, Lancs.

spectroscopic work † will lead to any final decision in the near future, the present calculations have been carried out using two alternative assignments, one favoured by the author (T) and the other that employed by Duchesne (D). The assignments are summarized in Table 1; they differ in the magnitude of the uncertain B_{1g} C–Cl stretching frequency, and in the allocation of the two infra-red-active C–Cl stretching modes. The symmetry classification is given by Herzberg (1945).

Table 1. Vibrational Assignments for Tetra-chloro-ethylene

	A_g	B_{1g}	B_{2u}	B_{3u}
$\nu_{C=C}$	1571			
ν_{C-Cl}	447	512(T) 1000(D)	913(T) *782(D)	*782(T) 913(D)
$\delta_{\widehat{CCl_2}}$	237			387
$\delta_{\widehat{C}}$		347	332	

All values are in cm^{-1}.

* The above value is that given by Herzberg; Duchesne (1948) uses 792 and Wu (1946) gives 802 cm^{-1}.

§ 3. SYMMETRY COORDINATES, KINETIC ENERGY MATRICES AND THE POTENTIAL FUNCTION

Tetra-chloro-ethylene falls into the symmetry point group V_h; the nine planar vibrations arise from one cubic and three quadratic factors of the secular equation. The symmetry coordinates employed here for factoring are given in Table 2; they are not normalized. For the displacement coordinates, see Figure 1. The derived kinetic energy matrices are given in Table 3; the nomenclature of the author (Torkington 1949 b) is used, the matrices **A** being related to the inverse kinetic energy matrices **G** introduced by Wilson (1939) as follows:

Table 2. Symmetry Coordinates * for Tetra-chloro-ethylene, (Planar Vibrations)

$$A_g \begin{cases} \Delta_1 = \Delta r_{25} \\ \Delta_2 = \Delta r_{12} + \Delta r_{23} + \Delta r_{45} + \Delta r_{56} \\ \Delta_3 = r_1(\Delta\theta_{13} + \Delta\theta_{46} - \Delta\theta_{15} - \Delta\theta_{35} - \Delta\theta_{24} - \Delta\theta_{26}) \end{cases}$$

$$B_{1g} \begin{cases} \Delta_4 = \Delta r_{12} - \Delta r_{23} - \Delta r_{45} + \Delta r_{56} \\ \Delta_5 = r_1(\Delta\theta_{15} - \Delta\theta_{35} - \Delta\theta_{24} + \Delta\theta_{26}) \end{cases}$$

$$B_{2u} \begin{cases} \Delta_6 = \Delta r_{12} - \Delta r_{23} + \Delta r_{45} - \Delta r_{56} \\ \Delta_7 = r_1(\Delta\theta_{15} - \Delta\theta_{35} + \Delta\theta_{24} - \Delta\theta_{26}) \end{cases}$$

$$B_{3u} \begin{cases} \Delta_8 = \Delta r_{12} + \Delta r_{23} - \Delta r_{45} - \Delta r_{56} \\ \Delta_9 = r_1(\Delta\theta_{13} - \Delta\theta_{46} - \Delta\theta_{15} - \Delta\theta_{35} + \Delta\theta_{24} + \Delta\theta_{26}) \end{cases}$$

* These coordinates are essentially the same as those given by Kilpatrick and Pitzer (1947) for ethylene; but note their error in including CH_2 deformation in the B_{2u} bending coordinate.

$$\mathbf{A} = M\mathbf{G}, \qquad \ldots\ldots(1)$$

where M is an arbitrary mass. The elements of **A** are then dimensionless quantities; by choosing the correct M, the off-diagonal elements in symmetrical molecules can often be made simple numbers. Here, M is chosen to be m_2, the mass of the

---

† Recently, some low-frequency infra-red bands obtained with a Thallium Bromide/Iodide prism, were reported by Plyler (1948); they are at 427, 403, 347, and 287 cm^{-1}. 403 and 347 may correspond to 387 and 332, accepted here. Possible combinations are: 782–347=435(B_{2u}); 913–512=401(B_{3u}); 782–447=335(B_{3u}). The remainder of the spectrum was not measured, and Herzberg's frequencies are accepted here until confirmation of these new values is obtained.

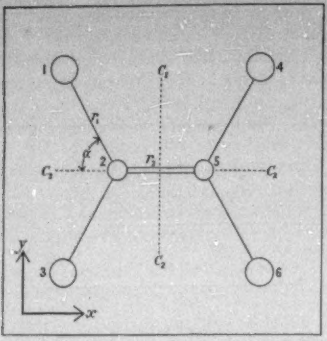

Figure 1. Coordinates for tetra-chloro-ethylene.

carbon atom. The secular equation for the molecular vibrations is as follows:

$$|\mathbf{dA}-\lambda\mathbf{I}|=0, \qquad \ldots\ldots(1\,a)$$

where **d** is the matrix of force constants for the coordinates which define **A**, and **I** is the unit matrix; the fundamental vibration frequencies ν_i, in cm^{-1}, are related to the roots λ_i as follows:

$$\lambda_i=4\pi^2c^2\nu_i^2M, \qquad \ldots\ldots(1\,b)$$

where c is the velocity of light in cm/sec.

Table 3. Kinetic Energy Matrices for the Planar Vibrations of Tetrachloro-ethylene

$$A_g\left[\begin{array}{ccc} 2 & -4\cos\alpha & 8\sin\alpha \\ & 4\left(\dfrac{m_{\mathrm{C}}}{m_{\mathrm{Cl}}}+2\cos^2\alpha\right) & -16\sin\alpha\cos\alpha \\ & & 16\left(\dfrac{m_{\mathrm{C}}}{m_{\mathrm{Cl}}}+2\sin^2\alpha\right) \end{array}\right]\begin{array}{l} \ldots\ldots\nu_{\mathrm{C=C}} \\ \ldots\ldots\nu_{\mathrm{C-Cl}} \\ \ldots\ldots\delta_{\widehat{\mathrm{CCl_2}}} \end{array}$$

$$B_{1g}\left[\begin{array}{cc} 4\left(\dfrac{m_{\mathrm{C}}}{m_{\mathrm{Cl}}}+2\sin^2\alpha\right) & -8(2a+\cos\alpha)\sin\alpha \\ & 4\left\{\dfrac{m_{\mathrm{C}}}{m_{\mathrm{Cl}}}+2(2a+\cos\alpha)^2\right\} \end{array}\right]\begin{array}{l} \ldots\ldots\nu_{\mathrm{C-Cl}} \\ \ldots\ldots\delta_{\widehat{\mathrm{CCCl}}} \end{array}$$

$$B_{2u}\left[\begin{array}{cc} 4\left(\dfrac{m_{\mathrm{C}}}{m_{\mathrm{Cl}}}+2\sin^2\alpha\right) & -8\sin\alpha\cos\alpha \\ & 4\left(\dfrac{m_{\mathrm{C}}}{m_{\mathrm{Cl}}}+2\cos^2\alpha\right) \end{array}\right]\begin{array}{l} \ldots\ldots\nu_{\mathrm{C-Cl}} \\ \ldots\ldots\delta_{\widehat{\mathrm{CCCl}}} \end{array}$$

$$B_{3u}\left[\begin{array}{cc} 4\left(\dfrac{m_{\mathrm{C}}}{m_{\mathrm{Cl}}}+2\cos^2\alpha\right) & -16\sin\alpha\cos\alpha \\ & 16\left(\dfrac{m_{\mathrm{C}}}{m_{\mathrm{Cl}}}+2\sin^2\alpha\right) \end{array}\right]\begin{array}{l} \ldots\ldots\nu_{\mathrm{C-Cl}} \\ \ldots\ldots\delta_{\widehat{\mathrm{CCl_2}}} \end{array}$$

$a=(r_1/r_2)$, (r_1=C–Cl distance, r_2=C–C distance); m_{C}=mass of carbon atom; m_{Cl}=mass of chlorine atom; $2\alpha=\widehat{\mathrm{ClCCl}}$.

Electron-diffraction studies of chlorinated ethylenes indicate that α is probably less than 60°; Brockway, Beach and Pauling (1935) give $\widehat{\mathrm{Cl–C–Cl}}=116°$ in

CH_2=CCl_2, but because of uncertainty, the value $\alpha = 60°$ is used here. Since the symmetry coordinates in Table 2 are not normalized, the force constants in the general valence-force potential function are obtained by simply adding the components from each symmetry factor.‡ The relation is shown in Table 4; in all cases, k refers to the C–Cl stretching constant, f to the bending constant, and d to the stretching–bending interaction constant, in the force constant matrices corresponding to the unnormalized symmetry coordinates of Table 2.

Table 4. Constants of the Valence-force Potential Function for the Planar Vibrations of Tetra-chloro-ethylene

Valence-force constant going with :	Component from : A_g	B_{1g}	B_{2u}	B_{3u}		
C=C stretching	(*b*) d_{11}	–	–	–	Principal constants	
C–Cl stretching	k	k	k	k		
$\widehat{CCl_2}$ deformation	f	–	–	f		
$\widehat{CCCl}$ deformation	f	f	f	f		
					Description of interaction	
$\Delta r_{12} . \Delta r_{25}$	(*b*) d_{12}	–	–	–	$\Delta r_{C=C} . \Delta r_{C-Cl}$	Interaction Constants
$\Delta r_{12} . \Delta r_{23}$	k	$-k$	$-k$	k	$\Delta r_{C-Cl} . \Delta r_{C-Cl}$	
* $\Delta r_{12} . \Delta r_{45}$	k	$-k$	k	$-k$		
* $\Delta r_{12} . \Delta r_{56}$	k	k	$-k$	$-k$		
† (*a*) $\Delta r_{25}(\Delta\theta_{13}-\Delta\theta_{15}-\Delta\theta_{35})$	(*b*) d_{13}	–	–	–	$\Delta r_{C=C} . \Delta\theta_{CCl_2}$	
$\Delta r_{12} . \Delta\theta_{13}$	d	–	–	d	$\Delta r_{C-Cl} . \Delta\theta_{CCl_2}$	
* $\Delta r_{12} . \Delta\theta_{46}$	d	–	–	$-d$		
$\Delta r_{12} . \Delta\theta_{15}$	$-d$	d	d	$-d$	$\Delta r_{C-Cl} . \Delta\theta_{CCCl}$	
* $\Delta r_{12} . \Delta\theta_{35}$	$-d$	$-d$	$-d$	$-d$		
* $\Delta r_{12} . \Delta\theta_{24}$	$-d$	$-d$	d	d		
* $\Delta r_{12} . \Delta\theta_{26}$	$-d$	d	$-d$	d		
* $\Delta\theta_{13} . \Delta\theta_{46}$	f	–	–	$-f$	$\Delta\theta_{CCl_2} . \Delta\theta_{CCl_2}$	
(*a*) $\Delta\theta_{13} . \Delta\theta_{15,35}$	$-f$	–	–	$-f$	$\Delta\theta_{CCl_2} . \Delta\theta_{CCCl}$	
* $\Delta\theta_{13} . \Delta\theta_{24,26}$	$-f$	–	–	f		
$\Delta\theta_{15} . \Delta\theta_{35}$	f	$-f$	$-f$	f	$\Delta\theta_{CCCl} . \Delta\theta_{CCCl}$	
$\Delta\theta_{15} . \Delta\theta_{24}$	f	$-f$	f	$-f$		
$\Delta\theta_{15} . \Delta\theta_{26}$	f	f	$-f$	$-f$		

(*a*) Conventional interaction for symmetry coordinates used.

(*b*) Elements (as indicated by the subscripts) from the first row and column of the force constant matrix associated with the A_g factor of the kinetic energy matrix in Table 3.

* Provisionally put equal to zero.

† The coordinates for angular deformation are in all cases actually $r_{CCl}\Delta\theta$, as in Table 2.

---

‡ The force constants so obtained are identical with those formed by the transformation $d=P^t d' P$. where d' is the matrix of symmetry constants for the symmetry coordinates $\Delta' = P\Delta$, P being the matrix for the transformation to symmetry coordinates from the valence coordinates Δ. (t denotes transpose). For comparison with alternative force fields, note that if all interactions are zero $(2f_{CCl_2}+f_{CCCl})=16f_{A_g, B_{3u}}$, where the f's are bending constants. Since f_{CCCl} differs so appreciably in the B_{1g} and B_{2u} factors, no attempt is made here to carry it over to the A_g and B_{3u} factors.

There are twenty-one force constants in the most general valence-force potential function for the planar vibrations of tetra-chloro-ethylene; the symmetry of the system allows of only fifteen independent constants. If only interactions between adjacent bonds and angles are considered significant, the eight constants indicated must be put equal to zero. This leads to the following relations between the symmetry constants:

$$k_{B_{1g}}=k_{B_{2u}}; \qquad k_{A_g}=k_{B_{3u}}, \qquad \ldots\ldots(2)$$

$$d_{A_g}=d_{B_{3u}}=-d_{B_{1g}}=-d_{B_{2u}}, \qquad \ldots\ldots(3)$$

$$f_{A_g}=f_{B_{3u}}, \qquad \ldots\ldots(4)$$

the subscripts referring to the symmetry factor. Since the constant for the interaction $\Delta r_{12}\,.\,\Delta\theta_{13}$ is unlikely to be negligible, d_{A_g} will have a non-zero value. With the relations (2) and (3), the following empirical relation arises between two of the interaction constants:

$$2\,d(\Delta r_{12}\,.\,\Delta\theta_{13})+d(\Delta r_{12}\,.\,\Delta\theta_{15})=0, \qquad \ldots\ldots(5)$$

the brackets referring to the interactions. Since such an empirical relationship is unlikely to be real, it is probable that too many constants have been eliminated. It may be noted that the relations (2) are reasonable; in the B_{1g} and B_{2u} modes, the C–Cl stretching vibrations are antisymmetrical in each CCl_2 group, while in the A_g and B_{3u} modes they are symmetrical. The interactions $\Delta\theta_{15}\,.\,\Delta\theta_{24}$ and $\Delta\theta_{15}\,.\,\Delta\theta_{26}$ both become zero if $f_{B_{2u}}=f_{B_{1g}}$; if in addition $f_{A_g}=f_{B_{1g}}$, then the interaction $\Delta\theta_{15}\,.\,\Delta\theta_{35}$ also becomes zero.

§4. THE METHOD OF ANALYSIS

The idea of obtaining ranges of solutions for force constants was introduced by Duchesne (1942); general treatments of the second degree equation have been given by Glockler and Tung (1945) and by the author (1949 a), who examined the nature of the normal modes associated with the different possible solutions and gave formulae. The latter has also extended the treatment to equations of higher degree, though not so explicitly. The most convenient formulae for second degree equations are given below; the force constants d_{ij} are the elements of the matrix **d** going with the kinetic energy matrix **A** derived from the coordinates Δ_1, Δ_2 and the elements $V_{ij}(\nu_{i,j})$ are the fractions of the potential energy in the terms involving $d_{ij}\Delta_i\Delta_j$ for the mode $\nu_{i,j}$. The quantities $\rho_{1,2}$ are defined as follows:

$$\rho_{1,2}=(\Delta_{1,2}/\Delta_{2,1})(\nu_{1,2}). \qquad \ldots\ldots(6)$$

They give the form of the vibration for the modes $\nu_{1,2}$; ν_i is the mode for which Δ_i is the approximate normal coordinate.

$$\left.\begin{aligned} d_{11}&=d_{11}'[1+(R^2/D)(\lambda_2/\lambda_1)],\\ d_{22}&=d_{11}'[p^2+(S^2/D)(\lambda_2/\lambda_1)],\\ d_{12}&=d_{11}'[p-(RS/D)(\lambda_2/\lambda_1)].\end{aligned}\right\} \qquad \ldots\ldots(7)$$

$$\left.\begin{aligned} V_{11}(\nu_1)&=[(S^2d_{11})/(A_{11}'\lambda_1)],\\ V_{22}(\nu_1)&=[(R^2d_{22})/(A_{11}'\lambda_1)],\\ V_{12}(\nu_1)&=2[(RSd_{12})/(A_{11}'\lambda_1)].\end{aligned}\right\} \qquad \ldots\ldots(8)$$

$$\left.\begin{aligned} V_{11}(\nu_2) &= p^2[(Dd_{11})/(A_{11}'\lambda_2)], \\ V_{22}(\nu_2) &= [(Dd_{22})/(A_{11}'\lambda_2)], \\ V_{12}(\nu_2) &= -2p[(Dd_{12})/(A_{11}'\lambda_2)]. \end{aligned}\right\} \qquad \ldots\ldots(9)$$

$$\left.\begin{aligned} \rho_1 &= (S/R), \\ \rho_2 &= -(1/p), \end{aligned}\right\} \qquad \ldots\ldots(10)$$

where $A_{11}' = (A_{11} + 2pA_{12} + p^2A_{22})$, $d_{11}' = (\lambda_1/A_{11}')$, $D = (A_{11}A_{22} - A_{12}^2)$, $R = (A_{12} + pA_{22})$, $S = (A_{11} + pA_{12})$.

All results are expressed in terms of the single parameter p, which can be varied at will. It is the ratio (c_{12}/c_{11}) of coefficients in the first row of the matrix for the transformation to normal coordinates, $\boldsymbol{\eta} = \mathbf{c}\boldsymbol{\Delta}$. The ration of the coefficients (c_{22}/c_{21}) in the second row is $-(S/R)$. For the special case of tetra-chloro-ethylene, the following additional formulae are obtained for the directions of the displacement vector of chlorine atom 1, as a function of p, the angle α being assumed to be 60°.

$$B_{1g}\left\{\begin{aligned} \tan\beta_1 &= [\{\sqrt{3} - p(1 + c_1')\}/\{1 + p\sqrt{3}(1 + c_1'')\}], \\ \tan\beta_2 &= -[1 + 2(m_{\mathrm{Cl}}/m_{\mathrm{C}})]^{-1}[(1 + p\sqrt{3})/\{\sqrt{3} - p(1 + c_2)\}]. \end{aligned}\right\} \qquad \ldots\ldots(11)$$

$$B_{2u}\left\{\begin{aligned} \tan\beta_1 &= [(\sqrt{3} - p)/(1 + p\sqrt{3})], \\ \tan\beta_2 &= -[1 + 2(m_{\mathrm{Cl}}/m_{\mathrm{C}})]^{-1}[(1 + p\sqrt{3})/(\sqrt{3} - p)]. \end{aligned}\right\} \qquad \ldots\ldots(12)$$

$$B_{3u}\left\{\begin{aligned} \tan\beta_1 &= [(\sqrt{3} + 2p)/(1 - 2p\sqrt{3})], \\ \tan\beta_2 &= -[1 + 2(m_{\mathrm{Cl}}/m_{\mathrm{C}})][(1 - 2p\sqrt{3})/(\sqrt{3} + 2p)], \end{aligned}\right\} \qquad \ldots\ldots(13)$$

where, in the B_{1g} modes, $c_1' = 8a(1 + a)c_1$, $c_1'' = 8a^2c_1$, $c_1 = [(m_{\mathrm{C}}/m_{\mathrm{Cl}}) + 2(1 + a)]^{-1}$, $c_2 = 8a[(m_{\mathrm{C}}/m_{\mathrm{Cl}}) + 2]^{-1}$. In each case, β_i is the angle arc tan $(-y_1/x_1)$ for the mode ν_i, ($i = 1$, stretching mode, $i = 2$, bending mode), where x_1, y_1 are the Cartesian displacements of atom 1 referred to the axes shown in Figure 1; for a 'pure' stretching mode, $\beta_1 = 60°$, the chlorine atoms being displaced along the lines of the C–Cl bonds, and for a 'pure' bending mode $\beta_2 = 150° \equiv -30°$, the displacements being normal to the C–Cl bonds.

The cubic A_g factor is treated by the method introduced by the author (1949). Three sets of solutions are obtained, using three combinations of the symmetry coordinates given in Table 2. The force constants corresponding to the coordinates in Table 2 are given by the formula

$$d_{ij} = \sum_{k=1}^{3} e_{ik}e_{jk}(\lambda_k/C_k), \qquad \ldots\ldots(14)$$

where e_{ik}, e_{jk} are elements from the matrices $\mathbf{e}$ given in Table 5, and the C_k are defined by

$$C_1 = 2C_1', \qquad C_2 = 16\epsilon C_2', \qquad C_3 = 1024\epsilon^3 C_3', \qquad \ldots\ldots(15)$$

ϵ being the mass-ratio $m_{\mathrm{C}}/m_{\mathrm{Cl}}$.

Table 5. Derivation of Force Constants for the A_g Factor

(*a*) Forming new coordinate $\Delta_1' = \Delta_1 + p\Delta_2$

$$\mathbf{e} = \begin{bmatrix} 1 & 2\{1 - (2\epsilon + 1)p\} & -16\sqrt{3}\epsilon \\ p & 2(1 - p) & 0 \\ 0 & 0 & 8\epsilon \end{bmatrix}$$

$C_1' = C_2' = \{1 - 2p + (2\epsilon + 1)p^2\}$.

(*b*) Forming new coordinate $\Delta_1'=\Delta_1+p\Delta_3$

$$\mathbf{e}=\begin{bmatrix} 1 & 2(1+2\sqrt{3}p) & -16\epsilon\{\sqrt{3}+4(\epsilon+2)p\} \\ 0 & 2\{1+4\sqrt{3}p+4(2\epsilon+3)p^2\} & -32\epsilon p \\ p & 2(1+2\sqrt{3}p)p & 8\epsilon(1+2\sqrt{3}p) \end{bmatrix}$$

$$C_1'=\{1+4\sqrt{3}p+4(2\epsilon+3)p^2\},\quad C_3'=\{1+4\sqrt{3}p+8(\epsilon+2)p^2\},\quad C_2'=C_1'C_3'.$$

(*c*) Forming new coordinate $\Delta_2'=\Delta_2+p\Delta_3$

$$\mathbf{e}=\begin{bmatrix} 1 & 2(1-2\sqrt{3}p) & -16\epsilon(\sqrt{3}+2p) \\ 0 & 2 & -32\epsilon p \\ 0 & 2p & 8\epsilon \end{bmatrix}$$

$$C_1'=1,\qquad C_2'=C_3'=(1+4p^2).$$

The components in the displacements corresponding to the above three types of solution are given below as matrices $[\Delta_i(\nu_j)]$.

Table 6. Matrices giving Forms of Vibration for the A_g Factor

(*a*) With $\Delta'_1=\Delta_1+p\Delta_2$

$$\begin{bmatrix} 1 & -p & 0 \\ -\{1-2\epsilon p/(1-p)\} & 1 & 0 \\ 2\sqrt{3} & -2\sqrt{3}p & 1 \end{bmatrix}$$

(*b*) With $\Delta_1'=\Delta_1+p\Delta_3$

$$\begin{bmatrix} 1 & -\{4p^2/[1+4\sqrt{3}p+8(\epsilon+2)p^2]\} & -p \\ -1 & 1 & 0 \\ 2\{\sqrt{3}+4\epsilon p/(1+2\sqrt{3}p)\} & \{4p/[1+4\sqrt{3}p+8(\epsilon+2)p^2]\} & 1 \end{bmatrix}$$

(*c*) With $\Delta_2'=\Delta_2+p\Delta_3$

$$\begin{bmatrix} 1 & 0 & 0 \\ -1 & 1 & -p \\ 2\sqrt{3} & 4p & 1 \end{bmatrix}$$

The directions of the displacements of atom 1 for the above three solutions are as follows:

(*a*) $\Delta_1'=\Delta_1+p\Delta_2$.

$$\tan\beta_1=\sqrt{3},\quad \tan\beta_2=\sqrt{3},\quad \tan\beta_3=-(1\sqrt{3})\ \text{(independent of } p\text{)}. \qquad \ldots\ldots(16)$$

(*b*) $\Delta_1'=\Delta_1+p\Delta_3$.

$$\left.\begin{aligned} &\tan\beta_1=-(1/\sqrt{3}),\qquad \tan\beta_3=-(\sqrt{3}+8p)^{-1}, \\ &\tan\beta_2=\{[\sqrt{3}+14p+8(\epsilon+2)\sqrt{3}p^2]/[1+2\sqrt{3}p+8\epsilon p^2]\}. \end{aligned}\right\} \qquad \ldots\ldots(17)$$

(*c*) $\Delta_2'=\Delta_2+p\Delta_3$.

$$\left.\begin{aligned} &\tan\beta_1 \text{ indeterminate, } (x_1=y_1=0), \\ &\tan\beta_2=\{(\sqrt{3}+2p)/(1-2\sqrt{3}p)\}, \\ &\tan\beta_3=-\{(1-2\sqrt{3}p)/(\sqrt{3}+2p)\}. \end{aligned}\right\} \qquad \ldots\ldots(18)$$

If the cubic factor is expanded, the following relations are obtained between the force constants and the fundamental vibration frequencies:

$$\left.\begin{aligned}
&2[d_{11}-2d_{12}+4\sqrt{3}\,d_{13}+(2\epsilon+1)k+4(2\epsilon+3)f-4\sqrt{3}d]=\lambda_1+\lambda_2+\lambda_3,\\
&8\epsilon[(k+4f)d_{11}-4(\sqrt{3}d+2f)d_{12}+4(\sqrt{3}k+2d)d_{13}-d_{12}{}^2-4d_{13}{}^2\\
&\qquad\qquad+8(\epsilon+2)(kf-d^2)]=\lambda_1\lambda_2+\lambda_1\lambda_3+\lambda_2\lambda_3,\\
&128\epsilon^2[(kf-d^2)d_{11}+2dd_{12}d_{13}-fd_{12}{}^2-kd_{13}{}^2]=\lambda_1\lambda_2\lambda_3,
\end{aligned}\right\} \qquad \ldots\ldots(19)$$

where λ_1, λ_2 and λ_3 are derived from the three fundamentals, k, f and d are the constants for C–Cl stretching, Cl–C–Cl deformation, and stretching–deformation interaction (identical with the elements d_{22}, d_{33} and d_{23} of the force constant matrix associated with the coordinates of Table 2), and d_{11}, d_{12} and d_{13} are the elements from the first row of the force constant matrix, being the constants for C=C stretching, C=C stretching C–Cl stretching interaction, and C=C stretching Cl–C–Cl bending interaction. If k, f and d are carried over from the B_{3u} factor, to satisfy relations (2), (3) and (4), equations (19) become

$$\left.\begin{aligned}
&d_{11}-2d_{12}+4\sqrt{3}d_{13}=(1/2)[(\lambda_1+\lambda_2+\lambda_3)-(\lambda_1'+\lambda_2')],\\
&(k+4f)d_{11}-4(\sqrt{3}d+2f)d_{12}+4(\sqrt{3}k+2d)d_{13}-d_{12}{}^2-4d_{13}{}^2\\
&\qquad\qquad=(1/8\epsilon)[(\lambda_1\lambda_2+\lambda_1\lambda_3+\lambda_2\lambda_3)-\lambda_1'\lambda_2'],\\
&[\lambda_1'\lambda_2'/64\epsilon(\epsilon+2)]d_{11}+2dd_{12}d_{13}-fd_{12}{}^2-kd_{13}{}^2=\lambda_1\lambda_2\lambda_3/128\epsilon^2,
\end{aligned}\right\} \qquad \ldots\ldots(20)$$

where λ_1' and λ_2' are for the B_{3u} vibrations. Equations (20) may be solved for d_{11}, d_{12} and d_{13}, at a series of values for k, f and d. The best procedure is to eliminate d_{11} from the last two equations (20), using the first equation; the two second-degree equations in d_{12}, d_{13} so obtained are those for two ellipses. Allowed values of k, f and d are those for which the ellipses intersect, the solution for d_{12} and d_{13} being given by the points of intersection. Substitution of these solutions in the first equation gives d_{11}. Since there are real points of intersection allowed only over a certain range of solutions, the allowed solutions for d_{11}, d_{12} and d_{13}, when plotted for the three pairs of constants, will lie on closed curves.

§ 5. RESULTS OF THE ANALYSIS

If the relations (2), (3) and (4) are to hold, the different symmetry factors must all be solved simultaneously; if the two assignments of Table 1 are used there are four possible fits for the pair B_{1g}, B_{2u} and two for the pair A_g, B_{3u}, which can be correlated in four possible ways:

(i) B_{1g}(T), B_{2u}(T); B_{3u}(T), A_g.
(ii) B_{1g}(D), B_{2u}(D); B_{3u}(D), A_g.
(iii) B_{1g}(T), B_{2u}(D); B_{3u}(D), A_g.
(iv) B_{1g}(D), B_{2u}(T); B_{3u}(T), A_g.

Since there is no certainty that the interactions between non-adjacent bonds and angles are negligible, and in order to obtain a clearer picture of the situation, reasonable ranges of allowed solutions have been obtained for each symmetry

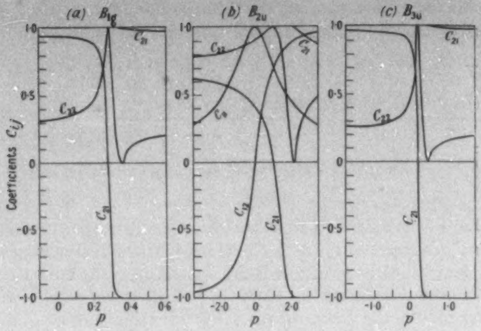

Figure 2. Coefficients in the transformations to normal coordinates (conventionally normalized to unity).

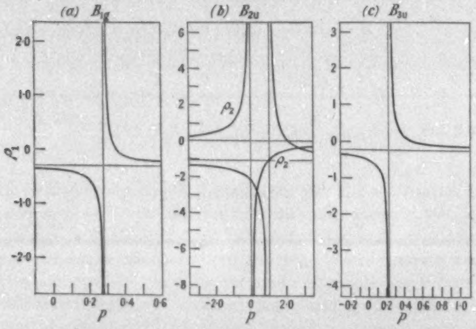

Figure 3. The compositon of the displacements.

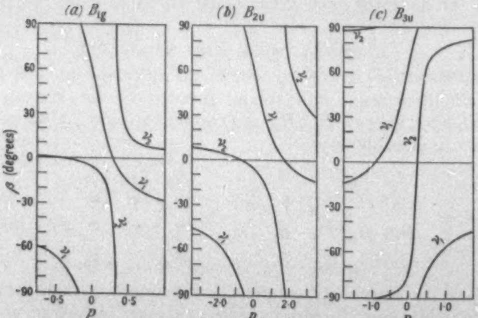

Figure 4. The directions of the displacement vectors.

factor independently, using equations (7) to (14). The normalized coefficients in the transformations to normal coordinates for the three second-degree factors are shown plotted in Figure 2; those from the first row are independent of the initial coordinates and are given only in the B_{2u} plot for comparison. The composition of the displacements is shown in Figure 3; ρ_2 is independent of the initial coordinates and is given only in the B_{2u} plot for comparison. The direction of the displacement vector of chlorine atom 1 (cf. Figure 1) is given in Figure 4. These three quantities are independent of the vibrational assignment. The force constants and potential energy distributions * are shown in Figures 5 to 10.

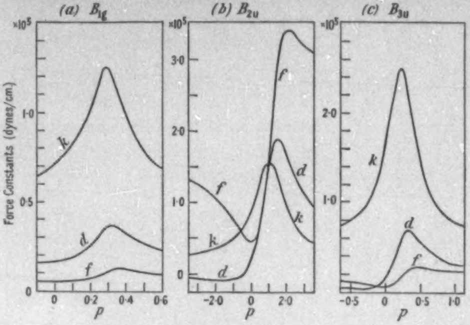

Figure 5. Force constants with assignment T.

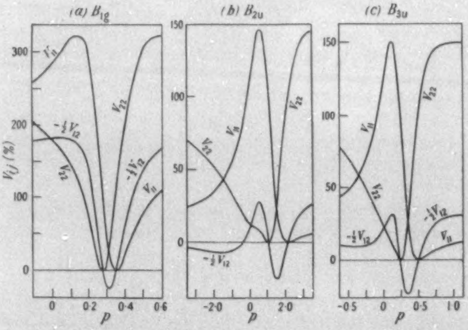

Figure 6. Distribution of the potential energy in the stretching modes, with assignment T.

In each case the parameter is p, so that the different curves for each symmetry factor are readily correlated. It is instructive to compare these plots with those for the triatomic molecule (Torkington 1949 a). The curves for the constants are all essentially similar; each has a maximum and a minimum (asymptotic for k at $p = \infty$), the coordinates p of which are independent of the vibrational assignment, and determined only by the kinetic energy matrix elements; the maximum

---

* In all cases the numbering 1, 2 refers to coordinates Δ_1 (stretching) and Δ_2 (bending) in each symmetry factor. $V_{12}(\nu_2)$ is omitted for the sake of clarity.

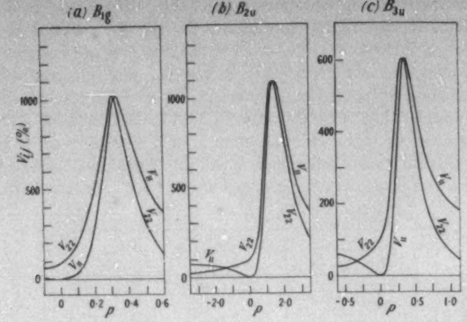

Figure 7. Distribution of the potential energy in the bending modes, with assignment T.

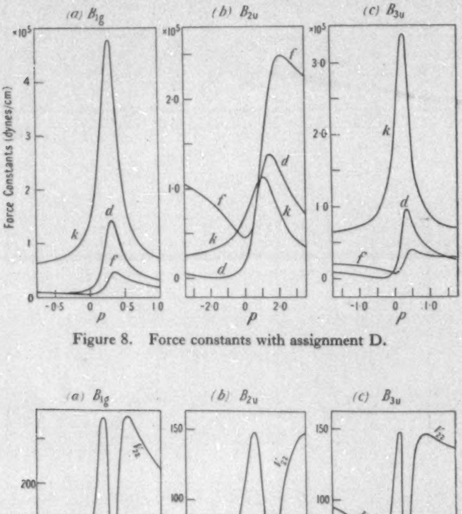

Figure 8. Force constants with assignment D.

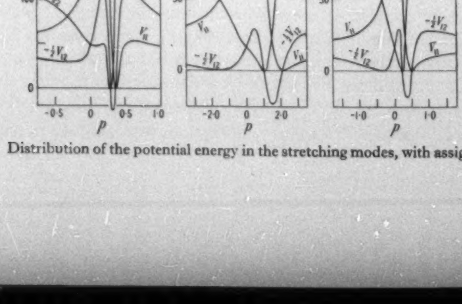

Figure 9. Distribution of the potential energy in the stretching modes, with assignment D.

and minimum values of the constants depend on the vibration frequencies. In all the curves for the second-degree factors, the maxima of k lie beyond the range of possible values, with the possible exception of B_{1g}(T), assuming this to be 0·7 to 1·2 × 10⁵ dynes/cm. There are therefore two bands of possible solutions, one on each side of the maxima. Here the left-hand band corresponds to smaller values of f and d; for the B_{2u} factor it is the only range of solutions allowed, the right-hand band being associated with f values which are impossibly high. It may be remarked that for the B_{3u} factor the f values on the right-hand side are improbably high; the comparable constant in ethylene and ethylene-d_4 is of magnitude 0·069 to 0·070 × 10⁵ dynes/cm. and the bond-length r_1 is included in the coordinate. Examination of the energy plots shows that the two bands of solutions correspond to alternative assignments of the vibration frequencies

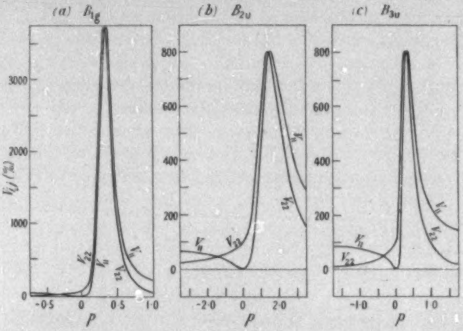

Figure 10. Distribution of the potential energy in the bending modes, with assignment D.

within each symmetry factor; on the left-hand side the mode ν_1 is largely determined by the coordinate Δ_1 and ν_2 by Δ_2, while on the right-hand side ν_1 is determined largely by Δ_2 and ν_2 by Δ_1. Clearly, then, the left-hand side is the only one to be considered here. In the energy plots, the maxima of $V_{11}(\nu_1)$, $V_{22}(\nu_1)$ are the same height, corresponding to identical values of the interaction constant d (cf. the plots for the triatomic molecule); the same applies to the pair $V_{11}(\nu_2)$, $V_{22}(\nu_2)$, and to the minima of $V_{12}(\nu_1)$, (maxima of $-\frac{1}{2}V_{12}$, the quantity plotted).

The plots for the cubic A_g factor cover a smaller range of solutions than those for the second-degree factors; they are chosen to correspond to possible values of the C=C stretching constant, the limits of which are taken here to be 8·0 to 10·0 × 10⁵ dynes/cm. Only the principal components are shown in the energy plots for solutions (*a*) and (*b*), the others being either negligible or nearly constant. Inspection shows that inclusion of C–Cl stretching or Cl–C–Cl deformation in the new coordinate Δ_1' formed from Δ_1, the valence coordinate for C=C stretching, leads to a lowering of the C=C stretching constant, d_{11}. The magnitude of the C=C stretching constant has been the major problem in past analyses of the potential function of tetra-chloro-ethylene; low values of 6·25 (Duchesne 1937, 1938), and 6·18 (Thompson and Linnett 1937), were obtained before a proper allowance for possible interactions had been made; more recently, Duchesne

(1942, 1943, 1948), has given selected solutions covering a range of values for the C=C stretching constant. The present analysis shows more clearly the association of the allowed relative values of all the constants, and the implication of different solutions in terms of the properties of the normal modes. From Figure 11 (*a*), it is seen that a lowering of the constant d_{12} for $\Delta r_{C=C} \cdot \Delta r_{C-Cl}$ interaction from about 1·0 to 0, keeping the constant d_{23} for $\Delta r_{C-Cl} \cdot \Delta \theta_{CCl_2}$ interaction at zero, is associated with a lowering of the C=C stretching constant d_{11} from 10·5 to 8·0. From Figure 11 (*b*), a raising of d_{13} for $\Delta r_{C=C} \cdot \Delta \theta_{CCl_2}$ interaction from about $-0\cdot25$ to 0 is associated with a decrease in d_{11} from 10·5 to 8·8, d_{12} remaining relatively unaffected. From Figure 11 (*c*), d_{11} is practically independent of variation in the C–Cl stretching constant $d_{22} \equiv k$, and in the Cl–C–Cl bending constant $d_{33} \equiv f$, while these, and the constant d_{12}, are both rather sensitive to the magnitude of $d_{23} \equiv d$ for $\Delta r_{C-Cl} \cdot \Delta \theta_{CCl_2}$ interaction; clearly, by varying d_{12} and d_{23} simultaneously d_{11} can be kept at any reasonable value chosen. It has been pointed out by the author (1949) that the most obvious way of giving the C=C stretching constant a reasonable value is to give a fairly high positive value to d_{12}, of the order of 0·5; this value may be reduced by giving d_{13} small positive values, $<0\cdot2$. There is nothing particularly striking in the energy curves in Figure 12; the principal components range from about 80 to 120%, except for ν_2 and ν_3 in case (*c*): $(\Delta_2' = \Delta_2 + p\Delta_3)$. Here, for $p = 0\cdot5$, both modes have equal contributions from the square terms for C–Cl stretching and C–Cl bending, the interaction being small and positive for ν_2 and large and negative for ν_3.

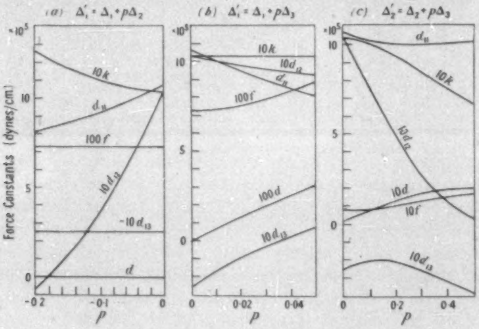

Figure 11. Force constants for the A_g factor.

The four possible solutions for the correlation of the B_{1g} and B_{2u} factors are given in Table 7. If it is allowable to correlate in this way, i.e. if the relevant interactions are really negligible, the proper solution for this pair of symmetry factors will be one of the four. Assignment T leads to a much lower value of the B_{1g} bending constant, and to a rather higher value for the C–Cl stretching constant. Assignment D is given here for completeness and comparison; it has already been dealt with by Duchesne but he uses different coordinates. The solution for B_{1g}(D) lies in the band applicable when the higher frequency is a bending mode; the same applies to the pair B_{1g}(T), B_{2u}(D). This might be considered as some evidence against the old assignment. The interaction term in the B_{1g} and B_{2u}

Table 7. Correlation of the B_{1g} and B_{2u} Factors

	(i)		(ii)		(iii)		(iv)	
	B_{1g}(T)	B_{2u}(T)	B_{1g}(D)	B_{2u}(D)	B_{1g}(T)	B_{2u}(D)	B_{1g}(D)	B_{2u}(T)
k	0·8935		0·8170		0·7134		0·7760	
f	0·0634	0·4466	0·2363	0·4890	0·1018	0·4485	0·0822	0·4708
d	0·2053		0·3711		0·2411		0·0920	
ρ_1	−0·4188	−2·121	−0·2481	−2·508	−0·2106	− 2·198	−0·3156	−1·944
ρ_2	−7·479	151·5	−1·168	−3·799	−1·781	−16·29	2·878	4·852
β_1	28° 8′	60° 23′	−26° 10′	45° 15′	−17° 47′	56° 29′	−72° 39′	71° 39′
β_2	−9° 57′	−4° 46′	7° 28′	−8° 16′	13° 17′	−5° 32′	− 0° 56′	−2° 47′
$V_{11}(\nu_1)$	325·49	111·80	49·08	136·44	99·10	121·56	76·23	96·29
$V_{22}(\nu_1)$	131·68	12·42	230·68	12·98	319·11	15·81	81·04	15·45
$V_{12}(\nu_1)$	−357·17	−24·21	−179·76	−49·42	−318·21	−37·37	−57·27	−11·74
$V_{11}(\nu_2)$	65·28	0·01	300·02	16·16	402·08	0·64	39·08	6·08
$V_{22}(\nu_2)$	259·08	99·39	118·42	139·61	182·08	106·38	34·26	86·92
$V_{12}(\nu_2)$	−224·36	0·60	−318·44	−55·77	−484·16	−7·02	26·66	7·00

(Force constants in units of 10^5 dynes/cm.; components V_{ij} of the potential energy as percentages of the total; molecular dimensions : $r_{C=C}=1{\cdot}353$ A., $r_{C-Cl}=1{\cdot}69$ A., all angles 120°.)

factors appears to be rather important. It should be mentioned here that this interaction, and the large discrepancy between the B_{1g} and B_{2u} bending constants, might possibly be much modified by the inclusion of van der Waals forces in the treatment.* This has been done for some trihalides and tetrahalides by Linnett and Heath (1948). They use a repulsion potential for non-bonded halogen atoms; such a repulsion between atoms 1 and 4, and between atoms 2 and 6 (see Figure 1) would account for the C=C–Cl bending being more difficult in the B_{2u}

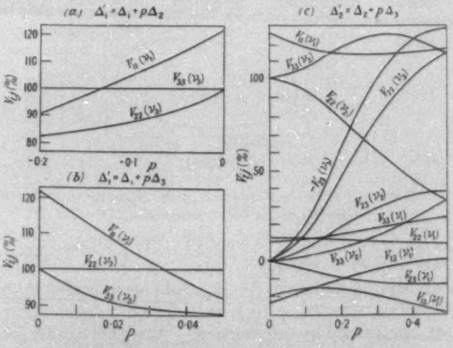

Figure 12. Distribution of the potential energy in the A_g modes.

---

* There is a similar but smaller discrepancy between the B_{1g} and B_{2u} bending constants in ethylene; the values with the symmetry coordinates of Table 2 are 0·100 and 0·142 × 10^5 dynes/cm. respectively (Torkington 1949 d). It may be observed that the B_{1g} and B_{2u} stretching constants in C_2H_4 are nearly equal, (1·24 and 1·27 × 10^5 dynes/cm.); since the degree of anharmonicity in C_2Cl_4 will be less than in C_2H_4 it is justifiable to assume the constants equal in the former, provided there is no interaction between the two ends of the molecule.

than in the B_{1g} mode. It is of interest that the four chlorine atoms are very nearly at the corners of a square. There is therefore no anomaly in the Cl–C–Cl angle being less than 120°, as accepted; the van der Waals repulsions in the equilibrium position will approximately balance, and the deviation from the ideal trigonal angle can be accounted for by the partial hybridization.*

We must now consider the possibility of correlating the A_g and B_{3u} factors mutually and with the pair already dealt with. Firstly, the condition of equation (3) cannot hold with any combination of assignments possible; therefore some of the interactions $\Delta r_{12} . \Delta\theta_{35}$, $\Delta r_{12} . \Delta\theta_{24}$ and $\Delta r_{12} . \Delta\theta_{26}$ must be real. If we assume that only the band of solutions on the left-hand side need be considered for the B_{3u} factor, then the interaction constant d cannot exceed 0·1. Using assignment T, it is found that only a fairly narrow band of B_{3u} solutions ($p \simeq -0{\cdot}12$ to $-0{\cdot}225$) gives real solutions for d_{11}, d_{12} and d_{13} in equations (20). The range of values covered is as follows:—$d_{11} \sim 7{\cdot}3$ to $13{\cdot}3 \times 10^5$, $d_{12} \sim -0{\cdot}3$ to $+2{\cdot}2 \times 10^5$, $d_{13} \sim -0{\cdot}55$ to $+0{\cdot}1 \times 10^5$ dynes/cm. Since the solutions lie on closed curves there are two possible solutions for each of the interaction constants at each value of the C=C stretching constant (Figure 13). Duchesne, using assignment D for the fitting, obtained only constants corresponding to the positive ranges for d_{12} and d_{13}; it is important to realize that the negative range is also allowed. With analogous coordinates, the constant d_{13} for ethylene (Kilpatrick and Pitzer 1947) has a value of the order $-0{\cdot}14 \times 10^5$ dynes/cm.† It would seem probable that the negative constant was also the correct one in tetra-chloro-ethylene, rather than that the difference in sign was caused by substitution. A negative value for d_{12} in ethylene has also been reported‡ (Manneback and Verleysen 1936, Tchang 1938). The

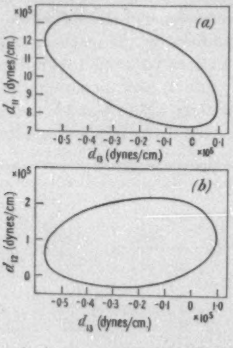

Figure 13. Allowed solutions for the force constants of the A_g factor, carrying over k, f and d from the B_{3u} factor (using assignment T).
(a) d_{11}, (b) d_{12}, plotted against d_{13}.

---

* The resultant vectors of the repulsions will of course be inclined to the C–Cl bonds, tending to slightly reduce the Cl–C–Cl angle. The author is grateful to Dr. Linnett for drawing his attention to this fact.

† It must be remembered that the constant for the angle coordinate in dynes/rdn × 10^{-8} is $r_1 d_{13}$; this interaction is therefore much larger in C_2Cl_4 than in C_2H_4.

‡ But the dimensions of Badger (1934), were used (with $H\widehat{C}H = 126°$); a later analysis has shown that d_{12} is definitely positive (Torkington, to be published).

balance of evidence is therefore in favour of there being a negative constant for $\Delta r_{C-C} \cdot \Delta\theta_{CCl}$, interaction and a small negative one for $\Delta r_{C=C} \cdot \Delta r_{C-Cl}$ interaction in tetra-chloro-ethylene. This interpretation avoids the large stretching–stretching interaction constant; though there is some theoretical justification for such a constant in conjugated systems (Coulson and Longuet-Higgins 1948). There are exact solutions with $d_{12}=0$ at $d_{11}=10{\cdot}4$ and $7{\cdot}4$.* The corresponding values for d_{13} are $-0{\cdot}50$, $-0{\cdot}06$‡ $\times 10^5$ dynes/cm.

Using Table 4, a table for the valence-force constants for tetra-chloro-ethylene may now be drawn up. Four alternative sets of constants are given in Table 8, derived from (i) and (iv) of the correlations outlined at the beginning of this section, and taking for the A_g factor the two solutions with $k_{C=C} \sim 9{\cdot}0 \times 10^5$ dynes/cm. These are as follows:

(*a*) With negative interactions,

$d_{11}=9{\cdot}088$, $d_{12}=-0{\cdot}220$, $d_{13}=-0{\cdot}374$ $\times 10^5$ dynes/cm.
$k=1{\cdot}193$, $f=0{\cdot}0786$, $d=0{\cdot}0692$

(*b*) With positive interactions,

$d_{11}=9{\cdot}036$, $d_{12}=1{\cdot}350$, $d_{13}=0{\cdot}0870$ $\times 10^5$ dynes/cm.
$k=1{\cdot}053$, $f=0{\cdot}0872$, $d=0{\cdot}0534$

k, f and d satisfy the B_{3u} factor, with assignment T, at (*a*) $p=-0{\cdot}125$, (*b*) $p=-0{\cdot}20$.

Table 8. Typical Valence-Force Constants for Tetra-chloro-ethylene (in units of 10^5 dynes/cm.)

	(*a*)			(*b*)		
	(i)		(iv)	(i)		(iv)
C=C stretching		9·088			9·036	
C–Cl stretching	4·173		3·938	3·892		3·657
Cl–C–Cl deformation		0·157			0·174	
Cl–C=C deformation	0·667		0·710	0·684		0·727
$\Delta r_{12} . \Delta r_{25}$		−0·220			1·350	
$\Delta r_{12} . \Delta r_{23}$	0·599		0·834	0·318		0·553
$\Delta r_{25}(\Delta\theta_{13}-\Delta\theta_{15}-\Delta\theta_{35})$		−0·374			0·087	
$\Delta r_{12} . \Delta\theta_{13}$		0·138			0·107	
$\Delta r_{12} . \Delta\theta_{15}$	0·272		0·046	0·304		0·077
$\Delta r_{12} . \Delta\theta_{35}$	−0·549		−0·322	−0·517		−0·291
$\Delta\theta_{13} . \Delta\theta_{15,35}$		−0·157			−0·174	
$\Delta\theta_{15} . \Delta\theta_{35}$	−0·353		−0·396	−0·336		−0·379
$\Delta\theta_{15} . \Delta\theta_{24}$	0·383		0·389	0·383		0·389
$\Delta\theta_{15} . \Delta\theta_{26}$	−0·383		−0·389	−0 383		−0·389

Interpretations of the signs of cross-terms are now available. According to Heath and Linnett (1948) the signs of the constants for interactions $\Delta r_1 . \Delta r_2$ and $(\Delta r_1+\Delta r_2)\Delta\theta$ in a triatomic system are respectively negative and positive if determined by the changes in hybridization due to orbital-following; the former becomes positive if determined by repulsions between the non-bonded atoms. Coulson, Duchesne and Manneback (1948) obtain a positive constant for $\Delta r_1 . \Delta r_2$ interaction determined by hybridization changes, but their argument is less convincing and the result of Heath and Linnett will be accepted here. If only the interactions involving alternate atoms are considered, any polyatomic molecule can be analysed into a number of triatomic systems. In tetra-chloro-ethylene, there are only ClCCl and ClCC systems to consider. The CCl_2 bond–bond interaction is positive here, implying that it is determined by Cl. . . .Cl repulsion. The constants d in the A_g and B_{3u} factors are also positive, whichever solution is absolutely correct. If both the bond-angle interaction constants in CCl_2 and ClCC are positive, then the first must be greater (the second is positive, from the analysis of the B_{1g} and B_{2u} modes). This difference could arise from a Cl. . . Cl repulsion greater than Cl. . . C, though the hybridization components may be determining. The constant for $\Delta r_{C=C}\,.\,\Delta\theta_{CCl_2}$ interaction becomes meaningless (cf. Torkington 1949); $d(\Delta r_{C=C}\,.\,\Delta\theta_{CCCl})$ has opposite sign to d_{13}, which would therefore be expected to be negative here. d_{12} will be negative or positive according as hybridization changes or Cl. . . C repulsions are determining. A large positive d_{12}, of the order suggested by Duchesne seems unlikely unless, possibly, there is real conjugation; from the present point of view, the repulsion Cl. . . C would have to be much greater than Cl. . . Cl. A moderate repulsion would partially balance the hybridization constant, giving the small negative d_{12} suggested as correct here. The large constant for $\Delta\theta_{15}\,.\,\Delta\theta_{24}$ interaction, which does not fall into a triatomic system, can be accounted for by Cl. . . Cl repulsion between the two ends of the molecule, as mentioned previously. It is probable that such repulsions would not introduce appreciable interaction between other coordinates at opposite ends of the molecule, though there would almost certainly be some;* the main effect would be to make $f(A_g)$ exceed $f(B_{3u})$. That this can be achieved without lowering d_{11} or altering the signs of d_{12} and d_{13} is clear from Figure 11 (*c*).

---

*Compare the early values of $k_{C=C}$, with interactions assumed zero, and the recent work of Linnett, Heath and Wheatley (1949), who find 7·16 in C_2H_4 and C_2D_4, using their orbital valency force field with no interaction other than those derived from van der Waals forces.

ACKNOWLEDGMENTS

The author wishes to express his appreciation of the kindness of Professor C. A. Coulson in granting him facilities at the Department of Theoretical Physics, King's College, London, and to Messrs. Courtaulds Limited for making the present programme of work possible.

APPENDIX I

DERIVATION OF FORMULAE

Formulae (7) to (10) are obtained as follows. In the general case, if the transformation to normal coordinates be written $\boldsymbol{\eta}=\mathbf{c}\boldsymbol{\Delta}$ then

$$\mathbf{cAc}'=\mathbf{I}, \qquad \ldots\ldots(\mathrm{i})$$

$$\mathbf{c}'\boldsymbol{\Lambda}\mathbf{c}=\mathbf{d}, \qquad \ldots\ldots(\mathrm{ii})$$

where **d** and **A** are as already defined, and $\boldsymbol{\Lambda}$ is the diagonal matrix of the characteristic roots λ_1 to λ_n of the product matrix **dA** (cf. Wilson 1941). For the second-degree equation, let **c** be written

$$\begin{bmatrix} K_1 & K_1 p_1 \\ K_2 p_2 & K_2 \end{bmatrix}$$

---

* A recent analysis of the vibrations of the ethylenes C_2H_4, C_2D_4 (Torkington, to be published) has shown definitely that there are real interactions between the two ends of these molecules.

where p_1 and p_2 are arbitrary parameters and K_1 and K_2 normalizing constants. Then it follows from (i) that $p_2 = -R/S$, $K_1^2 = (A_{11}')^{-1}$, $K_2^2 = S^2K_1^2/D$, where A'_{11}, D, R and S are as already defined. p_2 is thus defined in terms of p_1, and the force constants are given by (ii) in terms of the single parameter $p(=p_1)$. The quantities ρ_1 and ρ_2 are obtained directly from the elements of $\mathbf{c}^{-1}$, the matrix for the inverse transformation $\boldsymbol{\Delta} = \mathbf{c}^{-1}\boldsymbol{\eta}$; in the general case, the components in the displacement for the ith normal mode ν_i are given by the elements of the ith column of $\mathbf{c}^{-1}$. Here, $\rho_1 = -c_{22}/c_{21}$, $\rho_2 = -c_{11}/c_{12}$. The energy distributions are found in the diagonal elements of $(\mathbf{c}^{-1})'\mathbf{d}(\mathbf{c}^{-1}) = \boldsymbol{\Lambda}$, derived from (ii), in which the potential energy for ν_i is normalized to $\frac{1}{2}\lambda_i$. In the second-degree equation, expansion of the left-hand side gives:

$$V_{11} : V_{22} : V_{12} :: \begin{cases} d_{11} : p_2^2 d_{22} : -2p_2 d_{12} & \text{for } \nu_1, \\ p_1^2 d_{11} : d_{22} : -2p_1 d_{12} & \text{for } \nu_2. \end{cases}$$

The formulae given for the cubic equation (equations (14) and (15) and Tables 5 and 6) follow directly from the application of theory discussed in a previous paper (Torkington 1949). If a new coordinate $\Delta_i' = \Delta_i + p\Delta_j$ replaces the initial valence-coordinate Δ_i, p being an arbitrary parameter, then the initial matrix $\mathbf{A}$ becomes $\mathbf{A}' = \mathbf{PAP}^t$; where $\mathbf{P}$ is the unit matrix with an additional element p in the ijth position, and t denotes transpose. If the conditions for the reduction of $\mathbf{d}'\mathbf{A}'$ to Jacobian canonical form are applied, $\mathbf{d}'$ being the force constant matrix for $\mathbf{A}'$, then we obtain solutions for $\mathbf{d}'$ in terms of the variable parameter p. The valence-force constants $\mathbf{d}$ corresponding to $\mathbf{d}'$ but going with the initial set of coordinates, are readily obtained from $\mathbf{d}'$:—

$$2V = \boldsymbol{\Delta}^t\mathbf{d}\boldsymbol{\Delta} = (\boldsymbol{\Delta}')^t\mathbf{d}'(\boldsymbol{\Delta}') = \boldsymbol{\Delta}^t\mathbf{P}^t\mathbf{d}'\mathbf{P}\boldsymbol{\Delta}.$$

Hence $\mathbf{d} = \mathbf{P}^t\mathbf{d}'\mathbf{P}$. The constants d_{ij} are conveniently derived from the rows of the matrix $\mathbf{e}$, as in (14), (15) and Table 5; the corresponding displacements are given in terms of the initial Δ_i by the matrices $\mathbf{h}$ of Table 6, components for the kth mode being proportional to elements of the kth column. $\mathbf{e}$ is an unnormalized transpose of $\mathbf{c}$, and the formulae are special cases of equation (ii) above; $\mathbf{h}$ is $\mathbf{c}^{-1}$ unnormalized. The potential energy distributions are obtained from $\mathbf{d}$ and $\mathbf{h}$.

Formulae (11) to (13) and (16) to (18) giving the directions of the displacement vectors follow directly from the form of the vibration as described by ρ_i or h_i. By applying the conditions imposed by symmetry on each factor, the displacements Δ_k may be expressed in terms of the Cartesian components of the displacement vector of atom 1 only for the second-degree factors; for the cubic factor, the additional vector x_2 is required. If, in a given factor, $\Delta_k = a_{k1}\mathbf{x}_1 + a_{k2}\mathbf{y}_1 + a_{k3}\mathbf{x}_2$, then for the second-degree factors ($a_{k3} = 0$),

$$\begin{cases} \tan\beta_1 = (a_{21}S - a_{11}R)/(a_{22}S - a_{12}R), \\ \tan\beta_2 = (a_{11} + ap_{21})/(a_{12} + pa_{22}) \end{cases}$$

and for the cubic factor,

$$\tan\beta_i = (2\sqrt{3}h_{2i} + h_{3i})/(8h_{1i} + 2h_{2i} - \sqrt{3}h_{3i}).$$

Percentage Increments for Force Constants of Tetra-chloro-ethylene, for Standard Deviations (Assignment T)

	p	0·75		0·5		0·25		0		−0·25	
		(i)	(ii)	(i)	(ii)	(i)	(ii)	(i)	(ii)	(i)	(ii)
B_{1g}	k	0·025	−0·538	0·721	− 3·13	−0·915	2·35	−0·493	0·555	−0·254	0·336
	f	2·47	−9·96	2·87	−10·96	0·794	−3·39	2·41	−8·39	2·27	−8·20
	d	1·53	−5·74	2·08	− 7·73	−0·127	−0·051	1·25	−3·88	1·39	−3·86

	p	3	2	1	0	−1
B_{2u}	k	0·479	−0·089	−3·62	−2·04	−0·99
	f	2·98	1·11	−2·32	1·62	1·31
	d	2·21	0·639	−3·42	−2·08	8·46

	p	1	0·5	0	−0·5
B_{3u}	k	0·540	−1·45	2·89	1·44
	f	−3·36	−3·61	−3·55	−1·80
	d	−2·74	−3·24	−2·08	−7·41

Deviations : B_{1g} (i) $\Delta\alpha=+1°$; (ii) $\Delta r_{C-Cl}=+0{\cdot}1$ A. (or $\Delta r_{C=C}=-0{\cdot}076$ A.)
B_{2u}, B_{3u} $\Delta\alpha=+1°$.

Percentage Increments to the Force Constants of Tetra-chloro-ethylene, for Standard Frequency-Increments (Assignment T)

	p	0·75		0·5		0·25		0		−0·25	
	k	0·665	4·86	1·91	3·01	3·85	0·145	6·10	1·21	0·53	0·51
B_{1g}	f	2·62	1·96	3·42	0·777	2·99	1·42	0	4·12	0·34	5·35
	d	1·53	3·58	2·81	1·68	3·62	0·484	0	2·78	−0·54	6·65
	p	3		2		1		0		−1	
	k	1·51	1·91	1·98	0·61	2·20	~0	1·96	0·67	1·49	1·98
B_{2u}	f	2·18	0·063	2·20	0·003	1·90	0·83	0	6·12	1·00	3·34
	d	2·06	0·394	2·22	−0·05	2·19	0·022	0	6·12	9·23	−19·5
	p	1		0·5		0		−0·5			
	k	0·75	2·02	1·99	1·18	2·10	0·973	0·796	3·62		
B_{3u}	f	2·43	0·111	2·57	0·001	0	5·23	1·36	2·46		
	d	1·86	1·45	2·56	0·035	0	5·24	−6·27	18·0		

(First column : $\Delta\nu_1 = +10\ \text{cm}^{-1}$; second column : $\Delta\nu_2 = +10\ \text{cm}^{-1}$, $\nu_1 > \nu_2$).

Percentage Increments for the Replacement of ^{35}Cl by ^{37}Cl, B_{1g} Factor (Assignment T)

p	0·75	0·5	0·25	0	−0·25
k	5·25	4·72	5·49	4·81	5·32
f	3·28	3·43	4·97	4·75	4·55
d	4·74	4·32	5·56	5·82	6·22

The matrices **a** are as follows:

$$\begin{array}{ccc} B_{1g} & B_{2u} & B_{3u} \\ \begin{bmatrix} -2 & 2\sqrt{3}\mu \\ -2\sqrt{3} & -2(\mu+8a) \end{bmatrix} & \begin{bmatrix} -2 & 2\sqrt{3}\mu \\ -2\sqrt{3} & -2\mu \end{bmatrix} & \begin{bmatrix} -2\mu & 2\sqrt{3} \\ 4\sqrt{3}\mu & 4 \end{bmatrix} \end{array}$$

$$\begin{array}{c} A_g \\ \begin{bmatrix} 0 & 0 & -2 \\ -2 & 2\sqrt{3} & 2 \\ 4\sqrt{3} & 4 & -4\sqrt{3} \end{bmatrix} \end{array}$$

where $\mu = 1 + 2m_{\text{Cl}}/m_{\text{C}}$, $a = r_{\text{C-Cl}}/r_{\text{C=C}}$.

The values of the parameter p satisfying the conditions for maximum and minimum force constants in a second-degree secular equation are as follows:

Minimum d_{11}	$\pm\infty$	Minimum d_{22}	0
Maximum d_{11}	$-(A_{12}/A_{22})$	Maximum d_{22}	$-(A_{11}/A_{12})$

Minimum d_{12}	$-(A_{11}/A_{22})^{1/2}$
Maximum d_{12}	$(A_{11}/A_{22})^{1/2}$

APPENDIX II

ACCURACY AND ERRORS

The calculations in this paper have been based on a standard molecular model, with angles of 120° and ^{35}Cl atoms. This was thought preferable to using an exact value for a somewhat uncertain angle, and a mean atomic mass; it is probable that isotopic shifts for this type of molecule will be studied within a reasonable period of time. For correcting force constants as found necessary, and to illustrate errors introduced by uncertainties in molecular dimensions, and in the vibration frequencies the following tables have been constructed for the assignment T. The isotope effect is best treated as a frequency correction, but to demonstrate the order of the effect introduced by using isotopic replacement in the formulae, data have been calculated for the B_{1g} factor.

For adjusting any chosen solution for the cubic A_g factor, the following variational treatment is very convenient (cf. Torkington 1949 b). The derivative $(\partial\lambda_k/\partial d_i)$ for any mode ν_k with respect to a force constant d_i can be written

$$(\partial\lambda_k/\partial d_i) = (\mathbf{PD})_{ki},$$

where the subscript ki refers to the kith element of the product matrix **PD**. **P** is a function of the frequencies and masses only, and **D** of the initial force constants:

$$\mathbf{P} = \begin{bmatrix} \dfrac{2\lambda_1^2}{(\lambda_1-\lambda_2)(\lambda_1-\lambda_3)} & \dfrac{-8\epsilon\lambda_1}{(\lambda_1-\lambda_2)(\lambda_1-\lambda_3)} & \dfrac{128\epsilon^2}{(\lambda_1-\lambda_2)(\lambda_1-\lambda_3)} \\ \dfrac{-2\lambda_2^2}{(\lambda_1-\lambda_2)(\lambda_2-\lambda_3)} & \dfrac{8\epsilon\lambda_2}{(\lambda_1-\lambda_2)(\lambda_2-\lambda_3)} & \dfrac{128\epsilon^2}{(\lambda_1-\lambda_2)(\lambda_2-\lambda_3)} \\ \dfrac{2\lambda_3^2}{(\lambda_1-\lambda_3)(\lambda_2-\lambda_3)} & \dfrac{-8\epsilon\lambda_3}{(\lambda_1-\lambda_3)(\lambda_2-\lambda_3)} & \dfrac{128\epsilon^2}{(\lambda_1-\lambda_3)(\lambda_2-\lambda_3)} \end{bmatrix}$$

$$\mathbf{D}=\begin{bmatrix} i=1 & i=2 & i=3 \\ 1 & -1 & 2\sqrt{3} \\ (k+4f) & -\{2(\sqrt{3}d+2f)+d_{12}\} & \{2(\sqrt{3}k+2d)-4d_{13}\} \\ (kf-d^2) & (dd_{13}-fd_{12}) & (dd_{12}-kd_{13}) \\ & & \\ i=4 & i=5 & i=6 \\ (2\epsilon+1) & -2\sqrt{3} & 4(2\epsilon+3) \\ \{d_{11}+4\sqrt{3}d_{13}+\epsilon' f\} & \{-2\sqrt{3}d_{12}+4d_{13}-\epsilon' d\} & \{4d_{11}-8d_{12}+\epsilon' k\} \\ (d_{11}f-d_{13}^2) & (d_{12}d_{13}-d_{11}d) & (d_{11}k-d_{12}^2) \end{bmatrix}.$$

$$(\epsilon'=8(\epsilon+2))$$

In $\mathbf{D}$, the order of the columns is such that $i=1$ to 6 gives derivatives of d_{11}, d_{12}, d_{13}, k, d, f in that order. The theorem follows immediately from varying the d_{ij} and λ_k of equation (19):

$$\mathbf{\Lambda}_1\mathbf{D}\Delta\mathbf{d}=\mathbf{L}\Delta\boldsymbol{\lambda};$$

$$\mathbf{L}^{-1}\mathbf{\Lambda}_1\mathbf{D}\Delta\mathbf{d}=\Delta\boldsymbol{\lambda}; \qquad \mathbf{L}^{-1}\mathbf{\Lambda}_1=\mathbf{\Lambda}_2\mathbf{H}\mathbf{\Lambda}_1=\mathbf{P}.$$

$\Delta\mathbf{d}$ and $\Delta\boldsymbol{\lambda}$ are the column matrices $\{\Delta d_i\}$, $\{\Delta\lambda_k\}$, ($i=1$ to 6 as above, $k=1$ to 3) The subsidiary matrices are as follows:

$$\overset{\mathbf{L}}{\begin{bmatrix} 1 & 1 & 1 \\ (\lambda_2+\lambda_3) & (\lambda_1+\lambda_3) & (\lambda_1+\lambda_2) \\ \lambda_2\lambda_3 & \lambda_1\lambda_3 & \lambda_1\lambda_2 \end{bmatrix}} \quad \overset{\mathbf{\Lambda}_2}{\begin{bmatrix} (\lambda_1-\lambda_2)(\lambda_1-\lambda_3) & 0 & 0 \\ 0 & (\lambda_1-\lambda_2)(\lambda_2-\lambda_3) & 0 \\ 0 & 0 & (\lambda_1-\lambda_3)(\lambda_2-\lambda_3) \end{bmatrix}^{-1}}$$

$$\overset{\mathbf{H}}{\begin{bmatrix} \lambda_1^2 & -\lambda_1 & 1 \\ -\lambda_2^2 & \lambda_2 & -1 \\ \lambda_3^2 & -\lambda_3 & 1 \end{bmatrix}} \quad \overset{\mathbf{\Lambda}_1}{\begin{bmatrix} 2 & 0 & 0 \\ 0 & 8\epsilon & 0 \\ 0 & 0 & 128\epsilon^2 \end{bmatrix}}.$$

Substituting from solution (*a*) (i) of Table 8, the following derivatives are obtained :

			$(\partial\lambda_k/\partial d_{ij})$			
d_{ij} k	d_{11}	d_{12}	d_{13}	k	d	f
1	1·968	−2·169	6·703	2·391	−7·388	22·835
2	0·032	0·174	0·159	0·953	0·871	0·796
3	0·0007	−0·0047	0·0665	0·0287	−0·411	5·859

(The above are matrix elements; for the off-diagonal elements d_{12}, d_{13}, and d, multiply by the factor 2 (for $d_{ij}=d_{ji}$, $i\neq j$).)

The relative sensitivities of the different modes to particular constants are interesting; it should be remembered that a given increment $\Delta\lambda_k$ has a greater absolute, as well as percentage effect, for lower frequencies. Using the above derivatives to attempt to eliminate d_{12}, we find that $\Delta d_{12}=+0{\cdot}22$ gives

$$\Delta\boldsymbol{\lambda}=\{-0{\cdot}954+0{\cdot}0763-0{\cdot}00206\},$$

these increments corresponding to $\Delta\boldsymbol{\nu}=\{-43{\cdot}6+11{\cdot}9-0{\cdot}62\}$, in cm⁻¹.*

---

* The variational treatment has been found to be quite accurate; here the correct frequency increments are −43·4, +11·3 and −0·65 cm⁻¹.

The large $\Delta\nu_1$ is balanced by $\Delta d_{11} = +0{\cdot}485$, which produces an additional increment $\Delta\lambda_2 = +0{\cdot}0153$. The increments in k, f and d for $\Delta\alpha = -2°$, giving an angle Cl–C–Cl of 116°, give $\Delta\lambda_2 \simeq -0{\cdot}048$, leaving an uncorrected

$$\Delta\lambda_2 = +0{\cdot}044\,(\sim 7\ \text{cm}^{-1});$$

the additional increment $\Delta\lambda_1$ is only small, being balanced by $\Delta d_{11} \simeq +0{\cdot}06$. To reduce the error of $+7\ \text{cm}^{-1}$ in ν_2, we can use $\Delta d_{13} = -0{\cdot}13_8$, but the balancing increment for ν_1 is then $\Delta d_{11} \simeq +1{\cdot}0$. The error in ν_2 cannot be caused by an error in $\nu_{\text{C–Cl}}(B_{3u})$, (see Table 1); any shifts are in the wrong direction. It seems possible that there is no real interaction $\Delta r_{\text{C=C}} \cdot \Delta r_{\text{C–Cl}}$; the error of $+7\ \text{cm}^{-1}$ in ν_2 is inside the accepted range for liquid–vapour shifts, and there are anharmonic properties to be considered also. If d_{12} has zero magnitude, then it is almost certain that the C=C stretching constant is greater than $9{\cdot}5 \times 10^5$ dynes/cm. in tetra-chloro-ethylene.

REFERENCES

Brockway, L. O., Beach, J. Y., and Pauling, L., 1935, *J. Amer. Chem. Soc.*, **57**, 2693.

Coulson, C. A., Duchesne, J., and Manneback, C., 1948, *Victor Henri Mem. Vol.* (Liège: Desoer).

Coulson, C. A., and Longuet-Higgins, H. C., 1948, *Proc. Roy. Soc.* A, **193,** 456

Duchesne, J., 1937, *Nature, Lond.*, **139,** 288, 634; 1938, *Ibid.*, **142,** 256; 1942, *Physica, La Haye*, **9,** 249; 1943, *Mem. Soc. Roy. Liege*, 429; 1948, *Victor Henri Mem. Vol.* (Liège : Desoer).

Glockler, G., and Tung, Y. Y., 1945, *J. Chem. Phys.*, **13,** 388.

Heath, D. F., and Linnett, J. W., 1948, *Trans. Faraday Soc.*, **44,** 556.

Herzberg, G., 1945, *Infra-red and Raman Spectra of Polyatomic Molecules* (New York: D. Van Nostrand Co., Inc.; London : Macmillan and Co. Ltd.).

Kilpatrick, J. E., and Pitzer, K. S., 1947, *J. Res. Bur. Stand., Wash.*, **38,** 191.

Linnett, J. W., and Heath, D. F., 1948, *Trans. Faraday Soc.*, **44,** 561, 878, 884.

Linnett, J. W., Heath, D. F., and Wheatley, P. J., 1949, *Trans. Faraday. Soc*, **45,** 1.

Manneback, C., and Verleysen, A., 1937, *Ann. Soc. Sci., Brux.*, **56,** 349.

Plyler, E. K., 1948, *J. Chem. Phys.*, **16,** 1008.

Tchang, Y. L., 1938, *Ann. Soc. Sci., Brux.*, **58,** 87.

Thompson, H. W., and Linnett, J. W., 1937, *J. Chem. Soc.*, 1393.

Torkington, P., 1949 a, *J. Chem. Phys.*, **17,** 357; 1949 b, *Ibid.*, **17,** 1026; 1949 c, *Trans. Faraday Soc.*, **45,** 445; 1949 d, *J. Chem. Phys.*, **17,** 1279; 1950, *Trans. Faraday Soc.*, **46,** 27.

Wilson, E. B., Jr., 1939, *J. Chem. Phys.*, **7,** 1047; 1941, *Ibid.*, **9,** 76.

Wu, T. Y., 1946, *Vibrational Spectra and Stucture of Polyatomic Molecules* (Ann Arbor, Michigan, U.S.A. : J. W. Edwards).

The Electronic Structure and the Bond Lengths of Ovalene

By A. J. BUZEMAN
Wheatstone Physics Laboratory, King's College, London

Communicated by C. A. Coulson; MS. received 12th January 1950

ABSTRACT. The method of molecular orbitals has been applied to find the bond orders and the bond lengths of ovalene $C_{32}H_{14}$.

A comparison with the preliminary experimental values of Donaldson and Robertson shows general agreement.

§ 1. INTRODUCTION

In this paper the molecular orbital treatment is given of the polynuclear hydrocarbon ovalene $C_{32}H_{14}$ (see Figure). This compound has recently been prepared by Clar (1948) and its detailed structure is being investigated by Donaldson and Robertson (1949), using x-ray methods. It will evidently be of interest to compare their values for the bond lengths, when they are finally determined, with those obtained below by essentially theoretical arguments. A brief comparison with their preliminary values is given at the end of this paper.

The electronic wave function of the π electrons is expressed as a product of linear combinations of atomic orbitals.

The secular equation is found in the ordinary way (Lennard-Jones and Coulson 1939) and is solved subject to the following approximations:

(*a*) All Coulomb integrals α_i are assumed to be equal ($=\alpha$),
(*b*) All resonance integral β_{ij} between π electrons on adjacent atoms are assumed to be equal ($=\beta$),
(*c*) All other resonance integrals are neglected.

These approximations are just the same as those used in the work of Moffitt and Coulson (1948) on pyrene and coronene.

From the roots of the secular equation $x^\nu=(\alpha-E^\nu)/\beta$, where E^ν is the energy associated with the νth molecular orbital, the coefficients c^ν are calculated and each molecular orbital is normalized; from this there follow the bond orders $p_{ij}=\Sigma_\nu n^\nu c_i^\nu c_j^\nu$, where n^ν is the number of electrons occupying the νth orbital (Coulson 1939).

The bond lengths are found from the graph of bond length against bond order $r=f(p_{ij})$.

Table 1

	Mobile order	Bond length (A.)
Ethane	0	1·541
Graphite	0·535 [a]	1·421 [d]
Ethylene	1	1·340 [b, c]

a Coulson (1939). *b* Gallaway and Barker (1942).
c Thompson (1939). *d* Nelson and Riley (1945).

Treatment and results. The symmetry of the molecule is similar to that in pyrene (Moffitt and Coulson 1948), so that the complete secular determinant of 32 rows and columns may be factorized into four smaller ones of orders 9, 9, 7 and 7. The two seven-rowed determinants are identical with those found in phenanthrene, the results of which were used (Coulson, unpublished work and Coulson and Longuet-Higgins 1947). The nine-rowed determinants could be expanded and both the energies and coefficients found without difficulty.

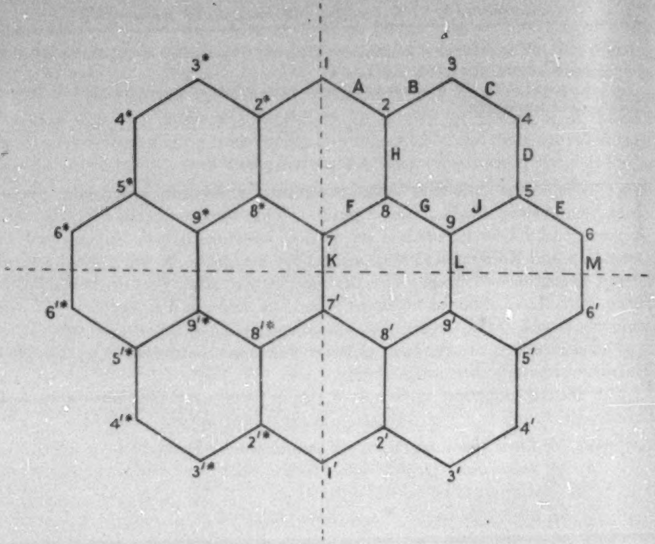

The resulting bond orders and lengths are shown in Table 2.

Table 2

Bond	Mobile bond order	Length (A.)	Bond	Mobile bond order	Length (A.)
A	0·604	1·410	G	0·526	1·424
B	0·511	1·427	H	0·508	1·428
C	0·763	1·380	J	0·535	1·422
D	0·519	1·425	K	0·497	1·430
E	0·557	1·418	L	0·521	1·425
F	0·541	1·421	M	0·726	1·387

The third decimals of the bond length values are useful if these values are considered relative to each other, but are not reliable absolutely.

To prevent numerical errors the coefficients as well as the bond order values have been checked as follows:

The sum of the fractional charges on each nucleus should be unity: $\sum_{r}(c_i^r)^2 = 1$, and the bond orders should satisfy the relation

$$\sum_{ij} p_{ij} = -\sum_{r} \tfrac{1}{2} x^r n^r$$

(Coulson 1939), where the first summation is taken over all the carbon–carbon bonds of the molecule.

Table 3 shows that the general variations between the lengths of the main types of bond are the same as those found experimentally by Donaldson and Robertson, but that the theoretical values are all somewhat larger than the experimental ones.

Table 3.

	Average values (A.) Experimental	Theoretical
Exposed bonds	1·37	1·382
Outer bonds	1·39	1·420
Inner bonds	1·41	1·425

It may be of interest that the 'exposed' bonds C and M have by far the highest orders, as is also found in coronene and pyrene (Moffitt and Coulson 1948). The order of bond C is even higher than those of similar bonds in coronene.

The central naphthalene portion shows no great variety in its bonds: the high α–β bond order which appears in naphthalene (Coulson 1948) is decreased by the surrounding nuclei.

Note added in proof. Since this paper was written the preliminary work of Donaldson and Robertson, to which reference was made at the beginning, has been completed. Professor Robertson authorizes the publication of their final experimental data, so that a better comparison may be made with our theoretical values.

Using the same naming of the bonds as in the figure, the experimental values for the bond lengths are as follows, in which the figure in brackets denotes the excess of theoretical over experimental:

A, 1·404 (+0·006); B, 1·441 (−0·014); C, 1·345 (+0·035);
D, 1·433 (−0·008); E, 1·403 (+0·015); F, 1·428 (−0·007);
G, 1·426 (−0·002); H, 1·435 (−0·007); J, 1·416 (+0·006);
K, 1·461 (−0·031); L, 1·442 (−0·017); M, 1·383 (+0·004).

The agreement is astonishingly good, much better than could have been expected. The mean deviation is only 0·0127 A.

Sincere thanks are due to Professor J. M. Robertson for his kindness in providing these figures in advance of publication.

ACKNOWLEDGMENTS

The writer wishes to thank Professor C. A. Coulson for suggesting this problem and for many helpful discussions.

REFERENCES

Clar, E., 1948, *Nature, Lond.*, **161**, 238.
Coulson, C. A., 1939, *Proc. Roy. Soc.* A, **169**, 413; 1948, *Proc. Phys. Soc.*, **60**, 257.
Coulson, C. A., and Longuet-Higgins, H. C., 1947, *Rev. Sci., Paris*, **85**, 929.
Donaldson, D. M., and Robertson, J. M., 1949, *Nature, Lond.*, **164**, 1002.
Gallaway, W. S., and Barker, E. F., 1942, *J. Chem. Phys.*, **10**, 88.
Lennard-Jones, J. E., and Coulson, C. A., 1939, *Trans. Faraday Soc.*, **35**, 811.
Moffitt, W. E., and Coulson, C. A., 1948, *Proc. Phys. Soc.*, **60**, 309.
Nelson, N. B., and Riley, D. P., 1945, *Proc. Phys. Soc.*, **57**, 477.
Thompson, H. W., 1939, *Trans. Faraday Soc.*, **35**, 697.

Hyperfine Structure and Nuclear Spin of Yttrium, $^{89}_{39}$Y

By H. KUHN and G. K. WOODGATE
Clarendon Laboratory, Oxford

MS. received 2nd February 1950

ABSTRACT. By the use of a liquid-air-cooled hollow-cathode tube with very low current densities it was possible to resolve hyperfine structure in the arc spectrum of yttrium. The value of the nuclear spin was found to be $I=\frac{1}{2}$ and the sign of the magnetic moment to be negative. This agrees with recent results of Crawford and Olson, who determined the nuclear spin from the intensity ratio of a hyperfine-structure doublet in the second spark spectrum of yttrium.

---

§ 1. INTRODUCTION

SEVERAL investigators (Schüler and Schmidt 1934, Williams and Granath 1938, Wittke 1940) have examined lines of the arc spectrum and of the first and second spark spectra of yttrium by means of interferometers, but have not been able to detect hyperfine structure. Kruger and Challacombe (1935 a) observed doublet structures in some lines of the Y II spectrum, and concluded that the nuclear spin of yttrium was $\frac{1}{2}$, but later (1935 b) found that this structure was spurious, and not a hyperfine structure. Several authors, quoting this value of the spin in recent theoretical papers, seem to have overlooked the latter publication. From this earlier work it can only be concluded that the magnetic moment of yttrium must be very small.

In a new attempt to determine the nuclear spin of yttrium, the four red lines arising from the term doublet $4d5s5p\,^2D_{5/2,\,3/2}$ and the ground term doublet $4d5s^2\,^2D_{5/2,\,3/2}$ of the arc spectrum (Meggers and Russell 1929) were investigated.

§ 2. LIGHT SOURCE AND INTERFEROMETER

The light source was a liquid-air-cooled hollow-cathode discharge tube. This was made from a copper–glass seal, the glass tube of which supported a stainless-steel anode. The cathode was an aluminium block which fitted tightly into the copper tube and which had a cavity of 0·5 cm. diameter and 1·5 cm. depth. The discharge tube was connected to a liquid-air trap containing a few grains of charcoal.

Pure yttrium oxide powder was made into a paste with water and was spread over the walls of the cavity. In order to reduce the oxide, hydrogen was admitted into the system before each exposure and a discharge was passed for a few minutes, at a current of 130 ma. The system was then exhausted, and the carrier gas, which was either neon at a pressure of 0·7 mm. or argon at a pressure of 0·2 mm. Hg, was introduced. Currents ranging from 50 down to 7 ma. were used in the discharge.

The high-resolution instrument was a Fabry–Perot etalon placed between the collimator and the prism of a spectrograph of focal length 150 cm. After some exploratory work with spacings of 0·75 and 3 cm., a 5 cm. spacer was used in the final exposures. The aperture of the etalon was 5 cm. in diameter.

§ 3. RESULTS

As the discharge current was reduced, the ratio of the intensities of the yttrium lines to those of the rare gas lines decreased noticeably; also the lines 6191 A. and 6402 A. became progressively narrower. In the line 6435 A. a doublet structure became visible at currents below 25 ma., while the line 6222 A. was much wider than the two lines mentioned first and showed a marked asymmetry, with the intensity tailing off towards shorter wavelengths. The resolution within the line 6435 A. improved with decreasing current, but below 15 ma. no further improvement could be noticed. The lowest current used was 7 ma. The variation of current did not produce any observable change in the intensity ratio or spacing of the components, and the appearance of the four yttrium lines was the same whether neon or argon was used in the discharge tube.

At a current of 10 ma. the doublet structure of the line 6435 A. could be measured conveniently. At this current the time of exposure required was generally 45 minutes for the line 6435 A. and 2 hours for the line 6222 A.

The doublet splitting of the line 6435 A. was measured on several plates and found to be $0{\cdot}016 \pm 0{\cdot}001$ cm^{-1}. Photometer tracings of these plates, on which intensity marks were also produced, gave a ratio between 1·2 and 1·3 for the peak intensities of the two components.

In order to get an estimate of the width of the unresolved structure of the line 6222 A., the distance of the wing from the maximum was measured and found to be about 0·012 cm^{-1}.

§ 4. DISCUSSION OF THE RESULTS

Yttrium consists of one isotope only, of mass 89. The doublet structure of the line 6435 A. and the asymmetric broadening of the line 6222 A. must both be ascribed to hyperfine structure, caused by the nuclear spin. The fact that the splitting appears only at the lowest current densities excludes self-reversal as a possible cause. Any line due to impurities or to other transitions in yttrium would have revealed its nature by a change of the intensity ratio of the doublet with variation of current or of other conditions of the discharge.

In a transition between two terms for both of which the value of J is $\frac{5}{2}$, a doublet structure can only be caused by a nuclear spin of $I=\frac{1}{2}$. The next higher value permissible, $I=\frac{3}{2}$, would give rise to a pattern of four lines, or even more if both terms have comparable splitting factors. The doublet structure of the line 6435 A. is sufficiently well resolved to exclude this or any higher value of I.

The spectrum and the term structure of yttrium resemble very closely those of scandium, and the hyperfine structure of the two scandium lines $3d4s^2\,{}^2D_{5/2}$—$3d4s4p\,{}^2D_{5/2}$ and $3d4s^2\,{}^2D_{3/2}$—$3d4s4p\,{}^2D_{3/2}$ corresponding to the yttrium lines 6435 A. and 6191 A. has been investigated by Kopfermann and Rasmussen (1934). Our observations for yttrium can be explained by the plausible assumption that the ratios of the splitting factors of the four terms concerned are roughly the same for yttrium as for scandium. The diagrams in the Figure have been drawn according to this assumption. Without claiming to be quantitatively correct, they show that the largest splitting is to be expected in the line 6435 A., a somewhat smaller splitting in the line 6222 A., and considerably narrower structures in the two other lines. The fact that the weaker component is on the short wavelength side, in both lines 6435 A. and 6222 A., shows that the magnetic moment of yttrium is negative. This is expressed in the term diagram by the order of the doublet components of each term, which is opposite to that in scandium. The absolute values of the splitting factors have been chosen to fit our value of the splitting of the line 6435 A. It is about 25 times smaller than in scandium.

The measured value, 1·2 to 1·3, of the intensity ratio of the components contains no correction for incomplete resolution and is perfectly consistent with our interpretation of the structure for which an intensity ratio of 1·4 is to be expected theoretically.

The resolution of the doublet structure shows that the width of the lines is about 0·015 cm^{-1}. If this value is taken as pure Doppler width, the temperature of the radiating atoms is found to be 150° K. Owing to instrumental and other causes of broadening, this estimate is an upper limit, and the actual temperature of the yttrium atoms must have been between 100° and 150° K.

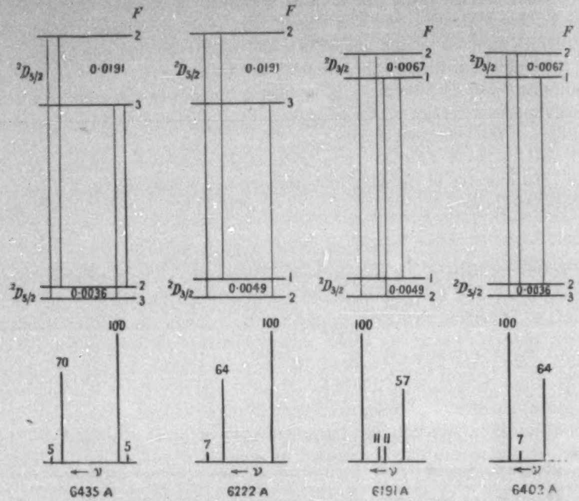

Lines arising from the transitions 4d5s^2 $^2D_{5/2,3/2}$—4d5s5p $^2D_{5/2,3/2}$ with approximate values for the splitting.

While this work was in progress, Crawford and Olson (1949) reported the discovery of hyperfine structure in the Y III line 2817 A. (5s $^2S_{1/2}$—5p $^2P_{3/2}$). From a measurement of the intensity ratio of the components of the doublet, they conclude that the value of the nuclear spin is $\frac{1}{2}$ and that the magnetic moment is negative (the value found is $\mu = -0{\cdot}14$). Our results provide an independent confirmation of these conclusions. The value $I = \frac{1}{2}$ for the spin of the nucleus $^{89}_{39}Y$, which is of considerable interest for the theory of nuclear shell structure, can thus be regarded as well established.

ACKNOWLEDGMENT

The authors are indebted to Dr. J. R. Marsh for the supply of very pure yttrium oxide.

REFERENCES

Crawford, M. F., and Olson, N., 1949, *Phys. Rev.*, **76**, 1528.
Kopfermann, H., and Rasmussen, E., 1934, *Z. Phys.*, **92**, 82.
Kruger, P. G., and Challacombe, C. N., 1935 a, *Phys. Rev.*, **47**, 798; 1935 b, *Ibid.*, **48**, 111.
Meggers, W. F., and Russell, H. N., 1929, *Nat. Bur. Stand., Wash., Sci. Pap.* No. 55, **2**, 733.
Schüler, H., and Schmidt, T., 1934, *Naturwissenschaften*, **22**, 839.
Williams, D. T., and Granath, L. P., 1938, *Phys. Rev.*, **54**, 338.
Wittke, H., 1940, *Z. Phys.*, **116**, 547.

The Angular Distribution of Protons from the Reaction ^{27}Al (d, p) ^{28}Al

By J. R. HOLT and C. T. YOUNG
George Holt Physics Laboratory, University of Liverpool

MS. received 16*th February* 1950; *read at Summer Meeting at Liverpool* 8*th July* 1950

ABSTRACT. Experiments are described in which a differential ionization chamber was used in the measurement of angular distributions of disintegration particles. Results are given for seven groups of protons from the (d, p) reaction with aluminium in which deuterons having energies of 4·6, 5·8 and 7·5 MeV. were used. The distribution curves are of complicated form, with a general tendency for the protons to be emitted in the forward direction.

§ 1. INTRODUCTION

Up to the present time few investigations have been made of the angular distribution of the disintegration products from nuclear reactions. Such investigations are of interest, as the results may be expected to throw some light on the mechanism of the nuclear processes involved and on the properties of the associated nuclear energy levels.

We have made measurements of the angular distributions of several groups of protons emitted as a result of the bombardment of aluminium with deuterons. Deuteron energies of 4·6, 5·8 and 7·5 MeV. were employed in the experiments.

Similar measurements on the protons from (d, p) reactions have been reported for oxygen and carbon by Heydenburg and his co-workers (Heydenburg and Inglis 1948, Heydenberg, Inglis, Whitehead and Hafner 1949), using deuterons having a maximum energy of 3·5 MeV., and for nitrogen by Wyly (1949), using deuterons having,a maximum energy of 3·0 MeV.

§ 2. APPARATUS

The deuterons were accelerated in the 37-inch cyclotron of this laboratory and had an initial energy of 8·0 MeV. The beam was resolved in the stray field of the magnet by passage through two adjustable slits mounted in a tube, 5 feet long, connected with the main vacuum chamber. It emerged from the end of this tube through a mica window and entered the scattering chamber through a second mica window separated from the first by an air gap of 2 mm. In this gap mica sheets of various thicknesses could be placed in order to reduce the energy of the beam. A diagram of the experimental arrangement is shown in Figure 1.

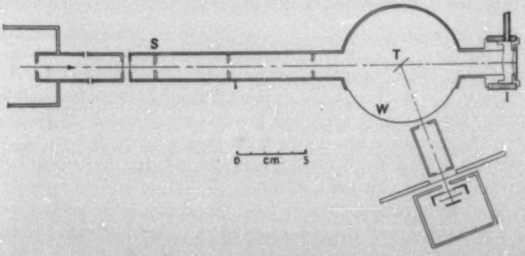

Figure 1. Arrangement of apparatus for observing the angular distribution of disintegration particles.

The target T was in the form of a strip of aluminium foil 1·5 cm. wide and about 3 cm. long, suspended from a metal plate with its longer dimension vertical and weighted at its lower end. The metal plate was attached to a cone joint, so that the angle between the plane of the target and the direction of the beam could be readily adjusted.

The beam was defined by a circular aperture S, 4 mm. in diameter, in a tube forming the entrance to the target chamber. After passing through the target the beam entered an ionization chamber I consisting of two aluminium foils separated by a distance of 4 mm. The space between the foils contained air at a pressure of 10 cm. Hg. The foils were insulated from each other and served as the electrodes of the ionization chamber. The beam was able to pass through the foils and to impinge on a fluorescent screen external to the apparatus. With the target foil adjusted so that its plane was parallel with the direction of the beam, the shadow of the target on this screen was used to help in the alignment of the apparatus.

A measure of the integrated beam current falling on the target was obtained by means of the ionization chamber. A potential of 500 volts was applied between the aluminium windows by placing a battery in series with an insulated lead connecting the outer aluminium foil with the grid of an electrometer triode. A condenser having a capacity of 24 μF. was connected between the grid and ground. Disintegration particles from the target were counted during the experiment for periods of time which were fixed by the charging of this condenser to a potential difference of 3 volts. This change in potential was measured by means of a milliammeter in the anode circuit of the triode.

The target chamber was evacuated and particles from nuclear reactions in the target emerged into the air through a window W in the curved side of the target chamber. This was in the form of a slot 8 mm. high and 10 cm. long. It was sealed with a sheet of 'Cellophane' 3·5 mg/cm^2 thick. Between this window and the counter which was used for detecting the particles was an absorption cell, in which the air pressure could be varied, and a metal disc carrying a number of calibrated mica absorbers. Both of these could be controlled remotely.

The counter was a differential ionization chamber filled with pure argon at atmospheric pressure. This, together with the absorption cell and disc, was mounted on a turntable which could be rotated about a vertical axis through the target. The counter could thus be set to receive particles emitted from the target at any angle between 25° and 145°, measured from the direction of the incident beam. The aperture of the counter was 7 mm. and the diameter of the deuteron beam at the target was 4 mm. The separation of the target and counter was 9·5 cm.; thus, the angle between the extreme rays accepted by the counter was 7°.

§ 3. PROCEDURE

The current of deuterons passing through the target was about 0·01 μa. during the experiments. The dimensions of the differential ionization chamber and the setting of the amplifier were such that protons were counted if they came to the end of their range within a certain region having limits 0·8 cm. apart. These conditions and the small angle of acceptance of the chamber necessitated the use of a target of aluminium having a thickness of 5·08 mg/cm^2, in order that the rate of counting of the proton groups of long range should be several hundred per minute. The background counting rate of the chamber with the cyclotron in operation was about 10 per minute.

An aluminium foil of the above thickness causes a decrease of 0·35 Mev. in the energy of the beam of deuterons passing normally through it. The effect on the resolving power of the arrangement, produced by this spread in the energy of the bombarding particles, was minimized by adjustment of the angle between the plane of the target and the direction of the beam. This angle was arranged so that the disintegration particles, which were detected at a particular setting of the angle of the differential chamber, always emerged from the side of the target opposite to that on which the deuterons impinged and had the smallest possible spread in energy. When particles were being detected at the extreme angle of 140° the target had to be inclined at an angle of 155°. The target was of such width that it still received the whole cross section of the beam even at this angle. Provided that the target is uniform, the number of atoms within the beam is inversely proportional to the sine of the angle of inclination. A correction of this form was made to the measured intensity of the disintegration particles when the angle of inclination was altered. With the differential chamber at a fixed angle it was verified experimentally that this correction gave the result within a few per cent. The validity of such a correction depends on the excitation function for the reaction being constant through the interval of energies encountered during the passage of the deuteron beam through the target.

In determining the angular distribution for a particular group of disintegration protons, the spectrum of proton ranges in the neighbourhood of the group was carefully plotted at each angle of the differential chamber. A measure of the intensity of a particular group of protons was obtained by finding the area enclosed by the peak belonging to this group. Background effects were subtracted during this procedure. It can be shown that the value thus obtained for this area is equal to the product Nx, where N is the total number of protons belonging to the group which enter the chamber in the standard interval of time, and x is the effective depth of the chamber. This method of measuring the relative intensities of proton groups does not demand that the shape of the peaks in the spectrum should always be the same; it requires only that the effective depth of the differential chamber should be constant. The actual value of this depth is immaterial.

The value of the effective depth depends on the adjustment of the pulse amplifier and discriminator. In order that corrections could be made for small drifts in the amplifier system during the course of a series of measurements, checks were made at regular intervals of the intensity of a certain group of protons at an angle of emission of 90°.

§ 4. RESULTS

The protons emitted from aluminium in the (d, p) reaction have been investigated by Pollard, Sailor and Wyly (1949), using deuterons having an energy of 3·8 Mev. They found thirteen groups of protons having ranges greater than that of the elastically scattered deuterons; the Q-value for the proton group of longest range was $+5{\cdot}45 \pm 0{\cdot}05$ Mev. Most of their measurements were made with the detector at an angle of 90° with the deuteron beam, but some results were obtained at 0° which indicate considerable differences in the relative intensities of the groups of protons.

In the course of the present series of experiments the spectrum of the protons was measured at 90°; it has the same general shape as that published by Pollard, Sailor and Wyly. Designating by p_0 the proton group of longest range, the

Q-values found for the groups p_0 to p_9 agree within the limits of experimental error with the values obtained by the previous workers. We have not investigated in detail the shape of the proton spectrum in the region of ranges shorter than that of group p_9.

For the purpose of measuring angular distributions, it was convenient to divide the spectrum into five regions and to investigate each of these in separate experiments. The first region was that containing the peak belonging to the proton group of longest range. The other peaks were taken in pairs (p_1p_2), (p_3p_4) and (p_6p_7). The peak p_5 had an intensity too small for measurement.

These regions of the spectrum are shown in the curve of Figure 2, which was taken with the differential chamber at an angle of 90°. In this diagram are shown the lines which were drawn in order that the effect of the tails of the adjacent peaks could be subtracted from the area beneath the curve before the true area enclosed by a particular peak was measured by applying Simpson's Rule.

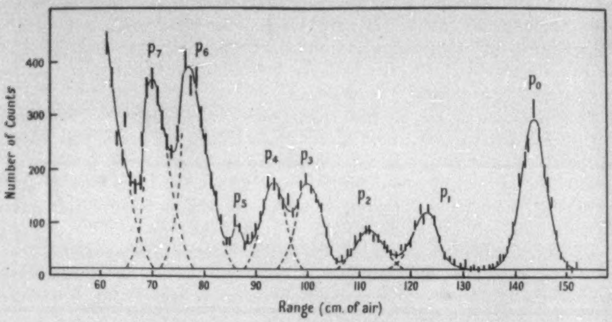

Figure 2. Spectrum of the protons from the reaction ^{27}Al (d, p) ^{28}Al at an angle of observation of 90°.

The results of the measurements of angular distributions are displayed in the curves of Figures 3 to 7. The relative intensities per unit solid angle in the system in which the centre of mass is at rest are plotted as a function of the angle of emission in that system. The probable errors shown include the effect of drifts in the amplifier and the uncertainties associated with the measurement of the areas beneath the peaks. Measurements on group p_0 were carried out at three values of the energy of the incident deuterons, namely 7·5, 5·8 and 4·6 MEV. (Figures 3 (*a*), (*b*), (*c*)). The lower energies were obtained by placing mica absorbers in the path of the beam. Groups p_1 and p_2 were investigated with incident deuterons having energies of 7·5 and 4·6 MEV. (Figures 4 and 5), and the remaining groups with deuterons of energy 7·5 MEV. (Figures 6 and 7).

One of the most obvious general features of the results is the increase in the intensity of the emitted protons towards the forward direction of the deuteron beam. A similar effect has been noticed in the distribution of neutrons from (d, n) reactions with deuterons having energies in the region of those used in the present experiments (Ammiraju 1949, Falk, Creutz and Seitz 1949, Roberts and Abelson 1947). It seems possible that this may be interpreted in terms of the 'stripping' process of the deuteron which has been proposed as a mechanism for these reactions by Peaslee (1948).

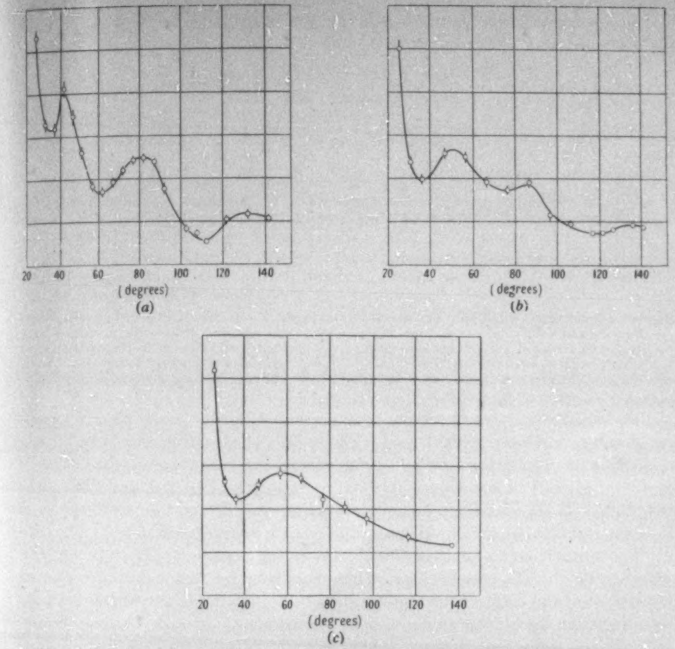

(*a*)

(*b*)

(*c*)

Figure 3. Relative numbers of protons of the group p_0 emitted into a fixed solid angle at various mean angles of emission in the centre-of-mass system :
(*a*) with incident deuterons of energy 7·5 MEV.,
(*b*) with incident deuterons of energy 5·8 MEV.,
(*c*) with incident deuterons of energy 4·6 MEV.

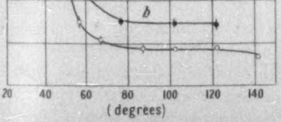

Figure 4. Relative numbers of protons of the group p_1 emitted into a fixed solid angle at various mean angles of emission in the centre-of-mass system :
(*a*) with incident deuterons of energy 7·5 MEV.,
(*b*) with incident deuterons of energy 4·6 MEV.

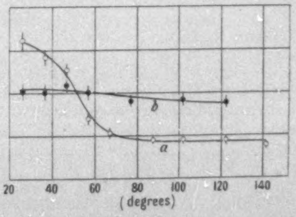

Figure 5. Relative numbers of protons of the group p_2 emitted into a fixed solid angle at various mean angles of emission in the centre-of-mass system :
(*a*) with incident deuterons of energy 7·5 MEV.,
(*b*) with incident deuterons of energy 4·6 MEV.

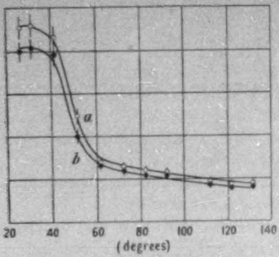

Figure 6. Relative numbers of protons emitted into a fixed solid angle at various mean angles of emission in the centre-of-mass system, with incident deuterons of 7·5 Mev. energy: (*a*) for group p_3, (*b*) for group p_4.

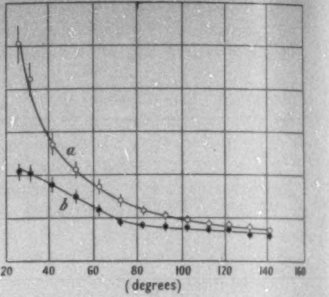

Figure 7. Relative numbers of protons emitted into a fixed solid angle at various mean angles of emission in the centre-of-mass system, with incident deuterons of 7·5 Mev. energy: (*a*) for group p_6, (*b*) for group p_7.

The distribution curves for the proton group of longest range show a complicated variation of intensity with angle (Figure 3). In the curve taken with 7·5 Mev. deuterons there is, superimposed on the general increase towards small angles, a periodic variation of intensity with maxima at angles of 40°, 80° and 130°. The two curves for incident deuterons with energies of 5·8 and 4·6 Mev. appear to indicate a gradual change in shape as the energy is decreased.

The present series of experiments are to be regarded only as preliminary investigations. The measurements carried out thus far demonstrate the interesting nature of the form of the angular distribution of the disintegration particles resulting from the bombardment of light elements with deuterons having energies in the region from 5 to 10 Mev. They indicate the need for extended measurements using a variety of elements which are in the form of thin targets and in which the energy of the beam is varied by small amounts.

Note added in proof. Recent work using a photographic emulsion as the detector of protons indicates that the intensity of the proton group p_0 with a bombarding energy of 7·5 Mev. increases by a factor of 30 between the direction 25° and the forward direction.

REFERENCES

Ammiraju, P., 1949, *Phys. Rev.*, **76**, 1421.
Falk, C. E., Creutz, E., and Seitz, F., 1949, *Phys. Rev.*, **76**, 322.
Heydenburg, N. P., and Inglis, D. R., 1948, *Phys. Rev.*, **73**, 230.
Heydenburg, N. P., Inglis, D. R., Whitehead, W. D., and Hafner, E. M., 1949, *Phys. Rev.*, **75**, 1147.
Peaslee, D. C., 1948, *Phys. Rev.*, **74**, 1001.
Pollard, E. C., Sailor, V. L., and Wyly, L. D., 1949, *Phys. Rev.*, **75**, 725.
Roberts, R. B., and Abelson, P. H., 1947, *Phys. Rev.*, **72**, 76.
Wyly, L. D., 1949, *Phys. Rev.*, **76**, 104.

Photodisintegration of the Heavy Elements

By R. W. PARSONS and C. H. COLLIE
Clarendon Laboratory, Oxford

MS. received 27th February 1950, *and in amended form* 14*th April* 1950

ABSTRACT. The photo thresholds for the emission of neutrons by the following elements have been determined. The threshold in MV. is given in the brackets following the symbol: Pt (6·1±0·1); Au (8·1±0·1); Hg (6·6±0·2); Tl (7·3±0·25); Pb (6·9±0·1); Bi (7·2±0·1); Th (6·0±0·15); U (5·8±0·15).

The neutrons were detected by the Szilard and Chalmers method of chemical concentration and the γ-rays obtained from a small betatron. Rough values of the total cross sections can be estimated from the results.

---

§ 1. INTRODUCTION

One way of obtaining data about the ground state of nuclei is to measure the threshold energy for photo-nuclear disintegration. Most measurements along these lines have investigated the production of artificial radioactivity in foils exposed to the γ-ray beam. This requires a rather intense source of γ-rays in order to obtain sufficient activity for accurate measurement near the threshold where the yield is in any case small. Thus McElhinney *et al.* (1949) using the 20 MV. betatron at Illinois had available an intensity of 50 r/min. at 1 metre. Some reactions cannot be investigated by this method because the resulting isotope is inactive.

The small betatron installed in the Clarendon Laboratory (Tuck, Wilkinson and Rettie 1948), while reliable in operation over long periods, owing to its small relative aperture, has too small a yield (4 r/hr/metre) for the direct activation of foils to be a practical method of measurement, but it has been found possible to make accurate measurements by detecting the neutrons formed directly in the reaction. For absolute work this method may offer some advantages owing to its greater sensitivity. On the other hand it is no longer possible to be sure which isotope is giving the neutrons since the end product is not identified.

§ 2. EXPERIMENTAL METHOD

The measurements were made quite simply in the apparatus shown in Figure 1. An annular glass vessel filled with ethyl iodide (2·8 litres) is placed in the γ-ray beam from the betatron. The specimen to be irradiated in the form of a cylindrical slug about 3 cm. diameter and 2½ cm. long is placed in the centre of the annulus so that the photo neutrons formed in it have for the most part to pass through the ethyl iodide, where they are slowed down by collisions with the hydrogen in to the region (40 ev.) where they are easily captured by the iodine. After exposure for 30 minutes the radioactive iodine is extracted from the bulk of ethyl iodide, by shaking with dilute sodium sulphite solution in a separating funnel, precipitated as silver iodide and counted in the usual way. This method of chemical concentration first described by Szilard and Chalmers (1934) was found to be quite effective and reproducible if the procedure described in detail by Shaw and Collie (1949) was adhered to. The superficial density of the silver iodide film was chosen so that the correction for absorption of the β-rays was negligible as was found in the experiments of Collie, Shaw and Gale (1950). During the exposure the beam was monitored by a dosemeter, of the type described by Wyatt (1949), which was placed in a standard position in the direct beam behind the specimen. Results were only accepted if the dosemeter reading remained constant to within 10% during an exposure; in these circumstances the mean dose recorded is sufficiently accurate and the error introduced by the decay of the radio-iodine during the exposure is sufficiently small to be neglected. For example, in the extreme cases of a steady drift about the mean from +5% to −5% or of an abrupt change of the γ-ray level by 10% half way through an exposure the error introduced in a 30 minute run in taking the mean γ-ray level is less than 1%. The observed results were corrected to a standard exposure as follows. The specimen and ethyl iodide tube were removed from the beam and the betatron expander pulse adjusted while the machine was still running, so that the circulating electrons hit the target with an energy of 9 MEV. The dosemeter reading was then taken and the observed readings linearly corrected to an arbitrary reading R on the scale. By this method all iodine counts are referred to a γ-ray beam produced by a standard number of electrons falling upon the target, i.e. that number of electrons which produced the arbitrary reading R on the dosemeter when they struck the target with 9 MEV. energy. In this way the very difficult calibration of the dosemeter in terms of quanta of different energies is avoided, and the only assumptions made are that the variations of betatron output with time are small over the period of a measurement and that electrons once accepted into a stable orbit remain in it until made to hit the target by actuating the extractor coil. Both these assumptions can be verified experimentally by watching the γ-ray output as displayed on the control panel oscillograph.

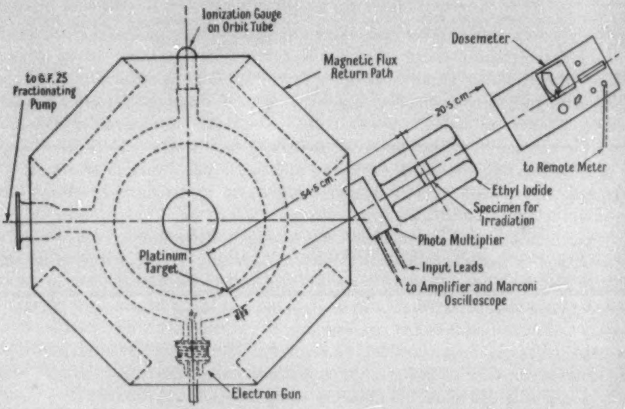
Ionization Gauge on Orbit Tube
Dosemeter
Magnetic Flux Return Path
to G.F. 25 Fractionating Pump
20·5 cm.
54·5 cm.
to Remote Meter
Ethyl Iodide
Specimen for Irradiation
Photo Multiplier
Platinum Target
Input Leads
to Amplifier and Marconi Oscilloscope
Electron Gun

Figure 1. Plan view of ethyl iodide chamber in the x-ray beam.

After correction most of the results were found to be well represented by a power law of the type $N=A(E-E_0)^n$ in which N is the observed iodine activity, and E the maximum energy of the electrons producing the γ-ray beam, obtained from the measured magnetic field in the betatron orbit. E_0 and n are constants obtained graphically by trial and error. The value of the exponent n varied between 1·1 and 1·5; E_0 was taken to be the threshold energy of the reaction. The electron energy E was calculated from the measured value of the magnetic field for the circulating electrons. This was obtained by measuring on a bridge the E.M.F. induced in a small search coil placed at the target radius. The search coil was calibrated both by measuring its area and by comparing it with a calibrated fluxmeter. The thresholds obtained in this way are shown in the Table and typical experimental results are plotted in Figure 2. The greatest source of error in these measurements is the neutron background. The background intensity was approximately symmetrical about the target and was thought to be due to neutrons produced in the Pt target of the betatron by a (γ, n) reaction. This interpretation was consistent with the observed (γ, n) threshold for platinum but the background intensity was too weak for a direct determination of its threshold energy. The relationship between N, the observed iodine count, the dosemeter reading and the magnetic field in the betatron orbit at expansion is not a simple one, involving as it does the shape of the quantum yield curve from the betatron target and the variation with energy of the probability of capturing a neutron in the rather shallow ethyl iodide layer. As these factors do not follow exact simple laws the linear logarithmic plot found can only be due to chance disposition of the apparatus. While it is useful in evaluating comparative values of the nuclear thresholds, its value in determining their absolute values is problematical.

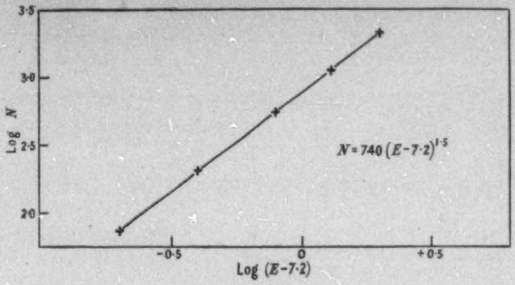

Figure 2.

§ 3. DISCUSSION

The threshold values are in reasonable agreement with those of other workers and show the expected alternations between elements of odd and even atomic numbers, superimposed upon a general fall with increasing nuclear mass. Results for different nuclei may be compared by plotting the difference between the observed threshold and a figure calculated from Weiszäcker's semi-empirical formula (Mayer 1948) as is done in Figure 3. The empirical formula for the binding energy takes into account the alternate strong and weak binding of the last neutron with increasing Z. For all the isotopes with even Z investigated in this series of experiments there is a series of isotopes differing in mass by a single unit so that the nucleus formed by neutron emission is a stable isotope of the same element. For the isotopes of odd Z this is not so and the isotope formed is presumably a β-radioactive isotope which decays subsequently into the element of next higher Z. Thus for example the photodisintegration of lead will probably proceed according to the scheme

$$^{207}_{82}\mathrm{Pb}+h\nu\rightarrow{}^{206}_{82}\mathrm{Pb}+{}^{1}_{0}\mathrm{n}\quad\text{or}\quad{}^{208}_{82}\mathrm{Pb}+h\nu\rightarrow{}^{207}_{82}\mathrm{Pb}+{}^{1}_{0}\mathrm{n}$$

in which all the isotopes concerned are known stable isotopes of lead. However, for an element of odd Z such as thallium the presumed change is

$$^{205}_{81}\mathrm{Tl}+h\nu\rightarrow{}^{204}_{81}\mathrm{Tl}+{}^{1}_{0}\mathrm{n}\rightarrow{}^{204}_{82}\mathrm{Pb}+\bar{\beta}$$

in which chain $^{204}_{81}\mathrm{Tl}$ is a known radioactive element of period 4·23 minutes and $^{204}_{82}\mathrm{Pb}$ is a known stable isotope of lead. The emission of a negative electron after removal of a neutron from the nucleus is not surprising since we are irradiating heavy nuclei with a large neutron excess. Similar schemes involving known nuclei can be written down for all the elements investigated except bismuth, which has a single isotope $^{209}_{83}\mathrm{Bi}$. For bismuth no scheme involving known nuclei can be drawn up and the simplest hypothesis is that the changes taking place are

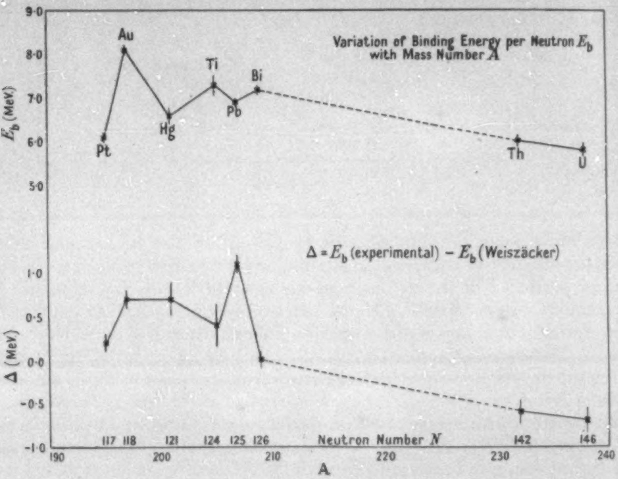

Figure 3.

$$^{209}_{83}\mathrm{Bi}+h\nu\rightarrow{}^{208}_{83}\mathrm{Bi}\rightarrow{}^{208}_{82}\mathrm{Pb}+h\nu\quad\text{(K capture).}$$

It is possible that $^{208}_{83}\mathrm{Bi}$ emits an α-particle but recent work (Perlman *et al.* 1950) makes this improbable. The sharp fall in E_b which occurs at bismuth is somewhat unexpected but is quite definite. The nuclei $^{208}_{82}\mathrm{Pb}$ and $^{209}_{83}\mathrm{Bi}$ are particularly interesting ones to study since they both have closed neutron shells of 126 neutrons, and in addition lead has a closed proton shell according to the well-known classification by Mayer (1948). According to her views $^{208}_{82}\mathrm{Pb}$ should be particularly stable while $^{209}_{83}\mathrm{Bi}$ should also be a strongly bound nucleus. As our measured threshold for lead almost certainly refers to the odd isotope $^{207}_{82}\mathrm{Pb}$ our results for what they are worth are not in complete agreement with the view that ${}^{209}_{83}\mathrm{Bi}$ is a particularly strongly bound nucleus. This conclusion is not in disagreement with the recent measurements of Perlman *et al.* (1950) on the stability of the heavy nuclei. It would be extremely interesting to have thresholds for the separate isotopes of lead, particularly ${}^{208}\mathrm{Pb}$, with its supposed closed shells for both the neutrons and protons, and experimental work on this problem has been started.

The order of magnitude of the absolute cross section for photodisintegration can be estimated from our measurements by making use of the absolute cross section for the photodisintegration of the deuteron which is approximately known over a wide energy range.

A specimen of deuterium oxide (20 gm.) was irradiated and the iodine count determined at various electron energies. The approximate shape of the spectral distribution of the betatron γ-ray output was then calculated by combining the known photodisintegration yield curve for deuterium (Halpern and Woodward 1948) with the absolute sensitivity of the ethyl iodide for detecting neutrons. The latter was obtained by making measurements with calibrated photo neutron sources. The two sources used, (ThC Be) and (ThC D), had been calibrated in a 'manganese tank'.

The spectrum found agreed well with what might have been expected, being intermediate between a thin and a thick target yield curve as calculated by Heitler (1936).

In a theoretical paper Wigner (1948) has shown that the photo cross section σ near threshold should be given by the relationship $\sigma = A(E-E_0)^{1/2}$. The values of A which fit our results best are given in the Table, and the order of agreement between experimental and calculated points is shown in Figure 4.

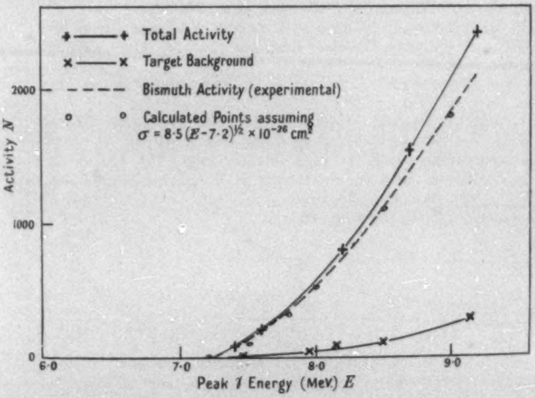

Figure 4.

As will be seen the cross sections obtained are high and fit in reasonably well with the view that all the neutrons in a heavy nucleus are taking part in the process of absorbing energy from the γ-ray beam as first suggested by Goldhaber and Teller (1948). The values of A for lead and platinum have been calculated on

Element	Threshold energy	*A*	Element	Threshold energy	*A*
Platinum	$6{\cdot}1 \pm 0{\cdot}1$	$3{\cdot}5 \times 10^{-26}$	Lead	$6{\cdot}9 \pm 0{\cdot}1$	$12{\cdot}5 \times 10^{-26}$
Gold	$8{\cdot}1 \pm 0{\cdot}1$		Bismuth	$7{\cdot}2 \pm 0{\cdot}1$	$8{\cdot}5 \times 10^{-26}$
Mercury	$6{\cdot}6 \pm 0{\cdot}2$		Thorium	$6{\cdot}0 \pm 0{\cdot}15$	3×10^{-26}
Thallium	$7{\cdot}3 \pm 0{\cdot}25$		Uranium	$5{\cdot}8 \pm 0{\cdot}15$	6×10^{-26}

the assumption that only the isotope of highest odd mass number is taking part. We could not obtain good agreement between calculated and measured yield curves for gold, mercury and thallium. In the case of mercury and thallium this could be due to the presence of other isotopes with different thresholds. This explanation cannot apply to gold which has only one isotope. In any case the values of A obtained might be in error by a factor of 3 owing to the crude assumptions made in reducing the observations.

ACKNOWLEDGMENTS

We have in particular to thank Dr. J. L. Tuck and Mr. D. G. Wyatt, without whose unselfish work on the commissioning of the betatron these measurements could not have been made. The gold was lent by Dr. J. G. Milne, and we have to thank Mr. A. H. Parker for his good offices in making the platinum readily available to us. The thorium was supplied by the courtesy of the Director of Atomic Energy Research Establishment, Harwell. We have to thank Lord Cherwell for his continued interest and advice, and the Carnegie Trustees for financial assistance to one of us (R. W. P.).

REFERENCES

Collie, C. H., Shaw, P. F. D., and Gale, H. J., 1950, *Proc. Phys. Soc.* A, **63,** 282.
Goldhaber, M., and Teller, E., 1948, *Phys. Rev.*, **74,** 1040.
Halpern, I., and Woodward, W. M., 1948, *O.N.R. Technical Report No.* 27, M.I.T.
Heitler, W., 1936, *Quantum Theory of Radiation* (Oxford : University Press).
Mayer, M. G., 1948, *Phys. Rev.*, **74,** 235.
McElhinney, J., Hanson, A. O., Becker, R. A., Duffield, R. B., and Diven, B. C., 1949, *Phys. Rev.*, **75,** 542.
Perlman, I., Ghiorso, A., and Seaborg, G. T., 1950, *Phys. Rev.*, **77,** 26.
Shaw, P. F. D., and Collie, C. H., 1949, *Chem. Soc.*, **264,** 1217.
Szilard, L., and Chalmers, T. A., 1934, *Nature, Lond.*, **134,** 462.
Tuck, J. L., Wilkinson, K. J. R., and Rettie, R. S., 1948, *Nature, Lond.*, **161,** 472.
Wigner, E. P., 1948, *Phys. Rev.*, **73,** 1002.
Wyatt, D. G., 1949, *J. Sci. Instrum.*, **26,** 13.

Gamma and Beta Ray Spectroscopy with Proportional Counters in Magnetic Fields

By S. C. CURRAN, A. L. COCKROFT and G. M. INSCH
Department of Natural Philosophy, University of Glasgow

MS. received 27th March 1950

ABSTRACT. Proportional counters operating in a ' condensing ' type of magnetic field can be used as β- or γ-ray spectrometers up to at least 2 Mev. Results for P32 and annihilation γ-radiation are given.

It has been shown in earlier work (Curran, Angus and Cockroft 1948, 1949) that the proportional counter can be used as a spectrometer in the analysis of beta, gamma and x-radiations within the energy range from about 100 ev. to 200 kev. This was particularly important in view of the severe difficulties encountered in this same region in attempting investigations by established methods. This successful application of the counter encouraged the authors in the attempt to extend its useful range to several Mev. and so to include the medium and hard radiations emitted by most radioactive materials. The following account demonstrates that such an extension is possible when the proportional counter is operated in a magnetic field of the 'condensing' type obtained at the edge of the poles of a magnet.

Electrons diverging from a source (C or S of inset, Figure 1), suitably situated in the fringing field of a magnet, are forced to circulate round the periphery of the poles (Thibaud *et al.* 1938). If the magnetic field is intense and the lines converge strongly, nearly 100% of the particles will be prevented from reaching the walls of the vessel even when they have energies of the order of 1 Mev. Now if the vessel is a proportional counter filled with gas, the paths of the particles can be restricted so that they lie entirely within the gas and they expend all of their

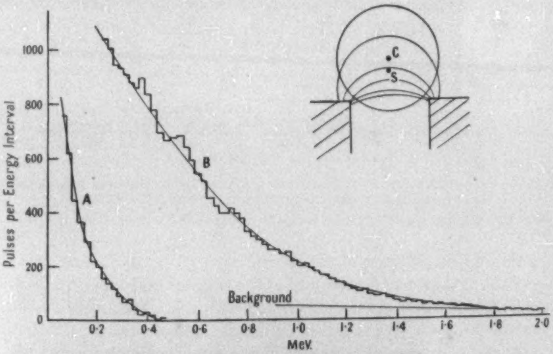

Figure 1. Histograms of beta rays of P32.
Curve A, no field; curve B, with field; can be normalized by making areas under them equal.

energy in the process of ionization. In these circumstances the impulses from the counter will be proportional to the energies of the fast particles. The results given here were obtained with a straight counter of moderate size (wire length 15 in., diameter 4 in.) situated in the fringing field of a large magnet with circular poles, but it is easy to design a simple and suitable magnet specially for the purpose. The pressure in the counter need not be high since the particles perform open loops and have a relatively small displacement per turn. Thus the total length of path covered by a particle usually exceeds the total displacement from source to end of track by a factor of more than 10. On the other hand, high pressure results in greater loss of energy per turn at a fixed field value and so may be useful in assisting the complete escape of particles from the source. This is an important advantage if high fields are employed in analysing energetic particles since slower particles, if present, tend to be turned back into the source. For the same reason high pressure is advantageous when large sources must be used.

Figure 1 gives the results of an analysis of the β-radiation of P32 (upper limit 1·70 MEV.). The pressure in the counter was only 70 cm. Hg (60 cm. of argon + 10 cm. of CH_4). The source had a strength of 5×10^{-9} curies, and it formed a thin deposit on part of the central wire. Clearly in zero field the great majority of the beta-rays strike the wall of the counter and expend a small fraction of their energy in the gas. As the magnetic field was applied a very striking growth of the average pulse size was observed on the cathode-ray tube. The actual value of the magnetic field was unimportant above a fairly definite lower limit which could be determined by visual observation. With a field of approximately 5,000 gasus at the source the histogram of the pulses given in curve B (Figure 1) was obtained. Comparison of curves A and B demonstrates the remarkable ability of this type of field to concentrate the particle tracks within the gas so that nearly 100% of them expend all their energy in ionization. With the field applied, an approximately correct spectrum of P32 is observed. The experiment was regarded as exploratory in nature, yet the energy distribution given by B is

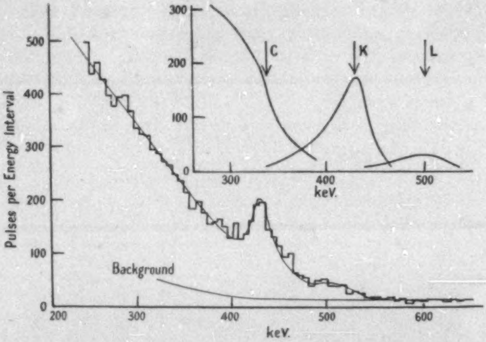

Figure 2. Histogram of secondary electrons produced by annihilation gamma radiation. Source of ^{64}Cu in copper covered with gold foil (16 mg/cm^2).
Inset figure shows resolution into Compton electrons (C); photo-electrons (K, L).

found to agree fairly closely with the theoretical Fermi distribution for an allowed transition down to approximately 0·9 MeV. This is consistent with observations made with more orthodox spectrometers (Siegbahn 1946). The complete histogram was recorded in less than two minutes with the very weak source.

The system is admirably suited to the investigation of γ-spectra. A test source (S, Figure 1, inset) was mounted on a probe running parallel to the central wire and maintained at the voltage corresponding to its position in the field. (Such an arrangement is one of several that can likewise be adopted for the general examination of β-ray materials.) The source consisted of a small piece of ^{64}Cu (3×10^{-7} c.) within a copper-walled capillary sheathed in gold foil (16 mg/cm^2). The total pressure of the gas was 160 cm. Hg. With the magnetic field applied, the spectrum of Figure 2 was obtained within a few minutes. The histogram is readily separated into three components as in the inset figure. The energy distributions of both Compton and photo-electrons gives the value $h\nu = 0{\cdot}51$ MeV. for the quantum energy. (It should be noted that here the spectrum is plotted as pulses per energy interval and not per momentum interval.) Clearly the device is capable of giving high accuracy—here the resolution depends entirely on the thickness of the gold foil since the intrinsic line width at 0·5 MeV. is less than 1%.

Although no detailed examination of the effect of the field on the value of gas gain has been completed, check experiments show that there is no appreciable change in the size of calibrating pulses produced by X-rays absorbed in the gas up to field values $H = 10^4$ gauss. This should be so since the ratio R of magnetic to electric force on an electron in the vicinity of the wire $= 300\,Hv/X\mathbf{c}$ and at $H = 10^4$ gauss, $v = 10^6$ cm/sec., $X = 10^4$ volts/cm., $R = 0{\cdot}01$. The electron thus moves essentially under the influence of the electric field. The proportional tube offers a compact β- and γ-spectrograph of solid angle 4π, capable of investigating radiations extending over the whole range observed in radioactive disintegrations.

REFERENCES

CURRAN, S. C., ANGUS, J., and COCKROFT, A. L., 1948, *Nature, Lond.*, **162,** 302; 1949, *Phil. Mag.*, **40,** 36, 53.

SIEGBAHN, K., 1946, *Phys. Rev.*, **70,** 127.

THIBAUD, J., CARTAN, L., and COMPARAT, P., 1938, *Techniques actuelles en physique nucléaire* (Paris : Gauthier-Villars).

Magnetization Curves for Polycrystalline Ferromagnetics

By H. LAWTON and K. H. STEWART
Cavendish Laboratory, Cambridge

Communicated by D. Shoenberg; MS. received 12th January 1950, and in amended form 1st April 1950

ABSTRACT. Recently described developments have led to greatly improved agreement between theory and experiment for the magnetization curves of single crystals of iron and iron–silicon in the region where magnetization proceeds by rotation of domain vectors against the action of magnetocrystalline forces, i.e. in the range 10–500 oersteds. On the basis of the assumption that in polycrystalline material the magnetization is approximately uniform from grain to grain, which is rendered plausible by consideration of internal demagnetizing effects, a method is developed for deriving the magnetization curves of such material by averaging the fields required to produce a given magnetization in the different constituent grains, rather than by averaging the magnetizations produced in the different grains by a given field. The application of this method to specimens with known distributions of grain orientations is shown to give results in fair agreement with experiment.

THE magnetization curves of well annealed ferromagnetics in fields large compared with their coercive force are determined almost entirely by their 'magnetocrystalline anisotropy'. Akulov (1931) showed that this anisotropy could be specified by one, or possibly two, coefficients, and he was able to calculate magnetization curves for single crystals with simple orientations relative to the field, which agreed well with experiment. His methods did not give good results when applied to crystals with arbitrary orientations, but nevertheless Gans (1932) used Akulov's equations to derive a magnetization curve for polycrystalline material with its grains oriented at random. This curve did not agree well with experiment.

Recent work (Néel 1944, Lawton and Stewart 1948) has shown that, unless the orientation is simple, demagnetizing fields set up by any transverse components of magnetization have a very important influence on magnetization processes, and that, if these effects are allowed for, Akulov's equations give results in good agreement with experiment for single crystals of any orientation. The problem of calculating magnetization curves for polycrystalline specimens can therefore be approached with more confidence.

The magnetization in a polycrystal subject to a uniform external field will vary from grain to grain. It is not possible to obtain the mean magnetization by averaging the magnetization that each grain would have if subject to the given external field, because in fact each grain is also subject to demagnetizing fields due to its own magnetization and that of all the other grains. It is difficult to allow for the effects of these fields in detail, but it is a fair approximation in many materials, and one leading to simple results, to assume that they cause the magnetization to be the same in magnitude and direction in every grain. The assumption of uniform magnetization was used by Akulov (1930) in calculating the magnetization curve for a polycrystal, not because he thought it was justified, but because it facilitated calculation. Nevertheless, and although he used expressions for the magnetizations of the component crystals which are now known to be incorrect, his results agreed much better with experiment than the later, more refined, calculations of Gans. The approximation can only be justified by considering special models such as that of a spherical grain with one orientation surrounded by material with a different orientation. If the sphere, because of its different orientation, had an intensity of magnetization I_2, different from the magnetization, I_1, of its surroundings, then a demagnetizing field $4\pi(I_1-I_2)/3$ would act on the spherical grain and tend to change I_2 to the value I_1. Because, in iron, fields of a few hundred gauss suffice to change the magnetization from zero to saturation, whatever the orientation, we may conclude that I is unlikely to vary by as much as 100 gauss from one grain to another. A more exact calculation could only be made by assigning a value for the permeability of the grain in question and its surroundings, and would not be of much interest unless the shapes of the grains could also be specified more realistically.

We assume, therefore, that in a polycrystal magnetized to a mean intensity I, the local field H acting on each grain is that required to bring its magnetization to the value I. This local field is made up of the externally applied field H_a and the local demagnetizing field H_d. If the specimen as a whole is of a shape with negligible demagnetizing coefficient, then the average of H_d over the whole specimen is zero, so that the average of H is equal to H_a. In order to obtain a magnetization curve for a given polycrystalline specimen we must therefore calculate, for any value of I, the fields H required to produce this value in each grain, and then find the volume average of H, which is equal to the applied field H_a, and can thus be plotted against I to give the required curve.

The general principles for the calculation of H in terms of I have been considered in a paper on single crystals (Lawton and Stewart 1948). It was shown that for single crystals there is, in general, a unique distribution of domain micromagnetization corresponding to any given value of the macroscopic magnetization. Methods were indicated for calculating the field, H, required to produce a given distribution and hence a given magnetization $\mathbf{I}$. It was found that, except for very large H, the possible values of $\mathbf{I}$ were restricted by the demagnetizing fields. In flat discs, for example, the macroscopic magnetization is constrained to lie close to the plane of the disc, while in long rods it is still more narrowly restricted, being forced to lie very nearly parallel to the axis of the rod. The most convenient way to find the domain distribution and the field H corresponding to a given magnitude and direction of $\mathbf{I}$ is thus to use the results already obtained for single crystal long rods; H in any crystal with magnetization $\mathbf{I}$ will be the same as in a long rod whose axis has the same crystal direction as $\mathbf{I}$ and which is magnetized to an intensity I.

The basic assumption of this treatment, rendered plausible as an approximation by the consideration above of demagnetizing effect, is that in each grain of a polycrystal $\mathbf{I}$ is constrained by demagnetizing fields to be very nearly equal to the mean $\mathbf{I}$ for all grains. The value of H in each grain would then be the same as that in a long rod cut from a single crystal with the same orientation as the grain, the axis of the rod being in the direction of the mean magnetization of the polycrystal and the magnetization of the rod equal to $\mathbf{I}$. H will not, in general, have the direction of the rod axis, but we can assume that the average transverse component over all grains will be zero, and to find the average H we may take the average of the component of H parallel to $\mathbf{I}$ (the direction of the axes of the rods). This longitudinal component of H is the quantity calculated as 'H_e' in the paper on single crystals and used to plot magnetization curves—graphs of I versus H_e.

The method of calculating a magnetization curve for a polycrystal is therefore as follows. The orientations of a fair sample of the grains are measured, and a magnetization curve plotted for each grain using the relations between I and H_e appropriate to a long rod with the orientation in question. Then for a number of values of I the corresponding values of H_e in each grain are averaged, weighting the values according to the volumes of the grains if necessary, and these average values are plotted as H_a against the I values to give the polycrystalline magnetization curve. The results of this procedure for two specimens of 3% silicon–iron alloy are shown in Figures 1 and 2. The orientations of ten of the grains, which were of average size about 0·05 cm^2, were measured by an optical method using etch-pit reflections. Experimental points obtained by the use of a ballistic galvanometer are also shown. The agreement is on the whole less good than would be expected, even in view of the rather crude assumption as to uniformity of magnetization. It is possible that a non-representative sample of grains was measured, or that internal stresses have some influence on the magnetization.

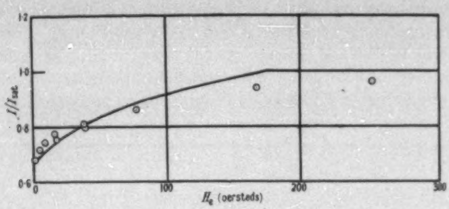

Figure 1. Calculated magnetization curve for polycrystalline silicon-iron; experimental points shown by circles.

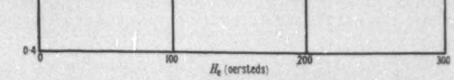

Figure 2. Calculated magnetization curve for silicon-iron (‘ Hipersil ’ at 25° to rolling direction); experimental points shown by circles.

Calculations have also been made for a polycrystal with its grains oriented quite at random. Points representing the grain orientations could be supposed uniformly distributed over the surface of a unit sphere, and it is not difficult to obtain average values of H_e corresponding to any given I by integrating H_e, as given by the equations of the paper on single crystals, over the surface of the sphere. The only difficulty is that the equations defining H_e as a function of I are not the same for all parts of the magnetization curve; there are four distinct regions, characterized by the number of favourable directions among which the domain magnetizations are distributed, and each region has its own equations. It is possible, however, to calculate, for any given magnetization, which representative points correspond to crystal grains in each state of magnetization and so to mark on the unit sphere the limits within which each equation must be integrated. The result of this calculation for a random polycrystal is shown in Figure 3, which shows the curve observed by Gans and an experimental curve he used as a check (from values in *International Critical Tables*, Vol. VI, p. 378). The latter is not very valuable as it is not at all certain that the grain orientations were random or the material strain-free.

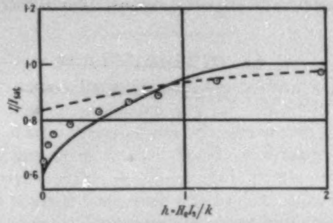

Figure 3. Magnetization curves for polycrystalline material with random orientation of grains. Dotted curve calculated by Gans (1932), full curve by the methods of the present paper, experimental points from the *International Critical Tables*.

The method described here does not, of course, give any useful results below the 'knee' of the magnetization curve; it is assumed that magnetocrystalline forces are the only ones acting, so that the knee is reached in an infinitesimal field and no hysteresis effects occur. At the other extreme, too, in very high fields, the method fails to give useful results; it should still predict the value of I to about the same percentage accuracy as in lower fields, but the interest in high fields lies mainly in the small difference $I_{sat} - I$, and this cannot be found at all precisely on the assumption that demagnetizing fields produce complete uniformity of I in all grains. A treatment of the 'law of approach' in very high fields, taking account of demagnetizing effects, has been given by Néel (1948), and a transition from the curve of Figure 3 to his curve should take place when the field is so high that the distinction between separate domains in the grains becomes blurred, i.e. for $I/I_{sat} \sim 0{\cdot}95$.

ACKNOWLEDGMENT

This work forms part of a programme of research sponsored by the Electrical Research Association, to whom we are indebted for permission to publish.

REFERENCES

Akulov, N. S., 1930, *Z. Phys.*, **66**, 533; 1931, *Ibid.*, **67**, 794.
Gans, R., 1932, *Ann. Phys., Lpz.*, **15**, 28.
Lawton, H., and Stewart, K. H., 1948, *Proc. Roy. Soc.* A, **193**, 72.
Néel, L., 1944, *J. Phys. Radium*, Ser. 8, **5**, 241; 1948, *Ibid.*, **9**, 193.

Magnetite Inclusions in Mica

By D. A. RICHARDS

Physics Department, University College of Wales, Aberystwyth

MS. received 30th November 1949; *in amended form 30th March* 1950

ABSTRACT. The paper describes the investigation of the orientation of magnetite inclusions in mica using electron diffraction by transmission through composite films. The diffraction pattern obtained indicates that the magnetite is a single crystal with its (111) planes parallel to the cleavage plane of mica and one of the face diagonals parallel to the *b* axis of mica. The technique for preparing the thin films is described in some detail.

§ 1. INTRODUCTION

In sheets of mica a number of inclusions are usually found in the crystal structure, these inclusions having considerable extension in the plane of cleavage and being comparatively thin perpendicular to this plane. The most frequent inclusion is magnetite, Fe_3O_4, which gives the mica its characteristic brown marking. The pattern of the markings is frequently in directions at 60° to each other, i.e. following the pseudo-hexagonal surface structure of the mica cleavage plane. Under a low-power microscope the markings have a characteristic fern-like structure with side growths at 60° to the general direction of crystal growth, the edges of the growths also retaining the 60° structure. This is an example of the growth of a crystal on a crystalline substrate. The present paper describes an investigation of the orientation of the epitaxial growth with respect to the substrate orientation, using electron diffraction, by transmission through thin composite films of mica and magnetite.

§ 2. PREPARATION OF THE THIN FILMS

Films of mica thin enough to give the Kikuchi pattern of hexagonal spots may easily be prepared by the following technique.

A small amount of water-soluble adhesive—in this case Seccotine—is smeared on a freshly cleaved surface of mica. A piece of good quality cartridge paper is then placed over the mica and the two are firmly clamped together, so that the adhesive is squeezed out into a thin film and allowed to dry in the clamped position. If after drying the paper is stripped from the mica, a mica film thin enough to show interference colours will be detached with it. When the original mica sheet is relatively thick the paper can be stripped merely by warming the paper and mica sheet on the radiator pipes. The mica film is then detached from the paper and adhesive by floating, mica film upwards, on distilled water. The water diffuses through the paper, causing swelling of the adhesive, and if one edge of the paper is submerged with a glass rod, the water advances over the upper surface of the paper and under the mica, which is left floating on the surface. The mica is lifted out by means of a small plate of glass and transferred for washing, first in dilute caustic soda solution and finally in distilled water, to ensure the removal of all the adhesive. It must be emphasized that since the upper surface of the mica film is never wetted it always floats on the liquid surface and this greatly facilitates the transfer of the film to the specimen holder. Films have been obtained by this method which are too thin to give interference colours by reflected light.

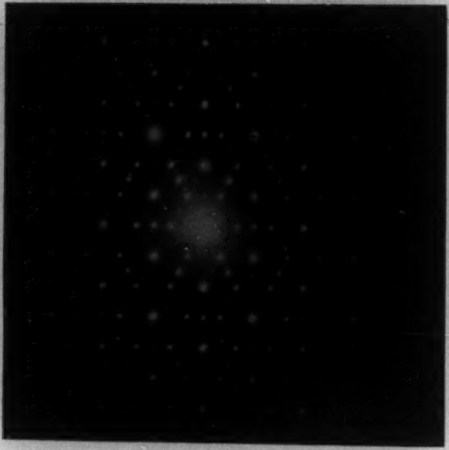

Figure 1.

This technique has been used to prepare the specimens in the present investigation but there are a number of added difficulties, since, in the original mica sheet, one does not know at what depth the inclusion occurs.

The original mica film was therefore first split with a razor blade to give a relatively thin film, until interference colours were seen above the inclusion. Repeated operation of the paper stripping technique then gave a composite film of mica and magnetite.

The area of the magnetite inclusion is often small, so that the specimen has to be mounted on a thin brass plate with a hole approximately 0·1 mm. in diameter.

§ 3. THE DIFFRACTION CAMERA

The camera was of the cold cathode type, operated at about 30 kv. supplied by a 50 c/s. A.C. transformer, rectified and smoothed with a 0·02 MF. condenser and a series resistance. The camera was provided with a focusing coil (Finch and Quarrell 1933) similar in design to that used by Tilman (1934). In this investigation, however, the focusing coil was only used to direct the electron beam on to the specimen, the specimen holder forming the second diaphragm of the electron collimating system. This holder enabled four different specimens to be carried in the camera at the same time. The camera was fitted with the plate-changing device described by Richards and Bound (1937) enabling twelve exposures to be made without letting down the vacuum. Comparison photographs of the split shutter type are also possible.

§ 4. RESULTS AND DISCUSSION

While a large number of specimens with a magnetite inclusion were prepared, it was only in comparatively few cases that the magnetite was thin enough to give a satisfactory diffraction pattern. Generally speaking, films which appeared brown on microscopic examination were too thick. The best photograph, shown in Figure 1 (see Plate), was obtained with a specimen which was so thin that it appeared grey by transmitted light.

Figure 1 shows the characteristic Kikuchi N pattern of hexagonal spots with spots varying in intensity and also spots at some of the midpoints of the sides of the equilateral triangles of the mica pattern. In addition a large number of faint spots may be seen; these will be discussed later.

The structure of magnetite has been investigated by W. H. Bragg (1915), Wyckoff (1922) and Huggins (1923). The structure is cubic with $a=8{\cdot}41$ A. and the space group O_h^7. With this space group, quoting Wyckoff, first order reflections are obtained from (h, k, l) planes if h, k and l are odd, quoting Astbury and Yardley (1924), $(h, k, 0)$ is quartered if $(h+k)$ is odd and halved if $(h+k)$ is even.

As is well known, in order that the (h, k, l) planes shall give rise to a diffracted beam, the (h, k, l) point of the reciprocal lattice must lie on the sphere of reflection. With electrons accelerated through approximately 30 kv. the wavelength is so small that the sphere of reflection may be regarded as a plane for the relatively small angles of diffraction involved. To give the sixfold symmetry of Figure 1 the (111) vector of the reciprocal lattice must be in the direction of the incident beam, so that, to be on the plane of reflection, the algebraic sum of the indices of the planes giving reflections must be zero. Using the known spacing of magnetite, indices have been assigned to the spots of the diffraction pattern (Figure 1) and are shown in Figure 2 as black circles.

The x-ray structure of muscovite (mica) have been analysed by Jackson and West (1930, 1933) and is discussed fully by W. L. Bragg (1937). An electron diffraction investigation is reported by Darbyshire (1933). The crystal is monoclinic with $a = 5{\cdot}18$ A., $b = 9{\cdot}02$ A., $c = 20{\cdot}04$ A., $\beta = 95^\circ 30'$. The SiO_4 groups form an almost exact two-dimensional hexagonal lattice in the plane of cleavage. The spots identified as being due to mica are indicated in Figure 2 as white circles.

The diffraction pattern is consistent with the assumption that the orientation of the magnetite inclusion is controlled by the mica (the (111) planes of magnetite being parallel to the cleavage plane of mica), owing to the fact that the face diagonal of the magnetite unit cell is almost exactly four times the hexagon edge of the surface pattern of mica.

The relative intensities of the 220, 440, 660, 880 reflections of magnetite by x-rays are given by W. H. Bragg (1915) as 43, 270, 8, 13 respectively. Bearing in mind that electron diffraction intensities will fall off with much greater rapidity, and that the 440 and 880 reflections coincide with reflections from the mica planes, the intensities for these spots appear to be correct as regards order of magnitude on visual examination

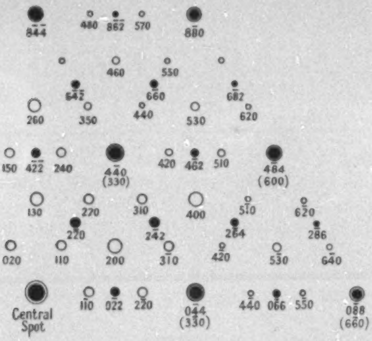
$8\bar{4}\bar{4}$
480
$8\bar{6}\bar{2}$
570
$8\bar{8}0$
460
550
$6\bar{4}\bar{2}$
$6\bar{6}0$
$6\bar{8}2$
260
350
440
530
620
150
$4\bar{2}\bar{2}$
240
$4\bar{4}0$
(330)
420
$4\bar{6}2$
510
$4\bar{8}4$
(600)
130
270
310
400
$5\bar{1}0$
$6\bar{2}0$
$2\bar{2}0$
$2\bar{4}2$
$2\bar{6}4$
$2\bar{8}6$
020
110
200
$3\bar{1}0$
$4\bar{2}0$
$5\bar{3}0$
$6\bar{4}0$
Central Spot
$1\bar{1}0$
$0\bar{2}2$
$2\bar{2}0$
$0\bar{4}4$
$(3\bar{3}0)$
$4\bar{4}0$
$0\bar{6}6$
$5\bar{5}0$
$0\bar{8}8$
$(6\bar{6}0)$

Figure 2.

A peculiarity of the diffraction pattern shown in Figure 1 is that each spot is surrounded by a hexagonal array of spots with a spacing corresponding to half orders of the mica spacings. These may be accounted for by assuming that the incident beam suffers double elastic scattering, first by the magnetite and secondly by mica. Spots due to magnetite, having indices each divisible by four, coincide with the mica spots. The remaining spots of the magnetite pattern lie at the centres of the equilateral triangles of the mica pattern; these reflected beams, diffracted again by the mica, give rise to the faint array of 'half order' spots. The incident beam can, of course, equally well be diffracted first by mica and then by magnetite.

The Kikuchi N pattern of mica, generally obtained with a thin film, is a hexagonal array of spots whose intensity gradually falls off with increasing angle.

This is not what would be expected from the x-ray data unless double elastic scattering is assumed in the mica film. In Figures 1 and 2 the intensities of the spots are more in accordance with the x-ray data of Jackson and West (1933) than is usually the case, suggesting that the thickness of mica in the composite film is too small to give appreciable double scattering in mica.

§ 5. CRYSTAL GROWTH

In some specimens of mica, the magnetite inclusion appeared as a diffuse patch, in others the magnetite was localized, and under microscopic examination some specimens were observed to be uniformly wide, with a width of the order 0·1 mm. and length up to 5 cm. The optical density appeared to be uniform, indicating that the thickness of the inclusion was also uniform. Although a sample of such a specimen was, with difficulty, isolated and mounted, it proved to be too thick to give a pattern by transmission. It was not possible therefore to investigate the factors governing crystal growth. Nevertheless it is reasonable to suppose that the direction of growth represents the direction of the most exact fit of the mica and magnetite lattices. The hexagonal surface pattern of mica is distorted with a contraction of 0·58% in the direction of the *a* axis. This slightly favours crystal growth of magnetite in the two directions inclined at 30° to the *a* axis rather than in the direction of the *b* axis. The length of the face diagonal of the magnetite unit cell is 11·89 A. Four times the length of the pseudo-hexagon of the surface pattern of mica in the direction of the *b* axis is 12·03 A. compared with 11·98 A. in the preferred direction. The bias in favour of the preferred directions is small; nevertheless, visual observations of some specimens does show the inclusion in two directions inclined at 60° to each other with little growth in the third direction.

ACKNOWLEDGMENTS

The author is indebted to Professor R. M. Davies in whose laboratories the investigation was carried out, and to the authorities of the Cardiganshire General Hospital who presented the high tension set to the Physics Department of the University College of Wales, Aberystwyth.

REFERENCES

Astbury, W. T., and Yardley, K., 1924, *Phil. Trans. Roy. Soc.* A, **224**, 221.

Bragg, W. H., 1915, *Phil. Mag.*, **30**, 305.

Bragg, W. L., 1937, *Atomic Structure of Minerals* (Oxford : University Press), p. 205.

Darbyshire, J. A., 1933, *Z. Kristallogr.*, **86**, 313.

Finch, G. I., and Quarrell, A. G., 1933, *Proc. Roy. Soc.* A, **141**, 339.

Huggins, M. L., 1923, *Phys. Rev.*, **21**, 514.

Jackson, W. W., and West, J., 1930, *Z. Kristallogr.*, **76**, 211; 1933, *Ibid.*, **85**, 160.

Richards, D. A., and Bound, R. A. M., 1937, *J. Sci. Instrum.*, **14**, 902.

Tilman, J. R., 1934, *Phil. Mag.*, **18**, 656.

Wyckoff, R. W. G., 1922, *J. Amer. Chem. Soc.*, **44**, 1914.

Transition Effect of Extensive and Local Penetrating Cosmic-Ray Showers in Colombo

By V. APPAPILLAI and A. W. MAILVAGANAM
University of Ceylon, Colombo, Ceylon

Communicated by L. Jánossy; MS. received 11*th November* 1949, *and in amended form* 30*th January* 1950

ABSTRACT. An account is given of the experiments on the transition effects of local and extensive penetrating cosmic-ray showers at Colombo (geomagnetic latitude 4° S.). A comparison of the present results with those reported for higher latitudes indicates that there is no observable latitude effect of the local penetrating showers. Contrary to the findings of Broadbent and Jánossy, the transition effect of the extensive showers in paraffin appears comparable in magnitude with the effect in lead.

---

§ 1. INTRODUCTION

The properties of penetrating cosmic-ray showers have been extensively investigated by Jánossy and his co-workers. Jánossy and Rochester (1944) were the first to show that the accurate representation of the transition effect of these showers in lead required the superposition of two exponential absorption functions, one corresponding to a mean free path of 1 cm. of lead and the other to a mean free path of 4·6 cm. of lead. This has been confirmed by further investigation by Broadbent and Jánossy (1947 a) who showed that the penetrating showers observed were of two types: (*a*) penetrating showers not associated with extensive air showers, called local penetrating showers, and (*b*) penetrating showers associated with extensive air showers, called extensive penetrating showers. The transition effect in lead of the local penetrating showers corresponded to a mean free path of the order of 5 cm. of lead and that of the extensive penetrating showers to a mean free path of 1 cm. of lead. When paraffin was used as the absorber the local penetrating showers showed a transition effect which was the same as in lead on the equivalent mass scale, while the extensive penetrating showers showed no transition effect at all. The transition effect in lead of the extensive air showers was therefore interpreted as apparent and due to electron cascades.

The purpose of the present experimental investigation has been to repeat and extend the observations on the transition effect of penetrating cosmic-ray showers carried out previously in Manchester by Jánossy and his co-workers. Also, as Colombo is situated close to the geomagnetic equator (geomagnetic latitude 4° S.), the possibility of a latitude effect was borne in mind.

There is no reason to assume a latitude effect of the extensive penetrating showers, as on any model, the primary energy required to start such a shower must be well above the limit of latitude-sensitive energies. Hence, in order to investigate a possible latitude effect of the local penetrating showers, it seemed desirable to separate the local from the extensive penetrating showers as the latter was expected to give rise to a latitude-insensitive background only. This separation was in the first instance effected by the use of an anti-coincidence method; but since it is known that the rate of coincidences between a penetrating shower arrangement and an extension increases steadily with increasing extension even if the area of the extension is large compared with that of the penetrating shower arrangement (Broadbent and Jánossy 1947 b), the separation effected by the method of anti-coincidences could not be regarded as complete. It was hoped to improve the separation by observing the local penetrating showers produced in paraffin as, according to the work of Broadbent and Jánossy (1947 a), the transition effect of extensive penetrating showers in paraffin is negligible. However, repeating the measurements of Broadbent and Jánossy in Colombo, we found comparable transition effects in lead and in paraffin. Owing to the statistical uncertainty both of our readings and of those of Broadbent and Jánossy (1947 a) one cannot conclude that there is necessarily a contradiction between the results: the two sets of measurements might be interpreted as opposite deviations from a mean curve (we hope to come back to this point in a later work). At any rate in view of our results it is doubtful whether observations on the transition effect of local penetrating showers in paraffin could be regarded as more sensitive for the detection of a latitude effect.

§ 2. EXPERIMENTAL METHOD

In order to be able to compare our results with those of Broadbent and Jánossy (1947 a) taken at Manchester, our experimental arrangement was made identical with that used at Manchester.

The Geiger-Müller counters used were of the copper-in-glass type, 40 cm. long and 3 cm. in diameter, filled with a mixture of alcohol vapour (1·5 cm. Hg) and of argon (11 cm. Hg). These counters were arranged in three trays, t, m, b, separated by 15 cm. of lead. Each tray had eight counters covering an area of 1,000 cm^2. The counters in the top tray were divided into three independent groups t_1, t_2, t_3, the groups t_1 and t_3 having three counters each and the group t_2 having only two counters, the counters in a group being connected in parallel. The middle and the bottom trays, m and b, were each split into two independent groups (m_1, m_2 and b_1, b_2) of four counters each, also connected in parallel. The m and b trays were shielded at the sides and ends by about 50 cm. of lead. Sevenfold coincidences $P = (t_1t_2t_3m_1m_2b_1b_2)$ were recorded. These coincidences were almost entirely due to penetrating showers of both types—local and extensive.

To sort out the two types of showers a fourth tray E, having twenty-one counters effectively connected in parallel and covering an area of 2,500 cm^2, was placed near the top tray. The distance between the t and E trays, from centre to centre, was about 60 cm. Eightfold coincidences PE were recorded on a separate meter. These coincidences were due to the simultaneous passage of at least one particle through the counters of the E tray. Hence the PE counts gave the rate of the extensive penetrating showers, and $P - PE$ counts the rate of the local penetrating showers.

The apparatus was periodically tested for background counts and efficiency. The starting potentials and plateaux of the counters were also checked at intervals of a week. Records obtained with faulty counters were rejected. Table 1 gives a comparison of the performance of our apparatus and that of Broadbent and Jánossy.

The measured meson flux in Colombo is less than that at Manchester by about 10 per cent, which is about the value obtained by other workers. The comparison shows that the penetrating shower apparatus set up in Colombo was very similar in its performance to that used at Manchester.

In our experiments we have used lead and paraffin as absorbers. They were cast into square slabs or plates with 50 cm. side. The absorbers were placed close above the top tray t of the shower apparatus. When using lead as the absorber light wooden frames were placed between the plates so as to distribute the lead evenly in the volume occupied by the mass-equivalent thickness of paraffin. The absorbers were changed every week and lead and paraffin absorbers were used alternately. In order to avoid errors arising from loss of efficiency of counters, barometer effect etc., observations with a given thickness of absorber were made at regular intervals throughout the course of the entire experiment.

Table 1

	Colombo	Manchester
Total meson flux (counts/hr.)	5000	5600
Resolving time (sec.)	10^{-4}	$0·5\times10^{-4}$
Casual coincidences, P (counts/hr.)	0·016	0·007
Knock-on showers, five-fold (counts/hr.)	0·010	0·003
Casual coincidences, PE (as percentage of P rate)	1	0·5
Efficiency of E counters for PE coincidences (%)	96	99

§ 3. RESULTS

The results of our investigations taken during a period of about 4,000 hours are given in Table 2. The deviations shown are standard deviations.

Table 2

Absorber	Thickness (gm/cm^2)	Time (hr.)	Coincidence counts		Shower rate (counts/hr.)	
			P	PE	Local	Extensive
Paraffin	0	504·8	91	57	0·067±0·015	0·113±0·015
	8·1	452·0	135	75	0·133±0·017	0·166±0·019
	16·2	504·0	165	87	0·155±0·018	0·173±0·018
	24·3	504·0	213	107	0·210±0·020	0·212±0·021
Lead	11·1	475·4	140	81	0·124±0·016	0·170±0·019
	22·2	599·5	233	126	0·179±0·018	0·210±0·019
	62·2	525·0	182	79	0·196±0·019	0·150±0·017
	124·4	553·8	288	123	0·298±0·023	0·222±0·020

The atmospheric pressure during the course of the work was recorded on a barograph. A study of the records indicates that the average barometric pressure has been 76 cm. of mercury throughout the duration of the experiment. The only noticeable variation was of the semi-diurnal type, of amplitude 3 mm. Hg. Because of this small variation in pressure and its regular periodicity, the results shown are regarded as free from errors arising from the barometer effect. Also corrections in respect of the fivefold knock-on rates, accidental coincidences, and inefficiency of the E counters have been neglected. These corrections have remained almost constant during the experiment; further, they add to the background counts and do not influence the transition effect.

(i) *Local Showers*

The results for local penetrating showers are represented graphically in Figure 1. The continuous curve and the points marked indicate our results and the dotted curve is a representation of the results of Broadbent and Jánossy

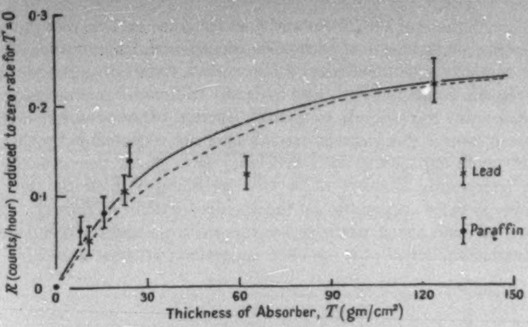

Figure 1. Transition effect of local penetrating showers.

(1947 a). The two curves have been reduced to the same rate for thickness $T=0$. In the first place we see that the points for paraffin and lead fall very nearly on the same curve. This is a confirmation of the result obtained by Broadbent and Jánossy, viz. that the transition effect of local penetrating showers is mass-dependent. Secondly we find that there is no observable latitude effect in the transition curves. A careful analysis of the two curves by the method of curve fitting gives the results of Table 3.

Table 3

	Colombo	Manchester
Mean free path of shower-producing primaries (gm/cm²)	37±4	46±6
Estimated maximum rate of showers produced by absorber T (counts/hr.)	0·236±0·026	0·234±0·022

The estimated maximum shower rate for Colombo appears to be the same as that for Manchester, but the difference in the two maximum shower rates has a standard deviation of 15 per cent. It is interesting to note that a recent estimate of the latitude effect of local penetrating showers by Heitler and Jánossy (1949) leads to a value of the order of 20 per cent.

One reading for lead of thickness 62·2 gm/cm² has had to be disregarded in obtaining the best fit for the curve. Our independent observations for this point show a consistently low value of shower rate. Since the deviation of this point from the curve is nearly three times the standard deviation, it is not unlikely that the deviation is genuine.

(ii) *Extensive Showers*

The results obtained for the transition effect of extensive penetrating showers are shown in Figure 2. Here again the points for paraffin and lead appear to fall on the same curve. Broadbent and Jánossy (1947 a) have observed a transition effect in lead but not in paraffin. According to these authors the observed transition effect in lead is due to an increased probability of discharge of the counters of the top tray t of the shower apparatus by the electron cascades produced in the lead absorber. The effect then does not correspond to a genuine production of penetrating showers.

Our results show a definite transition effect in paraffin of the same order of magnitude as in lead. However, as stated earlier, it is still possible to reconcile our results with those of Broadbent and Jánossy if we assume that the two sets of measurements correspond to opposite deviations from a mean curve. It may then be that the actual transition effect of the extensive penetrating showers in paraffin is not negligible compared with that in lead. Since the maximum thickness of paraffin employed corresponds to a small fraction of one cascade unit, it seems reasonable to assume that electron cascades are not responsible for this transition effect. It would appear therefore necessary to consider the transition effect of extensive penetrating showers in paraffin as being due to the production of penetrating particles in paraffin by the incident extensive shower. The direct production of penetrating particles by the electron–photon component of the main shower is unlikely, but it has been suggested (Broadbent and Jánossy 1948) that they may be produced through an intermediate link. The soft component of the main shower may give rise to fast nucleons which in turn produce mesons in the absorber. The transition effect of the extensive penetrating showers in lead would therefore appear to be due to production by the main shower of (*a*) electron cascades and (*b*) mesons through an intermediate link. In the case of paraffin, owing to the small thicknesses employed the second possibility would appear to be more likely; but since the transition effect of the extensive penetrating showers in paraffin is not negligible compared with the effect in lead, one is led to conclude that the indirect meson production considered by Broadbent and Jánossy may be responsible for part at least of the transition effect of the extensive penetrating showers.

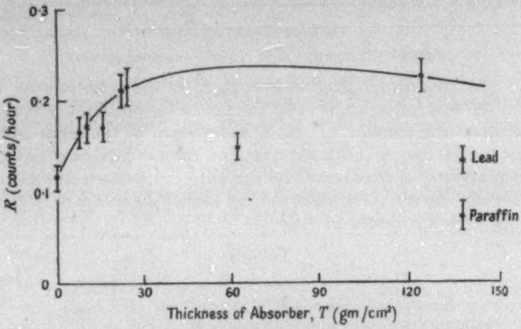

Figure 2. Transition effect of extensive penetrating showers.

§ 4. CONCLUSIONS

The transition effects of local penetrating showers in lead and in paraffin are in agreement with those reported by Broadbent and Jánossy (1947 a). The point for lead thickness $T = 62{\cdot}2\ \text{gm/cm}^2$ (Figure 1) lies off the curve. If this deviation is found to be real, it would be of interest regarding the mechanism of production of local penetrating showers.

With regard to extensive penetrating showers we have found distinct transition effects both in lead and in paraffin. These results do not bear out the observations of Broadbent and Jánossy (1947 a).

ACKNOWLEDGMENTS

In conclusion we wish to express out thanks to Professor L. Jánossy for his continued interest in the work and for his helpful criticism in the preparation of this paper, and to the Council of the University of Ceylon for a generous grant to defray the expenses of the investigation.

REFERENCES

Broadbent, D., and Jánossy, L., 1947 a, *Proc. Roy. Soc.* A, **190,** 497; 1947 b, *Ibid.*, **191,** 517; 1948, *Ibid.*, **192,** 364.

Heitler, W., and Jánossy, L., 1949, *Proc. Phys. Soc.* A, **62,** 374.

Jánossy, L., and Rochester, G. D., 1944, *Proc. Roy. Soc.* A, **183,** 181.

A Note on the Size–Frequency Distribution of Penetrating Showers

By ALLADI RAMAKRISHNAN
University of Manchester

Communicated by L. Jánossy; MS. received 6th March 1950

ABSTRACT. Heitler and Jánossy have calculated the probability that *n* mesons are produced due to nucleon–nucleon collisions by a fast nucleon in its passage through matter of a given thickness. In this note the results of Heitler and Jánossy are obtained by the direct method of writing the integro-differential equations of the problem using the Markoff nature of the process.

Recently Heitler and Jánossy (1949) have calculated the probability that *n* mesons are produced when a fast primary nucleon hits a compound nucleus, on the assumption that in a single nucleon–nucleon collision only one meson is produced (purely plural production). In this note we shall deduce the results of Heitler and Jánossy by a simpler and more direct method. For convenience we shall use the notation of Heitler and Jánossy.

Let $\phi(E',E)\,dE'$ be the cross section for the emission of a meson with energy $E-E'$, i.e. the primary nucleon drops from the energy state E to the state between E' and $E'+dE'$ in a collision with a single nucleon. We have to calculate the probability that a nucleon of a certain initial energy E_0 undergoes n collisions (i.e. n mesons are produced) in passing through matter of thickness x, given that there are N nucleons per unit volume. This means that the probability per unit thickness that a nucleon of energy E drops to E' is given by $N\phi(E',E)\,dE'$. Defining $\Pi(n,E_0,E,x)\,dE$ as the joint probability that a nucleon of energy E_0 (initially at $x=0$) after passing through a distance x has undergone n collisions and has an energy between E and $E+dE$, we at once write the diffusion equation, using the Markoff nature of the process,

$$\frac{\partial\Pi(n,E_0,E,x)}{\partial x} = -\,\Pi(n,E_0,E,x)\int_0^E N\phi(E',E)\,dE' + \int_E^{E_0}\Pi(n-1,E_0,E',x)N\phi(E,E')\,dE'. \qquad \ldots\ldots(1)$$

This equation (1) is quite general and into this equation we introduce the assumptions of Heitler and Jánossy.

Let us first make the assumption of a cut-off for the cross section function, i.e. that

$$\phi(E', E) = 0 \quad \text{if} \quad E < E_c$$

where E_c is the critical energy. If this assumption is made, equation (1) breaks up into two parts; writing

$$\Pi^{(1)}(n, E_0, E, x) \equiv \Pi(n, E_0, E, x) \qquad (E < E_c),$$

$$\Pi^{(2)}(n, E_0, E, x) \equiv \Pi(n, E_0, E, x) \qquad (E > E_c),$$

we have

$$\frac{\partial \Pi^{(2)}(n, E_0, E, x)}{\partial x} = -\Pi^{(2)}(n, E_0, E, x) \int_0^E N\phi(E', E)\, dE' + \int_E^{E_0} \Pi^{(2)}(n-1, E_0, E', x) N\phi(E, E')\, dE', \qquad \ldots\ldots(2)$$

$$\frac{\partial \Pi^{(1)}(n, E_0, E, x)}{\partial x} = \int_{E_c}^{E_0} \Pi^{(2)}(n-1, E_0, E', x) N\phi(E, E')\, dE'. \qquad \ldots\ldots(3)$$

With Heitler and Jánossy we assume:

(1) That $\phi(E', E)\, dE'$ can be expressed in the homogeneous form $\phi(E'/E)\, dE'/E$.

(2) That the distribution of the initial energy E_0 is given by

$$F(E_0)\, dE_0 = \gamma \left(\frac{E_c}{E_0}\right)^{\gamma+1} \frac{dE_0}{E_c}.$$

Note that
$$\int_{E_c}^{\infty} F(E_0)\, dE_0 = 1.$$

For convenience we write

$$\phi\left(\frac{E'}{E}\right)\frac{dE'}{E} = \phi\omega\left(\frac{E'}{E}\right)\frac{dE'}{E}, \qquad \int_0^E \omega\left(\frac{E'}{E}\right)\frac{dE'}{E} = 1.$$

ϕ is thus the total cross section and is independent of the energy state of the primary nucleon in view of the homogeneity assumption.

Since we are interested in the probability p_n of the occurrence of n mesons irrespective of the energy state of the primary nucleon, we further define $p_n^{(1)}$ as the probability that n collisions have occurred and the energy of the primary is reduced to a value below the critical energy:

$$p_n^{(1)} = \int_{E_c}^{\infty} F(E_0)\, dE_0 \int_0^{E_c} \Pi^{(1)}(n, E_0, E, x)\, dE,$$

$p_n^{(2)}$ as the probability that n collisions have occurred and the energy of the primary is still above the critical energy:

$$p_n^{(2)} = \int_{E_c}^{\infty} F(E_0)\, dE_0 \int_{E_c}^{E_0} \Pi^{(2)}(n, E_0, E, x)\, dE.$$

Then
$$p_n = p_n^{(1)} + p_n^{(2)};$$

p_n is the required probability.

On performing the integration over E and E_0 we obtain

$$\frac{\partial p_n{}^{(2)}}{\partial x} = -p_n{}^{(2)}N\phi + p_{n-1}{}^{(2)}N\phi\omega_{\gamma+1}, \qquad \ldots\ldots(4)$$

$$\frac{\partial p_n{}^{(1)}}{\partial x} = p_{n-1}{}^{(2)}N\phi(1-\omega_{\gamma+1}), \qquad \ldots\ldots(5)$$

where
$$\omega_\gamma = \int_0^E \omega\left(\frac{E'}{E}\right)\left(\frac{E'}{E}\right)^{\gamma+1}\frac{dE'}{E'}.$$

The solution of equation (4) is

$$p_n{}^{(2)} = \frac{(\phi Nx)^n}{n!}\exp(-\phi Nx)\,\omega_{\gamma+1}{}^n.$$

Substituting $p_n{}^{(2)}$ into the equation (5),

$$p_n{}^{(1)} = \Gamma_n(\phi Nx)\omega_{\gamma+1}{}^{n-1}(1-\omega_{\gamma+1}),$$

where $\Gamma_n(a)$ is the incomplete gamma function defined by

$$\Gamma_n(a) = \int_0^a \frac{z^{n-1}}{n-1!}e^{-z}\,dz.$$

These were the formulae obtained by Heitler and Jánossy. It is to be noted that these simple solutions are possible only because we have averaged over the initial energy spectrum. If we were dealing with a nucleon of a defined energy $E_0 > E_c$ at $x=0$ the problem would have been much more complicated. But even in that case a simplification is possible if we do not assume any cut-off, i.e. if we take $E_c = 0$ (an unreal assumption). We do not then have a splitting up of the fundamental equation. If we define $\Pi(n, E_0)$ as the probability that n collisions have occurred, given that the initial energy is E_0, we obtain the equation

$$\frac{\partial \Pi(n, E_0, x)}{\partial x} = \{-\Pi(n, E_0, x) + \Pi(n-1, E_0, x\}\phi N. \qquad \ldots\ldots(6)$$

Compare this equation (6) with (4). The solution of equation (6) is

$$\Pi(n, E_0, x) = \Pi(n, x) = \frac{(\phi Nx)^n}{n!}e^{-\varphi Nx};$$

$\Pi(n, E_0)$ is independent of E_0. It is a Poisson distribution. If the initial energy E_0 is far greater than E_c then, for small thicknesses where the average number of mesons produced is not so great as to reduce the energy of the primary nucleon below the critical energy, the Poisson formula must be a good approximation.

REFERENCE

Heitler, W., and Jánossy, L., 1949, *Proc. Phys. Soc.* A, **62**, 669.

The Density Spectrum and Structure of Extensive Cosmic-ray Air Showers at Sea Level

By D. BROADBENT, E. W. KELLERMANN*, and M. A. HAKEEM
The Physical Laboratories, The University, Manchester

Communicated by P. M. S. Blackett; MS. received 28th December 1949

ABSTRACT. Showers have been examined in the density range 5–500 particles/m² using two trays of Geiger counters 5 m. apart, the discharges of individual counters being recorded using neon lamps. The observed showers are compared with a theoretical analysis based on the usual assumptions that the incident densities are uniform over the extent of the apparatus and distributed according to the spectrum $N(x)=Bx^{-\gamma}$ per hr. per m². The comparison shows (i) that in the density range examined the above spectrum applies only for a vanishingly small area of observation, with $\gamma=1\cdot425\pm0\cdot022$, $B=620$, and with no evidence for a change of γ with density, and (ii) that for the separation of 5 m. employed, the density can *not* be regarded as uniform over the extent of the apparatus. It is shown that this second conclusion is capable of explaining many of the differences found between the results of other authors obtained on the assumption of uniformity of density: in particular, it is concluded that there is yet no significant evidence for a change of γ with altitude.

§1. INTRODUCTION

Much work has been done in the past few years upon the extensive atmospheric showers of cosmic radiation, and the analysis of experimental data has almost entirely been based upon the following assumptions:

(i) the average incident particle density is, for a given shower, constant over the extent of the experimental arrangement;

(ii) the spatial distribution of the particles is purely random;

(iii) the rate of incidence of showers with particle density equal to or greater than x per square metre upon the apparatus is given by

$$N(x)=Bx^{-\gamma}, \qquad \ldots\ldots(1)$$

with B and γ independent of x.

It is well known that from these three assumptions the rate of coincidences between n counters each of area S is

$$r(n)=B\gamma\int_0^\infty (1-e^{-Sx})^n \cdot \frac{dx}{x^{\gamma+1}} \qquad \ldots\ldots(2)$$

and most of the work reported has, in principle, tested this expression for various values of n and S. It has been found generally that the observed coincidence rates are consistent with a value of γ of about 1·5. The precise values of γ obtained from this expression differ, however, according to the method used and the geometry of the apparatus (see, for example, the useful summary given by Cocconi and Tongiorgi (1949)), but the physical significance of these differences is not immediately obvious. They indicate, clearly, some incorrectness in the three assumptions above, but do not indicate where it lies.

---

* Now at the University of Leeds.

In particular, the fact that the expression (2) can always be made to express given experimental data by choosing an appropriate value of γ does not imply that the only incorrectness lies in the assumption of constant γ and that it can be removed by taking γ to be a weak function of the density.

The present work is an attempt specifically to test the validity of the basic assumptions. This is important not only to enable a clearer picture of shower structure to be determined, but also because these assumptions are implicit in the analyses so far made to obtain information about the penetration of extensive showers, which is much greater than that expected due to electrons and photons only.

§ 2. THE EXPERIMENTAL ARRANGEMENT

The experiment was performed in the University of Manchester, at an altitude of 50 m. above sea level. The apparatus consisted of two identical groups of G-M counters, placed with their centres 5 m. apart. The counters were of conventional design of 1 mm. Pyrex glass with 0·1 mm. sheet-copper cathodes, filled with argon–alcohol vapour mixture, and each group was placed in a thermostated aluminium box, with only a 1 mm. lid some 5 mm. above it. The boxes were placed in the open air away from walls etc. and each raised on two brick columns about 50 cm. from the ground. Each group consisted of five large counters, each 63 cm. × 3½ cm., and one small counter 5 cm. × 2 cm., and the impulses of each counter were transmitted by its own separate cathode follower, also located in the box, through coaxial cable to the control point inside the laboratory. The disposition is represented in Figure 1.

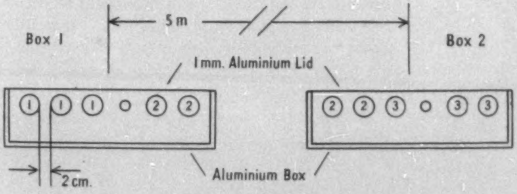

Figure 1. The experimental arrangement.
The numbers indicate the coincidence groups to which a counter belongs ; numbered counters each 63 cm. × 3½ cm., unnumbered counters each 5 cm. × 2 cm.

All counters were arranged with their axes parallel, and separated from each other by about 2 cm., so that the effective counter area was unchanged for particles incident at angles up to about 45° from the vertical.

To detect the extensive showers the ten large counters were arranged in a three-fold coincidence system, the three coincidence groups containing respectively 3, 4 and 3 counters. The coincidence group to which counters belonged is indicated by the number 1, 2 or 3 in Figure 1. It will be noted from this figure that the coincidence grouping was symmetrical between the two boxes, and that each shower recorded had a minimum spread of 5 metres, and that the two small counters were not part of any coincidence group, so that they did not contribute to the selection of showers. The impulses of each counter, including the two small ones, also went to its own separate recording circuit, where they were mixed with a 'master pulse' derived from the coincidence circuit and occurring each time the latter responded to an incident shower. Indication by means of a small neon lamp was received from the recording circuit when the master pulse and the counter pulse coincided. The twelve neon lamps were photographed, together with a clock, an aneroid barometer and a telephone-message register each time a shower was recorded, and during the resetting period of the camera the coincidence system was rendered inoperative so that the next shower could not be recorded until after resetting was completed. It was thus possible to determine precisely which of the twelve counters had been discharged by each shower recorded. The coincidence circuit had a resolving time of 1 μsec., and the recording circuits a resolving time of 2 μsec., so that chance coincidences could in all cases be neglected. The whole system was carefully screened against external and internal interference and the coincidence and recording circuits thoroughly tested at least once every two days, the test being done both with artificial pulses and with counter pulses. In a series of about 2,000 trials the neon lamps never failed to respond under operating conditions to the impulses given them by the recording units; this means that within the statistical accuracy of the results, possible inefficiency of the lamps due to such failure can completely be neglected.

The most stringent test of the correct working of the apparatus was afforded by the photographic records themselves. Because of the symmetry of the arrangement, any event in box 1 should be paralleled by an equal rate of the similar event in box 2: thus, for example, the rate of showers which discharge three large counters in box 1, and simultaneously four large counters in box 2, should be the same as the rate of showers discharging four counters in box 1 and three in box 2. Table 1 illustrates the results obtained from the 3,039 showers recorded during the present experiments; each entry indicates the number of showers observed in which n_1 counters were discharged in box 1 simultaneously with n_2 in box 2.

Table 1. Observed Numbers of Events discharging n_1 and n_2 Counters

	$n_1=$ 1	2	3	4	5
$n_2=1$	0	449	177	57	22
2	436	326	194	81	31
3	179	191	152	89	51
4	69	73	90	68	58
5	12	25	45	54	110

The symmetry of the table about the diagonal indicates very satisfactorily the excellent working of the apparatus. The small counters also behaved correctly according to this test, but the statistics are much poorer as only 125 showers occurred in which either or both of the small counters was discharged.

Tests of this character were carried out at intervals as the data accumulated; emphasis upon the reliable working of the apparatus is made because of its necessity for the methods of analysis employed.

In the present paper we deal only with the data obtained by considering the discharges of the large counters; the events which involved also discharges in one or both of the small counters will be discussed in a subsequent paper.

§ 3. EFFECT OF BAROMETRIC FLUCTUATIONS

Barometric fluctuations will be of importance only if they lead to changes in the relative rates of showers of various densities. It is known that the expression (1) is approximately true, and, since the effect of barometric changes during the experiment is in any case small, we can for the discussion of this effect assume (1) to be completely true. Any change in B caused by barometric variation will not affect the relative rates of showers of different densities, and so can be neglected. A change in γ, however, would affect the relative rates, but from previous experiments (see § 8) it may be concluded that between sea level and about 3,000 m. the change in γ, if it exists, is not likely to be greater than 0·1 for arrangements comparable with the present, therefore the change in γ due to the barometric fluctuations of the order 1 cm. Hg observed during our experiments (corresponding to changes in altitude of 100 m.) is entirely negligible. We conclude then, that except in so far as we may deal with the absolute rate of events, the barometric changes produce no significant effect.

§ 4. ANALYSIS OF DATA OBTAINED FROM THE LARGE COUNTERS

(i) *Introduction*

We consider here the only discharges of the large counters, and calculate on the basis of the three original assumptions the relative rates to be expected of records involving particular combinations of counter discharges. These are compared with the observed rates and the deviations found are discussed critically. It is possible to establish whether they can be accounted for by simple Poisson fluctuations, and it is concluded that some deviations are too large to be accounted for in this way, and that, therefore, the explanation of them lies in inaccuracies in the original assumptions.

(ii) *Notation*

We classify the observed showers in three ways. Denote by n_1 and n_2 ($n_1, n_2 = 0, 1 \ldots 5$) the total number of large counters discharged in boxes 1 and 2 respectively by a given shower (these figures are obtained directly, of course, from the photographic records); then a shower discharging n_1 and n_2 counters respectively will be referred to as an event $(n_1\,;\,n_2)$ and the classification into events of this kind as the distribution $(n_1\,;\,n_2)$.

The second classification is in terms of the sum $(n_1 + n_2)$, in terms, that is, of the total number of counters discharged in both boxes by a given shower. A shower discharging a total of $(n_1 + n_2)$ counters will be referred to as an event $(n_1 + n_2)$ and the classification into such events as the distribution $(n_1 + n_2)$.

The third classification is in terms of the difference $(n_1 - n_2)$, that is, of the difference in the numbers of counters discharged in the two boxes by a given shower. A shower giving rise to this difference $(n_1 - n_2)$ will be referred to as an event $(n_1 - n_2)$ and the classification into such events as the distribution $(n_1 - n_2)$.

A few examples will clarify and illustrate these distributions. Reference to Figure 1 will show that certain events in the distribution $(n_1\,;\,n_2)$ cannot be recorded since they do not give rise to a three-fold coincidence; these are the events $(0\,;\,n_2)$, $(n_1\,;\,0)$ and $(1\,;\,1)$. In addition, as has been mentioned previously, the symmetry of the counter arrangement implies that the rates of events $(n_1\,;\,n_2)$ and $(n_2\,;\,n_1)$ are the same.

Several different events $(n_1\,;\,n_2)$ may be classed as the same event (n_1+n_2): thus, for example, events (1 ; 3), (2 ; 2), (3 ; 1) are all classed as events $(n_1+n_2=4)$. Because of the three-fold selection, events (n_1+n_2) with $n_1+n_2=0, 1, 2$ are not recorded; (n_1+n_2) thus varies from 3 to 10.

The third classification of events is in terms of (n_1-n_2). As with the last distribution several events $(n_1\,;\,n_2)$ may each be classed as the same event (n_1-n_2); thus, events (5 ; 2) (4 ; 1), are all classed as events $(n_1-n_2=+3)$. In addition the three-fold selection limits the events in the distribution (n_1-n_2) to those with $(n_1-n_2)=0, \pm 1, \ldots \pm 4$.

(iii) *The Distribution* $(n_1\,;\,n_2)$

We calculate first, on the basis of the initial assumptions, the expected relative rates of the various events making up this distribution.*

The probability that a shower of uniform density x per unit area (the unit area defined as the sensitive area of one counter) discharges a particular counter is $(1-e^{-x})$, and the probability that it does not discharge a particular counter is e^{-x}.

The probability of a particular n_1 counters in box 1 being discharged, and the remaining $5-n_1$ not being discharged by a shower of density x per unit area is therefore

$$(1-e^{-x})^{n_1}e^{-(5-n_1)x} \qquad \ldots\ldots(3)$$

and similarly, the probability of discharging a particular n_2 counters in box 2 and not discharging the remaining $5-n_2$ counters is

$$(1-e^{-x})^{n_2}e^{-(5-n_2)x}. \qquad \ldots\ldots(4)$$

The product of (3) and (4) therefore gives the probability that the shower produces a particular one of the various combinations of counter discharges each of which is an event $(n_1\,;\,n_2)$. If this product is further multiplied by $w(n_1\,;\,n_2)$, which is the total number of such combinations which can give rise to a three-fold coincidence, we obtain finally the total probability that the shower of density x per unit area produces a recorded event $(n_1\,;\,n_2)$ to be

$$w(n_1\,;\,n_2)(1-e^{-x})^{n_1+n_2}e^{-\{10-(n_1+n_2)\}x}. \qquad \ldots\ldots(5)$$

By multiplying (5) by the differential shower density spectrum and integrating over all shower densities we obtain the *rate of events* $(n_1\,;\,n_2)$ as

$$R(n_1\,;\,n_2)=w(n_1\,;\,n_2)B\gamma\int_0^\infty(1-e^{-x})^{n_1+n_2}e^{-\{10-(n_1+n_2)\}x}\frac{dx}{x^{\gamma+1}}. \qquad \ldots\ldots(6)$$

We calculate the value of this expression for all appropriate $n_1\,;\,n_2$, and for various values of γ between 1·2 and 1·8.

The quantities $w(n_1\,;\,n_2)$ can be readily determined: to illustrate the method we calculate here the value of $w(2;2)$. The only combinations of counter discharges which give an event (2 ; 2) and at the same time produce a three-fold coincidence are represented in Figure 2 (*a*), (*b*), (*c*).

---

* We assume throughout these calculations that the counters are of efficiency unity: the actual efficiency was better than 0·99 and it can be shown that the calculated rates are quite negligibly affected by this slight inefficiency. This is because recorded events $(n_1\,;\,n_2)$ are diminished due to inefficiency causing some real events $(n_1\,;\,n_2)$ to appear as events $(n_1-1\,;\,n_2)$ or $(n_1\,;\,n_2-1)$, and increased due to inefficiency causing some real events $(n_1+1\,;\,n_2)$ and $(n_1\,;\,n_2+1)$ to appear as events $(n_1\,;\,n_2)$. These two opposite effects are almost exactly equal, so that the net effect is negligible.

(*a*) involves any two out of the three group 1 counters and no counter out of the two group 2 counters in box 1, together with any one out of the two group 2 counters and any one out of the three group 3 counters in box 2. The number of possible combinations of type (*a*) is therefore $3.1.2.3=18$. Similarly the number of possible combinations of type (*b*) is $3.2.1.3=18$, and of type (*c*) $3.2.2.3=36$. Types (*d*) and (*e*) are examples of combinations which do not give a three-fold coincidence and so do not contribute. The value of $w(2;2)$ is thus $18+18+36=72$.

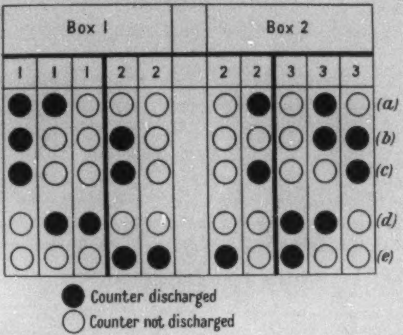

Figure 2. Combinations of counter discharges giving events (2; 2) : (*a*), (*b*), (*c*) represent the only types producing three-fold coincidences : (*d*), (*e*) are examples of types which do not give three-fold coincidences. The numbers indicate the coincidence groups.

Using this method we obtain Table 2 which gives the numerical values of $w(n_1;n_2)$ in terms of n_1 and n_2.

Table 2. $w(n_1;n_2)$ in Terms of n_1 and n_2

	$n_1=1$	2	3	4	5
$n_2=1$	0	18	27	15	3
2	18	72	87	45	9
3	27	87	99	50	10
4	15	45	50	25	5
5	3	9	10	5	1

We consider now the integral in equation (6). Putting $n_1+n_2=n$, and taking the total number of counters in the two boxes to be N, instead of 10, the integral becomes

$$I_N^n=B\gamma\int_0^\infty(1-e^{-x})^n\,e^{-(-Nn)x}\,\frac{dx}{x^{\gamma+1}} \qquad \ldots\ldots(7)$$

and indicates the rate of showers which discharge any particular group of n counters out of a total of N, and which do not discharge the remaining $N-n$. The value of this integral for a given γ can be written

$$\begin{aligned} I_N^n &= -B(-\gamma)!\sum_{p=0}^{n}(-1)^p\binom{n}{p}(N-n+p)^\gamma \\ &= -B(-\gamma)!\,J_N^n \qquad \ldots\ldots(8) \end{aligned}$$

providing the integral (7) exists.

The terms J_N^n may be most simply evaluated by a method indicated previously (Broadbent and Jánossy 1948). We form the difference scheme indicated below

$$\left.\begin{array}{lllll}
 & & \text{1st diff.} & & \text{2nd diff.} \\
0^\gamma & & & & \\
 & > & 1^\gamma-0^\gamma & & \\
1^\gamma & & & > & 2^\gamma-2\cdot1^\gamma+0^\gamma \\
 & > & 2^\gamma-1^\gamma & & \\
2^\gamma & & & > & 3^\gamma-2\cdot2^\gamma+1^\gamma \\
 & > & 3^\gamma-2^\gamma & & \\
3^\gamma & & & & \\
\cdot & & & & \\
\cdot & & & & \\
\cdot & & & & \\
(N-1)^\gamma & & & & \\
 & > & N^\gamma-(N-1)^\gamma & & \\
N^\gamma & & & &
\end{array}\right\} \qquad \ldots\ldots(9)$$

Each term in this scheme represents one of the quantities J_N^n, as may be seen by comparing with equation (8), and so (9) is exactly equivalent to

$$\begin{array}{llllllll}
 & & \text{1st diff.} & & \text{2nd diff.} & & & N\text{th diff.} \\
J_0^0 & & & & & & & \\
 & > & J_1^1 & & & & & \\
J_1^0 & & & > & J_2^2 & & & \\
 & > & J_2^1 & & & & & \\
J_2^0 & & & > & J_3^2 & & & \\
 & > & J_3^1 & & & & & \\
J_3^0 & & & & & & & \\
\cdot & & & & & & & \\
\cdot & & & & & & > & J_N^N \\
\cdot & & & & & & & \\
J_{N-1}^0 & & & & & & & \\
 & > & J_N^1 & & & & & \\
J_N^0 & & & & & & &
\end{array}$$

The values of J_N^n are therefore obtained by setting up the difference scheme (9) and taking the appropriate terms. For the present experiments we require the values of the quantities J_{10}^n, $n=3, 4 \ldots 10$, and for different values of γ, so the scheme was evaluated for $N=10$ and for $\gamma=1{\cdot}2$, $1{\cdot}3$, $1{\cdot}4$, $1{\cdot}45$, $1{\cdot}5$, $1{\cdot}55$, $1{\cdot}6$, $1{\cdot}7$ and $1{\cdot}8$.

We have, therefore, for a given γ,

$$R(n_1\,;\,n_2) \propto w(n_1\,;\,n_2)J_N^{n_1+n_2} \qquad \ldots\ldots(10)$$

(see equations (6), (7), (8)), and so by using Table 2 and the appropriate difference scheme, the relative values of the quantities $R(n_1\,;\,n_2)$ can be determined. These values can then be normalized to the total of 3,039 showers observed, and so give, for the specified γ, the expected numbers of the various events, that is, the expected distribution $(n_1\,;\,n_2)$. The calculated number of events $(n_1\,;\,n_2)$ for a given γ will be written $C_\gamma(n_1\,;\,n_2)$.

Table 3 gives the distribution $(n_1; n_2)$ obtained in this way for the various γ values taken, and also the observed distribution determined from an analysis of the photographic records (see also Table 1). The observed number of events $(n_1; n_2)$ will be written $O(n_1; n_2)$.

Table 3. Calculated Distribution $(n_1; n_2)$ as Function of γ; and the Observed Distribution

$(n_1; n_2)$	Obs. distrib.	Calculated distribution for given value of γ								
		1·20	1·30	1·40	1·45	1·50	1·55	1·60	1·70	1·80
(1; 2)	436	349	391	436	460	484	508	534	586	641
(2; 1)	449	349	391	436	460	484	508	534	586	641
(1; 3)	179	134	141	147	149	151	153	155	157	157
(2; 2)	326	357	376	391	398	404	409	413	418	419
(3; 1)	177	134	141	147	149	151	153	155	157	157
(1; 4)	69	35	35	35	35	34	34	33	32	30
(2; 3)	191	201	202	202	200	198	196	193	186	177
(3; 2)	194	201	202	202	200	198	196	193	186	177
(4; 1)	57	35	35	35	35	34	34	33	32	30
(1; 5)	12	5	5	5	5	5	5	4	4	4
(2; 4)	73	80	77	74	72	70	68	66	61	56
(3; 3)	152	175	170	163	159	150	150	145	134	123
(4; 2)	81	80	77	74	72	70	68	66	61	56
(5; 1)	22	5	5	5	5	5	5	4	4	4
(2; 5)	25	19	18	17	16	16	15	14	13	11
(3; 4)	90	108	102	94	91	87	83	79	70	62
(4; 3)	89	108	102	94	91	87	83	79	70	62
(5; 2)	31	19	18	17	16	16	15	14	13	11
(3; 5)	45	44	40	36	34	32	30	28	24	21
(4; 4)	68	110	100	90	85	79	75	70	61	52
(5; 3)	51	44	40	36	34	32	30	28	24	21
(4; 5)	54	84	74	64	59	55	50	46	39	32
(5; 4)	58	84	74	64	59	55	50	46	39	32
(5; 5)	110	280	222	175	155	137	120	107	82	63

We determine now the value of γ which gives a distribution best fitted to the observed one. This is done by a least squares method. For each of the distributions in Table 3 we find the deviation $\epsilon_\gamma(n_1; n_2) = C_\gamma(n_1; n_2) - O(n_1; n_2)$ between calculation and observation for each type of event; then $\epsilon_\gamma(n_1; n_2)^2$, and finally $\sum_{n_1; n_2} \epsilon_\gamma(n_1; n_2)^2$.

Table 4 gives the values of $\sum_{n_1; n_2} \epsilon_\gamma(n_1; n_2)^2$ and the corresponding values of γ, and these are shown graphically by curve II of Figure 3.

Table 4. $\sum_{n_1; n_2} \epsilon_\gamma(n_1; n_2)^2$ as Function of γ

$\gamma=$	1·20	1·30	1·40	1·45	1·50	1·55	1·60	1·70	1·80
$\sum_{(n_1; n_2)} \epsilon_\gamma(n_1; n_2)^2$	58265	28049	14104	12852	15078	20162	29716	57774	100510

The curve is a parabola and we take the value of γ best fitting the observations to be at the minimum. To determine this value, $\gamma_{\min}(n_1; n_2)$, accurately, and in particular to obtain its standard deviation, we proceed as follows. We adopt

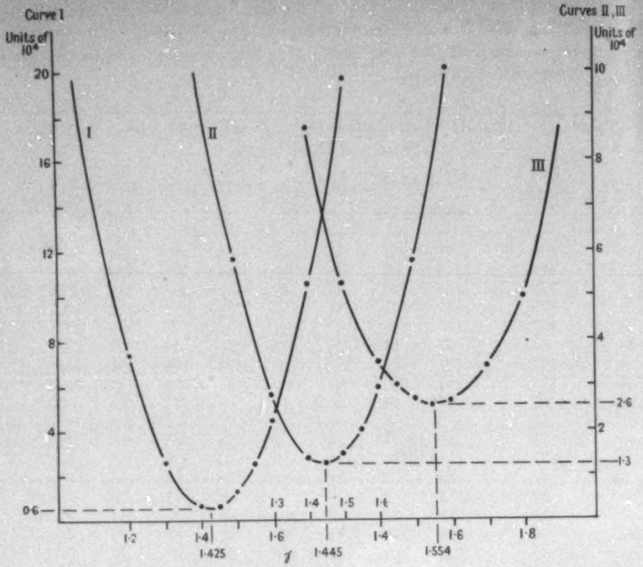

Figure 3.

Curve I: $\sum_{(n_1+n_2)} \epsilon_\gamma(n_1+n_2)^2$, Curve II: $\sum_{(n_1;\, n_2)} \epsilon_\gamma(n_1;\, n_2)^2$, Curve III: $\sum_{(n_1-n_2)} \epsilon_\gamma(n_1-n_2)^2$.

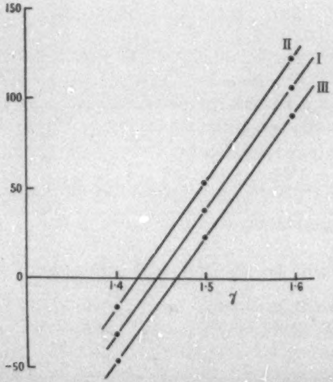

Figure 4. Determination of $\gamma_{\min}(n_1;\, n_2)$ and its standard deviation.

Curve I: $\Sigma c_i'(c_i-o_i)$, Curve II: $\Sigma c_i'(c_i-o_i)+(\Sigma c_i'^2 o_i)^{\frac{1}{2}}$, Curve III: $\Sigma c_i'(c_i-o_i)-(\Sigma c_i'^2 o_i)^{\frac{1}{2}}$.

for the moment a simplified notation and write c_1, c_2, etc. and o_1, o_2, etc. for the calculated and observed numbers of events in the distribution. The parabola is obtained by plotting

$$\sum_{n_1\,;\,n_2} \epsilon_\gamma(n_1\,;\,n_2)^2 \equiv \Sigma(c_i-o_i)^2$$

against γ, and the minimum is given by

$$\frac{\partial}{\partial\gamma}\Sigma(c_i-o_i)^2=0.$$

Using primes to denote differentiation with respect to γ this gives

$$\Sigma c_i'(c_i-o_i)=0. \qquad \ldots\ldots(11)$$

Table 3 enables the derivatives of the c_i''s to be obtained numerically using Stirling's formula, and this has been done for $\gamma=1{\cdot}4$, $1{\cdot}5$, $1{\cdot}6$. We then obtain the value of the left-hand side of equation (11) for these three values of γ, and when they are plotted against γ they give a straight line whose intersection with the γ-axis gives $\gamma_{\min}(n_1\,;\,n_2)$. This is line I of Figure 4. To determine the standard deviation of $\gamma_{\min}$ we must introduce into (11), which defines $\gamma_{\min}$, the statistical fluctuations of the c_i''s. We therefore get from (11) the equation

$$\Sigma c_i'(c_i-o_i)\pm d\{\Sigma c_i'(c_i-o_i)\}=0, \qquad \ldots\ldots(12)$$

where the second term is the standard deviation of the first arising from the fluctuations in the o_i's. Because the o_i's fluctuate randomly we have

$$d(\Sigma c_i'(c_i-o_i))=\left[\Sigma\left\{\frac{\partial}{\partial o_i}\{\Sigma c_i'(c_i-o_i)\}\,do_i\right\}^2\right]^{1/2}$$
$$=(\Sigma c_i'^2 o_i)^{1/2}$$

since we may for random fluctuations put $do_i^2=o_i$ etc. The standard deviation of $\gamma_{\min}$ is then determined by the intersection with the γ-axis of the two straight lines

$$\Sigma c_i'(c_i-o_i)\pm(\Sigma c_i'^2 o_i)^{1/2}=0, \qquad \ldots\ldots(13)$$

the second term in (13) is evaluated for $\gamma=1{\cdot}4$, $1{\cdot}5$, $1{\cdot}6$ as before, and the two lines obtained are II and III of Figure 4. We obtain finally

$$\gamma_{\min}(n_1\,;\,n_2)=1{\cdot}445\pm0{\cdot}022. \qquad \ldots\ldots(14)$$

(iv) *The Distribution* (n_1+n_2)

The expected numbers of the different events in this distribution are obtained immediately from those of the distribution $(n_1\,;\,n_2)$: this is clear, since, for example, the expected number of events with $n_1+n_2=4$, $C_\gamma(n_1+n_2=4)$, is given by $C_\gamma(1\,;3)+C_\gamma(2\,;2)+C_\gamma(3\,;1)$. A similar remark holds, of course, for the observed number of events, $O(n_1+n_2)$. Consequently, we obtain directly from Table 3 above, Table 5, giving the distribution (n_1+n_2) for the various γ values. It is interesting to note the intuitively unexpected result that while $C_\gamma(n_1+n_2)$ decreases for $n_1+n_2=3\ldots9$, it *increases* for $n_1+n_2=10$, very markedly for small γ, and this increase only disappears for $\gamma=1{\cdot}8$ approximately.

Table 6 gives the value of $\sum_{(n_1+n_2)}\epsilon_\gamma(n_1+n_2)^2$ for each value of γ; these are represented graphically by curve I of Figure 3.

Table 5. Calculated Distribution (n_1+n_2) as Function of γ and the Observed Distribution

(n_1+n_2)	Obs. distrib.	Calculated distribution for given value of γ									
		1·20	1·30	1·40	1·425*	1·45	1·50	1·55	1·60	1·70	1·80
(3)	885	697	783	873	896	919	968	1017	1067	1172	1282
(4)	682	625	657	685	691	697	707	716	723	732	734
(5)	511	471	475	473	471	470	465	460	453	436	415
(6)	340	345	335	321	317	313	305	295	286	265	242
(7)	235	255	240	223	218	214	204	195	189	166	146
(8)	164	197	179	161	157	152	143	134	126	109	93
(9)	112	169	148	128	124	119	110	101	92	77	64
(10)	110	280	222	175	165	155	137	121	107	82	63

* By interpolation between the values for $\gamma=1{\cdot}45$ and $\gamma=1{\cdot}40$.

Table 6. $\sum\limits_{(n_1+n_2)} \epsilon_\gamma(n_1+n_2)^2$ as Function of γ

γ	1·20	1·30	1·40	1·425	1·45	1·50	1·55	1·60	1·70	1·80
$\sum\limits_{(n_1+n_2)} \epsilon_\gamma(n_1+n_2)^2$	73856	26440	6592	5838	6450	12990	25948	45438	105914	196608

$\gamma_{\min}(n_1+n_2)$ and its standard deviation are obtained as before, and we find best agreement between observation and calculation for the distribution (n_1+n_2) when γ has the value

$$\gamma_{\min}(n_1+n_2)=1{\cdot}425\pm0{\cdot}022. \qquad ......(15)$$

(v) *The Distribution* (n_1-n_2)

This also may be deduced from the distribution $(n_1;\ n_2)$, remembering that, for example, $C_\gamma(n_1-n_2=+3)=C_\gamma(5;\ 2)+C_\gamma(4;\ 1)$. The treatment is exactly as before, and thus we obtain Tables 7 and 8 and curve III of Figure 3.

Table 7. Calculated Distribution (n_1-n_2) as Function of γ; and the Observed Distribution

(n_1-n_2)	Obs. distrib.	Calculated distribution for given value of γ								
		1·20	1·30	1·40	1·45	1·50	1·55	1·60	1·70	1·80
(−4)	12	6	6	5	5	5	5	4	4	4
(−3)	94	54	53	52	51	50	49	47	45	41
(−2)	297	257	258	257	255	254	251	249	242	234
(−1)	771	742	769	796	810	823	837	852	881	912
(0)	656	921	867	819	797	775	755	735	695	657
(+1)	790	742	769	796	810	823	837	852	881	912
(+2)	309	257	258	257	255	254	251	249	242	234
(+3)	88	54	53	52	51	50	49	47	45	41
(+4)	22	6	6	5	5	5	5	4	4	4

Table 8. $\sum\limits_{(n_1;\ n_2)} \epsilon_\gamma(n_1-n_2)^2$ as Function of γ

$\gamma=$	1·20	1·30	1·40	1·45	1·50	1·55	1·60	1·70	1·80
$\sum\limits_{(n_1-n_2)} \epsilon_\gamma(n_1-n_2)^2$	80722	52286	34932	30038	26546	25730	26828	34054	49766

The value of γ giving the best fit with this distribution is

$$\gamma_{\min}(n_1-n_2)=1{\cdot}554\pm0{\cdot}038. \qquad ......(16)$$

§ 5. DISCUSSION OF THE DIFFERENT VALUES OF $\gamma_{\min}$ OBTAINED

The values of $\gamma_{\min}$ obtained in the previous section for the three distributions $(n_1;\, n_2)$, (n_1+n_2) and (n_1-n_2) are respectively $1{\cdot}445 \pm 0{\cdot}022$, $1{\cdot}425 \pm 0{\cdot}022$, and $1{\cdot}554 \pm 0{\cdot}038$; we emphasize that these widely differing values are obtained, not as the results of three independent experiments, but as the results of three different analyses of the same set of data, and that, moreover, each method of analysis is, in terms of the initial assumptions, equally sound theoretically. We discuss now the significances of these differences.

The distribution $(n_1;\, n_2)$ is the most detailed, and adopting for the moment the simplified notation used previously, $\gamma_{\min}(n_1\,;\, n_2)$ is that γ which makes $\Sigma(c_i - o_i)^2$ a minimum, the c_i's being functions of γ. The distributions (n_1+n_2) and (n_1-n_2) are obtained by combining together the appropriate c_i's, and consequently $\gamma_{\min}(n_1+n_2)$ and $\gamma_{\min}(n_1-n_2)$ are those γ's which make expressions of the type $\Sigma\{(c_i+c_j+\ldots)-(o_i+o_j+\ldots)\}^2$ a minimum. It follows directly by differentiating the expressions $\Sigma(c_i-o_i)^2$ and $\Sigma\{(c_i+c_j+\ldots)-(o_i+o_j+\ldots)\}^2$ with respect to γ that they possess minima for the same γ only if $c_1=o_1$, $c_2=o_2$ etc. Consequently if the observed distribution $(n_1;\, n_2)$ is exactly equal to expectation for some particular γ, then all three distributions will give the same $\gamma_{\min}$. If this last condition does not hold, then it is to be expected that different $\gamma_{\min}$ will result.

Now if the initial assumptions are accurate, an indefinitely extended experiment would give observed values negligibly different from expectation for a particular γ, and hence identical values of $\gamma_{\min}$; these would also have negligible statistical error (because of the large number of observations). If the assumptions are inaccurate, an extended experiment would give observed values not equal to expectation for any γ, and hence would lead to different values of $\gamma_{\min}$; these $\gamma_{\min}$ would still have, however, negligible statistical error. In this extended experiment, then, any difference between the $\gamma_{\min}$ would indicate inaccuracy in the initial assumptions, and in general we can draw this same conclusion if the differences between the $\gamma_{\min}$ are large compared with their statistical errors. Accepting this criterion, we see it is satisfied for the extreme values of $\gamma_{\min}$ cited above, their difference being three times the standard deviation. We thus have direct evidence of incorrectness in the original assumptions.

There is further information supporting this view. If the observed rates are merely random fluctuations from the expected rates for a particular γ, then we expect, from the properties of random distributions, that the value of $\Sigma(c_i-o_i)^2$, averaged over a series of similar experiments, would be equal to Σc_i, that is, equal to 3,039, the total number of events recorded in each of the assumed experiments. For a single experiment, we are able to ascribe limits within which the observed value of $\Sigma(c_i-o_i)^2$ is likely to lie. These limits depend on the number of different types of events in the distribution used—that is, the number of terms of the form $(c_i-o_i)^2$—and if there are N such terms the limits for $\Sigma(c_i-o_i)^2$ are $\Sigma c_i \pm \Sigma c_i/(N/2)^{1/2}$[*].

In the three distributions taken there are 24 events of the kind $(n_1;\, n_2)$, 8 of the kind (n_1+n_2) and 9 of the kind (n_1-n_2); we thus form Table 9, which gives the values of $\sum\limits_{(n_1;\, n_2)} \epsilon_{\gamma\min}(n_1;\, n_2)^2$; $\sum\limits_{(n_1+n_2)} \epsilon_{\gamma\min}(n_1+n_2)^2$ and $\sum\limits_{(n_1-n_2)} \epsilon_{\gamma\min}(n_1-n_2)^2$ obtained (see Figure 3), and also the limits expected. It will be seen that distributions $(n_1; n_2)$ and (n_1-n_2) both give observed values completely outside any reasonable expectation, but that distribution (n_1+n_2) is normal. We take these wide disagreements as further evidence that the original assumptions are somewhere incorrect.

---

[*] The Γ-distribution: see for example, Jánossy, *Cosmic Rays*, p. 372 (Oxford: Clarendon Press).

Table 9. Observed and expected Values of $\Sigma\epsilon_{\gamma\,\mathrm{min}}{}^2$ for the three Distributions

Distribution	N	Observed $\Sigma\epsilon_{\gamma\,\mathrm{min}}{}^2$	Expected $\Sigma\epsilon_{\gamma\,\mathrm{min}}{}^2$
$(n_1; n_2)$	24	13000	3000± 900
(n_1+n_2)	8	6000	3000±1500
(n_1-n_2)	9	26000	3000±1400

§ 6. NATURE OF THE INACCURACIES IN THE ORIGINAL ASSUMPTIONS

On theoretical grounds the density within each shower is expected to decrease smoothly with increase in distance from the shower axis; the original assumption of uniform density is therefore only expected to be justified if the change of density over the extent of the apparatus is negligible. Here, then, is one possible source of inaccuracy. Theoretically too, considering an area over which the density may be regarded as uniform, the constant γ in the density spectrum is expected to change with density (Cocconi and Tongiorgi 1949); this gives a second possibility of error. The distribution of particles in the shower ceases to be strictly random, of course, if there is a density gradient within the shower, as indicated above, but such non-randomness is only appreciable if the change in average density is itself appreciable.

We may distinguish between such non-randomness and that due, for example, to the presence of associated pairs of particles, produced in the air near the apparatus or in the thin aluminium lid (measured in cascade units, the lid is equivalent to a few metres of air), or to the occasional particle whose direction may be so near the horizontal that it has an appreciable chance of passing through more than one counter. The scattering of particles in the large cascade length in air (about 300 m.) is such that only pairs formed very near the apparatus can be expected to contribute to the first effect, which is consequently expected to involve only some one or two per cent of the incident particles. From cloud chamber photographs of showers, which at sea level show most particles to be incident close to the vertical, it may be concluded that the second effect is likewise very small. It is important to realize, however, that each of these effects is identical at the two counter boxes and that consequently the assumption that the average density at the two boxes is the same is equally justified whether or not they exist. The only change to be expected on their account is that the fluctuations of density will not be strictly Poissonian as previously assumed, but in fact a little wider. A law of fluctuations a little wider than the simple Poissonian inserted into equation (6) will not however appreciably affect the calculated rates, certainly considerably less than a systematic difference in average density at the two boxes. We feel justified then, in neglecting the slight degree of association of the incident particles.

Evidence for association among the incident particles has been presented by Daudin (1949).

We discuss, then, the other two major possibilities mentioned, namely, that γ may change with shower density, and that a density gradient in the shower leading to a small change of density over the extent of the apparatus (such as is expected on cascade theory for instance), is in fact perceptible with the apparatus used. It is possible roughly to examine these possibilities separately with the distributions taken.

The distribution $(n_1 - n_2)$, which is in terms of the difference in numbers of discharges in the two boxes, is clearly sensitive to a change in average density over the extent of the apparatus. In contrast, however, it is relatively insensitive to a change in γ; this can be seen from Table 7, which shows that the expected distribution $(n_1 - n_2)$ is little affected for even large changes in γ. The distribution $(n_1 + n_2)$ which is of the total number of discharges in both boxes together (Table 5), is, on the other hand, far more sensitive to changes in γ (numerically about four times), and relatively less sensitive to changes in average density, since a small variation in density over the apparatus will not greatly affect the average total number of particles falling in it. Roughly, then, distribution $(n_1 - n_2)$ indicates whether or not the average density is really uniform, and distribution $(n_1 + n_2)$ whether or not γ changes with density. Reference to Table 9, however, shows that the distribution $(n_1 + n_2)$ is statistically normal (observed $\Sigma \epsilon_{\gamma\,\mathrm{min}}{}^2 = 6{,}000$: expected $3{,}000 \pm 1{,}500$), from which we conclude that the variation in average density is responsible for the discrepancies observed, and that there is no evidence for a change in γ. We remark particularly that we cannot assume that the distribution $(n_1 + n_2)$ is normal because of the effect of a change in average density cancelling out an increase in γ with density, since both these effects act in the same direction of reducing the expected numbers of high density events, and so would reinforce rather than cancel each other.

Examination of Tables 3 and 7 shows that the differences between the observed and calculated numbers of the various events confirm the idea of a difference in average density over the two boxes. From Table 7 ($\gamma_{\mathrm{min}} = 1{\cdot}554$) we see that the observed number of events $n_1 - n_2 = 0$ is less than expected, and that the observed numbers of events $n_1 - n_2 \geqslant |1|$ are consistently greater than expected. From Table 3 ($\gamma_{\mathrm{min}} = 1{\cdot}445$) we see that the numbers of events showing high density at both boxes—e.g. (5; 5), (4; 4)—are less than expected and that the numbers showing large density differences—e.g. (5; 1), (4; 1)—are greater than expected. These differences are just what would be expected, however, if, on the average each shower produced a different particle density at each of the two boxes. The difference in rates for a *single* event could, of course, be explained as an extreme statistical fluctuation, but the probability that *all* the events fluctuate simultaneously in the above manner is very remote. In contrast, Table 5 ($\gamma_{\mathrm{min}} = 1{\cdot}425$) shows no such systematic differences which might be attributed to a change in γ itself.

Cocconi and Tongiorgi (1949) consider that γ increases with density, a result in disagreement with the above conclusion. We have used Cocconi's equation, $\gamma = 1{\cdot}31 + 0{\cdot}038 \ln x$, to calculate what our distributions would be if γ changed in accordance with it. We use an approximate method as follows. The rate of events $(n_1; n_2)$ is proportional to

$$\int_0^\infty (1 - e^{-x})^n \, e^{-(N-n)x} \, \frac{dx}{x^{\gamma+1}},$$

where $n = n_1 + n_2$ and $N = 10$ (see equation (6)). The integrand has a maximum for a particular density, $x(n)$, dependent on the value of n, and we can assume approximately that the maximum contribution to the value of the integral comes from the neighbourhood of this value of the density. Cocconi's equation gives for this density a value of $\gamma = 1{\cdot}31 + 0{\cdot}038 \ln x(n) = \gamma(n, x)$ say, and we then evaluate the integral assuming γ constant and equal to $\gamma(n, x)$. Each of the integrals like the one above, for $n = 3, 4 \ldots 10$, is evaluated in this way for the appropriate $\gamma(n, x)$, and the rates obtained, to a first approximation, correspond to those obtained by assuming a continuously variable γ. The maxima of the integrands are obtained by differentiation and are given in Table 10 together with the corresponding $\gamma(n, x)$ from Cocconi's equation.

Table 10. Values of $x(n)$, $\gamma(n, x)$ and $\bar{x}(n)$

n	3	4	5	6	7	8	9	10
$x(n)$ (per m^2)	3	9	16	23	34	48	70	110
$\gamma(n, x)$	1·354	1·392	1·414	1·430	1·444	1·456	1·472	1·489
$\bar{x}(n)$ (per m^2)	9	15	22	32	43	60	97	350

The integrals are evaluated by the same method as before, the terms J^n_γ being obtained by interpolation between the known values for the various γ. The distributions obtained are given in Table 11, together with the corresponding values of $\Sigma\epsilon^2$. For convenience, the values of these latter quantities obtained on the assumption of constant γ (see Table 9) are also given.

Comparing the two sets of values, it will be seen that in each case the value assuming variable γ is considerably higher than the corresponding value assuming constant γ, so much so that the value even for the $(n_1 + n_2)$ distribution is now well outside probable error. In other words the assumption of a variable γ, so far from bringing experiment and theory into better agreement, in fact greatly worsens it; we maintain, therefore, our previous conclusion about the constancy of γ. This disagreement with the results of Cocconi and Tongiorgi may well be due to the large statistical error of their equation (see also § 8).

Table 11. The three Distributions calculated assuming $\gamma = 1{\cdot}310 + 0{\cdot}038 \ln x$

$(n_1; n_2)$	
(1; 2), (2; 1)	399
(1; 3), (3; 1)	149
(2; 2)	396
(1; 4), (4; 1)	36
(2; 3), (3; 2)	212
(1; 5), (5; 1)	5
(2; 4), (4; 2)	79
(3; 3)	174
(2; 5), (5; 2)	18
(3; 4), (4; 3)	101
(3; 5), (5; 3)	38
(4; 4)	95
(4; 5), (5; 4)	66
(5; 5)	168

$\Sigma\epsilon^2 = 18000$
(constant γ, 13000)

$(n_1 + n_2)$	
3	798
4	694
5	496
6	342
7	238
8	171
9	132
10	168

$\Sigma\epsilon^2 = 12000$
(constant γ, 6000)

$(n_1 - n_2)$	
±4	5
±3	54
±2	266
±1	778
0	833

$\Sigma\epsilon^2 = 38000$
(constant γ, 26000)

§7. AVERAGE DENSITIES OF RECORDING SHOWERS

It is of interest to determine the approximate average density of the showers recorded. For a given value of n, this is

$$\bar{x}(n) = \frac{\int_0^\infty x(1-e^{-x})^n\, e^{-(10-n)x}\, \frac{dx}{x^{\gamma+1}}}{\int_0^\infty (1-e^{-x})^n\, e^{-(10-n)x}\, \frac{dx}{x^{\gamma+1}}}, \qquad \ldots\ldots(17)$$

the approximation arising from neglect of the density gradient. The upper integral is the same as the lower with γ reduced by unity and so $\bar{x}(n)=\gamma J^n_{10}(\gamma-1)/J^n_{10}(\gamma)$; this can readily be evaluated using the difference schemes for γ and $(\gamma-1)$. The average densities obtained are given in Table 10, for $\gamma=1{\cdot}425$. The large increase in $\bar{x}(n)$ for $n=10$ is due to the fact that the requirement that even a single counter is *not* discharged effectively cuts out all showers of high density. The average number of large counters discharged per recorded shower was 4·95.

§8. DISCUSSION OF THE RESULTS AND COMPARISON WITH PREVIOUS WORK

The density range examined in the present experiments may reasonably be taken as 5–500 per m², and the separation of the counter boxes was 5 m. These figures are comparable with those for almost all arrangements that have been used for examining extensive showers, and our conclusion that the density gradient within the shower is not negligible implies that almost all other experiments performed will likewise have been affected by it. It follows then that the spectrum $N(x)=Bx^{-\gamma}$ can strictly be applied only to the case of a vanishingly small area of observation, and that for most experiments its use, without allowance being made for density gradient, will lead to error. In the present experiments the distribution (n_1+n_2) has been shown to be sensitive to changes in γ, and insensitive to the density gradient: we conclude therefore that over a vanishingly small area the spectrum $N(x)=Bx^{-\gamma}$ applies, with $\gamma=1{\cdot}425\pm0{\cdot}022$, as given by this distribution. This value is for the density range 5–500 per m², and over this range there is no evidence of a change of γ with density.

The spectrum cannot of course be assumed to hold down to zero density, since it would then contain an infinite number of particles; this was pointed out previously by Auger and Daudin (1945). γ must therefore decrease for sufficiently low densities, but no change will be detected experimentally until the apparatus becomes predominantly sensitive to densities at which γ has begun to decrease.

We must conclude then, that the spectrum probably holds at least down to densities of the order one per square metre.

We cannot from our experiments determine the precise nature of the density gradient, but it seems reasonable to exclude a shower structure such that there are violent and frequent variations of density over the extent of the apparatus. The structure given by formal cascade theory, with the density falling smoothly with distance from the shower axis, could well account for the results. Our experiments are being extended in order to obtain more detailed information about shower structure.

In previous work the two methods most often used to determine γ depend on (*a*) the comparison of the N-fold and $(N+1)$-fold coincidence rates using counters of the same area, and (*b*) the variation in counting rate of an N-fold coincidence set composed of counters each of area S, as S is varied. Assuming γ constant, this latter method, on the further reasonable assumption that all showers have a similar structure, can be shown to be unaffected by a density gradient, and to give γ as the slope of the graph of (log (counting rate), log S). If γ is not constant, the graph is not a straight line, and strictly its slope ceases to have a simple significance as before: the slope at a particular S, however, is usually taken as an approximation to the value of γ at a density equal to $1/S$.

Method (*a*), however, in contrast to method (*b*), proves not to be independent of density gradient. We can show this qualitatively as follows. Consider two counters C_1 and C_2 so close together at a point A that any change of density over them is negligible, and then move C_2 to a distant point B where the change in density is appreciable. Consider those showers whose mean density at the point A is x per counter. With both counters at A, the fraction of these showers recorded by C_1 is $(1-e^{-x})$, and the fraction recorded by both C_1 and C_2 is $(1-e^{-x})^2$; the ratio 2-fold/1-fold is clearly $(1-e^{-x})$. With C_2 at B, however, the same incident showers will to a first order be equally likely to have at B a density greater or smaller than the density x at A. If the former, the shower will be more likely to be recorded than with both counters at A; if the latter, less likely. But as the slope of the function $(1-e^{-x})$ decreases with increase in x, the increased probability in the former case is more than counterbalanced by the decreased probability in the latter. The mean probability that C_2 records a shower is therefore less than $(1-e^{-x})$, and consequently the two-fold rate is smaller than originally.* The ratio 2-fold/1-fold in the case where the density gradient is not negligible is therefore *less* than the value it has if the gradient is inappreciable. This argument can be used generally and indicates that the observed ratio $(N+1)$-fold/N-fold will be *less* than expected on the assumption of constant density, and consequently on this assumption, the value of γ deduced will always be *larger* than it should be: method (*a*) is thus unsound for measuring γ.

This conclusion may well assist in explaining our disagreement with Cocconi and Tongiorgi concerning the increase of γ with density, since they consider together values of γ determined by both methods, which the above analysis shows to be unjustifiable.

The expectation that method (*a*) will give a value of γ which is too high is confirmed by the results of many authors. At sea level Cocconi, Loverdo and Tongiorgi (1946) find a value 1·46 by method (*b*), and their coincidence rates analysed by method (*a*) give a value about 1·58; Treat and Griesen (1948) find 1·40 and 1·55 respectively for methods (*b*) and (*a*) at 3,200–4,300 m. altitude; and Loverdo and Daudin (1948) at 2,900 m. find 1·30 and about 1·60 respectively. All these values are for density ranges comparable to ours. These different values, which have been previously explained as due to experimental difficulties and inaccuracies, are now seen to follow directly from the fact that the density cannot be regarded as uniform over the extent of the apparatus.

This fact must also be considered in discussing the altitude variation of γ. The mean lateral spread of a given shower is inversely proportional to the atmospheric pressure, and consequently its mean particle density is inversely proportional to the square of the pressure. If, therefore, an apparatus is taken from sea level to high altitude, where, for example, the pressure is only one half as great, the distance between the counter trays must be doubled (because of the greater lateral spread) and the area of the trays quadrupled (because of the smaller particle density) if the apparatus is to bear the same geometrical relation to the showers as at sea level. Conversely, if the apparatus remains unchanged, its behaviour is as if it remained at sea level, but with the distance between trays reduced by a factor 2, and their areas reduced by a factor 4. Decreasing the distance between trays reduces the non-uniformity of density over them, and for method (*a*) leads to a decrease in the incorrectly high value of γ obtained.

---

* This leads to the familiar decrease in counting rate as the counters are separated (decoherence curve), and we remark in passing that this well-known and appreciable decrease even for distances up to 10 m. (say) itself indicates clearly (for any reasonable shower structure) the presence of a significant density gradient at these small counter separations.

From the values of γ given above for methods (*a*) and (*b*) (and particularly from the values of γ given by our methods of analysis) it must be concluded that the decrease in γ due to this cause may well be of the order 0·1–0·2. Decreasing the area of the trays has no effect unless γ varies with density. Although our experiments show no significant change in γ in the density range 5–500/m^2, we cannot of course exclude a weak increase with density (such an increase is expected theoretically and might be appreciable for high densities: Williams (1948), for example, gives values of γ equal to 1·5–1·9 for the density region 300–2,000/m^2), but it does seem reasonable to conclude that decreasing the area of the trays by a factor 4 will not, for method (*a*) increase γ by more than about 0·02. This increase is much less than the decrease due to diminishing the distance between trays, and so hardly affects the latter. From this discussion, then, we are led to expect that method (*a*) will give a decreasing value of γ with altitude unless the dimensions of the apparatus are suitably changed as the altitude increases, and that this decrease may be of the order 0·1–0·2. If it is possible to go to a sufficiently high altitude then the density over the apparatus will become sensibly uniform, and consequently the value of γ given by method (*a*) approaches the correct one as the altitude increases. Using method (*a*), and again for densities comparable to ours, Auger and Daudin (1945) find γ equal to 1·66 and 1·46 respectively at 0 and 2,560 m.; Maze, Freon and Auger (1948) find 1·67 and 1·41 respectively at 0 and 6,700 m.; from the coincidence rates of Cocconi, Loverdo and Tongiorgi (1946) may be deduced, by method (*a*), the values 1·58 and 1·36 at 0 and 2,200 m. In contrast method (*b*) seems to give no such differences with altitude: the uncorrected values of γ at 0 and 2,200 m. of Cocconi ,Loverdo and Tongiorgi (1946) are 1·46 and 1·45; and at 0 and 3,260 m. Cocconi and Tongiorgi (1949) find 1·34–1·53 and 1·33–1·51.

We conclude then, that the observed decrease of γ with altitude, using method (*a*) can well be explained as due to neglect of density variations in the showers, and since no significant difference is found using method (*b*), it must be concluded that there is yet no evidence for such a decrease.

We remark again that this last conclusion, and the previous one that γ is not found to change significantly with density, are made for the density region 5–500/m^2 only.

§ 9. ABSOLUTE RATE OF SHOWERS AND THE BAROMETER COEFFICIENT

The data were collected in 35 separate readings at an average barometric pressure of 757 mm. Hg, and the average rate of showers (corrected for camera resetting time) was 13·00 ± 0·23 per hour. This rate was used to calculate the expected number of showers in each reading, and these compared with observation. The sum of the squares of the deviations between expectation and observation was 3,200, and as this is not significantly different from the total number of showers recorded (3,039), it may be concluded that the data show no evidence for other than random fluctuations. It is not possible, therefore, to determine a value for the barometer coefficient.

We may, however, calculate a value of the constant B of the density spectrum. If the counters had been concentrated at a point the absolute rate of the three-fold coincidences would have been evidently, at constant atmospheric pressure,

$$B\gamma \int_0^\infty (1-e^{-3Ax})^2(1-e^{-4Ax})\frac{dx}{x^{\gamma+1}},$$

where A is the effective area of one large counter in m^2. The accuracy with which B, for this particular pressure, may be determined from this expression depends on the accuracy with which A, γ, and the rate are known. It is difficult to determine the exact sensitive area of a counter to better than 99% or so; the accuracy of γ is limited by the total number of showers recorded; and an accurate determination of the absolute rate is dependent on a knowledge of the barometer coefficient, so as to reduce all data to the same constant atmospheric pressure. This coefficient is, however, large and is only known approximately. There is difficulty, too, in determining the rate of coincidences with counter trays at zero separation, since for small separations (about 1m., say) it is likely that a large fraction of the rate is due not to true extensive showers, but to more local phenomena, for example small knock-on showers produced by mesons. Our own rate of 13 showers per hour for a 5 m. separation, will therefore be incorrect if used in the above expression for B, and the true rate can only be obtained by measuring the rates for various separations of the counters, and then extrapolating the results to zero separation. This process, especially as it would in practice involve correction for barometric fluctuations, is clearly one which would not easily give an accurate value of the zero rate.

We have measured the three-fold rate at 21 m. separation and find an extrapolated value of 14·5 per hour at 760 mm. pressure, assuming a barometer coefficient of 10% per cm. Hg, but in view of the above discussion this rate cannot be considered more accurate than perhaps within 10%. Because this error is so large, it is hardly worth correcting for the others, and so we calculate B using this rate and with $\gamma = 1{\cdot}425$, obtaining finally the spectrum $N(x) = 620x^{-1{\cdot}425}$ per hour per m^2 at 760 mm. pressure for the density range 5–500 per m^2. In view of all the errors mentioned, the coefficient may well be in error by 10–15%.

§ 10. CONCLUSIONS

Extensive showers have been examined in the density range 5–500 particles per m^2, in order to test the validity of the shower density spectrum $N(x) = Bx^{-\gamma}$ and the assumptions underlying its use. The extent of the apparatus was 5 m. and as a result of a detailed analysis it is shown that the assumption of constant density over it is not justified. The presence of appreciable density variations over even such small distances is shown to render incorrect the measurement of γ by the ordinary method using the ratio of N-fold/($N+1$)-fold coincidences, and so serves to explain the widely different values of γ obtained by other authors using this method and the method of measuring coincidence rate as a function of counter area. This latter method is independent of density variation over the apparatus. It is shown also that the observed decrease of γ with altitude may well be spurious, and due likewise to a neglect of such density variations.

It is concluded, however, that the spectrum $Bx^{-\gamma}$ applies for a vanishingly small area of observation, and over the density range examined γ is found to be $1{\cdot}425 \pm 0{\cdot}022$, with no evidence for a change in γ with density. The constant B is found to be 620, but because of the difficulty in determining it accurately, this value may be in error by some 10–15%.

ACKNOWLEDGMENTS

We are indebted to Professor P. M. S. Blackett for the provision of facilities to carry out this work and for his constant encouragement. The difference tables used in the calculations and most of the numerical work involved were done by Miss Elizabeth Sully, and we are greatly indebted to her for this. Acknowledgments are also due to Mr. D. Jakeman for help in running the apparatus in the later stages of the work.

We wish also to thank Professor L. Jánossy for much valuable advice and criticism.

REFERENCES

Auger, P., and Daudin, J., 1945, *J. Phys. Radium*, **6**, 233.
Broadbent, D., and Jánossy, L., 1948, *Proc. Roy. Soc.* A, **192**, 364.
Cocconi, G., Loverdo, A., and Tongiorgi, V., 1946, *Phys. Rev.*, **70**, 841.
Cocconi, G., and Tongiorgi, V. T., 1949, *Phys. Rev.*, **75**, 1058.
Daudin, J., 1949, *J. Phys. Radium*, **10**, 63.
Jánossy, L., 1948, *Cosmic Rays* (Oxford : Clarendon Press), p. 372.
Loverdo, A., and Daudin, J., 1948, *J. Phys. Radium*, **9**, 134.
Maze, R., Freon, A., and Auger, P., 1948, *Phys. Rev.*, **73**, 418.
Treat, J. E., and Greisen, K. I., 1948, *Phys. Rev.*, **74**, 414.
Williams, R. W., 1948, *Phys. Rev.*, **74**, 1689.

The Scattering of Neutrons by Deuterons

By S. L. MARTIN, E. H. S. BURHOP, C. B. ALCOCK
and R. L. F. BOYD
University College, London

Communicated by H. S. W. Massey; *MS. received 28th November* 1949

ABSTRACT. The photographic plate method has been used to investigate the angular distribution of deuterons recoiling after neutron impact. The deuteron recoils were produced in a thin target of heavy wax placed in contact with a C2 Ilford nuclear emulsion.

For neutrons of energy 2·6–3·1 Mev., produced in the d–d reaction, 2,000 deuteron recoils were measured. Owing to the short range of the recoils produced when neutrons of low energy are scattered through small angles, the technique is only applicable to the study of the angular distribution in the range 90°–180° in the centre-of-mass system. For angles between 120° and 180° the results of the present work are in satisfactory agreement with those of previous experimenters using different methods, and they agree with the theoretical form of the distribution calculated by Buckingham and Massey on the assumption of ordinary forces between nucleons. This agreement is not decisive, however, since in this region the calculated distributions for ordinary and exchange forces do not lie far apart. For smaller scattering angles where a decisive test could have been made, the method is too inaccurate.

For neutrons of energy from 4·0 to 6·0 Mev. and from 6·0 to 9·0 Mev., obtained from a Ra–Be source, the angular distribution over a much larger range of scattering angle has been obtained from the measurement of 1,200 deuteron recoils. The angular distribution for neutrons scattered through angles near 180° appears to be rather steeper than for slower neutrons; but the ratio of the differential cross section at 90° to that at 180° is found to be about 0·35–0·40, of the same order as for neutrons in the lower energy range.

Measurements of 1,000 proton recoils from the d–d neutrons showed an angular distribution for neutron scattering angles between 90° and 180° that was constant within the limits of the statistical error.

---

§ 1. INTRODUCTION

Although a good deal of attention has been paid to the study of collisions between neutrons and protons, less work has been done on neutron–deuteron collisions. Nevertheless, as has been pointed out by Buckingham and Massey (1941), it should be possible to obtain considerable information about the nature of the interaction between nucleons from an accurate investigation of the angular distribution of neutrons scattered by deuterons. Indeed, so long as homogeneous sources of neutrons of comparatively low energy were alone available, the study of n–d collisions seemed likely to yield more information about nuclear forces than n–p collisions because in the former case the nature of the interaction would be expected to influence the angular distribution for neutron energies of a few Mev., whereas in the case of n–p collisions, different assumed interactions do not show any marked difference in predicted angular distributions until neutrons in excess of 10 Mev. are used.

Although the recent development of high energy neutron sources has somewhat reduced this advantage of the use of n–d collisions as a means of studying the nuclear interaction, it can still supply important confirmatory evidence. Also, since the nuclear three-body problem has not been solved accurately, important evidence can be obtained about the validity of the resonating group structure method applied by Buckingham and Massey in their calculations on the n–d and n–p systems.

Early work on n–d collisions was carried out by Kruger, Shoupp, Watson and Stallmann (1938) and by Barschall and Kanner (1940). Recently the results of two further investigations have been published. Coon and Barschall (1946) have used an ionization chamber method to study the angular distribution. Such a method has the advantage of enabling a large number of deuteron recoils to be observed in a short time, thus reducing statistical uncertainties. On the other hand, since the angular distribution is deduced from the energy distribution of the recoils, it is difficult to allow for neutrons scattered before reaching the target, since the energy–angle criterion cannot be applied to the recoils. Of course neutrons scattered on to the target without loss of energy would not affect the energy distribution of the recoils but if some of the neutrons reaching the target have previously lost energy in collision with hydrogenous material, the recoil energy distribution would be distorted in a way that might prove difficult to correct.

Darby and Swan (1948) have used a cloud chamber containing CD_4 to study n–d collisions. This method has the advantage that the range–angle criterion can be applied to the recoils and those arising from neutrons that have been scattered before reaching the chamber, or those produced by proton contamination can be excluded. However, more labour is involved in obtaining and measuring the recoils, so that fewer are available to determine the angular distribution and the statistical uncertainties are larger.

We have applied the photographic plate technique to the study of n–d collisions. This method enables both the energy and the angle of the recoils to be determined so that proton recoils, and deuteron recoils from neutrons that have been scattered before reaching the target, can be excluded. The apparatus is simpler than the cloud chamber and its smaller bulk ensures that less trouble is experienced from neutrons scattered by the recording apparatus itself. Track measurement is less laborious than with the cloud chamber but it is still very slow, so that statistical uncertainties are more serious than in the case of the ionization chamber method. The method also suffers from some other disadvantages. The most serious of these arises from the hydrogen always present in the photographic emulsion. Thus proton recoils are always present and have to be distinguished from the deuteron recoils by means of the energy–angle criterion. At large angles of recoil the tracks are very short and it is difficult to make use of this criterion. Another disadvantage of the photographic method is the shrinkage of the emulsion due to processing. A correction has to be applied to depth measurements to allow for this shrinkage.

In spite of these difficulties the success achieved by Powell and his collaborators (Powell and Occhialini 1946, May and Powell 1947, Heitler, May and Powell 1947, Guggenheimer, Heitler and Powell 1947) in the use of the photographic emulsion for the study of other nuclear collisions, made it seem worth while to apply it in this case.

§ 2. EXPERIMENTAL DETAILS

(i) *Exposure of the Plates*

Two sources of neutrons were used in these experiments. Most of the measurements refer to d–d neutrons obtained from the bombardment of a heavy paraffin wax target by deuterons of energy 300 kev. in the generator of the Chemistry Department of University College, London. In this generator the target is at high potential and it was found most convenient to mount the photographic plate so that it received neutrons emitted in the direction of the deuteron beam. Since the target was effectively a thick one, the neutron energies were spread over a rather broad band in the range 2·6–3·1 Mev. The experiments showed, however, that most of the neutrons had an energy close to 3·0 Mev. The spread in neutron energies did not greatly increase the uncertainty in the determination because for recoil angles above 30°, a greater spread in the energy distribution of the recoils is produced by the difficulties of accurate measurement of the tracks. The diameter of the target was about 1 cm.

Some measurements have also been carried out using the neutrons obtained from a source consisting of 100 mg. Ra + Be. Although the neutrons from such a source are heterogeneous in energy, the measurement of any given deuteron recoil enables the calculation of both the initial energy and the angle of scattering of the neutron producing it, providing it can be assumed that the neutrons come directly from the source without previous scattering.

The photographic plates were contained in thin metal cassettes, a very thin film of heavy paraffin wax (with a deuterium content of 99% of the total hydrogen present) being almost in contact with the emulsion. The paraffin wax film was prepared by vacuum evaporation on to a thin copper sheet, special care being taken to ensure a uniform film thickness. For the d–d neutrons the film used was about 3μ thick while for the Ra–Be neutrons the thickness was about 12μ. In the former experiment the cassettes were mounted inside the thin metal electrode cowling of the generator with the centre of the plate approximately 10 cm. from the target, while in the latter experiment the distance from source to target was 30 cm. and a block of lead 5 cm. thick was placed directly in front of the source. In both experiments neutrons were incident on the paraffin wax film at a glancing angle of 15°, so that recoil deuterons projected by collision with the neutrons entered the photographic emulsion. The experimental set-up in the two cases is illustrated in Figure 1 (*a*) and (*b*).

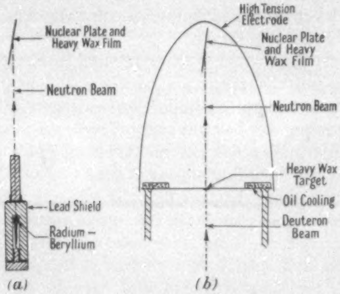

Figure 1.

One of the chief sources of uncertainty in experiments of this kind is caused by the neutrons which reach the paraffin wax film after scattering from surrounding objects. For the d–d neutrons, whose energy was known approximately, scattered neutrons could be excluded by applying an energy–angle criterion to the deuteron recoils (see §2 (vi)). Such a criterion was not applicable in the experiment with the Ra–Be neutrons and in this case the proportion of scattered neutrons reaching the wax film was made negligible by carrying out the exposures about 6 feet above the flat roof of a high building in University College, London, the source and plate being mounted on a very light framework. It was estimated that in this way the proportion of scattered neutrons was reduced to about 5%.

After exposure the plates were exposed to ThC′ alpha particles. The nuclear plate and the RaTh source were located at well defined positions and their relative orientation was such that the α-particle tracks entered the emulsion at an angle of $26 \pm 0{\cdot}5°$ to its surface at the centre. The angle of entry at any other part of the surface could be calculated from the geometry of the arrangement. These tracks were later used to provide continuous monitoring of any variation of the contraction factor of the emulsion that might occur during the processing and the period of measurement of the plate. The alpha particle tracks were confined to a few well defined areas of the plate, to avoid confusion with the deuteron recoils.

Ilford C2 plates were used in these experiments. For the experiments with d–d neutrons, an emulsion thickness of 50μ was used, while for the Ra–Be neutrons the emulsion thicknesses were 100μ and 200μ. Care was taken to process the plates under uniform conditions.

(ii) *Measurements of the Plates*

The plates were measured with a Cooke, Troughton and Simms, M4001 microscope. A ×95 oil immersion objective with a ×15 eye-piece containing a suitable graticule was used; the binocular system of the microscope introduced a further ×1·5 magnification. A protractor attached to the eye-piece enabled the measurement of the azimuthal angle of the recoil δ, relative to a plane perpendicular to the photographic plate and containing the centre of the source. The projected length l of the recoil on the plane of the emulsion surface could be measured directly by the graticule, and the difference of depth d in the emulsion, of the beginning and end of the recoil track could be estimated to better than 1μ. Knowing l, d, and the contraction factor of the emulsion σ, the angle of dip ϕ, of the recoil could be determined from the relation

$$\tan\phi = \sigma d/l.$$

If α is the angle which the incident neutron makes with the surface of the emulsion, the angle of recoil of the struck particle θ in the laboratory system is given by

$$\cos\theta = \cos\delta\cos\phi\cos\alpha + \sin\phi\sin\alpha.$$

The total length L of the recoil in the emulsion can be obtained from the relation $L^2 = l^2 + \sigma^2 d^2$. The range–energy relation for these emulsion has been measured by Lattes, Fowler and Cuer (1947). Using their results the energy of the recoil can be obtained.

At the centre of the plate the angle α was 15° to within about 0·5°, but corrections involving both α and δ had to be made at other points of the plate for changes in the direction of the incident neutrons. These corrections were small, however, because all the tracks measured lay within 1·5 cm. of the centre of the plate.

(iii) *Measurement of the Contraction Factor*

It is important to know accurately the ratio of the thickness of the emulsion before processing to its thickness after (contraction factor). Initially a measurement of this factor was made for the batch of plates used, by peeling off part of the emulsion of some of the plates before processing, and measuring its thickness with a micrometer. The thickness of the rest of the emulsion after processing was then measured by the microscope. The factor was found to be approximately 2·5 but the method was not very accurate. It was also feared that changes in the relative humidity might give rise to changes in the contraction factor after processing. Accordingly the method of continuously monitoring the contraction factor by means of the ThC′ alpha particles described above was adopted. The apparent angle of dip, β, of the alpha particles was measured each morning before commencing measurements of the recoils. If γ is the true angle at which the alpha particles enter the emulsion, the contraction factor is given by $\sigma = \tan\gamma / \tan\beta$. Small but real variations of σ were found from day to day; during the course of the measurements (about eight weeks) σ varied between 2·08 and 2·38.

(iv) *Determination of the Angular Distribution of n–p Recoils*

In order to test the method, over 1,000 proton recoils, produced by collisions of the d–d neutrons with protons present in the emulsion, were measured and their angular distribution determined. Only those proton recoils that began and ended in the emulsion were measured and a correction was applied for the loss of protons through the top and bottom of the emulsion. The correction factor for this loss, calculated along lines similar to those used by Powell and Occhialini (1946), varied from 1·66 for protons recoiling after a head-on collision to 1·07 for those recoiling at a large angle to the direction of the incident neutrons.

In the case of d–d neutrons the measurement of the proton recoils was also helpful in estimating the correction to be applied for the effect of neutrons not coming directly from the source. To enable this background correction to be made, all proton recoils beginning and ending in the emulsion were measured regardless of whether or not they would satisfy a range–angle criterion.

In most cases there was no difficulty in distinguishing between the beginning and the end of a proton recoil from the difference in the ionization density in the track. Many of the tracks also exhibited small angle scattering near the end of their range. Generally the start of the recoil was nearer the neutron source than the end but a few tracks were found in which the recoil appeared to be moving towards the source—evidently produced by neutrons not travelling directly from the source.

(v) *Determination of the Angular Distribution of the n–d Recoils*

The deuteron recoils from the heavy paraffin wax film were distinguished from proton recoils produced in the emulsion and leaving it through the surface by the fact that the deuteron recoils must be moving down into the emulsion and at the same time moving away from the source. Thus in Figure 2, if S is the position of the source, track A would be classed as a deuteron recoil while track B would be classed as a proton recoil originating in the emulsion and leaving through the surface. In a few cases this criterion would lead to the inclusion in the distribution of protons recoiling back towards the source after being struck by a neutron not proceeding straight from the source, but such events are comparatively rare. Moreover such recoils are almost certain to be excluded on application of the energy–angle criterion.

To reduce the labour of measurement and computation, recoils which would obviously lie far outside the allowable energy–angle criterion for the d–d neutrons were not measured. However, in deciding which tracks should be excluded a very liberal interpretation of the criterion was applied.

In spite of the criterion for distinguishing recoil deuterons from recoil protons, it is inevitable that some protons will find their way into the angular distribution. Thus protons that originate within 1μ of the top of the emulsion could hardly be distinguished from deuteron recoils entering from outside. For the d–d neutrons such protons can be distinguished from deuterons when the energy–angle recoil criterion is applied, if the recoil angle is not too large. At the larger recoil angles however, some protons are included in the angular distribution of the recoil deuterons and a correction has to be applied.

For the experiments with Ra–Be neutrons it was not possible to apply an energy–angle criterion to exclude recoils due to collision with protons near the surface of the emulsion. In this case the thicker film of heavy paraffin wax (12μ thick) was employed to reduce the proportion of such recoils. Owing to loss of energy of the recoil deuterons in this film before entering the emulsion the calculated energy of the incident neutron was subject to some uncertainty which became large for low-energy neutrons. The experiments with these neutrons could not be used to obtain information about the scattering of neutrons of energy less than 4 Mev. Even with a wax film of thickness 12μ, however, about 10% of the recoils included in the distribution may have been due to protons produced near the surface of the emulsion, and this must be remembered in interpreting the angular distributions obtained for the scattering of the Ra–Be neutrons.

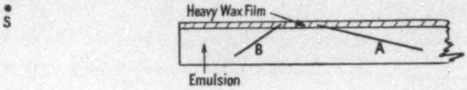

Figure 2.

Two thousand deuteron recoils were measured in the experiments with d–d neutrons and 1,200 in the experiments with Ra–Be neutrons.

(vi) *Accuracy of the Measurements*

The quantities measured with the microscope were l, d, δ. The projected length, l, of the track could certainly be determined to an accuracy of about $0{\cdot}5\mu$ by means of the graticule. The measurment of d, the difference of depth in the emulsion of the beginning and end of a recoil, involves two depth measurements, each of which may be determined to an accuracy of $0{\cdot}5\mu$, making an overall uncertainty in d of the order of 1μ. When this is multiplied by the contraction factor σ, the uncertainty in the overall depth determination becomes $2{\cdot}2\mu$, much the most important source of error in the measurements.

The error in measurement of δ is determined by the thickness of the track and the amount of small angle scattering of the track in the emulsion. The first 15μ of a track was usually available for measurement without serious error from scattering and this enabled the determination of δ to within 1·5° approximately. For tracks in which the projected length was less than 15 μ the errors in δ were correspondingly increased.

The actual energy E_n of the neutrons producing the recoil was obtained from the relation $E_d = (8/9)E_n \cos^2\theta$ where E_d is the energy of the recoil. At large recoil angles, θ, the accuracy of determination of both E_d and θ is diminished so that the accuracy of E_n decreases rapidly with increasing θ.

Table 1 shows how the mean error $\Delta_1 E_n/E_n$ in the determination of E_n, arising from errors in measurement of the recoils, increases with angle of recoil. This Table refers to the measurements with the d–d neutrons.

Table 1

$\cos\theta$	L	$\frac{\Delta L}{L}$	$\frac{\Delta E_\alpha}{E_\alpha}$	$\frac{\Delta \cos\theta}{\cos\theta}$	$\frac{\Delta\theta}{\theta}$	$\frac{\Delta_1 E_n}{E_n}$	$\frac{\Delta_2 E_n}{E_n}$	$\frac{\Delta E_n}{E_n}$
0·975	40	0·04	0·03	0·004	0·04	0·011	0·06	0·071
0·922	34	0·045	0·04	0·008	0·05	0·056	0·06	0·116
0·866	25	0·06	0·055	0·017	0·06	0·089	0·06	0·149
0·806	21	0·07	0·065	0·025	0·06	0·115	0·065	0·18
0·742	16	0·09	0·09	0·045	0·07	0·18	0·08	0·26
0·671	10·5	0·15	0·15	0·09	0·1	0·33	0·11	0·44

The errors listed here are mean errors for each value of θ. The actual fractional error for each value of θ varied according to the angle of dip, ϕ.

Another factor producing a further uncertainty in E_n arises from the finite thickness of the heavy paraffin wax film. At small angles of dip, ϕ, the uncertainty in range arising from this effect may be considerable. Accordingly only those tracks were accepted which satisfied a certain criterion with regard to ϕ. For the d–d neutrons the criterion used was as follows: For values of $\theta < 20°$, only tracks were accepted for which $\phi > 5°$. For values of $\theta > 20°$, only tracks were accepted for which $\phi > \frac{1}{4}\theta$. The average fractional error, $\Delta_2 E_n/E_n$, in E_n arising from loss of energy in the paraffin wax is given in column 8 of Table 1, and the total mean fractional uncertainty in the determination of E_n in the last column.

The fractional errors in E_n are large at large recoil angles, particularly when it is remembered that the maximum errors for individual tracks may be considerably larger than the mean errors given in Table 1. One would therefore expect that the range–angle criterion for distinguishing protons and deuterons would not be a very rigid one at large recoil angles and that there would be a considerable overlap in the proton and deuteron distributions at these angles. The errors in the determination of $\cos\theta$ however are much smaller than for E_n, so that one might expect the angular distribution of the recoil particles to be significant for the d–d neutrons out to an angle of recoil of 45°, corresponding to an angle of scattering of 90° of the neutron in the centre of mass system.

For the Ra–Be neutrons the discriminating criterion used for the angle ϕ was as follows: For values of $\theta < 15°$ only tracks were accepted for which $\phi > 15°$. For values of $\theta > 15°$, only tracks were accepted for which $\phi > \theta$. The application of a discriminating criterion is not so important in this case because the recoil range–angle criterion was not relied upon to distinguish between proton and deuteron recoils or to exclude neutrons which had not come straight from the source.

§ 3. RESULTS OF THE MEASUREMENTS WITH d–d NEUTRONS

(i) *n–p Collisions*

The 1,000 recoil protons were sorted out into groups according to their angle of recoil. If Θ is the angle of recoil in the centre-of-mass system, $\Theta = 2\theta$ where θ is the angle of recoil in the laboratory system. The angle of scattering of the neutron in the centre-of-mass system is then $\pi - \Theta$. Intervals in $\cos\Theta$ of 0·2 were taken in the grouping process. The number of proton recoils in any such interval should then be proportional to the differential cross section for scattering of the neutron through the angle $\pi - \Theta$ where Θ refers to the middle of the interval.

Figure 3 (*a*) and (*b*) shows the measured distribution in energy of the neutrons in two intervals of $\cos\Theta$, viz., 1·0 to 0·8 and 0·2 to 0 respectively. The histogram of Figure 3 (*a*) exhibits a fairly sharp energy maximum corresponding to a neutron energy a little less than 2·9 Mev. The observed energy spread could be accounted for by the inaccuracy of the measurement of the length of the tracks and the distribution of energy to be expected owing to the use of a 'thick' target in the generator. The histogram of Figure 3 (*b*) on the other hand indicates the way in which the energy distribution spreads out at large recoil angles owing to the increasing inaccuracy of the energy determination.

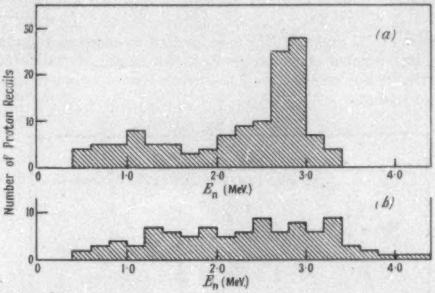

Figure 3. Apparent energy distribution of incident neutrons deduced from the energy of proton recoils for two ranges of $\cos\Theta$

(*a*) 1·0 to 0·8, (*b*) 0·2 to 0;

E_n is the incident neutron energy deduced from the energy–angle relation for the proton recoils.

The background in these curves arises from neutrons which have not travelled directly from the target to the photographic plate. The correction for this background was determined in the following way: For any given interval of $\cos\Theta$ the energy range containing neutrons coming directly from the source was found by inspection of the energy distribution curve. The number of recoils lying outside this range was determined and the mean number of background neutrons per unit energy range calculated. This was assumed also to give the background in the region of the distribution maximum. This procedure seemed to be justified since the background appeared reasonably constant outside the region of the maximum of the distribution.

It might have been thought that the background would introduce very serious error at large scattering angles where the maximum is so broad, but fortunately in this region the total background remains almost constant and, as it is now spread over a much larger range of apparent neutron energy, the background per unit energy range is correspondingly diminished.

Table 2 shows the results of the determination of the n–p scattering distribution.

Table 2

(1)	(2)	(3)	(4)	(5)	(6)
1·0 to 0·8	2·0 to 3·4	90	30	60	100 ± 9·2
0·8 to 0·6	2·0 to 3·4	83	28	55	90 ± 8·3
0·6 to 0·4	1·8 to 3·6	83	29	54	87 ± 8·7
0·4 to 0·2	1·6 to 3·6	82	25	57	87 ± 8·7
0·2 to 0	1·2 to 3·6	77	16	61	87 ± 8·7
0 to −0·2	1·0 to 4·0	86	15	71	93 ± 8·9
−0·2 to −0·4	1·0 to 4·0	63	12	51	61 ± 7·5
−0·4 to −0·6	1·0 to 4·0	36	15	21	23 ± 4·7

(1) interval of cos θ; (2) range of E_n corresponding to neutrons travelling direct from source (MEV.); (3) total number of proton recoils in the range; (4) background correction; (5) number of recoils from neutrons travelling directly from source; (6) number of recoils allowing for loss correction.

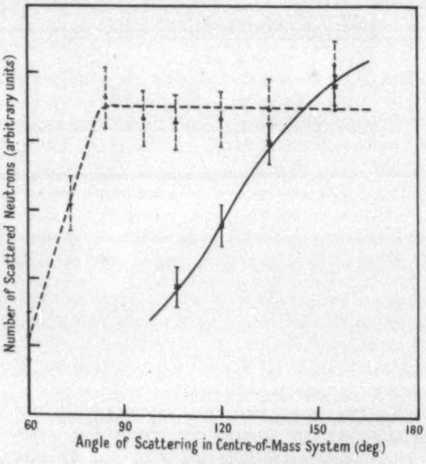

Figure 4. Comparison of angular distributions observed for n–p and n–d scattering for neutrons of 2·6–3·1 MEV. energy.

- - - - - n–p ———— n–d

The final column of Table 2 is obtained by allowing for the proton loss correction which takes account of the protons that pass out of the emulsion (see §2 (iv)). The figures in this column should be proportional to the differential cross section for scattering through the angle $\pi - \Theta$. They are plotted against Θ in Figure 4. It is seen that to within the limits of error of the measurement this cross section is constant for all angles up to $\Theta = 100°$. For larger angles the cross section falls away, evidently due to the increasing difficulty of observing the shorter recoils.

(ii) *n–d Collisions*

The 2,000 recoil deuterons were similarly sorted out according to their angle of recoil using intervals 0·2 of $\cos\Theta$. Figure 5 (*a*) and (*b*) shows the measured distribution in energy of the neutrons in two intervals of $\cos\Theta$, 1·0 to 0·8 and 0 to −0·2. To obtain these curves the energy–range relation appropriate for deuterons in the emulsion was used to determine the energy of the recoils and thence the supposed energy of the neutrons producing them. Two peaks are discernible in each of these curves, the peak at lower energy being attributable to deuteron recoils from the heavy paraffin wax film.* The peak at higher energy arises from proton recoils produced near the top of the emulsion. The proton peaks in these curves are not strictly comparable with each other because tracks were rejected during the course of the measurements if they would obviously fail to satisfy the range–angle criterion appropriate for deuteron recoils. Since it was easier to apply the criterion in the case of almost head-on collisions, fewer protons were included in the distribution for such collisions. This undoubtedly accounts for the maximum of the proton distribution occurring for too low an energy in Figure 5 (*a*). In Figure 5 (*b*) the maximum in the distribution occurs not far from its expected position (4·0 Mev.), indicating that in the angular range of this curve a much greater proportion of the protons was being included.

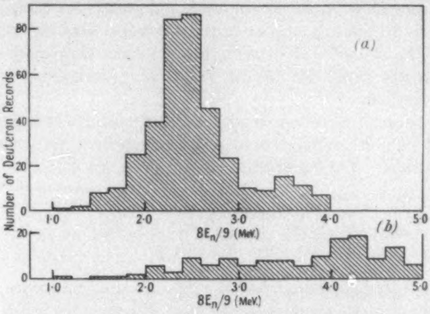

Figure 5. Apparent energy distribution of incident neutrons deduced from the energy of deuteron recoils for two ranges of $\cos\Theta$
(*a*) 1·0 to 0·8, (*b*) 0 to −0·2.

Corrections had to be applied to the deuteron distributions for the effect of neutrons not coming directly from the source ('background' correction), the overlap of the proton and deuteron distributions, and the loss of deuterons due to the fact that the percentage of recoils that enter the emulsion and satisfy the angle-of-dip criterion decreases with increase of the angle of recoil.

---

* In Figure 5 (*a*) and (*b*) the abscissae are (8/9) E_n, not E_n. This method of showing the results was used to avoid the necessity of multiplying each of the calculated neutron energies by 9/8.

(*a*) *Correction for background.* Owing to the existence of the proton peak on the high energy side of the deuteron distribution it was difficult to estimate the background correction by the method used in the proton case. For the smaller recoil angles ($\cos\Theta > 0{\cdot}4$) the proton and deuteron peaks were separated sufficiently well to enable an estimate of the background correction. The correction was consistent with that deduced from the proton recoil experiments. For larger recoil angles the background correction was estimated on the assumption that the total number of deuteron recoils due to the background in each interval 0·2 of $\cos\Theta$ was constant. This was approximately the case for the proton recoils.

(*b*) *The proton 'overlap' correction.* Owing to the finite depth of focus of the microscope objective it was inevitable that some protons originating near the surface of the emulsion would be included in the deuteron recoil distribution. Experience showed that recoils originating within about 1μ of the surface of the emulsion after processing could not be distinguished from those entering from outside, but recoils originating deeper in the emulsion than this could readily be distinguished. The number of proton recoils originating in this depth could be calculated directly from the proton recoil measurements, thus enabling a correction to be applied.

The accuracy of this correction depends directly on the estimate of the depth of emulsion from which protons could originate and still be counted as recoils entering from outside. We believe the correction is not likely to be in error by more than 25 per cent.

Having estimated the total number of proton recoils in the deuteron distributions the number overlapping the deuteron distribution at any given angle was obtained from the shape of the proton recoil distribution curves of § 3 (i).

(*c*) *The deuteron loss correction factor.* Since some deuterons recoiling at a certain angle either do not enter the emulsion at all or enter it at too small an angle of dip and are excluded by the dip angle criterion, a deuteron loss correction has to be calculated for each range of recoil angles. For an angle of recoil θ the fraction lost is given by ψ/π where $\cos\psi = (\sin\alpha\cos\theta - \sin\phi)/\cos\alpha\sin\theta$, and ϕ is the minimum angle of dip for which tracks of recoil angle θ are accepted. As before, α is the glancing angle of incidence of the neutrons on the surface of the emulsion.

Table 3 shows the results of the present measurements and the size of the various corrections. As before $\Theta = 2\theta$ is the recoil angle in the centre-of-mass system so that $\pi - \Theta$ is the scattering angle of the neutron in that system.

Table 3

(1)	(2)	(3)	(4) (*a*)	(5) (*b*)	(6)	(7) (*c*)	(8)
1·0 to 0·8	1·8 to 3·0	312	54	2	256	1·15	295 ± 16
0·8 to 0·6	1·8 to 3·4	224	66	5	153	1·58	241 ± 20
0·6 to 0·4	1·8 to 3·2	155	49	12	94	1·77	167 ± 19
0·4 to 0·2	2·2 to 3·6	122	42	17	63	1·88	118 ± 19
0·2 to 0	1·8 to 3·2	50	35	11	[4]	2	[8] ± 14

(1) range of $\cos\Theta$; (2) range of energy in deuteron distribution (MEV.); (3) total number of tracks; (4) background correction; (5) proton overlap correction; (6) corrected number of tracks; (7) deuteron loss factor; (8) total number of deuteron recoils.

Figure 4 shows the results of Table 3 for the differential cross section for n–d scattering plotted against the angle of scattering in the centre-of-mass system.

§4. RESULTS OF THE MEASUREMENTS OF n–d COLLISIONS USING Ra–Be NEUTRONS

Table 4 shows the results of the measurements with the Ra–Be neutrons. They were separated into two energy ranges, viz. (i) 4–6 Mev., and (ii) 6–9 Mev. The table shows the angular distribution, with the number of neutrons scattered in the interval of $\cos\Theta$ from 1·0 to 0·8 normalized to 1. The distribution (i) was obtained from the measurement of 400 tracks while 190 tracks were included in distribution (ii). For comparison the results of the measurements with the d–d neutrons in the energy range 2·6 to 3·1 Mev. are also included in Table 4.

Table 4. Number of Scattered Neutrons

Energy of incident neutrons	(i) 4 to 6 Mev.	(ii) 6 to 9 Mev.	(iii) 2·6 to 3·1 Mev.
Range of $\cos\Theta$			
1·0 to 0·8	1	1	1
0·8 to 0·6	0·52 ± 0·08	0·30 ± 0·06	0·81 ± 0·08
0·6 to 0·4	0·37 ± 0·06	0·32 ± 0·08	0·56 ± 0·09
0·4 to 0·2	0·46 ± 0·065	0·48 ± 0·11	0·40 ± 0·08
0·2 to 0	0·34 ± 0·06	0·39 ± 0·10	—
0 to −0·2	0·39 ± 0·07	0·44 ± 0·11	—
−0·2 to −0·4	0·27 ± 0·06	0·34 ± 0·11	—
−0·4 to −0·6	—	0·51 ± 0·14	—

Since the energy–angle criterion could not be applied to eliminate proton recoils produced near the top of the emulsion when using neutrons from the Ra–Be source the distributions (i) and (ii) contain some tracks due to proton collisions. The proportion of such tracks was reduced as much as possible by increasing the thickness of the heavy wax film, but under the conditions of the experiment it was estimated that about 10 per cent of tracks measured were due to protons. The effect of these is to make the proportion of recoils in the larger ranges of Θ too great.

Correction for neutrons not coming from the source was unnecessary for the Ra–Be neutrons owing to the absence of scattering material (see §2(i)). A 'deuteron loss' correction corresponding to the appropriate criterion for the dip angle ϕ had, however, to be applied to these results.

§5. DISCUSSION OF RESULTS AND COMPARISON WITH THEORY

It is clear that the angular distribution for n–d scattering is qualitatively different from that for n–p scattering. In Figure 6 are plotted the angular distributions calculated by Buckingham and Massey (1941) for collisions of neutrons of energy about 2 Mev. with deuterons, on the assumptions of exchange and ordinary forces respectively. They are compared with the present results and with those of Coon and Barschall (1946) and of Darby and Swan (1948) for d–d neutrons. The angular distribution measurements are relative and have to be fitted to the theoretical distribution arbitrarily at some point. Since the measurements for angles of scattering near 180° are most accurate, it is best to fit the distributions there.

For angles of scattering between 120° and 180° the three experimental determinations agree within limits of experimental error and follow rather more closely the theoretical curve for ordinary forces than that for exchange forces although the two theoretical curves are not sufficiently separated in this region to enable a definite decision on this point. For angles of scattering less than 120°, however, the curve of Coon and Barschall (1946) lies considerably above that of Darby and Swan (1948).

Unfortunately, as is clear from Table 3, the photographic method, for neutrons of energy as low as 2–3 Mev., becomes very inaccurate for angles of scattering less than 120° on account of the shortness of the recoils, which causes a large spread in the energy distribution, and makes the correction for 'background' neutrons and proton overlap very large. Since the two theoretical curves of Buckingham and Massey (1941) differ most in the range of scattering angles from 60° to 120° it is important to study particularly the form of the distribution in this region, but the photographic method does not appear appropriate for this purpose.

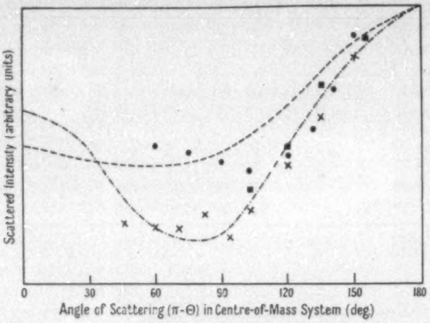

Figure 6. Comparison of experimental and theoretical angular distribution for d–d neutrons scattered by deuterons.

— — — — theoretical curve for exchange interaction (Buckingham and Massey).
—·—·—·— theoretical curve for ordinary forces.
● Coon and Barschall × Darby and Swan ■ Authors

For faster neutrons it is clear from Table 4 that the photographic plate method is applicable over a larger range of scattering angle. The calculations of Buckingham and Massey would lead one to expect the ratio of the differential cross section for scattering at 90° to that at 180° to increase with increase of neutron energy. The results shown in Table 4 do not provide evidence in support of this. In fact the tendency exhibited in this Table suggests a steeper angular distribution of the scattered neutrons for scattering angles near 180° at higher neutron energy.

The ratio of the differential cross section at 90° to that at 180° appears to be between 0·35–0·40 for both ranges of neutron energy but the limits of error are rather large. Recent measurements of Coon and Taschek (1949) using 14 Mev. neutrons give about 0·25 for this ratio.

ACKNOWLEDGMENTS

We are indebted to Professor S. Sugden of the Chemistry Department of this College for allowing us to use his neutron generator for these experiments, to Dr. L. H. Gray of the Hammersmith Hospital M.R.C. Radiotherapeutic unit for the loan of the Ra–Be neutron source, to the Atomic Energy Research Establishment, Harwell, for making available a small amount of heavy paraffin wax, to Professor

C. F. Powell of Bristol for helpful suggestions about the use of the photographic technique for scattering problems, and in particular for suggesting the method of continuously monitoring the contraction factor by means of alpha particles, and to Professor H. S. W. Massey for many useful discussions.

The research was supported in part by the award of a Special Development Grant by the Department of Scientific and Industrial Research. One of us (S.L.M.) wishes to thank the Council of the Melbourne Technical College, Australia, for granting him leave of absence and the financial assistance which enabled him to take part in this research.

REFERENCES

Barschall, H. H., and Kanner, M. H., 1940, *Phys. Rev.*, **58**, 590.
Buckingham, R. A., and Massey, H. S. W., 1941, *Proc. Roy. Soc.* A, **179**, 123.
Coon, J. H., and Barschall, H. H., 1946, *Phys. Rev.*, **70**, 592.
Coon, J. H., and Taschek, R. F., 1949, *Phys. Rev.*, **76**, 710.
Darby, J. F., and Swan, J. B., 1948, *Aust. J. Sci. Res.* A, **1**, 18.
Guggenheimer, K. M., Heitler, H., and Powell, C. F., 1947, *Proc. Roy. Soc.* A, **190**, 196.
Heitler, H., May, A. N., and Powell, C. F., 1947, *Proc. Roy. Soc.* A, **190**, 180.
Kruger, P. G., Shoupp, W. E., Watson, W. E., and Stallmann, F. W., 1938, *Phys. Rev.*, **53**, 1014.
Lattes, C. M. G., Fowler, P. H., and Cuer, P., 1947, *Nature, Lond.*, **159**, 301.
May, A. N., and Powell, C. F., 1947, *Proc. Roy. Soc.* A, **190**, 170.
Powell, C. F., and Occhialini, G. P. S., 1946, *Report of Cambridge Conference on Fundamental Particles* (London : Physical Society), p. 150.

DISCUSSION

Dr. R. A. Buckingham (*communicated*). The authors have made a comparison between their results and the theoretical calculations made some years ago by Professor Massey and myself. It happens that these calculations are being extended at the moment (mainly by Mr. J. Hubbard, of University College), and some of the results already obtained are very relevant to the work of Dr. Burhop and his colleagues. The theoretical angular distributions quoted by them were based on collisions involving 0 and 1 unit of relative angular momentum only, collisions involving more than this being neglected. At the time this was thought to be a fairly adequate approximation for the energies considered, and in one sense it is, as we find now that collisions involving 2 units of angular momentum do not contribute more than 4% to the total elastic cross section at 4 Mev., nor more than 10% at 11 Mev. The angular distributions are, however, appreciably affected even at 3–4 Mev., the effect being to enhance backward scattering at the expense of forward scattering of neutrons. At 4 Mev., for instance, the ratio of neutrons scattered at 180° (in the centre of mass system) to those at 90°, calculated for *exchange* forces, is reduced from about 0·5 to 0·3, and this latter value agrees much better with observations by the authors of this paper and by others, I think we may find that the improved calculations make exchange and ordinary forces less easy to distinguish on the evidence of angular distributions alone; but, as the evidence from the total cross section tends to favour exchange forces strongly, the existing experimental results as a whole point decisively to exchange forces.

Schwinger Potential in Nuclear Forces

By F. C. BARKER
Department of Mathematical Physics, The University, Birmingham

Communicated by R. E. Peierls; MS. received 5th January 1950

ABSTRACT. The properties of the potential derived from the mixed pseudoscalar–vector meson field are investigated and compared with the experimental data on the two-nucleon system. An attempt has been made to use methods which are more accurate than those formerly applied to this problem, and some of these may be useful in calculations with other potentials. It is found that agreement with experiment cannot be obtained for any choice of meson masses and coupling constants.

---

§ 1. INTRODUCTION

A meson potential has been suggested by Schwinger (1942), in which pseudoscalar and vector meson fields are combined in such a way that the inadmissible singularities in the non-central part of the interactions cancel. In the present paper this potential is investigated to see how far it can be made to give agreement with the existing experimental data on the two-nucleon system. This problem has been considered previously (Jauch and Hu 1944, Ramsey 1948, Wu and Foley 1949), but in each case the methods used do not seem to have been entirely adequate.

The static Schwinger potential contains four arbitrary parameters—the masses of the two mesons and two coupling constants. Certain experimental data are used for fixing these parameters, and the potential is then tested by the accuracy with which its predictions of other quantities agree with experiment. The experimental values of the relevant quantities are here taken as:

(*a*) singlet scattering length at zero energy (Bethe 1949)	$a_s = -(23{\cdot}75 \pm 0{\cdot}11) \times 10^{-13}$ cm.
(*b*) binding energy of the deuteron (Bethe 1949)	$E_0 = (2{\cdot}21 \pm 0{\cdot}02)$ Mev.
(*c*) quadrupole moment of the deuteron (Kellog *et al.* 1940, Nordsieck 1940)	$Q = (2{\cdot}73 \pm 0{\cdot}05) \times 10^{-27}$ cm^2
(*d*) proportion of D state in the deuteron (Millman and Kusch 1941, Arnold and Roberts 1947)	$P_D = (4 \pm 2)\%$
(*e*) triplet scattering length at zero energy (Bethe 1949)	$a_t = (5{\cdot}28 \pm 0{\cdot}11) \times 10^{-13}$ cm.
(*f*) singlet effective range: neutron–proton (Christian and Hart 1950),	$r_s < 3 \times 10^{-13}$ cm.
proton–proton (Bethe 1949)	$r_s = (2{\cdot}71 \pm 0{\cdot}13) \times 10^{-13}$ cm.
(*g*) total cross section for neutron–proton scattering at 100 Mev. (Hadley *et al.* 1949)	$\sigma = (6{\cdot}8 \pm 0{\cdot}7) \times 10^{-26}$ cm^2
anisotropy ratio for neutron–proton scattering at 100 Mev. (Hadley *et al.* 1949)	$\Gamma = \dfrac{d\sigma(\pi)}{d\sigma(\pi/2)} = 3{\cdot}5 \pm 1$

The wave equation describing the relative motion in the neutron-proton system is

$$\frac{\hbar^2}{M}\nabla^2\psi+(E-V)\psi=0,$$

where M is the nuclear mass (twice the reduced mass of the system) and E is the energy of relative motion. For the Schwinger potential, with a symmetrical mixture of charged and neutral mesons,

$$V=(\tau_1\,.\,\tau_2)\left[g_1{}^2\frac{e^{-\lambda r}}{r}+\frac{1}{3}\left(\frac{g_2}{\lambda}\right)^2\left\{J(r)(\sigma_1\,.\,\sigma_2)+K(r)S_{12}\right\}\right], \qquad \ldots\ldots(1)$$

where

$$J(r)=\kappa^2\frac{e^{-\kappa r}}{r}+2\lambda^2\frac{e^{-\lambda r}}{r},$$

$$K(r)=\left(\kappa^2+\frac{3\kappa}{r}+\frac{3}{r^2}\right)\frac{e^{-\kappa r}}{r}-\left(\lambda^2+\frac{3\lambda}{r}+\frac{3}{r^2}\right)\frac{e^{-\lambda r}}{r},$$

$$S_{12}=\frac{3(\sigma_1\,.\,r)(\sigma_2\,.\,r)}{r^2}-(\sigma_1\,.\,\sigma_2).$$

Here τ, σ are the isotopic spin and spin vectors for the nucleons and r their separation, $\kappa\hbar/c$, $\lambda\hbar/c$ are the masses of the pseudoscalar and vector mesons respectively, and $g_1{}^2/\hbar c$, $g_2{}^2/\hbar c$ are dimensionless coupling constants. The range κ^{-1} corresponding to the pseudoscalar meson mass is taken as unit of length, and $\hbar^2\kappa^2/M$ as unit of energy; then we use the dimensionless variables

$$x=\kappa r, \qquad k^2=ME/\hbar^2\kappa^2, \qquad \delta=\lambda/\kappa,$$

and differentiation with respect to x is denoted by a prime. In order to get a positive quadrupole moment, δ must be taken greater than 1.

§ 2. METHODS

(i) *Singlet State*

At zero energy, the singlet scattering length is defined by the radial wave function $u_s{}^0$ for the singlet S state, which satisfies

$$u_s{}^{0\prime\prime}=\alpha_s\left[\frac{e^{-x}}{x}+\gamma_s\frac{e^{-\delta x}}{x}\right]u_s{}^0, \qquad u_s{}^0\sim 1-x/\kappa a_s, \qquad \ldots\ldots(2)$$

where

$$\left.\begin{aligned}\alpha_s&=-\frac{Mc}{\kappa\hbar}\frac{g_2{}^2}{\hbar c}\frac{1}{\delta^2},\\ \gamma_s&=(2-g_1{}^2/g_2{}^2)\delta^2.\end{aligned}\right\} \qquad \ldots\ldots(3)$$

For a given pair of meson masses, the requirement that a_s should have the correct value provides a relation between α_s and γ_s, and hence between $g_1{}^2/\hbar c$ and $g_2{}^2/\hbar c$.

The equation (2) has been solved by an iteration method, starting from a suitable initial function $u_1(x)$ and defining successive functions $u_{n+1}(x)$ by

$$u_{n+1}{}''(x)=-\left[\frac{e^{-x}}{x}+\gamma_s\frac{e^{-\delta x}}{x}\right]u_n(x),$$

$$u_{n+1}(0)=0, \qquad u_{n+1}(x)\sim 1-x/\kappa a_s.$$

Since the scattering length a_s is negative, the wave function corresponding to the lowest eigenvalue α_s is nodeless. If we start from $u_1(x) \equiv x$, then all the $u_n(x)$ are nodeless and upper and lower limits can be given for α_s (Thomas 1937):

$$U_{n,\,n+1} \geqslant \alpha_s \geqslant L_{n,\,n+1},$$

where

$$U_{n,\,n+1} = \left[\int_0^\infty u_1 u_n''\,dx\right] \Big/ \left[\int_0^\infty u_1 u_{n+1}''\,dx\right], \qquad L_{n,\,n+1} = (u_n''/u_{n+1}'')_{\min}.$$

As $n \to \infty$, $U_{n,\,n+1}$ and $L_{n,\,n+1}$ converge to α_s. The expressions for these upper and lower limits increase rapidly in complexity as n increases, so only the first two or three of each have been calculated, and from these the eigenvalue α_s can be obtained with sufficient accuracy.

By using the definitions (3) it is found that for a given pair of masses, the relation between $g_1^2/\hbar c$ and $g_2^2/\hbar c$ is almost linear. (For $g_1^2/\hbar c \simeq 0$, which is the interesting region, the straight line obtained by joining the end points corresponding to $\gamma_s = 0, \infty$ gives values of $g_2^2/\hbar c$ less than the correct values by about 1 or 2%, depending on the masses concerned.) Although no explanation of this linearity property has been obtained, it has been found to hold for a large range of meson masses and for both real and virtual states, so that it seems safe to assume it in general. As the two cases $\gamma_s = 0, \infty$ correspond to single meson potentials for which the depth of the potential is known as a function of the meson mass, the end points are readily determined for any given pair of masses (see Appendix 1).

(ii) *Ground State of the Deuteron*

The ground state of the deuteron is the triplet state with $J = 1$ and even parity, for which the tensor interaction gives a coupling between the S and D state radial wave functions. Hence it is necessary to solve the pair of coupled differential equations

$$\left.\begin{aligned} u'' - \epsilon^2 u &= \alpha_t[f(x)u + 2^{3/2}g(x)w], \\ w'' - \frac{6}{x^2}w - \epsilon^2 w &= \alpha_t[2^{3/2}g(x)u + \{f(x) - 2g(x)\}w], \end{aligned}\right\} \quad \ldots\ldots(4)$$

where

$$\epsilon^2 = ME_0/\hbar^2\kappa^2,$$

$$\left.\begin{aligned} f(x) &= \frac{e^{-x}}{x} + \gamma_t\frac{e^{-\delta x}}{x}, \\ g(x) &= \left(1 + \frac{3}{x} + \frac{3}{x^2}\right)\frac{e^{-x}}{x} - \left(\delta^2 + \frac{3\delta}{x} + \frac{3}{x^2}\right)\frac{e^{-\delta x}}{x}, \end{aligned}\right\} \quad \ldots\ldots(5)$$

$$\left.\begin{aligned} \alpha_t &= -\frac{Mc}{\kappa\hbar}\frac{g_2^2}{\hbar c}\frac{1}{\delta^2}, \\ \gamma_t &= (2 + 3g_1^2/g_2^2)\delta^2, \end{aligned}\right\} \quad \ldots\ldots(6)$$

and u, w are the S, D state radial wave functions respectively. Various approximate methods are available for solving these equations, but none of those previously used (Jauch and Hu 1944, Wu and Foley 1949) seems sufficiently accurate (see Appendix 2), so we have integrated the equations numerically. This involves a trial and error determination of the eigenvalue α_t for a given γ_t, so that it is important to choose the initial trial value of α_t as accurately as possible.

Now for a given pair of masses, it is to be expected that the relation between $g_1^2/\hbar c$ and $g_2^2/\hbar c$ which yields the correct binding energy will be similar to the relation giving the correct value of the triplet scattering length, and, by a method similar to that used in the singlet scattering case, it is found that the latter relation is almost linear (when tensor forces are neglected). Thus we assume that the values of $g_1^2/\hbar c$, $g_2^2/\hbar c$ for the central potential giving E_0 correctly also satisfy a linear relation, and again the end points corresponding to $\gamma_t = 0, \infty$ are given by a simple formula holding for the single meson potential (Appendix 1). (From the results of some numerical integrations, it is found that this method gives values of $g_2^2/\hbar c$ which are about 1% too large, for $g_1^2/\hbar c \simeq 0$.) This triplet straight line cuts the one for the singlet state at a small positive value of $g_1^2/\hbar c$. Since the tensor interaction tends to increase the binding in the triplet state, the triplet $g_1^2/\hbar c - g_2^2/\hbar c$ curve for the tensor force case cuts the singlet line at an even smaller value of $g_1^2/\hbar c$. In most of the calculations, $g_1^2/\hbar c$ is first taken to be zero; the effect of introducing a non-zero value of $g_1^2/\hbar c$ is then readily obtained. The trial value to be taken for α_t in the equation (4) an be estimated from the triplet straight line, allowing for the effect of the tensor force.

Starting with the series solutions valid near the origin and near infinity, the equations (4) are integrated outwards and inwards respectively using the common numerical methods, and the solutions are fitted together at a suitable intermediate point, here taken as $x = 2$. The smoothness with which such a fit is possible provides the criterion by which the eigenvalue α_t may be approached. Usually two or three trials are necessary in order to determine the eigenvalue and accompanying eigenfunctions with the required accuracy (eigenvalue correct to, say, 1%).

The values of $g_2^2/\hbar c$ and the wave functions u, w corresponding to $g_1^2/\hbar c = 0$ are thus obtained. The change in $g_2^2/\hbar c$ caused by introducing a small non-zero value of $g_1^2/\hbar c$ is easily obtained from the equation (4), using (5), (6):

$$\left[\frac{dg_2^2}{dg_1^2}\right]_{g_1^2\hbar c=0} = -3\delta^2 \frac{\displaystyle\int_0^\infty \frac{e^{-\delta x}}{x}(u^2+w^2)\,dx}{\displaystyle\int_0^\infty [fu^2 + 2^{5/2}guw + (f-2g)w^2]\,dx},$$

where the integrals may be evaluated numerically. From this value of the slope and from the singlet straight line, the unique values of $g_1^2/\hbar c$, $g_2^2/\hbar c$ which satisfy the data (*a*), (*b*) for a given pair of masses are approximately determined. These values can be improved by numerical iteration (Hu and Massey 1949).

The quadrupole moment of the ground state of the deuteron is

$$Q = \frac{2^{1/2}}{10\kappa^2} \frac{\displaystyle\int_0^\infty x^2(uw - 2^{-3/2}w^2)\,dx}{\displaystyle\int_0^\infty (w^2+u^2)\,dx}. \qquad \ldots\ldots(7)$$

Q is zero when the tensor force vanishes, as is the case for $\delta = 1$; also for very large δ the main part of the potential, given in (5), has the very small range $(\delta\kappa)^{-1}$, and Q vanishes as δ^{-1} (Schwinger 1941). Thus for a fixed value of the lower mass, Q reaches a maximum at some finite value of δ.

The integrals in (7) have been evaluated numerically to give Q, using the wave functions u, w obtained for $g_1^2/\hbar c=0$. With a positive value of $g_1^2/\hbar c$, as is required if a_s is to be fitted in addition to E_0, it is clear from (5), (6) that a smaller value of Q is obtained for the same pair of meson masses.

Depending on whether the maximum value of Q lies above or below the experimental value, it is or is not possible to fit all the data (*a*), (*b*), (*c*) with a given lower mass. Now the effect of decreasing both masses by a factor χ^{-1}, keeping the mass ratio constant, is to increase Q by a factor somewhat less than χ^2. This is the case since the wave equations (4) depend on the absolute meson masses (as distinct from their ratio) only in the terms involving ϵ^2, and an increase in ϵ^2 causes u, w to be reduced at large distances relative to their values near the maxima, so that from (7) it can be seen that Q increases less rapidly than κ^{-2}. Thus for large meson masses, it is not possible to get agreement with the experimental data (*a*), (*b*), (*c*); for small masses it is possible with suitable choice of the mass ratio.

Calculations of P_{D}, the proportion of D state in the deuteron ground state, are closely connected with those of Q. The formula giving P_{D} in terms of the wave functions u and w is

$$P_{\mathrm{D}}=\frac{\int_0^\infty w^2\,dx}{\int_0^\infty (u^2+w^2)\,dx}.$$

P_{D} vanishes as $(\delta-1)^2$ for δ near 1, and as δ^{-2} for large δ. As the effect of a change of ϵ^2 in (4) is more or less to change u and w in the same way, it follows that P_{D} is roughly independent of the absolute values of the meson masses.

(iii) *Zero Energy Triplet State*

The calculation of the triplet scattering length taking into account the tensor coupling between S and D states would be very difficult. However, the potential including tensor force can be replaced by a central potential which gives the same binding energy of the deuteron with an error in the scattering length of the order of 1%, which is less than the experimental error. This can be seen from the formulae expressing the scattering length in terms of the binding energy for the central and tensor force cases (Chew and Goldberger 1949, Christian 1949),

$$\left(\frac{1}{\kappa a_{\mathrm{t}}}\right)_{\mathrm{central}}=-\epsilon+\epsilon^2\sum_{n=0}^{\infty}(-1)^n W_n{}^0\epsilon^{2n},$$

$$\left(\frac{1}{\kappa a_{\mathrm{t}}}\right)_{\mathrm{tensor}}=-\epsilon+\epsilon^2\sum_{n=0}^{\infty}(-1)^n W_n\epsilon^{2n},$$

where the ratio of W_n to $W_n{}^0$ differs from unity by a quantity of the order of P_{D} (Christian 1949). Further, the summations contribute only about 20% of the right hand sides.

Thus we consider the equation

$$u_{\mathrm{t}}''+k^2u_{\mathrm{t}}=\alpha_{\mathrm{t}}f(x)u_{\mathrm{t}}, \qquad \ldots\ldots(8)$$

with $f(x)$ given by (5). The values of α_{t} and γ_{t} are chosen for each pair of meson masses to give the right binding energy of the deuteron, and then the corresponding value of a_t is obtained by solving (8) with $k^2=0$ for the solution u_t^0 with asymptotic form

$$u_t^0 \sim 1 - x/\kappa a_t.$$

Numerical integration is again the most accurate method, both for obtaining the relation between α_t and ϵ, and for obtaining the value of a_t corresponding to a given α_t (see also Appendix 3).

(iv) *Singlet Effective Range*

If η_s is the singlet phase at energy k^2, then

$$k \cot \eta_s = -1/\kappa a_s + \tfrac{1}{2}\kappa r_s k^2 + \ldots, \qquad \ldots\ldots(9)$$

where r_s is the singlet effective range, given in terms of the zero energy singlet wave function u_s^0 by

$$\kappa r_s = 2\int_0^\infty [(1 - x/\kappa a_s)^2 - (u_s^0)^2]\, dx, \qquad u_s^0 \sim 1 - x/\kappa a_s.$$

Thus u_s^0 may be used for obtaining κa_s and κr_s, and thence κ^{-1} and r_s. An alternative method which was used here is due to Hulthén (1948)*. The wave function is written in the form

$$u_s(x) = \sin(kx + \eta_s) - y(x)\sin\eta_s, \qquad y(0)=1, \qquad y(\infty)=0,$$

and $y(x)$ is approximated to by a function depending on a number of parameters c_ν, which are determined together with the value of $\cot\eta_s$ by a variational method. Then κa_s, κr_s are given by (9). We have taken for $y(x)$ the function which Hulthén used for the meson potential :

$$y(x) = e^{-x} + (1 - e^{-x})\sum_{\nu=1}^{n} c_\nu e^{-\nu x}. \qquad \ldots\ldots(10)$$

By checking the results in a few cases using the wave function u_s^0 calculated by numerical integration, it is found to be sufficient to use only one parameter in $y(x)$ for the values of the ranges in which we are interested.

(v) *High Energy Scattering*

Numerical integration is used to obtain the total and differential cross sections for neutron–proton scattering at 100 MEV., for a particular set of coupling constants and meson masses which are chosen to fit low energy data. Born approximation is unreliable † except for determining the higher phases which are small. Phases up to $J=3$ are accurately determined for the coupled triplet states, to $J=4$ for the uncoupled triplet states and to $J=3$ for the singlet states. The integration is carried out to a distance $x=2{\cdot}5$, and the correction to the phases due to the potential outside this distance is calculated by use of a perturbation formula. The higher singlet phases are obtained by Born approximation. Then the differential and total cross sections are determined from these phases by the usual formulae (Hu and Massey 1949, Rohrlich and Eisenstein 1949).

---

* I wish to thank Dr. Hulthén for helpful correspondence regarding this method.

† Wu and Foley (1949) used Born approximation for the triplet state scattering, since for a square well it gives a fairly good value for the triplet cross section. However for a meson potential, Born approximation gives a very low value for the S phase.

§ 3. RESULTS

The experimental values of the singlet scattering length and the deuteron binding energy have been used to obtain the values of the coupling constants for various pairs of meson masses, and the results are given in the Table. The corresponding values of the quadrupole moment and proportion of D state are also tabulated.

For the lower meson mass equal to 300 *m*, and for $g_1^2/\hbar c=0$, the experimental value of Q is not reached for any value of δ, and for $g_1^2/\hbar c>0$, Q is still smaller. Even for the masses 150 *m*, 300 *m*, Q is only three-fourths of the experimental value, and for better agreement it would be necessary to take smaller values of one or both of these masses. This was not done as other quantities cannot be fitted with these small masses.

Results obtained by fitting Singlet Scattering Length and Binding Energy. $(g_2^2/\hbar c)_{\text{cent}}$ obtained by neglecting tensor force

Meson masses (unit electron mass)		$g_1^2/\hbar c=0$					$g_1^2/\hbar c$	$g_2^2/\hbar c$	Q/Q_{exp}	$P_{\text{D}}(\%)$
ps.	v.	$g_2^2/\hbar c$ (a_s fitted)	$(g_2^2/\hbar c)_{\text{cent}}$	$g_2^2/\hbar c$	Q/Q_{exp}	$P_{\text{D}}(\%)$	(a_s and E_0 fitted)			
			(E_0 fitted)							
300	300	0·085	0·127	0·127	0	0	0·030	0·096		
300	390	0·122	0·171	0·167	0·27	0·26	0·033	0·133		
300	600	0·212	0·271	0·255	0·39	0·92	0·031	0·224		
300	900	0·350	0·412	0·373	0·36	1·29	0·014	0·357		
300	1200	0·476	0·549	0·470	0·32	1·24	−0·003	0·474		
150	300	0·101	0·159	0·147	0·88	1·40	0·030	0·114	0·73	0·92

Values of the triplet scattering length a_t have been obtained from the central potential

$$\alpha_t\left(\frac{e^{-x}}{x}+2\delta^2\frac{e^{-\delta x}}{x}\right), \qquad \ldots\ldots(11)$$

corresponding to $g_1^2/\hbar c=0$, with α_t chosen to fit the deuteron binding energy. Curves of constant a_t value are shown as functions of the meson masses in the Figure.

Also plotted are curves on which the singlet effective range r_s is constant. r_s was calculated for the potential which gave the correct singlet scattering length, again with $g_1^2/\hbar c=0$, and hence cannot be directly compared with the value of a_t at the same point of the Figure.

In order to fit both E_0 and a_s, it is necessary to introduce a non-zero value of $g_1^2/\hbar c$, but it can be shown that this causes only small modifications in the values of a_t and r_s corresponding to a definite pair of meson masses. For the triplet potential, the introduction of a positive value of $g_1^2/\hbar c$ increases the proportion of the short range term, and so decreases the value of a_t (for $\kappa^{-1}\lesssim 2{\cdot}5\times10^{-13}$ cm.); this decrease can only be of the order of 1%, since a potential consisting of the short range term alone (corresponding to g_1^2/g_2^2 infinite) gives values of a_t at most 2% lower than those given by the mixed potential (11). Likewise for the singlet potential, increasing $g_1^2/\hbar c$ decreases the proportion of short range component and so increases the value of r_s, the percentage increase rising from zero at small κ^{-1} to about 2% at $\kappa^{-1}=2{\cdot}5\times10^{-13}$ cm. (for a_s, E_0 fitted and $\delta=2$).

Thus in using the Figure to obtain the values of a_t, r_s for a definite pair of masses and for a_s, E_0 fitted, corrections of the order of 1% should be applied, but these are insignificant in view of the experimental uncertainty in these quantities and also since an exact fit is not to be expected.

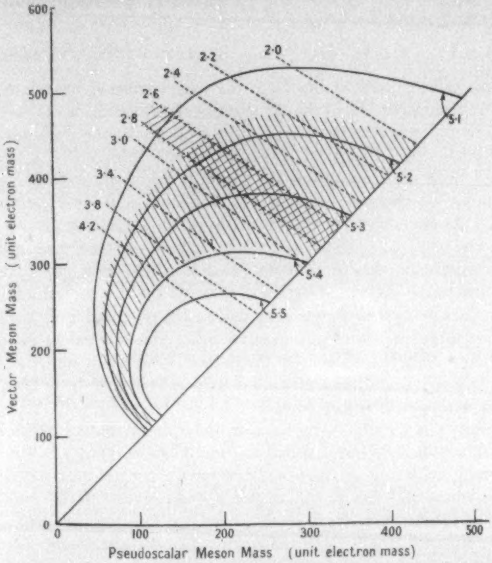

Triplet scattering length a_t and singlet effective range r_s as functions of meson masses, for approximate fitting of deuteron binding energy and singlet scattering length. Continuous curves: a_t constant (labelled in units 10^{-13} cm); broken curves: r_s constant (labelled in units 10^{-13} cm.). The hatched areas indicate the experimental values of a_t and r_s (proton–proton value).

The phases and cross sections for the scattering of 100 MeV. neutrons by protons have been calculated for the one set of potential constants which give reasonable agreement with some of the low energy data:

$$\kappa\hbar/mc=150, \quad \delta\kappa\hbar/mc=300, \quad g_1^2/\hbar c=0{\cdot}030, \quad g_2^2/\hbar c=0{\cdot}114.$$

The anisotropy ratios and total cross sections for the singlet, triplet and complete scattering are:

	Anisotropy ratio	Total cross section (10^{-26} cm^2)
singlet	81·6	13·6
triplet	8·0	10·5
complete	16·8	11·3

In the triplet scattering, higher phases have been neglected, so that the triplet and complete cross sections which are given are lower limits.

§ 4. DISCUSSION

With the symmetric static Schwinger potential it is impossible to get agreement with all the experimental data (*a*) – (*g*); even the low energy data cannot be fitted. If the masses and coupling constants in the potential are chosen to give E_0, a_s, a and Q correctly (this requires masses about 120 *m*, 290 *m*), then the values obtained for the remaining quantities are:

$$P_D \simeq 1\%, \quad r_s \simeq 4{\cdot}3 \times 10^{-13}\,\text{cm.}, \quad \sigma \simeq 11 \times 10^{-26}\,\text{cm}^2, \quad \Gamma \simeq 20.$$

Each of these differs considerably from the corresponding experimental value. The allowed variation of 2% in the value given in (*d*) for P_D is due to theoretical uncertainty in the contribution of relativistic effects to the deuteron magnetic moment (Sachs 1947, Primakoff 1947, Breit and Bloch 1947); since these contributions depend critically on the transformation properties of the meson field, we cannot say that the value of 1% obtained here for P_D disagrees with experiment. As the Schwinger potential is of the symmetric type, it is valid to compare the value of r_s which it predicts for the neutron–proton interaction with the accurately known experimental value for the proton–proton interaction. The theoretical value obtained here is too large, as are also the values of σ and Γ. By taking a more general exchange character of the potential, only slightly better agreement for these quantities can be obtained. Also low values for the masses such as are required here indicate that the potential cannot be regarded as derived from meson theory, since these mesons if they exist would have been observed in the cyclotron experiments at Berkeley.

Alternatively it is possible to fit E_0, a_s, a_t and r_s using masses 290 *m*, 360 *m*, but then the quadrupole moment is much too small (about $\frac{1}{4}Q_{\text{exp}}$). For simplicity the high energy scattering can be calculated for the central meson potential with mass 326 *m*, which also fits E_0, a_s, a_t and r_s (and gives $Q=0$); from previous calculations (Christian and Hart 1950, Chew and Goldberger 1948) it appears that the experimental data can be fitted approximately if the potential in odd states is zero (Serber exchange operator). By choosing the coupling of the neutral and charged mesons to the nucleons suitably, such a potential can be obtained; however the neutron–neutron interaction in even singlet states is then repulsive.

These results are in general agreement with the conclusions of Christian and Hart (1950), who studied various forms of potential. In particular they found that a Serber operator is required to explain the high energy data, and also that a large ratio of the tensor to the central part of the potential is needed to give a large enough quadrupole moment. These requirements cannot be satisfied simultaneously with the Schwinger potential.

A potential similar to the Schwinger potential, apart from the arrangement of the coupling constants, can be obtained from a mixed pseudoscalar–pseudovector field (Araki 1948 a, b, 1949, Sasaki *et al.* 1948, Hiroishi and Tanaka 1949). Then the central potential is the same for singlet and triplet states, so that a larger tensor force is required to give the deuteron binding energy and hence a larger quadrupole moment is obtained for the same pair of meson masses. However, it is easily seen by use of the straight line approximation that the singlet scattering length can be fitted only if one of the (essentially positive) coupling constants similar to $g_2^2/\hbar c$ is negative.

One may conclude that the Schwinger potential is unsuitable for describing the interaction between two nucleons. If the tensor force is large enough to give the correct quadrupole moment, then the singlet effective range and the total cross section and anisotropy ratio of the high energy neutron–proton scattering are too large. On the other hand, if the singlet effective range is fitted it is possible to get agreement with the high energy data, but then the non-central potential is far too small to give the correct quadrupole moment and also the neutron–neutron interaction in even singlet states is repulsive, in contradiction to experimental data on nuclear stability.

APPENDIX 1

Values of the depth α_t of the central meson potential for various ranges κ^{-1}, chosen to give the binding energy $E_0 = \hbar^2\kappa^2\epsilon^2/M$, have been obtained by Hulthén (1942) and are fitted by the formula

$$\alpha_t = 1{\cdot}6799 + 2{\cdot}2658\epsilon - 0{\cdot}2488\epsilon^2 + 0{\cdot}18457\epsilon^3 - 0{\cdot}07820\epsilon^4 + 0{\cdot}01333\epsilon^5. \qquad \ldots\ldots(\mathrm{A}\,1)$$

Also ϵ is related to the triplet scattering length a_t (see (A 4)):

$$\epsilon = 1/\kappa a_t + \tfrac{1}{2}\kappa r_t(1/\kappa a_t)^2 + O[(1/\kappa a_t)^3]$$

and to this order κr_t can be replaced by its value 2·1196 in the limit $\kappa^{-1} \to 0$ (Blatt and Jackson 1949). Thus α_t is obtained correct to order $(1/\kappa a_t)^2$, and the same formula holds for the depth α_s of the meson potential giving the singlet scattering length a_s:

$$\alpha_s = 1{\cdot}6799 + 2{\cdot}2658(1/\kappa a_s) + 2{\cdot}1525(1/\kappa a_s)^2 + \ldots \qquad \ldots\ldots(\mathrm{A}\,2)$$

The neglected terms are less than 0·001 for $\kappa^{-1} < 3 \times 10^{-13}$ cm.

The singlet potential in equation (2) reduces to the single meson form when $\gamma_s = 0$ and when $\gamma_s = \infty$; then (A 2) gives

$$\gamma_s = 0 \qquad \alpha_s = 1{\cdot}6799 + 2{\cdot}2658(1/\kappa a_s) + 2{\cdot}1525(1/\kappa a_s)^2 + \ldots$$

$$\gamma_s = \infty \quad \alpha_s\gamma_s/\delta = 1{\cdot}6799 + 2{\cdot}2658(1/\delta\kappa a_s) + 2{\cdot}1525(1/\delta\kappa a_s)^2 + \ldots$$

These two pairs of values of α_s, γ_s give according to (3) two pairs of values of $g_1^2/\hbar c$, $g_2^2/\hbar c$.

For the triplet state neglecting the tensor force, the same procedure can be used with (A 2) replaced by (A 1).

APPENDIX 2

The variation method used by Wu and Foley (1949) for solving the deuteron wave equations was based on the trial wave functions

$$u(x) = (1 - e^{-\beta x})\,e^{-\epsilon x},$$

$$w(x) = b(1 - e^{-\mu x})^2\,e^{-\epsilon x}.$$

This form for w does not have the correct asymptotic form

$$\left(1 + \frac{3}{\epsilon x} + \frac{3}{\epsilon^2 x^2}\right)e^{-\epsilon x},$$

and so it is unlikely that the quadrupole moment should be given accurately. Here we have tried a somewhat different method with better trial wave functions

$$u_1(x) = (1 - e^{-\beta x})e^{-\epsilon x},$$

$$w_1(x) = b(1 - e^{-\mu x})^4\left(1 + \frac{3}{\epsilon x} + \frac{3}{\epsilon^2 x^2}\right)e^{-\epsilon x}.$$

The parameters b, β, μ are chosen so that the functions $u_2(x)$, $w_2(x)$, obtained by iterating in the usual way (Hu and Massey 1949), have the same relative magnitudes as $u_1(x)$, $w_1(x)$ at the origin and at infinity.* In this way values of the coupling constants and quadrupole moment correct to a few percent can be obtained.

APPENDIX 3

The triplet scattering length a_t for a given range κ^{-1} may be determined by use of the relation between a_t, ϵ and the triplet effective range r_t. If η_t is the phase shift given by (8), then

$$k \cot \eta_t = -1/\kappa a_t + \tfrac{1}{2}\kappa r_t k^2 + O(k^4), \qquad \text{......(A 3)}$$

with

$$\kappa r_t = 2\int_0^\infty [(1 - x/\kappa a_t)^2 - (u_t^0)^2]\,dx, \qquad u_t^0 \sim 1 - x/\kappa a_t.$$

For the deuteron ground state, (A 3) gives

$$\epsilon = 1/\kappa a_t + \tfrac{1}{2}\kappa r_t \epsilon^2 + O(\epsilon^4). \qquad \text{......(A 4)}$$

Thus κa_t and κr_t may be determined from the solution u_t^0 of the zero energy wave equation, and then ϵ is determined from (A 4) to give κ^{-1}. For large ranges ($\kappa^{-1} \gtrsim 3 \times 10^{-13}$ cm.), the higher terms in (A 3) are important and this method fails.

Hulthén's method which was used for the singlet scattering could also be used for the triplet scattering (neglecting tensor forces) to determine κa_t and κr_t for a given α_t. Due to the fact that $|a_t|$ is much smaller than $|a_s|$, the method becomes inaccurate for smaller values of the range than in the singlet case, especially for large δ; for $\delta = 3$, the value of κa_t obtained using (11) and one parameter is about 30% too small for $\kappa^{-1} \simeq 1{\cdot}9 \times 10^{-13}$ cm. Some improvement is obtained by assuming a different form for $y(x)$ (for example, by replacing x on the right-hand side of (11) by δx), or by using more parameters. The results still become inaccurate at large ranges, and it is difficult to know the region of validity of the method until some accurate results have been obtained by other means. Moreover it is as simple to use numerical integration as to do this calculation with more than one parameter.

ACKNOWLEDGMENTS

The author wishes to thank Professor R. E. Peierls for suggesting this problem to him and for continued assistance throughout the investigation. Discussions with Dr. E. E. Salpeter have also proved helpful. Thanks are due to the University of Melbourne for a Research Scholarship which the author held while carrying out this work.

---

* This method of determining the parameters was suggested to me by Professor Peierls.

REFERENCES

ARAKI, G., 1948 a, *Phys. Rev.*, **74**, 985; 1948 b, *Prog. Theor. Phys.*, **3**, 422; 1949, *Ibid.*, **4**, 34.
ARNOLD, W. R., and ROBERTS, A., 1947, *Phys. Rev.*, **71**, 878.
BETHE, H. A., 1949, *Phys. Rev.*, **76**, 38.
BLATT, J. M., and JACKSON, J. D., 1949, *Phys. Rev.*, **76**, 18.
BREIT, G., and BLOCH, J., 1947, *Phys. Rev.*, **72**, 135.
CHEW, G. F., and GOLDBERGER, M. L., 1948, *Phys. Rev.*, **73**, 1409; 1949, *Ibid.*, **75**, 1637.
CHRISTIAN, R. S., 1949, *Phys. Rev.*, **75**, 1675.
CHRISTIAN, R. S., and HART, E. W., 1950, *Phys. Rev.* **77**, 441.
HADLEY, J., KELLY, E., LEITH, C., SEGRÈ, E., WIEGAND, C., and YORK, H., 1949, *Phys. Rev.*, **75**, 351.
HIROISHI, S., and TANAKA, H., 1949, *Prog. Theor. Phys.*, **4**, 231.
HU, T. M., and MASSEY, H. S. W., 1949, *Proc. Roy. Soc.* A, **196**, 135.
HULTHÉN, L., 1942, *Arkiv. Mat. Astr. Fys.*, **28 A**, no. 5; 1948, *Ibid.*, **35 A**, no. 25.
JAUCH, J. M., and HU, N., 1944, *Phys. Rev.*, **65**, 289.
KELLOG, J. M. B., RABI, I. I., RAMSEY, N. F., and ZACHARIAS, J. R., 1940, *Phys. Rev.*, **57**, 677.
MILLMAN, S., and KUSCH, R., 1941, *Phys. Rev.*, **60**, 91.
NORDSIECK, A., 1940, *Phys. Rev.*, **58**, 310.
PRIMAKOFF, H., 1947, *Phys. Rev.*, **72**, 118.
RAMSEY, W. H., 1948, *Proc. Phys. Soc*,. **61**, 297.
ROHRLICH, F., and EISENSTEIN, J., 1949, *Phys. Rev.*, **75**, 705.
SACHS, R. G., 1947, *Phys. Rev.*, **72**, 91.
SASAKI, M., NAKAMURA, S., and HAYAKAWA, S., 1948, *Prog. Theor. Phys.*, **3**, 454.
SCHWINGER, J., 1941, *Phys. Rev.*, **60**, 164; 1942, *Ibid.*, **61**, 387.
THOMAS, L. H., 1937, *Phys. Rev.*, **51**, 202.
WU, T.-Y., and FOLEY, H. M., 1949, *Phys. Rev.*, **75**, 1681.

The Rotation of Liquid Helium II

BY D. V. OSBORNE
Royal Society Mond Laboratory, Cambridge

Communicated by D. Shoenberg; *MS. received 8th March* 1950

ABSTRACT. An experiment is described in which the free surface of rotating liquid helium II is studied. It is shown that the results, which are the same as for any ordinary liquid, are not in accordance with the hypothesis that the superfluid component remains stationary. On this basis an estimate of the critical velocity for superfluidity is made and is compared with previous determinations.

IN the two-fluid model of liquid helium II (see, for example, Tisza 1938, 1947) the superfluid component is endowed with zero viscosity and no interaction with the normal fluid, and it should therefore obey the theorem of the conservation of circulation which is applicable to an ideal liquid. If we accept in addition the quantum statistics put forward by Landau (1941, 1944, 1947) we obtain the more rigorous condition that curl $\mathbf{v}_s = 0$. It is known in practice that superfluid behaviour is observed only at low velocities, and some of the various estimates of the critical velocity above which the flow loses its superfluid character will be given below.

There has been some discussion during the past two years about possible rotation experiments which could confirm the existence of conditions in which ideal liquid behaviour is manifested, and the present note describes one attempt at carrying out such an experiment (following a suggestion by Professor Peierls) by observing the shape of the free surface of rotating liquid helium.

For any ordinary liquid the free surface is a paraboloid of the form

$$z=\frac{\omega^2}{2g}r^2, \qquad \ldots\ldots(1)$$

where z and r are the vertical and radial coordinates of a point in the surface, referred to the vertex as origin, and ω is the angular velocity. This relation does not involve the density because both the centrifugal and the gravitational forces on an element of the fluid are proportional to its density. Liquid helium II, however, must be considered as a mixture of a normal component (density ρ_n) and a superfluid component (density ρ_s), and if the latter is entirely frictionless it will never be accelerated into rotation, so that the centrifugal force per unit volume will be proportional only to ρ_n while the gravitational force will be proportional to $\rho_n+\rho_s$. The usual derivation of equation (1) will no longer be valid, and to derive the shape of the surface under these conditions we must write down the equations of motion of the two components separately, i.e.

$$\frac{\partial \mathbf{v}_s}{\partial t}+\operatorname{grad}(G+\phi)=0, \qquad \ldots\ldots(2)$$

$$\frac{\partial \mathbf{v}_n}{\partial t}+\operatorname{grad}\left(G+\frac{\rho}{\rho_n}TS+\phi\right)=0, \qquad \ldots\ldots(3)$$

where $\mathbf{v}_n$ and $\mathbf{v}_s$ are the velocities of the normal and superfluid components respectively, G is the thermodymanic potential per unit mass of the entire fluid, S is the entropy per unit mass, ϕ the gravitational potential per unit mass, T the absolute temperature and $\rho=\rho_n+\rho_s$. These equations are readily obtained by calculating the energy changes involved in introducing a small element of the normal or superfluid component into the region under consideration. In the problem in hand we are supposing that $\mathbf{v}_s=0$ and that $\mathbf{v}_n$ has only a tangential component ωr at every point, so that (2) and (3) become

$$\operatorname{grad}(G+\phi)=0$$

and

$$-\omega^2\mathbf{r}+\operatorname{grad}\left(G+\frac{\rho}{\rho_n}TS+\phi\right)=0,$$

whence, using $\operatorname{grad} G=(1/\rho)\operatorname{grad} p-S\operatorname{grad} T$, and eliminating $\operatorname{grad} p$ or $\operatorname{grad} T$, we have

$$-\omega^2\mathbf{r}+\operatorname{grad}\frac{\rho}{\rho_n}TS=0, \qquad \ldots\ldots(4)$$

$$-\rho_n\omega^2\mathbf{r}+\operatorname{grad} p+\rho\operatorname{grad}\phi=0. \qquad \ldots\ldots(5)$$

If, for convenience, we adopt Tisza's assumption that $\rho S=\rho_n S_n$, where S_n is independent of temperature, we find from (4) that

$$\omega^2\mathbf{r}=S_n\operatorname{grad} T,$$

whence

$$T(r)=\frac{1}{2}\frac{\omega^2r^2}{S_n}+T(0). \qquad \ldots\ldots(6)$$

For a peripheral velocity, ωr, of 50 cm. sec^{-1} this gives

$$T(r)-T(0)=0{\cdot}73\times10^{-4}\text{ deg.},$$

so that ρ_n will not vary greatly with r, a fact which enables us to integrate equation (5) immediately. Putting $\phi = gz$, and treating ρ_n as constant, we find

$$p = \tfrac{1}{2}\rho_n\omega^2 r^2 - \rho g z + p_0, \qquad \ldots\ldots(7)$$

so that the free surface, given by p = constant, will be of the form

$$z = \frac{\rho_n}{\rho}\frac{\omega^2}{2g}r^2 \qquad \ldots\ldots(8)$$

where (r, z) now represents a point in the surface, and the origin of z has been chosen at the vertex. Therefore, although the superfluid does not rotate, the whole fluid has a single paraboloidal surface. The superfluid is "held in place" by means of the fountain effect, and equation (6) describes the temperature distribution that provides the necessary forces.

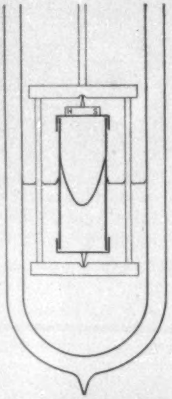

Figure 1. Apparatus for the rotation of liquid helium II.

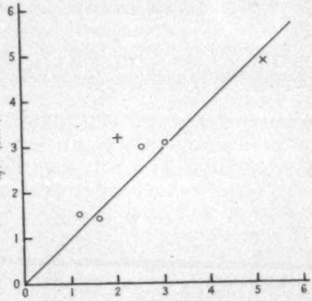

Figure 2. Full line : $z/r^2 = \omega^2/2g$.

Experimental points:
$\circ = 1{\cdot}20°$ K., $\rho_n/\rho = 0{\cdot}03$.
$+ = 1{\cdot}40°$ K., $\rho_n/\rho = 0{\cdot}08$.
$\times = 1{\cdot}59°$ K., $\rho_n/\rho = 0{\cdot}18$.

The apparatus is shown in Figure 1. Inside the cryostat a vertical glass tube, closed at the lower end by a brass cap, is mounted between point bearings at top and bottom, and carries a small horizontal bar magnet. A rotating magnetic field outside the Dewars enables the tube to be spun at speeds from 8 to 16 rev. sec^{-1}. The helium meniscus in the tube can be seen from outside the cryostat through clear strips in the silvering, and the profile is plotted out using a cathetometer. A correction has to be made to the abscissae because of the refraction of the light emerging from the cylinder; the correction for surface tension has been calculated to be negligible.

The surface was observed experimentally to be a paraboloid, and Figure 2 shows the measured values of the constant z/r^2 plotted against $\omega^2/2g$ for various angular velocities and temperatures. The full line having unit slope is what would be expected for an ordinary liquid (equation (1)), and the experimental points, which are for liquid helium II at temperatures where ρ_n/ρ is of the order of a few per cent, show clearly that equation (1) is at least much nearer the truth than equation (8).

The experiments were carried out in a cylindrical vessel of inside diameter 1·4 cm. rotating at speeds from 8 to 16 rev. sec^{-1}, so that the peripheral velocity ranged from 35 to 70 cm. sec^{-1}. We can certainly deduce, therefore, that there is no frictionless flow at speeds upwards of 35 cm. sec^{-1}. Kapitza (1941) found critical velocities in the neighbourhood of 100 cm. sec^{-1} for flow in a narrow channel, and Meyer and Mellink (1947) give 20 cm. sec^{-1} as a result of similar experiments. Daunt and Mendelssohn (1939) in their work on helium films arrived at a critical velocity of 20 cm. sec^{-1}, but this depends on the value assumed for the thickness of the film, and a recent estimate of film thickness by Atkins (to be published) leads to a velocity nearer 35 cm. sec^{-1}. The author has obtained superfluid velocities up to 35 cm. sec^{-1} in undistorted pulses of second sound.

The lower limit of 35 cm. sec^{-1} obtained from the results of the present experiment can be extended somewhat if we take account of the fact that, upon stopping the vessel, the surface becomes quite flat within a time of the order of ten seconds. If there were a critical velocity at, say, 10 cm. sec^{-1} we should expect the fluid to slow down until the velocity everywhere was less than this value, and then the superfluid should continue rotating, so that the paraboloidal surface ought to persist. Since no persistent curvature is obtained, we deduce that the critical velocity is not greater than about 15 cm. sec^{-1}, this being the smallest peripheral velocity which would correspond to a distinctly curved surface. This argument is open to the objection that, if the superfluid becomes turbulent during its initial retardation, the angular momentum might persist in the form of eddies rather than as a streamline motion, in which case no curvature of the surface as a whole is to be expected.

The prediction of Landau (1941, 1944, 1947) that curl $\mathbf{v}_s=0$ certainly does not hold for $v_s>35$ cm. sec^{-1}, but very little can be said about the range $v_s<35$ cm. sec^{-1}.

In conclusion, we note that the results reported here could be explained by the theory of Gorter and Mellink (1949) postulating a mutual friction between the two components, and that they do not satisfy the criterion $\omega<h/4\pi ma^2$ proposed by London (1946) for the existence of persistent currents.

REFERENCES

Daunt, J. G., and Mendelssohn, K., 1939, *Proc. Roy. Soc.* A, **170,** 423, 439.

Gorter, C. J., and Mellink, J. H., 1949, *Physica*, **15,** 285.

Kapitza, P. L., 1941, *J. Phys. U.S.S.R.*, **5,** 59.

Landau, L. D., 1941, *J. Phys. U.S.S.R.*, **5,** 71; 1944, *Ibid.*, **8,** 1; 1947, *Ibid.*, **11,** 91.

London, H., 1946, *Report of International Conference at Cambridge*—II. *Low Temperatures* (London: Physical Society), p. 48.

Meyer, L., and Mellink, J. H., 1947, *Physica*, **13,** 197.

Tisza, L., 1938, *Nature, Lond.*, **141,** 913; 1947, *Phys. Rev.*, **72,** 238.

LETTERS TO THE EDITOR

On the Inner Potential of Metals

As part of an investigation into the inner potential of solids, one of us (V.F.G.T.) recently prepared evaporated films of silver and gold which were single crystals and had a flat surface; the inner potential was measured by the standard technique for fast electrons (Thomson and Cochrane 1939). The results were: 23 volts for silver and 30 volts for gold.

These values are markedly different from those calculated by adding the Fermi energy of the conduction electrons and the work function, as suggested originally by Bethe (1928 a) and Rosenfeld and Witmer (1928). This method yields 10·2 volts for silver and 10·3 volts for gold.

It is apparent from the theory of metals that the original method of obtaining the inner potential is incorrect; a search of the literature shows that this point has been made, if somewhat obliquely, by Sommerfeld and Bethe (1933), at the end of a long footnote. This does not seem to have received any attention, and the older theoretical values are still quoted. The point at issue can be made briefly by noting that the conduction electrons even in their lowest state possess a certain amount of kinetic energy. This means that the average potential of an electron in a metal will be larger, in absolute magnitude, than that calculated on the original theory. The difference is not large for the lighter metals, and because of this (and of experimental errors) the difference has not been apparent before.

An attempt has also been made to calculate the mean potential using a modification of the Bethe (1928 b) theory. This leads to a value of 22 volts for silver and 35 volts for gold.

The flat surfaces of the metals were produced (*a*) by evaporating on to a slightly heated cleavage face of rocksalt and dissolving the rocksalt, (*b*) by evaporating on to cleaved surfaces of magnesium oxide and of mica heated to a high temperature. The experimental values of the inner potential were found to be the same within experimental error for surfaces produced by both methods. Fuller details will be given in a paper to be published shortly.

Physics Department,
Imperial College, London, S.W.7.
5th June 1950.

M. BLACKMAN.
V. F. G. TULL.

BETHE, H., 1928 a, *Naturwissenschaften*, **16**, 333; 1928 b, *Ann. Phys., Lpz.*, **87**, 55.
ROSENFELD, H., and WITMER, A., 1928, *Z. Phys.*, **49**, 534.
SOMMERFELD, A., and BETHE, H., 1933, *Handb. der Phys.*, **24** (2), 425.
THOMSON, G. P., and COCHRANE, W., 1939, *Theory and Practice of Electron Diffraction* (London: Macmillan and Co. Ltd.).

The ^{11}B (α, n) ^{14}N Reaction

The bombardment of ^{11}B by alpha-particles can lead to the emission of neutrons, protons and gamma-rays. This Letter gives the results of investigation of the neutrons and gamma-rays from these reactions for polonium alpha-particles of 5·3 MeV. energy.

The following measurements were made: (i) the energy spectrum of the emitted neutrons; (ii) the energy and intensity of the gamma-rays.

A thin 200 mc. polonium source (1 cm. square surface area, less than 100 μg/cm^2 thick on platinum foil) was placed in contact with a layer of separated ^{11}B (3 mg/cm^2) deposited on a copper sheet. The sheet was ground as thin as possible (1/10 mm.) in order to minimize gamma-rays resulting from inelastic scattering of neutrons in the copper.

The neutron spectrum and absolute intensity were found from the pulse height distribution of recoil protons in a methane filled ionization chamber (Beghian and Halban 1949). This was filled to 20 atmospheres pressure, and gave electron collection. A linear amplifier, discriminator, and single-channel pulse amplitude analyser were used in conjunction with the chamber. The overall performance of the equipment had been previously checked, and the discriminator bias settings calibrated using monoenergetic neutrons (2·5 MeV.) from a D+D source.

In the Figure is shown the neutron spectrum calculated from the pulse height distribution after corrections had been made for wall effect, and the screening effect of positive ions in the chamber. The spectrum shows a broad maximum around 2·5 MeV. in good agreement with the photographic plate measurements of Perlman, Richards and Speck (1946), who used a target of natural boron (80% ^{11}B, 20% ^{10}B). Thick target geometry does not permit sufficient resolution to identify weak groups.

The gamma-rays from the source were detected in a pair of thin-walled glass Geiger-Müller counters set up in coincidence, with a Perspex converter in front of the first counter producing the secondary electrons. The absolute sensitivity of this arrangement was measured with gamma-rays from ^{60}Co and ^{24}Na.

By placing aluminium foils between the two counters, the absorption curve of the secondary electrons was found. Knowledge of the form of the curve enabled us to determine the energy and estimate the degree of homogeneity of the gamma-rays.

Absorption curves were measured with the polonium in contact with the boron, and with polonium alone (in contact with a piece of silver foil to avoid gamma-rays produced by alpha-particles on atmospheric nitrogen). The difference between the two gave the absorption curve for gamma-rays from the alpha-particle bombardment of ^{11}B.

We were able to deduce from the shape of this curve the presence of one gamma-ray line of 2·2±0·2 MeV. energy; its intensity was 9% of the neutron flux and 2% of the polonium gamma-ray flux. It was only possible to measure this weak intensity in the presence of such a large background owing to the rapid increase in sensitivity of the coincident counters with energy in this region. (The polonium gamma-rays have an energy of only 0·8 MeV.)

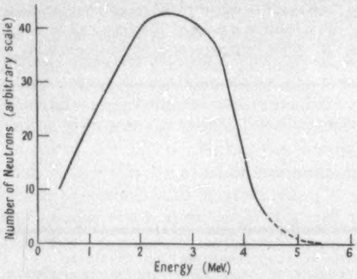

It is probable that these gamma-rays originate from an excited state of ^{14}N formed by the ^{11}B (α, n) reaction. Measurements made on the decay of ^{14}O by Sherr, Muether and White (1949), and the re-evaluation of the gamma-ray energy data in ^{13}C (p, γ) by Fowler, Lauritsen and Lauritsen (1948) both suggest the existence of a 2·3 MeV. level in ^{14}N.

It is unlikely that the gamma-rays are due to the reaction ^{11}B (α, p) ^{14}C. Creagon (1949) was unable to detect coincidences between protons from this reaction and any accompanying gamma-rays from a possible excited state of ^{14}C. It is also improbable that they originate in the 2·2 MeV. level of ^{11}B (Fulbright and Bush 1948) due to inelastic scattering of the alpha-particles with energies as low as 5·3 MeV.

We wish to thank Dr. W. D. Allen of Atomic Energy Research Establishment, Harwell, for supplying the separated boron specimen, Professor M. H. L. Pryce for interesting discussions, and Professor Lord Cherwell for affording us the facilities of his laboratory.

Clarendon Laboratory,
Oxford.
2nd May 1950.

L. E. Beghian.
M. A. Grace.
H. Halban.

Beghian, L. E., and Halban, H., 1949, *Proc. Phys. Soc.* A, **62,** 395.
Creagon, R. J., 1949, *Phys. Rev.*, **76,** 1769.
Fowler, W. A., Lauritsen, C. C., and Lauritsen, T., 1948, *Phys. Rev.*, **73,** 181; *Rev. Mod. Phys.*, **20,** 236.
Fulbright, H. W., and Bush, R. R., 1948, *Phys. Rev.*, **74,** 1323.
Perlman, I. F., Richards, H. T., and Speck, L., 1946, *M.D.D.C.*, 39.
Sherr, R., Muether, H. R., and White, M. G., 1949, *Phys. Rev.*, **75,** 282.

The Photo Threshold of ^{208}Pb

The threshold for the photo disintegration of $^{208}\text{Pb}(\gamma, n)^{207}\text{Pb}$ has been measured by the method previously described (Parsons and Collie 1950) and found to be $8{\cdot}1 \pm 0{\cdot}3$ Mev. The 31 grammes of lead extracted by Professor Soddy in his classic work on the isotopes of lead (Soddy 1916) was placed at our disposal with characteristic kindness. As the Clarendon betatron with its platinum target has a rather high neutron background the measurements were made with the 30 Mev. synchrotron at the Atomic Energy Research Establishment, Malvern, which has an aluminium target. Our value for the threshold is higher than that (7·37 Mev.) recently given by Kinsey, Bartholomew and Walker (1950). In our measurement the energy scale was calibrated by reference to the $^{63}\text{Cu}(\gamma, n)^{62}\text{Cu}$ threshold assumed to be at 10·9 Mev., but we were able to confirm that the ^{208}Pb threshold was about 1 Mev. above that for ^{207}Pb and ^{209}Bi by direct comparison under the same conditions as were used in the measurement of Professor Soddy's sample of ^{208}Pb. The difference between the observed threshold and that calculated from Weiszäcker's formula (ΔE_b) of Parsons and Collie (1950) is 1·2 Mev., which fits in well with our previous results and suggests that the expected discontinuity in the binding energy curve occurs at ^{209}Bi.

We have to thank Mr. D. W. Fry of the Atomic Energy Research Establishment for permission to use the synchrotron, and Professor Soddy for the loan of the lead.

Atomic Energy Research Establishment,
Malvern
and
Clarendon Laboratory,
Oxford.

R. W. Parsons.
D. J. Lees.
C. H. Collie.

5th June 1950.

Kinsey, B. B., Bartholomew, G. A., and Walker, W. H., 1950, *Phys. Rev.*, **78**, 77.
Parsons, R. W., and Collie, C. H., 1950, *Proc. Phys. Soc.* A, **63**, 839.
Soddy, F., 1916, *Ann. Rep. Chem. Soc.*, **13**, 247, 272.

The Photodisintegrations $^{6}\text{Li}(\gamma\text{D})^{4}\text{He}$ and $^{7}\text{Li}(\gamma\text{T})^{4}\text{He}$

Lithium loaded Ilford E_1 emulsions of thickness 200μ have been irradiated with γ-rays from the reaction $^{7}\text{Li}\ p\gamma^{8}\text{Be}$, $^{8}\text{Be}^{*}$ and a search has been made for events corresponding to the hitherto unobserved reactions

$$^{6}\text{Li}+\gamma={}^{4}\text{He}+{}^{2}\text{H}-1{\cdot}54\text{ Mev.} \qquad \ldots\ldots(1)$$

$$^{7}\text{Li}+\gamma={}^{4}\text{He}+{}^{3}\text{H}-2{\cdot}5\text{ Mev.} \qquad \ldots\ldots(2)$$

3 in. × 1 in. plates were located within a few centimetres of a thick metal lithium target which was watercooled and bombarded with 500 kev. protons from the Cavendish Laboratory H.T. set. An irradiation carried out over three consecutive days provided a suitable exposure, the total γ-ray dose being monitored by Geiger counter. The irradiated plates were temperature developed to obtain uniformity in depth but some under-development was employed to improve discrimination between particles of charge one and charge two.

In addition to numerous carbon stars (Hanni *et al.* 1948) 27 complete events have been found which correspond to reaction (2). They can be identified by the difference in ionization of the α-particle and triton, by a momentum balance involving the two charged particles and the incoming γ-ray, and from energy considerations. In addition, the scattering and, in the case of the triton, the increase in ionization towards the end of the track shows that the two charged particles comprising the event are moving in opposite directions.

In Figure 1 photomicrographs are reproduced which illustrate these points and show (*a*) an event produced by a γ-ray of 17·6 Mev. energy, (*b*) an event produced by a γ-ray of

14·8 Mev. energy, and (*c*) an event from the slow neutron reaction ^{6}Li (nα)^{3}H for comparison purposes. All are photographed at the same magnification.

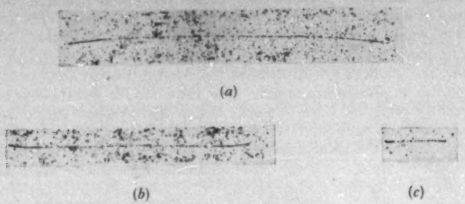
(*a*)

(*b*) (*c*)

Figure 1. Photomicrographs.

(*a*) Event ^{7}Li(γT)^{4}He produced by a 17·6 Mev. γ-ray.
(*b*) Event ^{7}Li(γT)^{4}He produced by a 14·8 Mev. γ-ray.
(*c*) Event ^{6}Li(nα)T produced by a slow neutron and included for comparison purposes.

Figure 2 is a number–energy histogram for the 27 events, from which it will be seen that two peaks, corresponding to the known γ-ray energies 14·8 Mev. and 17·6 Mev. (Walker and McDaniel 1948) are present. As anticipated from the shape and intensity of the two lines the lower energy distribution is broader than the higher one and contains fewer events.

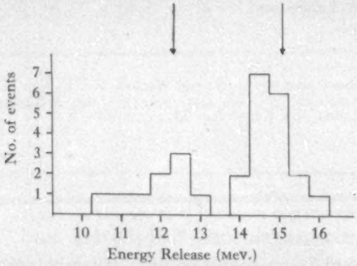

Figure 2. N$-$E$_T$ histogram where E$_T$=sum of energy of α-particle and triton. The arrows indicate the positions of the peaks to be expected from the 14·8 and 17·6 Mev. γ-rays.

The geometry of the irradiation and the calibration of the counters were not known well enough to enable the cross section for the reaction to be obtained directly. However, it can be calculated in terms of the ^{12}C$\gamma 3\alpha$ cross section by observing the relative frequencies of the two types of event in the emulsion. A correction is necessary for loss of events due to the escape of one or other of the tracks from the emulsion; this is large since the sum of the ranges of the α-particle and triton is approximately equal to emulsion thickness employed. Taking the densities of carbon and lithium in the emulsion to be 0·27 and 0·016 gm/cm^3 of unprocessed emulsion the ratio of the cross sections is found to be

$$\frac{\sigma\,{}^7\mathrm{Li}(\gamma\,{}^3\mathrm{H})\,{}^4\mathrm{He}\ 17{\cdot}6+14{\cdot}8}{\sigma\,({}^{12}\mathrm{C}\,\gamma 3\alpha)\ 17{\cdot}6+14{\cdot}8}=1{\cdot}5\pm 0{\cdot}4.$$

Accepting the value

$$\sigma\,({}^{12}\mathrm{C}\,\gamma 3\alpha)\ 17{\cdot}6+14{\cdot}8=(0{\cdot}8\pm 0{\cdot}3)\times 10^{-28}\ \mathrm{cm}^2$$

given by Wäffler and Younis (1949) for the ^{12}C$\gamma 3\alpha$ reaction induced by Li pγ radiation the ^{7}Li (γT) ^{4}He cross section is found to be

$$\sigma\,({}^7\mathrm{Li}\,\gamma\mathrm{T})\ 17{\cdot}6+14{\cdot}8=(1{\cdot}2\pm 0{\cdot}6)\times 10^{-28}\ \mathrm{cm}^2.$$

Although the statistics are poor the indication is that the cross sections at 14·8 and 17·6 Mev. respectively have roughly the same value.

Events corresponding to reaction (1) have not been observed though the lower abundance of the ^{6}Li isotope, and the greater probability of escape of the long deuteron track to be expected, reduces the chance of finding complete events in the emulsion from this reaction. An upper limit for the cross section in this case can be derived and is

$$\sigma\,(^6\text{Li}\gamma\text{D}\ ^4\text{He})\ 17{\cdot}6+14{\cdot}8 = (0{\cdot}4\pm0{\cdot}4)\times10^{-28}\ \text{cm}^2.$$

The author's thanks are due to Professor O. R. Frisch and Dr. D. H. Wilkinson for the hospitality of their laboratory, to Mr. G. A. Jones for running the H.T. set during the irradiations and to Miss P. A. Port and Mr. T. A. Brinkley for help with the microscope work.

Atomic Energy Research Establishment,
Harwell, Berks.
30th May 1950.

E. W. TITTERTON.

HANNI, von H., TELEGDI, V. L., and ZÜNTI, W., 1948, *Helv. Phys. Acta*, **21**, 203.
WÄFFLER, von H., and YOUNIS, S., 1949, *Helv. Phys. Acta*, **22**, 614.
WALKER, R. L., and MCDANIEL, B. D., 1948, *Phys. Rev.*, **74**, 315.

Unequal *g*-Values for the Different Magnetic Levels of an Atomic Energy Level.

During his recent stay in the U.S.A. one of the authors of this letter (Catalán) photographed, in collaboration with Dr. Van den Bosch, the manganese spectrum in a magnetic field of about 80,000 oersted. The plates were taken using the instruments of Prof. Harrison at the M.I.T. Plates taken with the same apparatus in 1939 have been also measured.

Many of the patterns are found to be asymmetrical. A careful study of these asymmetries and their quantitative interpretation, in terms of the theory of the Paschen–Back effect, has been made at the Bureau of Standards and the results are to be published shortly.

The distortions in the patterns are due to repulsions between magnetic levels with equal *M*-values, belonging to adjacent levels of a spectral term. The repulsions, being unequal for different *M*-values, alter the ordinary symmetrical positions of the magnetic levels, and hence an asymmetry appears in the positions of the magnetic lines of the pattern.

The theory of *partial* Paschen–Back effect provides a simple rule to obtain *g*-values in spite of the asymmetry. The rule consists in taking, not the individual differences of the magnetic lines from the centre line (without field), but the differences for the lines of equal order on each side of the centre.

The line λ4048.747 of MnI shows strong distortion, as evidenced by the unequal $\Delta\nu$ (Table 1). The differences between lines of equal order, *a–a′*, *b–b′*. . . . divided by $2a=7{\cdot}92$ (twice the value of the constant separation for the field used) give, in Lorentz units, the mean values of the negative and positive components of the pattern.

Table 1. $\lambda\,4048{\cdot}747$, $\text{a}^6\text{D}_{5/2}-\text{z}^6\text{D}_{3/2}$

	M	M'	ν	$\Delta\nu$		Sep. (cm^{-1})	Comp.	Interval
a	$-2\frac{1}{2}$	$-1\frac{1}{2}$	24700·06	1·14	*a*—*a′*	15·52	1·960	0·204
b	$-1\frac{1}{2}$	$-\frac{1}{2}$	698·92	0·88	*b*—*b′*	13·90	1·756	0·209
c	$-\frac{1}{2}$	$\frac{1}{2}$	698·04	0·60	*c*—*c′*	12·25	1·547	0·208
d	$\frac{1}{2}$	$1\frac{1}{2}$	697·44		*d*—*d′*	10·60	1·339	
m	$-1\frac{1}{2}$	$-1\frac{1}{2}$	24693·50	1·11	*m*—*m′*	2·48	(0·313)	0·207
n	$-\frac{1}{2}$	$-\frac{1}{2}$	692·39	0·84	*n*—*n′*	0·84	(0·106)	0·212
n′	$\frac{1}{2}$	$\frac{1}{2}$	691·55	0·53				
m′	$1\frac{1}{2}$	$1\frac{1}{2}$	691·02				Mean value $e=$	0·208
d′	$-\frac{1}{2}$	$-1\frac{1}{2}$	24686·84	1·05				
c′	$\frac{1}{2}$	$-\frac{1}{2}$	685·79	0·77				
b′	$1\frac{1}{2}$	$\frac{1}{2}$	685·02	0·48				
a′	$2\frac{1}{2}$	$1\frac{1}{2}$	684·54					

To obtain the mean interval $e=0{\cdot}208$, not only have the intervals between components been used, but also the interval 0·212 which results by doubling the p-component (0·106).

Each n-component provides an equation which, in addition to that given by *e*, enables the *g*-values of the two spectroscopic levels involved to be computed. The resulting *g*-values for each level are practically identical as is shown below.

Comp.	$a^6D_{5/2}$	$z^6D_{3/2}$
1·960	1·648	1·856
1·756	1·652	1·860
1·547	1·651	1·859
1·339	1·651	1·859

Most of the observed patterns are analogous to that detailed above, but there are a few which differ, and these differences make them extremely interesting. The main purpose of this letter is to explain such exceptional patterns. One belongs to λ3816·746 (Table 2)

Table 2. λ 3816·746, $a^6D_{5/2}-z^6F_{3/2}$

	M	*M′*	*ν*	Δ*ν*		Sep. (cm^{-1})	Comp.	Interval
a	$-2\frac{1}{2}$	$-1\frac{1}{2}$	26203·41	3·04	*a*−*a′*	20·12	2·541	0·556
b	$-1\frac{1}{2}$	$-\frac{1}{2}$	200·37	2·57	*b*−*b′*	15·72	1·985	0·653
c	$-\frac{1}{2}$	$\frac{1}{2}$	197·80	1·25	*c*−*c′*	10·55	1·332	0·558
d	$\frac{1}{2}$	$1\frac{1}{2}$	196·55		*d*−*d′*	6·13	0·774	
m	$-1\frac{1}{2}$	$-1\frac{1}{2}$	26196·94	3·12	*m*−*m′*	7·00	(0·884)	0·558
n	$-\frac{1}{2}$	$-\frac{1}{2}$	193·82	2·58	*n*−*n′*	2·58	(0·326)	0·652
n′	$\frac{1}{2}$	$\frac{1}{2}$	191·24	1·30				
m′	$1\frac{1}{2}$	$1\frac{1}{2}$	189·94					
d′	$-\frac{1}{2}$	$-1\frac{1}{2}$	26190·42	3·17				
c′	$\frac{1}{2}$	$-\frac{1}{2}$	187·25	2·60				
b′	$1\frac{1}{2}$	$\frac{1}{2}$	184·65	1·36				
a′	$2\frac{1}{2}$	$1\frac{1}{2}$	183·29					

The discordances between intervals in this pattern make it impossible to obtain a significant value for *e*. It may at first be thought that 0·653, so different from other intervals, might be due to an error in the measurements of the two lines which give it, but this is unlikely, since each of those lines gives the same interval with the adjacent line. The real existence of such an interval is supported by the fact that its value coincides with the value 0·652 which is double the p-component (0·326).

This particular pattern finds a simple explanation if the components arising from the two pairs of magnetic levels $z^6F_{3/2}{}^{\pm 3/2}$ and $z^6F_{3/2}{}^{\pm 1/2}$ are treated separately in calculating *g*-values, as shown in Table 3.

Table 3. λ 3816·746, $a^6D_{5/2}-z^6F_{3/2}$

	M	*M′*		Sep.	Comp.		*M*	*M′*		Sep.	Comp.
a	$-2\frac{1}{2}$	$-1\frac{1}{2}$	*a*−*a′*	20·12	2·541	*b*	$-1\frac{1}{2}$	$-\frac{1}{2}$	*b*−*b′*	15·72	1·985
d	$\frac{1}{2}$	$1\frac{1}{2}$	*d*−*d′*	6·13	0·774	*c*	$-\frac{1}{2}$	$\frac{1}{2}$	*c*−*c′*	10·55	1·332
m	$-1\frac{1}{2}$	$-1\frac{1}{2}$	*m*−*m′*	7·00	(0·884)	*n*	$-\frac{1}{2}$	$-\frac{1}{2}$	*n*−*n′*	2·58	(0·326)
m′	$1\frac{1}{2}$	$1\frac{1}{2}$				*n′*	$\frac{1}{2}$	$\frac{1}{2}$			
d′	$-\frac{1}{2}$	$-1\frac{1}{2}$				*c′*	$\frac{1}{2}$	$-\frac{1}{2}$			
a′	$2\frac{1}{2}$	$1\frac{1}{2}$				*b′*	$1\frac{1}{2}$	$\frac{1}{2}$			

The components 2·541 and (0·884) give two equations from which can be obtained the *g*-values for both levels involved. The same procedure is followed with the three pairs 0·774, (0·884) ; 1·985, (0·326) and 1·332, (0·326). The resulting *g*-values are :

Comp.	$a^6D_{5/2}$	$z^6F_{3/2}{}^{\pm 3/2}$	Comp.	$a^6D_{5/2}$	$z^6F_{3/2}{}^{\pm 1/2}$
2·541	1·657	1·067	1·985	1·659	1·007
0·774	1·658	1·068	1·932	1·658	1·006

The *g*-values for $a^6D_{5/2}$ are equal in both groups. In the case of $z^6F_{3/2}$ the *g*-values are equal inside each group, but they change very much from one group to the other. *The two pairs of magnetic levels of* $z^6F_{3/2}$ *have very different g-values.* The pair $M=\pm 1\frac{1}{2}$ has $g=1{\cdot}067$, equal to the Landé value, but the pair $M=\pm\frac{1}{2}$ has $g=1{\cdot}006$, very different from the Landé value.

The pattern for the line $a^6D_{1/2}$—$z^6F_{3/2}$, λ3843·988, supports this conclusion. For simplicity in Table 4 the wave-numbers of the magnetic lines have been omitted and only the separations are given.

Table 4. λ 3843·988, $a^6D_{1/2}-z^6F_{3/2}$

	M	*M′*		Sep.	Comp.		*M*	*M′*		Sep.	Comp.
a	$-\frac{1}{2}$	$-1\frac{1}{2}$	*a*−*a′*	0·51	0·064	*b*	$\frac{1}{2}$	$-\frac{1}{2}$	*b*−*b′*	−17·12	−2·162
a′	$\frac{1}{2}$	$1\frac{1}{2}$				*m*	$-\frac{1}{2}$	$-\frac{1}{2}$	*m*−*m′*	9·20	(1·162)
						m′	$\frac{1}{2}$	$\frac{1}{2}$			
						b′	$-\frac{1}{2}$	$\frac{1}{2}$			

The first group of components in Table 4 consists only of one line, and hence cannot give the g-values for the two levels involved. But as the g-value of $a^6D_{1/2}$ is known ($g=3{\cdot}328$) from other lines of the spectrum, the g-value for level $z^6F_{3/2}\pm^{3/2}$, $g=1{\cdot}067$, can be computed. The second group of lines gives $g=3{\cdot}324$ for $a^6D_{1/2}$ and 1·000 for $z^6F_{3/2}\pm^{1/2}$. It will be observed that the values for $z^6D_{1/2}$ are identical, but they are not those deduced in the two groups for $z^6F_{3/2}$.

A comparison between these results and those obtained with the line λ3816·746 above considered shows clearly the differences which exist in the g-values of the two pairs of magnetic levels of $z^6F_{3/2}$.

Spectral line	$z^6F_{3/2}\pm^{3/2}$	$z^6F_{3/2}\pm^{1/2}$
$a^6D_{5/2}-z^6F_{3/2}$	1·068	1·006
$a^6D_{1/2}-z^6F_{3/2}$	1·067	1·000

The patterns of lines λ3829·679 and λ3839·799, given in Table 5, will now be considered.

Table 5

λ 3829·679, $a^6D_{3/2}-z^6F_{1/2}$

	M	M'		Sep.	Comp.
a	$-1\frac{1}{2}$	$-\frac{1}{2}$	$a-a'$	24·56	3·102
b	$-\frac{1}{2}$	$\frac{1}{2}$	$b-b'$	5·03	0·635
m	$-\frac{1}{2}$	$-\frac{1}{2}$	$m-m'$	9·78	(1·235)
m'	$\frac{1}{2}$	$\frac{1}{2}$			
b'	$\frac{1}{2}$	$-\frac{1}{2}$			
a'	$1\frac{1}{2}$	$\frac{1}{2}$			

λ 3839·799, $a^6D_{1/2}-z^6F_{1/2}$

	M	M'		Sep.	Comp.
m	$-\frac{1}{2}$	$-\frac{1}{2}$	$m-m'$	10·83	(1·963)
a	$-\frac{1}{2}$	$\frac{1}{2}$	$a-a'$	15·54	1·368
a'	$\frac{1}{2}$	$-\frac{1}{2}$			
m'	$\frac{1}{2}$	$\frac{1}{2}$			

The g-values of $a^6D_{3/2}$ and $a^6D_{1/2}$ now obtained agree with those deduced from many other lines in this spectrum, and are very close to the values given by Landé (1·867 and 3·333)

Comp.	$a^6D_{3/2}$	$a^6D_{1/2}$	$z^6F_{1/2}$
3·102	1·868	—	−0·600
0·635	1·869	—	−0·599
1·368	—	3·331	−0·595

The g-value −0·598 computed for $z^6F_{1/2}$ is very different from the value given by Landé, −0·667. The authors suggest that this difference, and that mentioned before in $z^6F_{3/2}\pm^{1/2}$ may arise from a strong interaction between these magnetic levels which have equal M-values and belong to two adjacent levels of the same term. This hypothesis is sustained by the fact that the sum of the g-values for these two pairs of magnetic levels, with or without perturbation, remains constant, as is shown below :

$\pm 1\frac{1}{2}$	Landé	Observed
$z^6F_{3/2}$	1·067	1·003
$z^6F_{1/2}$	−0·667	−0·598
Sum	0·400	0·405

The magnetic levels $z^6F_{3/2}\pm^{3/2}$ cannot evidently experience perturbation from $z^6F_{1/2}$ because this level has no magnetic levels $M=\pm 1\frac{1}{2}$; its g-value in consequence agrees with the value given by Landé.

The outstanding result of this discussion is that a level $z^6F_{3/2}$ by the influence of an adjacent $z^6F_{1/2}$ exhibits two g-values, one for each pair of its magnetic levels. Hence in calculating its g-values it is not valid to use all the lines of the pattern at the same time; it is necessary to divide them into two groups and calculate the g-values for each group separately.

In view of these results it would seem necessary now to consider what significance must be attributed to the g-values, which are usually given to three places of decimals. Since in the past these values have been obtained without regard to the magnetic levels involved, the question arises as to what accuracy can be attributed to them. This matter will be discussed in a future communication.

Instituto de Optica,
Madrid.
1st June 1950

M. A. Catalán.
R. Velasco.

The Semi-Diurnal Variations of Atmospheric Pressure and of Cosmic-Ray Intensity

The determinations of the semi-diurnal period of cosmic rays have been critically surveyed (Nicolson and Sarabhai 1948). The two measurements, which extend over a sufficient length of time and are of satisfactory statistical accuracy, establish a correlation between the semi-diurnal variation of atmospheric pressure and that of cosmic-ray intensity. In the first (Rau 1939), quoted in this note as I, at a depth of 40 m. of water both maxima coincide. In the second (Duperier 1946), quoted as II, the maximum of cosmic-ray intensity occurs at the same time as the minimum of barometric pressure.

The correlation calculations of II result in $-0\cdot14\%$ for the solar semi-diurnal variation of cosmic-ray intensity and 0·022 cm. Hg for that of atmospheric pressure. From these values a barometric coefficient $-6\cdot4\%$ per cm. Hg is found which is twice the coefficient of the usual barometric effect $-3\cdot45\%$ per cm. Hg (Duperier 1944) and of the right phase. If we apply the same reasoning to I, the barometric coefficient is not of the correct phase.

The negative correlation of cosmic-ray intensity and barometric pressure in the barometric effect and its magnitude are explained by absorption in the increased air-mass and the decay of the μ-mesons. This latter is due to the increased altitude of the isobaric layer in which they are produced (Rathgeber 1938). The theory of the oscillations of the earth's atmosphere (Wilkes 1949) leads to the conclusion that a nodal surface of the semi-diurnal period occurs at a height of about 30 km. It is clear that if the μ-mesons recorded in I were produced above this node the observed positive correlation might be explained (Ehmert 1940). The analysis of the results of I leads to a height of production of 70 km. (Nicolson and Sarabhai 1948) and a range of the primaries of 0·1 gm. cm^{-2}. Taking into account that the mesons measured in II are produced by primaries of a range of 100 gm. cm^{-2}, it becomes evident that the range of the primaries would increase by a factor 10^3 for an estimated ratio of 5 in their energies. Further, the rocket measurements (Gangnes, Jenkins and Van Allen 1949) show that the increase in cosmic-ray intensity due to the production of secondaries starts only at a height below 40 km.

It is the purpose of the present note to propose an alternative explanation which is free from these objections and which is based on Duperier's observation of a positive correlation between cosmic-ray intensity and the temperature of the 100-mb. layer (Duperier 1949). The interpretation of this effect as a density effect due to the competition of the decay of π-mesons into μ-mesons and of their nuclear capture is assumed correct. In the oscillations of the atmosphere the atmospheric pressure at sea level varies as well as the altitude of the isobaric layers and their air density. As it has been shown that all three affect cosmic-ray intensity, its semi-diurnal variations under 40 m. of water S_{40} and without filter S_0 may be written :

$$\text{I.}\quad M_{40}+A_{40}+D_{40}=S_{40}=+0\cdot16\%,$$

$$\text{II.}\quad M_0+A_0+D_0=S_0=-0\cdot14\%,$$

in which M, A and D are the effects of the variations of air-mass altitude and density respectively.

All left-hand terms are unknown. From independent experiments and some approximations it is possible to obtain sufficient additional relationships to calculate A_0 and D_0.

Since the amplitude of the oscillations of barometric pressure is 0·022 cm. Hg and the coefficient of absorption without filter $-2\cdot28\%$ per cm. Hg, $M_0=-0\cdot05\%$. Using the relation that absorption coefficient $\mu=1\cdot56/h$ (Ehmert 1937), in which h is expressed in gm. cm^{-2}, $M_{40}=0\cdot022\times13\cdot6\times1\cdot56/5000=-0\cdot01\%$.

The altitude effect $A=\Delta h/L_\mu$, in which Δh is the altitude variation of the production layer and L_μ the mean free path of μ-mesons before decay. In terms of the mean life τ_μ, the rest mass E_μ and the total energy E, the relativity time transformation gives $L_\mu=c\tau_\mu E/E_\mu$. If the minimum ranges in I and II are in the ratio of the mass of the absorbers, $(10+40)/10=5$, the average energies of the μ-mesons in the layers in which they are produced are estimated to be in the same ratio. Thus supposing that these layers are subject to the same oscillations, the effects will be inversely proportional to the respective energies or $A_0 = 5A_{40}$.

According to the law of radioactive branching (Soddy 1909) the probability of a π-meson producing a μ-meson is

$$W = (1/L_\pi)/([1/L_\pi] + [\rho/R]) = R/(R + \rho L_\pi)$$

L_π is the mean free path of a π-meson before decay into a μ-meson, R the mean range in gm. cm^{-2} before capture, and ρ the density of the air of the layer in which the π-mesons decay. The density effect is then

$$D = (\delta W/\delta\rho)\Delta\rho = -RL_\pi\Delta\rho/(R + \rho L_\pi)^2.$$

Considering that L_π is proportional to the energy of the π-mesons, and that the ratio of their energies is about the same as that of the μ-mesons they produce, we obtain $D_{40} = 5D_0$. The values $A_0 = -0{\cdot}13\%$ and $D_0 = +0{\cdot}04\%$ are calculated from the above deductions.

We may now proceed to discuss the significance of these coefficients in terms of the semi-diurnal oscillations.

With $1/L_\mu = -3{\cdot}9\%$ per km. (Duperier 1949) determined experimentally, the amplitude of the semi-diurnal oscillations of the atmosphere at the height of production of μ-mesons is found

$$\Delta h = A/(1/L_\mu) = 0{\cdot}033 \text{ km.}$$

Bearing in mind that $\delta W/\delta\rho = (\delta W/\delta T)/(\delta T/\delta\rho) = \alpha(\delta T/\delta\rho)$ we derive, from the values given in II, from the average pressure 150 mb. of the layer in which we assume the π-mesons to decay, and from its temperature 220°K.,

$$\delta W/(\delta\rho/\rho) = -0{\cdot}24.$$

As $D = -(\Delta\rho/\rho)\delta W/(\delta\rho/\rho)$, the semi-diurnal relative variation of density becomes $\Delta\rho/\rho = -0{\cdot}17\%$. Taking into consideration that $\Delta\rho/\rho = -\Delta h/h$ for a layer of constant pressures at its upper and lower boundaries, it is deduced that an expansion of 1·7 m. per km. occurs in the 150-mb. layer in phase with the maximum of the semi-diurnal pressure variation.

An expansion of this value which takes place in a layer 16 km. high, the height of the 100-mb. layer, results in an oscillation of some 25 m. at the top of this layer. The results obtained for the altitude variations and for the density variations from two different effects agree. The comparison of our results with the values calculated from the theory of the oscillations of the atmosphere shows that although the magnitude of our results is about ten times as large, they are of the correct phase for altitudes of the producing layer below 20 to 30 km. Considering that our results might be in error by a factor 2 to 3 and that the theory of the atmospheric oscillations is not based on sufficient experimental data, the discrepancy cannot be considered to invalidate either of the two.

Physics Department,
University of Melbourne,
Australia.
28th May 1950.

H. D. RATHGEBER.

DUPERIER, A., 1944, *Terr. Magn. and Atmos. Elect.*, **49**, 1; 1946, *Nature, Lond.*, **157**, 296; 1949, *Proc. Phys. Soc.* A, **62**, 684.
EHMERT, A., 1937, *Z. Phys.*, **106**, 751; 1940, *Naturwissenschaften*, **28**, 28.
GANGNES, A. V., JENKINS, J. F., and VAN ALLEN, J. A., 1949, *Phys. Rev.*, **75**, 57.
NICOLSON, P., and SARABHAI, V., 1948, *Proc. Phys. Soc.*, **60**, 509.
RATHGEBER, H. D., 1938, *Naturwissenschaften*, **26**, 842.
RAU, W., 1939, *Z. Phys.*, **114**, 265.
SODDY, F., 1909, *Phil. Mag.*, **18**, 739.
WILKES, M. V., 1949, *Oscillations of the Earth's Atmosphere* (Cambridge: University Press).

The Mechanism of Colloid Agglomeration in the Formation of Bitter Patterns

Recently Bates and Neale (1950) described quantitative measurements on powder patterns, formed on silicon–iron single crystals, in which the spacing of the powder deposits was found to be twice the domain width. In this note, an explanation is given in terms of the mechanism of colloid deposition, and experimental support is furnished by some patterns observed on a cobalt single crystal.

In zero applied field the colloid particles are randomly orientated, and are attracted to the highly localized stray fields over the surface of a crystal produced by lines of free poles along the intersections of domain walls with the surface. However, when a field is applied parallel to the surface of the crystal, the colloid particles become more strongly magnetized and aligned parallel to the applied field. If this field is perpendicular to a Bloch wall, the colloid dipoles (approximate length 1 micron) are not longer attracted by the lines of free poles which occur at the domain boundaries, which are only about 0.1 micron wide. Instead, they are now attracted to less localized fields. The latter, in the case of the patterns of Bates and Neale, were produced by free poles of opposite sign formed on the crystal surface in alternate domains whose directions of magnetization were not quite parallel to the surface. That colloid deposition under such circumstances occurs only in *alternate* regions of the stray field was explained by Néel (1944). On reversing the applied field the favoured and unfavoured sets of stray fields should exchange positions owing to the reversed polarity of the colloid dipoles, provided that the underlying domain structure is unchanged. This is illustrated in Figures 1 (*a*), (*b*) and (*c*), see Plate, which are patterns observed on a crystal of cobalt whose surface makes a small angle (4°) with a prism plane. The lines are deposits on 180 degree boundaries in Figure 1 (*a*) with no applied field, and on *alternate* 180 degree boundaries in Figures 1 (*b*) and (*c*) where a field is applied parallel to the surface ; it is perpendicular to the lines in opposite senses in Figures 1 (*b*) and (*c*).

The mechanism described may be used to check directions of magnetization in secondary domain structures which are often formed to minimize the total energy of a crystal. An example is shown in Figures 2 (*a*), (*b*) and (*c*). The basic structure in these pictures is similar to that of Figure 1, but a twin band cuts the region investigated. To minimize the magnetostatic energy of the free poles formed on the sides of the twin, a secondary structure of dagger-like domains is formed. That these are regions of reversed magnetization is easily checked by application of a field as in Figures 1 (*b*) and (*c*). The asymmetrical distribution of colloid on the sides of the daggers can be correlated directly with their directions of magnetization.

The pattern observed for the same underlying domain structure appears markedly different according to the direction of the applied field. This is illustrated in Figures 3 (*a*) and (*b*) where a vertical field is applied in and out, respectively. The colloid dipoles are now aligned perpendicular to the surface of the specimen. Since the crystal surface is not exactly a prism plane, alternate domains will have positive and negative free poles at their intersections with the surface; hence the colloid will be attracted to alternate domains and will settle in bands as shown. Again, the oppositely magnetized daggers will be colloid-free when situated in a dark band. Reversal of the field produces a complementary pattern, Figure 3 (*b*).

A complete understanding of the method of colloid agglomeration in simple cases like those illustrated here is of great help in interpreting the more complicated patterns formed on cubic ferromagnetic single crystals, especially those due to secondary domain structure, owing to the greater number of directions of easy magnetization. It can be used either to predict the direction of magnetization in patterns, or conversely, in some cases, to determine the direction of inclination of the crystal surface to a simple crystal plane.

The above work was carried out under the supervision of Professor L. F. Bates, to whom the author records his best thanks. He is greatly indebted to Professor W. Sucksmith for the provision of the cobalt crystal, and to the Department of Scientific and Industrial Research for a maintenance allowance.

University of Nottingham.
23rd May 1950.

C. D. Mee.

Bates, L. F., and Neale, F. E., 1950, *Proc. Phys. Soc.* A, **63**, 374.
Néel, L., 1944, *J. Phys. Radium*, **5**, 241.

← 0·5 mm. →

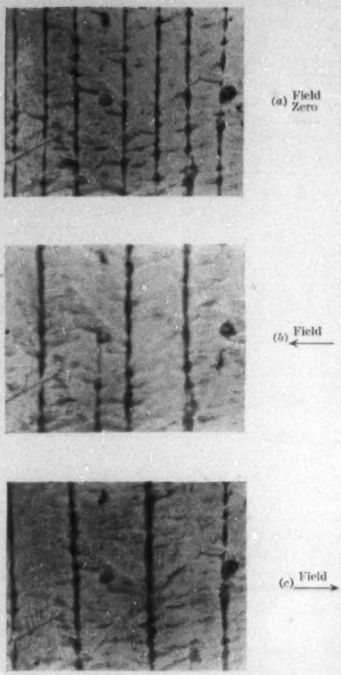
(a) Field Zero
(b) Field
(c) Field

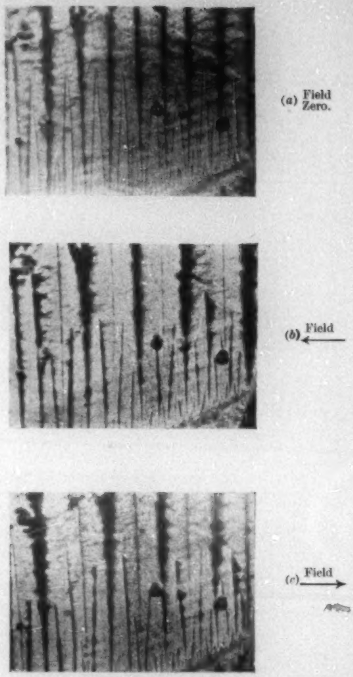
(a) Field Zero.
(b) Field
(c) Field

Figure 1. Hexagonal axis. ↕

Figure 2. Hexagonal axis. ↕

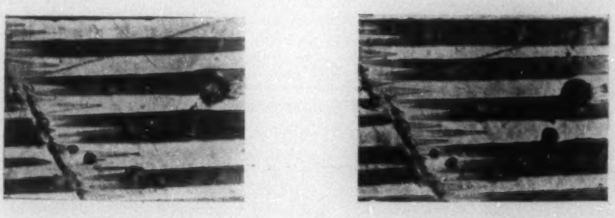

Vertical field " out ".
(a)

Vertical field " in ".
(b)

Figure 3. Hexagonal axis. ←→

CONTENTS FOR SECTION B

PAGE

Prof. S. **Tolansky** and Mr. N. **Barakat**. New Localized Multiple-Beam Interference Fringes formed with Curved Thin Sheets 545
Mr. P. A. **Wayman**. The Monocentric Schmidt–Cassegrain Cameras . . 553
Mr. A. E. J. **Holtham** and Mr. H. A. **Prime**. The Operation and Photographic Characteristics of a Kerr-cell Type of Electro-optical Shutter 561
Mr. F. J. **Bradshaw**. The Optical Emissivity of Titanium and Zirconium . . 573
Dr. R. **Bechmann**. Determination of the Elastic and Piezoelectric Coefficients of Monoclinic Crystals, with particular Reference to Ethylene Diamine Tartrate. 577
Mr. N. W. **Ramsey**. Some Measurements of the Resistivity of Good Insulators . 590
Mr. B. **Milnes** and Mr. R. S. **Unwin**. A Radio Meteorological Investigation in the South Island of New Zealand 595
Mr. C. C. **Newton**, Mr. F. J. **Hyde** and Mr. H. G. **Foster**. Ionospheric Cross-Modulation : Techniques of Measurement 616

Letters to the Editor :

Dr. R. **Street** and Mr. P. D. **Whitaker**. The Measurement of Microwave Power at Wavelengths of 3 cm. and 10 cm. 623
Dr. E. **Schwarz**. Photoconductive Cells of Cadmium Selenide . . . 624
Reviews of Books 626
Contents for Section A 629
Abstracts for Section A 630

ABSTRACTS FOR SECTION B

New Localized Multiple-Beam Interference Fringes formed with Curved Thin Sheets, by S. Tolansky and N. Barakat.

ABSTRACT. A description is given of the mode of formation and optical properties of some new sharp localized multiple-beam fringes produced by cylindrically curved thin sheets which are silvered upon both sides. Illumination with strictly parallel monochromatic light leads to sharp line fringes lying in a plane passing through the centre of curvature and perpendicular to the direction of incidence. An approximate theory is developed and checked by observation. The use of mica as the film leads to interesting birefringent doubling effects. These are complicated by differential phase change effects occurring on reflection at the silver surfaces. Fringe systems have been examined both in reflection and in transmission and related systems obtained with white light used together with a spectrograph. Cleavage step phenomena are revealed by the mica with high precision and high dispersion. It is proposed to name the monochromatic system ‘ fringes of equal tangential inclination ’.

The Monocentric Schmidt–Cassegrain Cameras, by P. A. Wayman.

ABSTRACT. Formulae are obtained for the leading coefficients in the plate-profile expansion of the monocentric Schmidt–Cassegrain cameras. These are used to derive expressions for the monochromatic and chromatic aberrations of the general monocentric system, and spot-diagrams are included to illustrate the image quality in a typical case. A comparison is made with an ordinary Schmidt camera, which has the same aperture and the same depth of figuring on the aspheric plate.

The Operation and Photographic Characteristics of a Kerr-cell Type of Electro-optical Shutter, by A. E. J. Holtham and H. A. Prime.

ABSTRACT. A Kerr-cell electro-optical shutter is described, the shutter action being controlled by a high voltage pulse applied to the cell electrodes. The exposure time used is 2×10^{-6} second, and provision is made for obtaining ‘ delayed ’ exposures up to times of the order of 10^{-4} second. The photographic limitations of the shutter are discussed and the formation of the image considered in some detail. The assumptions necessary for a quantitative photometric analysis of Kerr-cell exposures are stated and an approximate limit is set on the magnitude of errors resulting from such assumptions. The applications of the Kerr-cell technique to the measurement of particular spark channel characteristics are also described.

The Optical Emissivity of Titanium and Zirconium, by F. J. Bradshaw.

ABSTRACT. A method of measuring the optical emissivity of titanium and zirconium using eddy current heating is described. The specimen consisted of a cylinder of metal drilled with a small black-body hole, and its real and apparent temperatures were measured with an optical pyrometer at a mean wavelength of $0{\cdot}652\,\mu$. The variation of emissivity with temperature was investigated and the precautions taken to avoid errors are described.

Determination of the Elastic and Piezoelectric Coefficients of Monoclinic Crystals, with particular Reference to Ethylene Diamine Tartrate, by R. Bechmann.

ABSTRACT. The dynamic determination of elastic and piezoelectric coefficients of crystals belonging to the monoclinic sphenoidal class is discussed using the longitudinal mode of vibration for narrow bars, low-frequency longitudinal and face-shear modes for square plates containing the axis of symmetry, coupled modes for square plates perpendicular to the axis of symmetry and the thickness-shear mode for plates containing the axis of symmetry. A new set of values for the elastic and piezoelectric coefficients and their temperature coefficients for ethylene diamine tartrate is given based on this method. Some properties are considered of face-shear vibrating square plates of ethylene diamine tartrate rotated about the axis of symmetry as functions of the orientation, and of Y-cut plates as functions of the breadth–length ratio.

Some Measurements of the Resistivity of Good Insulators, by N. W. Ramsey.

ABSTRACT. Measurements of the resistivity of good insulators were carried out by measuring the loss of charge on a condenser. A knowledge of the dimensions of the insulator is not required. It was found that the insulation resistances of amber, alkathene, distrene and Perspex increase with time over a period of weeks, the final values being considerably higher than previously published figures. There is no significant difference between the values for the first three materials. The leakage time necessary for reasonable accuracy is indicated.

A Radio Meteorological Investigation in the South Island of New Zealand, by B. Milnes and R. S. Unwin.

ABSTRACT. A Föhn wind blowing off-shore produces super-refraction at radio frequencies. This results in the guiding of very high frequency radio waves beyond the horizon in a radio duct close to the sea surface. The problems involved and the experimental techniques adopted in a long term investigation of this phenomenon are described, and selected data are discussed. Field observations are presented in the form of isopleths of the relevant meteorological quantities and of modified refractive index over the area under investigation, together with contours of radio field strength for wavelengths of 300 cm., 60 cm., 10 cm. and 3 cm., corresponding to the particular meteorological situations described.

It is found that with off-shore winds of strength up to force 6 radio ducts of about 100 m. height are formed and the field strength everywhere beyond the horizon is much increased. In the duct itself, at ranges up to 200 km. from the coast, field strengths approximately equal to the free space level are obtained on wavelengths of 10 cm. and 3 cm., and up to 10 or 20 db. below this level on a wavelength of 60 cm. The duct is not sufficiently high to trap radiation at a wavelength of 300 cm. With stronger winds turbulence limits the duct height to 20 m. and radiation of wavelength above 10 cm. is no longer trapped. The presence of a local sea breeze underneath the off-shore drift has little effect on propagation normal to the coastline.

Ionospheric Cross-Modulation: Techniques of Measurement, by C. C. Newton, F. J. Hyde and H. G. Foster.

ABSTRACT. This paper describes the techniques developed at Birmingham University to measure the amplitude and phase of the ionospheric cross-modulation observed in the test transmissions which are described in detail elsewhere. The devices which were developed and the techniques of observation employed allowed trustworthy measurements to be made with comparative ease.